University of Wales Swansea
School of Engineering

Issues on the Finite Element Modelling of Degradation and Prediction of Failure in Finitely Straining Ductile Materials

Francisco Manuel Andrade Pires
Eng.Mec. (FEUP), M.Sc. (FEUP)

Thesis submitted to the University of Wales in candidature
for the degree of Doctor of Philosophy

September 2005

DECLARATION AND STATEMENTS

DECLARATION

This work has not previously been accepted in substance for any degree and is not being concurrently submitted in candidature for any degree.

Candidate: ________________________

Date: ________________________

STATEMENT 1

This thesis is the result of my own investigations, except where otherwise stated. Other sources are acknowledged by footnotes giving explicit references. A bibliography is appended.

Candidate: ________________________

Date: ________________________

STATEMENT 2

I am hereby consent for my thesis, if accepted, to be available for photocopying and for inter-library loan, and for the title and summary to be made available to outside organizations.

Candidate: ________________________

Date: ________________________

ACKNOWLEDGEMENTS

I would like to express my sincere gratitude to Dr E.A. de Souza Neto and Professor D.R.J. Owen, my supervisors, for their enthusiasm, guidance, constructive criticism and support during the course of this research.

Over the last four years, I received assistance and encouragement from many different people. I wish to acknowledge the entire Rockfield crew for providing a stimulating environment. I am grateful to Dr Attila Garai, Dr Jian Yu, Dr Mark Cottrell for teaching me the tricks of the trade and for ongoing technical discussion. Dr G.Q. Liu especially, has been of great help, and I wish to thank him for numerous helpful discussions and suggestions. I also wish to thank Mr James Amstrong for his patience and constructive criticism. For his enthusiastic help, advice and discussion I wish to acknowledge Dr Martin Dutko. Furthermore, warm thanks are also extended to Dr A.J.L. Crook. The managers of Rockfield Software Ltd., especially Dr J.M. Rance and Dr H.J. Anderson, are thanked for the cooperation and for keeping it all in perspective.

I am also grateful to my fellow researchers Antonio Orlando, Wulf Dettmer, Andreas Rippl, Holger Ettinger, Sava Slijepčević, Miguel Rodriguez Paz, Chenfeng Li, Mauricio Lobão and many more, for countless discussions and for making my stay in Swansea enjoyable.

I would also like to thank the colleges of DEMEGI – Department of Mechanical Engineering and Industrial Management, Faculty of Engineering. Particularly, Professor V.S. Silva e Sá and Dr J.A. César de Sá who suggested the topic of research and supported my decision to pursue Ph.D. studies at Swansea.

I would like to acknowledge the financial support received from *Portuguese Science and Technology Foundation* (FCT), Grant ref. SFRH/BD/1078/2000.

For the unconditional incentive and constant optimism received, I wish to express the greatest gratitude to my parents and sister, without which none this would have been achievable.

Finally, I am especially grateful to Silvina, for her dedication, understanding and companionship during this hectic period.

To my parents
my sister and Silvina

SUMMARY

ASPECTS of constitutive modelling and numerical prediction of failure in finitely straining ductile metals are investigated in this thesis. Attention is focused on the construction of a framework for prediction of failure. The development of a model for finite strain elasto-(visco)plastic damage; a low order finite element for the numerical treatment of incompressibility and an adaptive mesh refinement strategy for this class of problems, constitute the building blocks of the overall approach. Emphasis is given to the efficient numerical simulation of the proposed theories in large scale problems.

The characterisation of material response has to account for the interaction between the different phenomena that precede fracture initiation. The derivation of constitutive models is addressed within Continuum Damage Mechanics theory. Particularly, the effect of micro-crack closure which may dramatically decrease the rate of damage growth under compression is emphasised.

With regard to the computational treatment of incompressibility, a new technique which allows the use of simplex finite elements in the large strain analysis of nearly incompressible solids is proposed. It is based on relaxation of the excessive volumetric constraint by the enforcement of near-incompressibility over a *patch* of elements. The new elements are implemented within an implicit quasi-static and an explicit transient dynamic finite element environment.

With the aim of achieving an effective and robust adaptive strategy for this class of problems, a new damage-based error indicator which represents the essential features of the phenomena under consideration is addressed. The idea is to correlate the adaptive procedure with the failure mechanism.

The algorithms for numerical integration of the corresponding path dependent constitutive equations are discussed in detail. The strategy for numerical simulation of the associated incremental boundary value problems relies on fully implicit and explicit displacement based finite element procedures.

The robustness and efficiency of the proposed framework is illustrated by means of numerical examples. These are compared with experiments and numerical results obtained by other authors.

Contents

1 Introduction **1**
1.1 The scope of the thesis . . . 3
1.1.1 Continuum constitutive modelling . . . 3
1.1.2 Element technology for near incompressibility . . . 4
1.1.3 Adaptive remeshing for history dependent problems . . . 4
1.1.4 Numerical aspects . . . 5
1.2 Layout . . . 5

2 Physical aspects of deforming metals **8**
2.1 Structure of metals . . . 9
2.1.1 Crystal structure . . . 9
2.1.2 Phases and precipitates . . . 11
2.1.3 Physical mechanisms of deformation . . . 12
2.2 Damage mechanisms and their appearance . . . 14
2.2.1 Ductile damage at room temperature . . . 14
2.2.2 Ductile damage at elevated temperatures . . . 17
2.2.3 Brittle damage . . . 17

3 Continuum mechanics and thermodynamics **19**
3.1 Kinematics of deformation . . . 20
3.1.1 Configurations and motions of continuum bodies . . . 20
3.1.2 Material and spatial descriptions . . . 22
3.1.3 The deformation gradient . . . 23
3.1.4 Polar decomposition. Stretches and rotation . . . 25
3.1.5 Strain Measures . . . 26
3.1.6 The velocity gradient. Rate of deformation and spin . . . 27
3.1.7 Superimposed rigid body motions and objectivity . . . 27

3.2 Stress and Equilibrium . . . 28
3.2.1 The Cauchy stress tensor . . . 29
3.2.2 Alternative stress tensors . . . 30
3.3 Fundamental laws of thermodynamics . . . 31
3.3.1 Conservation of mass . . . 31
3.3.2 Momentum balance . . . 31
3.3.3 The first principle . . . 32
3.3.4 The second principle . . . 32
3.3.5 The Clausius-Duhem inequality . . . 32
3.4 Constitutive theory . . . 33
3.4.1 Thermodynamics with internal variables . . . 33
3.4.2 Phenomenological and micromechanical approaches . . . 36
3.4.3 The purely mechanical theory . . . 37
3.4.4 The constitutive initial value problem . . . 37
3.5 Weak equilibrium. The principle of virtual work . . . 37
3.5.1 The spatial version . . . 38
3.5.2 The material version . . . 38

4 Finite element modelling of finite strain plasticity 39
4.1 Finite strain elasto-plasticity. A brief review . . . 40
4.2 Hypoelastic-based plasticity models. Rate forms . . . 40
4.2.1 Objective stress rates . . . 41
4.2.2 Hypoelastic-based plasticity models . . . 42
4.2.3 Integration algorithms and incremental objectivity . . . 44
4.2.4 Integration of Green-Naghdi rate-based model . . . 44
4.3 Explicit dynamic finite element solution strategy . . . 47
4.3.1 The discretised dynamic equations . . . 48
4.4 Hyperelastic-based multiplicative finite plasticity . . . 51
4.4.1 Multiplicative elasto-plasticity kinematics . . . 51
4.4.2 The logarithmic elastic strain measure . . . 53
4.4.3 A general isotropic large strain plasticity model . . . 54
4.4.4 The general elastic predictor/return mapping algorithm . 56
4.4.5 The incremental boundary value problem . . . 59
4.5 Implicit quasi-static finite element solution strategy . . . 62
4.5.1 The Newton-Raphson scheme. Linearization . . . 63

5 Damage constitutive modelling and failure in ductile metals 64
5.1 Introduction . . . 65
5.2 Continuum damage mechanics . . . 66
5.2.1 Original development. A brief review . . . 66
5.2.2 Ductile Plastic Damage . . . 68
5.3 Lemaitre's elasto-plastic damage theory . . . 70
5.3.1 Original model . . . 71

5.3.2 Improved model 76
5.4 Elasto-plastic damage model with crack closure 82
5.4.1 The constitutive model 83
5.4.2 Integration algorithm 87
5.4.3 The tangent operator 96
5.4.4 Numerical Examples 98
5.5 Elasto-viscoplastic damage model with crack closure 107
5.5.1 The constitutive model 107
5.5.2 Integration algorithm 109
5.5.3 Consistent tangent operator 116
5.6 Concluding remarks 117

6 Finite element technology for finite nearly isochoric deformation 119

6.1 Introduction 120
6.2 F-bar methodology 121
6.2.1 Stress computation 122
6.2.2 The modified F-bar deformation gradient 123
6.3 Nodal average volume technique 124
6.3.1 The average nodal volume change ratio 125
6.3.2 F-bar based average nodal volume triangle 126
6.3.3 Numerical assessment 130
6.3.4 Closing remarks 138
6.4 F-bar patch method 139
6.4.1 The proposed F-bar-patch method 139
6.4.2 The modified F-bar deformation gradient defined for a patch of elements 140
6.4.3 Plane strain problems 141
6.4.4 Element tangent stiffness matrix 142
6.4.5 Computational implementation aspects 145
6.4.6 Numerical examples 148
6.4.7 Explicit implementation 168
6.4.8 Numerical examples 170
6.5 Concluding remarks 176

7 Adaptive remeshing for history dependent problems in solid mechanics 178

7.1 Introduction 179
7.2 Entity based model description 180
7.3 *A posteriori* error estimates 180
7.3.1 Error estimation for non-linear problems. A brief overview 181
7.3.2 Residual and recovery based error indicators 183
7.3.3 Error indicators for failure analysis 186

7.3.4 Error indicator based on damage dissipation 188
7.4 Prediction of the new mesh density 190
7.5 Mesh regeneration 191
7.6 Transfer operations for evolving meshes 192
7.6.1 Smoothing transfer for implicit and explicit schemes . . . 194
7.6.2 The transfer operation 195
7.6.3 Mapping of internal variables - Transfer operator $\mathcal{T}_1$ . . . 198
7.6.4 Mapping of the nodal variables - Transfer operator $\mathcal{T}_2$ . . 203
7.6.5 Mapping of the contact variables - Transfer operator $\mathcal{T}_3$. 204
7.7 Numerical examples 204
7.7.1 Suitability for adaptive analysis 204
7.7.2 Mesh prediction based on damage dissipation 210
7.8 Concluding remarks 219

8 Conclusion and Final Remarks 220
8.1 Summary and conclusions 221
8.1.1 Damage constitutive modelling 221
8.1.2 Element technology for near incompressibility 221
8.1.3 Adaptive remeshing for history dependent problems . . . 222
8.2 Suggestions for future research 223

A Isotropic functions of a symmetric tensor 247
A.1 Isotropic tensor-valued functions 248
A.2 Spectral decomposition 248
A.2.1 Spectral theorem 248
A.2.2 Eigenprojections 249
A.2.3 Characteristic equation. Principal invariants 249
A.3 A class of isotropic tensor functions 251
A.3.1 Two dimensions 252
A.3.2 Three dimensions 252

B Linearisation of the internal virtual work 254
B.1 The virtual work equation 254
B.2 Virtual work linearisation 255
B.2.1 Map internal virtual work to the material configuration . 255
B.2.2 Linearisation in the material configuration 256
B.2.3 Map the linearised expression to the spatial configuration 257

CHAPTER 1

INTRODUCTION

OVER the last years, there has been an increasing industrial awareness of the potential benefits that accrue from employing scientifically-based approaches in the conception of new products. This is particularly true in the design of complex geometries with tight mechanical and safety specifications. The conception of such products requires careful planning of every stage. It is necessary to ensure that the designed products and processes are optimised, specially in competitive sectors of manufacturing industry, and comply with both functionality and low production cost. To overcome the challenging problems encountered during the design stage and maintain a competitive edge, it is of the utmost importance to be constantly up-to-date with the latest scientific and technological progress.

The need for reliable and robust tools in engineering design allied to the advent of digital computers, has triggered the gradual evolution of numerical techniques. The remarkable improvements in numerical models and associated algorithms and, more importantly, dramatic increases in computational power/cost ratios have made a great impact on the acceptance of numerical techniques within both research and industrial environments. Computational procedures, mostly based on the finite element method, have been continually developed and improved, for both linear and nonlinear applications. Particularly, in the context of nonlinear solid mechanics problems, considered in this work, there has been considerable advancement in several topics of finite element research. In many areas, such techniques have reached a high degree of predictive capability and, today, are of considerable assistance to the designer and essential instruments to address realistic engineering problems.

During the initial development of computer codes for stress analysis, the constitutive description of the material response has been mostly dominated by the classical and mathematically established theories of elasticity and elasto-(visco)plasticity. Over the years, the finite element procedures originally based in such material models have been continuously modified and adapted to cope with more complex deformation processes involving, large deflections, finite strains and viscous effects, etc. One of the most outstanding examples of developments in the field of nonlinear solid mechanics, which have had a major impact on simulation of forming processes, are the strides that have been made in the numerical solution of large deformation problems at finite inelastic strains, and, in particular, finite strain plasticity problems (Perić & Owen, 2004). The formulation of rigorous solution procedures has been the subject of intense debate over the last two decades or so and only recently has some consensus been reached on an appropriate constitutive theory based on tensorial state variables to provide a theoretical framework for the macroscopic description of a general elasto-(visco)plastic material at finite strains.

Despite such advances, several issues still remain open, such as the modelling of material failure that may result from the gradual internal microstructural deterioration associated with high straining. In such cases, the development of new and more refined constitutive models deserves careful consideration, and the topic remains a fruitful area of research.

A general feature encountered in the FE simulation of finite strain (visco) plasticity problems is that the optimal mesh configuration changes continually throughout the deformation process requiring mesh coarsening as well as mesh refinement during use of any adaptive remeshing process. Considerable benefits may accrue by implementation of such strategies in terms of robustness and efficiency, realizing that the requirements of computational efficiency are ever increasing. At the same time, error estimation procedures will play a crucial role in quality assurance by providing reliable finite element solutions.

In many cases, the computational treatment of the problem, is far simpler when lower order elements are adopted. This is particularly true in large scale problems, which may require the incorporation of adaptive mesh refinement techniques, and where a number of complex interacting phenomena, such as frictional contact, high strains, progressive material degradation, may be present. In addition, the adopted finite elements should be able to produce accurate solutions under constitutive constraints such as the nearly incompressibility that characterises ductile metals.

Obviously, the final objective is to provide cost effective computer programs which can accurately predict the behaviour of materials under a broader range of circumstances. Therefore, the development of robust and efficient numerical methods, suitable to the numerical simulation of large scale problems, must accompany the derivation of such new theories.

1.1 The scope of the thesis

The purpose of this thesis is to construct an efficient framework, which incorporates several numerical techniques, to model the gradual internal deterioration of ductile metals and predict material failure in relevant practical problems. Due to the diversity and complexity of the physical phenomena involved, several different computational aspects of the problem have been addressed, leading to the enhancement of existing algorithms and development of new techniques. Attention is focused in the derivation of:

- Constitutive models for elastoplastic and elasto-viscoplastic damage at finite strains. The main objective is to include the effect of micro-crack closure in the conventional Lemaitre isotropic ductile damage model (Lemaitre, 1985a,b);
- A technique which allows the use of simplex finite elements (three noded triangle in 2-D and four noded tetrahedron in 3-D), in the large strain analysis of nearly incompressible solids;
- An efficient adaptive remeshing strategy that includes the use of *a posteriori* error estimates, using Zienkiewicz & Zhu (1987) projection/recovery technique, here based on the *rate of damage work* together with appropriate transfer operators. The aim is to correlate the adaptive procedure with the underlying failure mechanism;

Emphasis is given to the issues related to continuum modelling as well as to the computational aspects relevant to the application of the proposed models in large scale numerical simulations in both *implicit* and *explicit* time integration schemes.

1.1.1 Continuum constitutive modelling

Crucial to the characterisation of material response close to rupture is the appropriate formulation of constitutive equations which account for the interaction between the different phenomena that precede fracture initiation. Damage and plasticity are undoubtedly coupled, as the presence of internal deterioration introduces local stress concentrations which may in turn drive plastic deformation. One possible alternative to describe the coupling between damaging and material behaviour is the adoption of the so-called *Continuum Damage Mechanics* (CDM) theory (Kachanov, 1958; Chaboche, 1981; Lemaitre, 1984; Krajčinović, 1985). According with this approach, the development of constitutive models is based on the assumption that the progressive internal deterioration observed prior to the onset of a macro-crack can be effectively represented by one or more internal variables of scalar, vectorial or tensorial nature. Such variable(s) - named the damage variable(s) - can be seen as phenomenological, averaged counterparts of microscopic measures of defects within a *representative volume element*. Their evolution must be defined by thermodynamically consistent constitutive relations, usually represented by a set of differential equations in time. Based on a solid mathematical and thermodynamical foundation, Continuum Damage Mechanics is today recognised as an effective tool of mathematical modelling, which can help bridge the gap between the microscopic analysis of the internal deterioration of the materials and engineering models suitable for design. In this context, a purely phenomenological approach to the description of internal degradation is adopted. The need for consideration of micro-crack closure effects will be particularly emphasised in the development of models for damage in ductile materials.

1.1.2 Element technology for near incompressibility

One aspect of paramount importance is the fact that the adopted finite elements must be able to cope with the wide range of techniques employed in the simulation of complex problems. This is particularly true in the context of industrial forming processes, where complex geometry and contact conditions are typically present and many problems are characterised by extremely high strains. Even when the initial geometry is simple, the presence of very large strains may lead to poorly shaped elements unless some form of adaptive remeshing is used. In addition, the adopted finite elements should be able to produce accurate solutions under constitutive constraints such as the nearly incompressibility that characterises ductile metals. As the incompressibility limit is approached, conventional displacement-based finite elements with low order shape functions are known to perform poorly, showing the typical *volumetric locking* behaviour which may completely invalidate the finite element solution.

This topic constitutes one of the most challenging tasks in finite element research. Due to their inherent simplicity, standard isoparametric simplex elements (linear triangles in 2-D and linear tetrahedra in 3-D) are known to provide an excellent framework in which contact conditions coupled with the necessary remeshing procedure can be dealt with in an effective and efficient manner. Therefore, the numerical treatment of incompressibility, was addressed here with the development of a methodology which extends the so-called *F-bar* procedure proposed by de Souza Neto *et al.* (1996) so as to accommodate simplex elements in the large strain analysis of nearly incompressible solids.

1.1.3 Adaptive remeshing for history dependent problems

For a finite element solution to have practical industrial use, predicted fields such as stresses, inelastic strains and, particularly in the present context, damage fields (including the possible prediction of material failure location), must be contained within acceptable bounds of error. Error bound solutions can only be attained if appropriate mesh quality is maintained throughout the entire simulation. In addition to acceptable element aspect ratio, mesh quality implies sufficient refinement in areas where the relevant fields present steeper gradients. These areas are the portions of the workpiece where most of the *action* localises, i.e., where the relevant dissipative mechanisms are most active. In order to effectively model material failure the essential idea is to correlate the adaptive procedure to the underlying failure mechanism. In this thesis, the damage model that includes micro-crack closure is employed to derive an error measure based on rate of *damage work*. Therefore, the adaptive procedure should not only capture the progression of the plastic deformation but also provide refined meshes at regions of possible material failure.

1.1.4 Numerical aspects

The use of path dependent constitutive equations, as is the case for damage models, leads invariably to the necessity of formulating algorithms for numerical integration of the associated rate constitutive equations. To integrate the constitutive equations for finite strain elasto-(visco)plastic damage, algorithms based on the operator split method, which generalizes the standard return mappings of the infinitesimal theory, are used.

The basic strategy for the numerical simulation of the models derived in this thesis relies on displacement based incremental finite element procedures, in conjunction with the strain driven numerical integration procedures mentioned above. Since the equations associated with such constitutive models are in general highly non-linear, the use of appropriate methods for solution of non-linear problems is of crucial importance in determining the overall efficiency of the proposed constitutive-numerical framework. The exact linearisation of the field equations provides the basis of the standard Newton-Raphson iterative scheme for solution of the associated nonlinear boundary value problem (Hughes & Pister, 1978). We remark that, within the present framework, consistent linearisation is regarded as a crucial aspect of the formulations presented. The asymptotically quadratic rates of convergence resulting from the exact linearisation of the field equations more than justify the importance of this issue.

1.2 Layout

The thesis is divided into eight chapters. After this introductory one, Chapter 2 reviews some physical aspects related to mechanisms of deformation and damage that lead to fracture onset of ductile metals.

Chapter 3 This chapter sets out the basic concepts of continuum mechanics and thermodynamics which form the basis for the constitutive models developments in the subsequent chapters.

Chapter 4 In many applications the infinitesimal deformation hypothesis cannot be introduced without significant loss of accuracy. Therefore, this chapter is devoted to the theory and finite element implementation of *finite strain* elasto-plasticity and visco-plasticity. The theory and numerical algorithms discussed here are an extension of the *infinitesimal* ones.

Chapter 5 In this chapter, models for finite strain ductile damage for rate independent and rate dependent materials are developed. These isotropic damage models include the important effect of micro-crack closure and preserve the classical return mapping algorithms employed in the integration of the constitutive equations of infinitesimal elastoplasticity. The prediction of failure in ductile metals is based on fracture indicators and the scalar damage variable.

Chapter 6 The numerical treatment of incompressibility for low order displacement based finite elements is addressed in this chapter. Firstly, an assessment of the average nodal volume formulation for the analysis of nearly incompressible solids under finite strains, is undertaken. Secondly, a methodology which allows the use of simplex finite elements is proposed. The derivation of the exact tangent moduli, employed in the solution of the implicit iterative scheme, is described in detail. Finally, the same concept is adapted for use within an explicit transient dynamic finite element environment.

Chapter 7 For a finite element solution to have practical industrial use, predicted fields must be contained within acceptable bounds of error. Error bound solutions can only be attained if appropriate mesh quality is maintained throughout the entire simulation. An overview of the existing error estimates and transfer operators for inelastic problems is included and an *a posteriori* error indicator using the Zienkiewicz & Zhu (1987) projection/recovery technique and based on ductile fracture concepts is suggested, i.e., *rate of damage work*, for ductile metals.

Chapter 8 In this chapter the main issues addressed in the thesis are summarized and the conclusions of this work are presented along with suggestions for future research.

In addition to the above, two appendices are included. Appendix A is concerned with isotropic tensor-valued functions of a symmetric tensor which are exploited throughout the thesis. It presents some important basic properties as well as formulae that can be used in practice for the computation of function values and function derivatives. In Appendix B we present the derivation of the linearised version of the virtual work equation. In particular, we show the basic steps in the linearisation of the virtual work equation leading to the *F-bar-Patch* element tangent stiffness expressions proposed in chapter 6.

It is worth noting that part of the research work provided in this thesis has been presented in references (Owen *et al.* , 2002; Andrade Pires *et al.* , 2003a,b; Owen *et al.* , 2003; de Souza Neto *et al.* , 2003; Owen *et al.* , 2004c,b,a; Andrade Pires *et al.* , 2004a,b,c; de Souza Neto *et al.* , 2005b).

CHAPTER 2

PHYSICAL ASPECTS OF DEFORMING METALS

SINCE the identification of dislocations and relative motion, or *slip*, on specific crystallographic planes in the 1930's, enormous advances have been made in understanding the underlying physics of plastic deformation. This has lead to the development of theories of plasticity, including the description and evolution of polycrystalline texture, dislocation interactions and hardening laws. Bolstered by the advances in high-resolution electron microscopy, the examination of the atomic-level structure brought new insights to the physical phenomena. Much has been revealed about the physics of strain hardening, dislocation interactions, effects of second phases and high angle boundaries.

Several theories (or analytical models) were devoted to the formulation of constitutive models to describe the actual behaviour of materials. Despite some great strides in enriching the arsenal of methods for handling a variety of practically important problems, continuum mechanics models, that are a true representation of the physics of real material systems, for a wide range of circumstances remains still an elusive goal.

The objective of this chapter is to give a general idea of the structure, mechanisms of deformation and gradual internal deterioration of metals, commonly used in engineering practice. The understanding of the underlying physical phenomena is necessary in order to formulate the hypothesis upon which the macroscopic phenomenological theories, presented in Chapters 3 – 5, can be based. The continuum models, must indeed integrate the phenomena associated with discrete entities such as atoms, crystals, molecules, cells, etc., to the level of homogeneous continuum models.

2.1 Structure of metals

A summary of the physical concepts that underly the structure of metals and mechanisms of deformation is presented in this section. The material reviewed here is quite basic and is meant to refresh some important concepts that will be used in forthcoming chapters. A more comprehensive account of the subject can be found, for instance, in Dieter (1986).

2.1.1 Crystal structure

The great majority of metals and alloys which are used in engineering practice consist of *polycrystaline aggregates*, that is, they are composed of large numbers of *grains*, each of which has the structure of a simple crystal - *monocrystal.* These grains can be seen by examining a suitably prepared, polished section using a light microscope. The grain diameters can vary from some microns to several millimeters and the borders between adjacent grains are known as *grain boundaries* (see Figure 2.1).

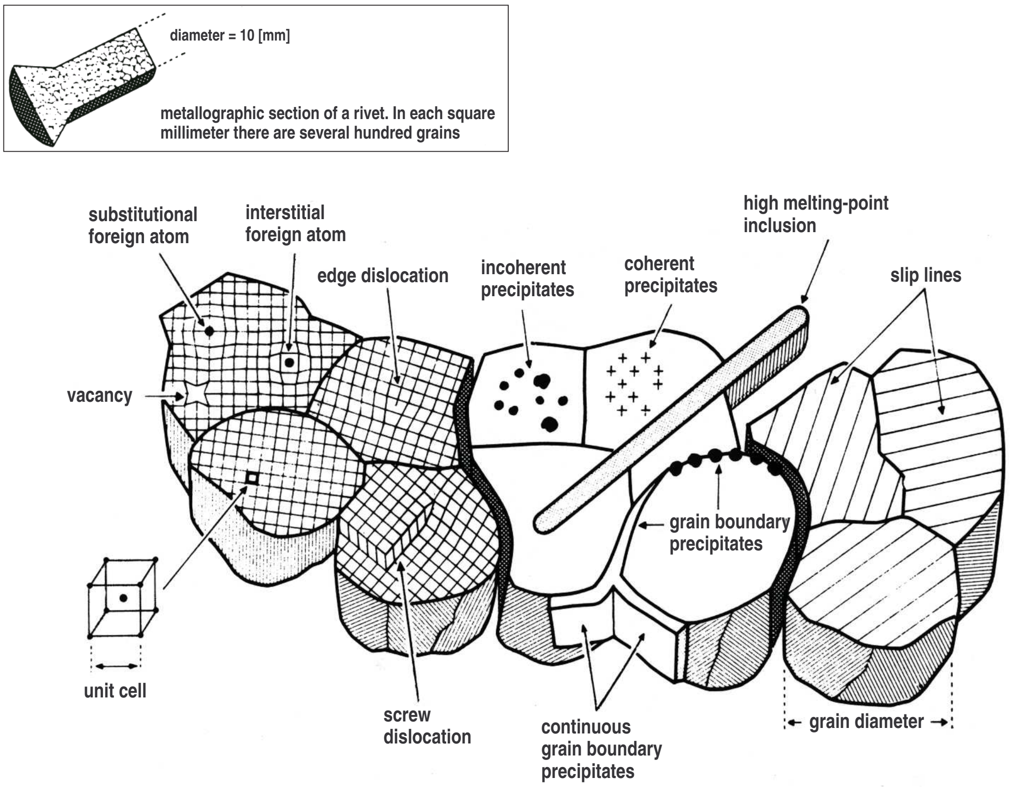
diameter = 10 [mm]
metallographic section of a rivet. In each square millimeter there are several hundred grains
substitutional foreign atom
interstitial foreign atom
edge dislocation
incoherent precipitates
coherent precipitates
high melting-point inclusion
slip lines
vacancy
grain boundary precipitates
unit cell
screw dislocation
continuous grain boundary precipitates
grain diameter

Figure 2.1: Structure of a polycrystalline metal based on the example of an iron rivet (reproduced from Engel & Klingele (1981)).

Inside each grain the atoms are arranged in a three-dimensional geometric fashion and are held together by electromagnetic forces between the electrons of neighbouring atoms. The order of magnitude of the "radius" of an atom varies from 10^{-7} to 10^{-6} $[mm]$ and the bond between atoms results from the sharing of electrons in the outer shells. The stable three-dimensional arrangement of atomic packing is determined by the *minimum energy* required to fit the atoms together in a regular pattern. It should be noted, that in Figure 2.1, the lattice spacing is largely exaggerated, for illustrative purposes, in relation to the grain size. The most common metallic lattices belong to one of the following systems: cubic centered (CC) crystals, face centered cubic (FCC) crystals and close packed hexagonal (CPH) crystals (see Figure 2.2). These lattices possess axes and planes of symmetry, the latter being in general the planes in which the atoms are most densely packed and which possess a lower resistance to shear. Those planes are called *slip* or *glide* planes. Within each slip plane there are in turn preferred *slip directions*, which once more are those of the atomic rows with the greatest density, for the same reason. A slip plane and a slip direction are said to form a *slip system.*

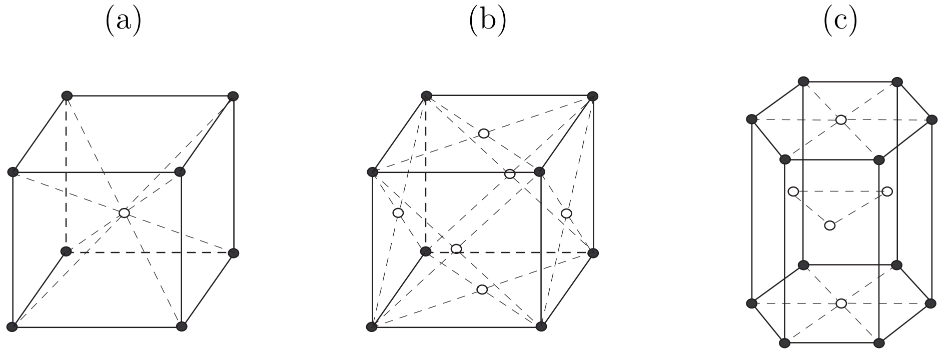

Figure 2.2: Cell structures. Schematic illustration: (a) CC crystals; (b) FCC crystals and (c) CHC crystals.

The structure of the perfect crystal, as described above, would yield higher cohesive forces binding atoms together, for a small displacement of the atoms from their original position, than an actual crystal is observed to sustain. In a real crystal, experimental evidence shows that the *elastic* deformation ceases after a *macroscopic* shear strain of order 10^{-4}, whereas a perfect crystal should attain an elastic shear strain of order 10^{-1}. This discrepancy can only be explained by the presence of defects that disturb the crystal lattice, formed during growth or introduced by subsequent handling. These imperfections are generally classified as *point and surface* defects and *dislocations* (line defects).

Point and surface defects When a foreign atom occupies the place of an atom of the host lattice, this is referred to as a *substitutional* impurity atom. If the foreign atom is located between the atoms of the host lattice, this is referred as an *interstitial* impurity atom. An unoccupied lattice site in known as a *vacancy.* These imperfections result in a local distortion of the lattice (see Figure 2.1). Another type of deficiency, which is characterized by the surfaces of separation between crystals or parts of a crystal where the orientations are different, is known as *surface defects.* Their thickness is of the order of 8-10 atomic radii. Typical examples are grain boundaries in polycrystals, dislocation loops and cells, twin crystal boundaries, interface between two phases (some of these defects are schematically illustrated in Figure 2.1).

Dislocations (line defects) The most important lattice defects in grains are known as *dislocations* and they are the main source of plastic flow in metals. A line of dislocation is a defect in the arrangement of atoms which is repeated periodically and which represents the equilibrium state of atoms with slightly different magnetic fields. Dislocations are created during the growth of the crystals and their density is very high in most of metals. An *edge dislocation* in a crystal can be visualized as one line on one side of which an extra half-plane of atoms has been introduced, as depicted in Figure 2.1, for a simple cubic lattice. At a sufficient number of atomic distances away from the dislocation line, the lattice is virtually undisturbed. A *screw dislocation* is exemplified by a local rotation of the upper part of the crystal (see Figure 2.1).

2.1.2 Phases and precipitates

Most metals and alloys are generally produced in a liquid state, and their structure is formed as they solidify when cooled. The term *phase* signifies crystallites having the same crystal structure and similar chemical composition. Although alloys can have a single phase, the majority consists in more than one phase. The different phases are formed either during cooling from the molten state or during the subsequent heat treatment as a consequence of the temperature dependence of the solubilities of the component elements. If a metal lattice contains more foreign atoms than it can dissolve at any given temperature, then the super-saturation results in the formation of finely dispersed particles of a second phase known as precipitates. *Coherent precipitates* show a close relationship with the parent lattice. *Incoherent precipitates* are those with their own phase boundaries (Figure 2.1).

A favored region for precipitation is the grain boundary. Grain boundary precipitates may completely surround the grains as a continuous layer. High melting point inclusions which have been present as a suspension in the metallic melt can be found irregularly distributed through the subsequent formed grain structure (see Figure 2.1).

Remark 2.1 *Considering the random orientation of individual grains and defects in a typical metal, the overall behaviour of the aggregate in many cases, is* *largely isotropic. However, in practice, when subjected to finite inelastic straining, polycrystalline metals rarely remain truly isotropic but, under a wide range of circumstances, the isotropic hypothesis provides a very good approximation. Typical phenomena as the* **Bauschinger effect** *and* **preferred orientation***, which occur as a result of different plastic deformation of grains with different orientations, demonstrate the important effect of crystalline structure on the plastic behaviour. In such cases the assumption of isotropy can not be introduced without substantial loss of accuracy of the constitutive model.*

2.1.3 Physical mechanisms of deformation

Elastic deformation

Elasticity is directly related to the relative movement of atoms. The physical study of the properties of a lattice leads to the theory of elasticity. The observed macroscopic effect is the result of the variations in the interatomic spacing necessary to balance the external loads, and also reversible movement of dislocations. These geometrical adjustments are essentially *reversible*. In a purely elastic deformation, the initial configuration of atoms is restored upon the removal of the load.

Permanent deformation

Plastic or viscoplastic permanent deformations occur at the *grain level*, and correspond to a relative displacement of individual blocks or layers of metal along definite lattice planes within each grain, which remain when the load is removed. Depending on the case, the deformations are purely *intragranular* (inside the grains) or involve *intergranular* displacements. The ratio of joint deformation to grain deformation remains small, but it generally increases with increasing temperature and also decreasing strain rate.

Deformation by slip and twinning The symmetry planes in the crystal lattice, which are also the reticular planes of the most densely packed atoms, form the parallel planes with the greatest distance between them. It is therefore on these planes that slip due to shear can occur in the direction of maximum shear stress. They occur in the form of parallel slip bands which result in steps on the exterior of the surface samples [see Figure 2.3(a)] or in the form of twins which consist of slips symmetric with respect to a plane [see Figure 2.3(b)]. Twinning is probably the most characteristic deformation that occurs at average room temperature. It occurs in CC and CPH crystals in conjunction with slips, but also in FCC crystals where the energy of stacking defects is low. These defects, slips and twinnings, are, in fact, heterogeneous deformations at the crystal level, but may be considered homogeneous at the macroscopic level.

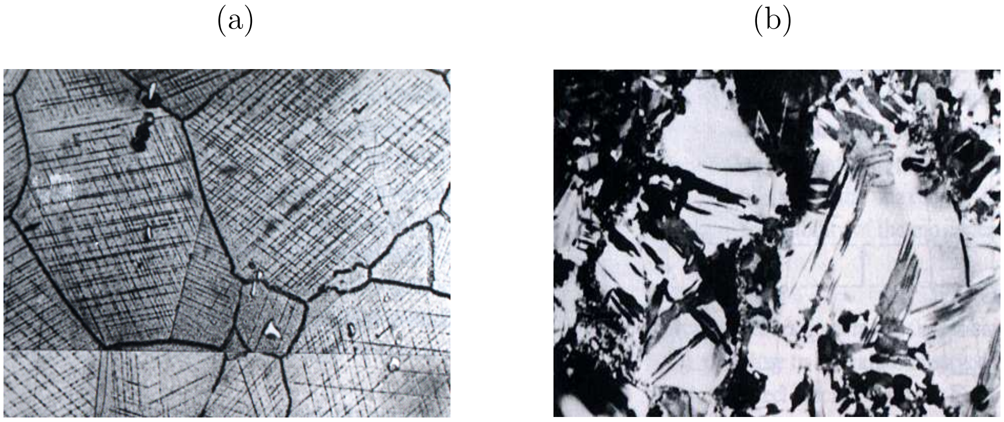

Figure 2.3: Microscopic aspect. (a) Slip bands in nickel based Waspaloy; (b) Twinning deformation in zinc (reproduced from Lemaitre & Chaboche (1990)).

Deformation by dislocation movements The presence of dislocations considerably reduces the stability of the crystal lattice. Their mobility is the essential cause of permanent deformations, homogeneous at the macroscale. Large dislocations movements increase the density of dislocations which, in turn, increases the number of blockings and leads to further hardening. When, under an external load, an edge or screw dislocation moves across a crystal, irreversible displacement occurs - *slip displacement* (see Figure 2.4). This displacement mechanism requires the breaking of bonds only in the vicinity of the dislocation line, and successively from one atom to the next. In the more complex case of a dislocation loop, the plane of the loop can digress into another plane (a perpendicular one for example) arising from its "pure screw" point to avoid an obstacle such as an impurity - *deviated slip*.

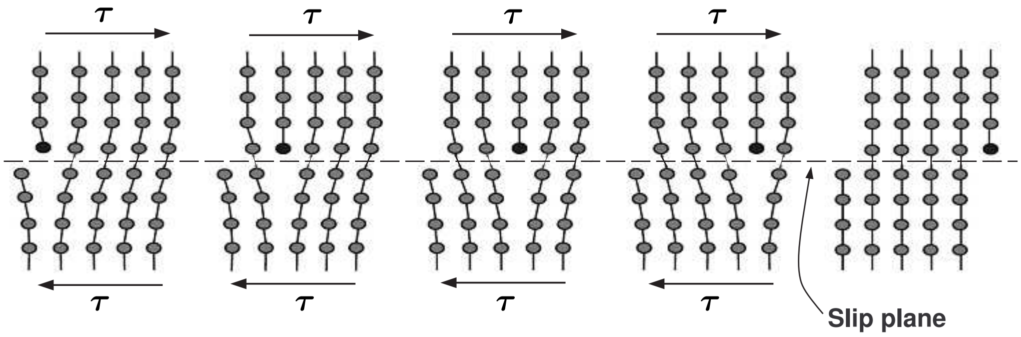

Figure 2.4: Movement of an edge dislocation under a shear stress.

An edge dislocation can move perpendicularly to its slip plane with the transport of material. If a void is close to a dislocation line, then a distortion of the lattice results in the rearrangement of the whole row of atoms. Thus, in this mechanism called *climb displacement*, the dislocation climbs up by one interatomic space. This displacement mechanism, linked to the diffusion of vacancies or foreign atoms, is favored by thermal activation. The rate of dislocation displacement (slip or climb) can either be very low or very high depending on the applied stress, nevertheless, it cannot be higher than the speed of sound of the material under consideration.

2.2 Damage mechanisms and their appearance

Several internal metallurgical defects are an outcome of the material production method. Typically, metals and alloys are produced in a liquid state and as the temperature of the liquid decreases, the interatomic distances become smaller. The critical distance, at which bonding occurs, is reached at several, randomly distributed sites and these constitute the first germs or nuclei of crystal growth. The lattices are formed in the same crystalline system but in random directions. Each nucleus develops into a crystal whose growth is limited by the neighbouring crystals. Generally, voids and crevices are formed due to:

- shrinkage during solidification. This leads to the formation of cavities or to interfacial separation in the pasty state,
- trapped gas bubbles,
- the accumulation of non-metallic impurities on the melt,
- defective or insufficient bonding of the grains,
- presence of hydrogen.

Of course, many of these defects may be present alone or combined together. The internal deterioration (or simply *damage*) evolution includes nucleation of new, and propagation and clustering of existing microcracks. Driven by the stress concentration (hot spots) microcracks grow along the internal surfaces of poor cohesive strength (weak links such as grain boundaries, interfaces separating phases of different properties) and heterogeneities (inclusions) which are also typical microcrack nucleation sites. In general, both hot spots and weak links are randomly distributed within the material microstructure.

Damage can manifest itself in various ways depending upon the nature of the material, type of loading and temperature. In metals, the mechanical degradation may be roughly divided into: *ductile* and *brittle* damage.

2.2.1 Ductile damage at room temperature

When subjected to an increasing external force, metals and alloys are able to deform and relieve the stresses by means of slip processes. Depending on the type of metal lattice, the crystallites have a variable number of slip systems.

The relative motion, or slip, is not the simultaneous displacement of many atoms in the same direction for the same distance. Instead, the atoms are displaced individually and consecutively.

The result of the movement of dislocations, which can also cut and penetrate each other, is the externally observed change in the shape of the material. This results in slip lines becoming visible on external surfaces. The process just described results in the plastic deformation of a specimen. With increasing deformation, the number of lattice defects increases. The dislocations mutually interact with each other and their movement is also hindered by second phases, *i.e.* precipitates. The possibilities of slip are therefore continuously reduced and finally exhausted, so that no further deformation can occur. The noticeable increase in hardness and strength which occur during this process is known as *work-hardening.* The further application of force brings about the fracture of the material. This process applies only to materials of high purity and this type of deformation and fracture can best be observed in single crystals – *monocrystals.*

The metals which are used for practical applications are not pure. They consist of a multitude of densely packed crystallites with diameters in the micron range and they contain impurities, in the widest sense (see Figure 2.1). Some of these impurities, which may be intentionally added or accidentally present as contaminants, are incorporated in the crystal lattice. However, there are always impurity particles which are physically distinct from the metal phase. This is equivalent to an array of holes, distributed through the metal matrix, with the second phase particles being located within them (see Figure 2.5). Plastic extension of and elemental volume of metal causes the holes to be enlarged. The material between the holes necks down, resulting in the adjacent material being subjected to intensive shearing. Eventually, with continued extension, all that remains are the thin ridges marking the lines of separation

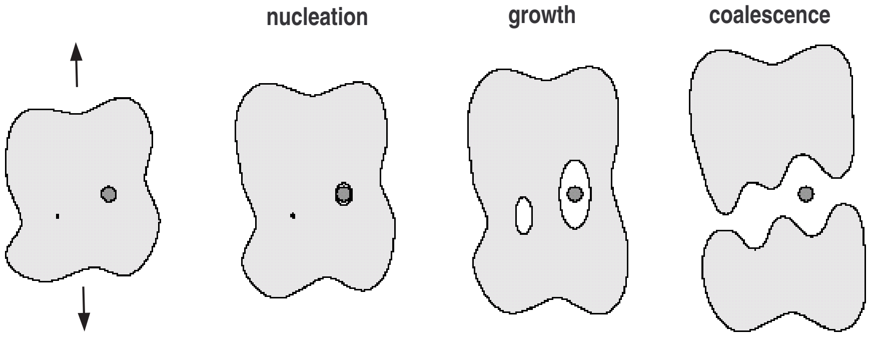

Figure 2.5: Schematic representation of the nucleation, growth and coalescence of voids. Voids can initiate by dislocation pile-ups at grain boundaries, secondary phase particles or inclusions.

between holes. Finally, the last connecting points are split, leaving two fracture surfaces. The size and shape of the fracture surface depends mostly on the type of inclusions present. Elongated inclusions lead to the formation of channel-shaped micro-craters. Thus, the micro-craters in heavily rolled products are always oriented in the rolling direction. The depth of the micro-craters is a measure of the formability and fracture toughness of the matrix. Ductile materials form deep micro-craters. Less easily deformable materials, or materials whose formability has been largely exhausted due to cold working, form very flat micro-craters.

The stresses during plastic deformation, and the relative displacements within the material before fracture, determine the alignment of the micro-craters. Hydrostatic tension produces normal micro-craters whilst tear micro-craters result if the stress state consists of unequal, mutually perpendicular stresses. The latter are always formed during the rupture of the surface layers, since the state of plane stress in this region favours this kind of deformation and fracture. Shear stresses cause the formation of shear micro-craters, which, in extreme cases, can be markedly elongated. Shear micro-craters are always found in the shear lips of catastrophic ruptures. Shear lips consist of surfaces inclined at approximately 45° to the main fracture surface.

As a result of the intensive deformation leading to fracture, the inner surfaces of the micro-craters are not smooth, but instead criss-crossed with intersecting slip bands. Polycrystalline metals, in particular, depict multiple slip to allow each individual grain to deform in conformity with neighbouring grains and the resulting wavy slip pattern is known as *serpentine glide.* Although micro-crater formation occurs more frequently in cases of *transcrystalline* fracture [see Figure 2.6(a)], there are nevertheless many cases in which micro-craters form on grain boundary surfaces. In such cases, the grain bound-

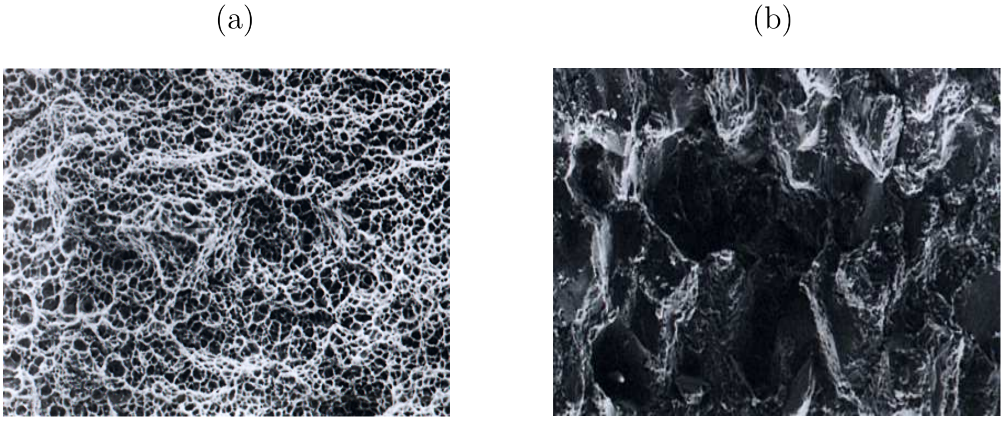

Figure 2.6: Ductile damage in metals. Microscopic aspect. (a) Transcrystalline ductile fracture; (b) Intercrystalline ductile fracture (reproduced from Lemaitre & Chaboche (1990)).

ary regions are more deformable than the grain centers [see Figure 2.6(b)].

2.2.2 Ductile damage at elevated temperatures

Rupture in the solid state

The rupture of metallic materials at elevated temperatures produces failure of the ductile micro-crater type. A remarkable feature of this type of fracture is the considerable extension undergone by the voids before separation and the appearance of broad shear walls with shear micro-craters. The type of plastic deformation occurring here might almost be described as resembling that of a chewing gum. These observations apply both to rapid tensile loading and loading under conditions of creep. Creep processes cause the formation of multiple micro-cracks on various planes inside the material and as a result, a rough, terraced surface is often observed.

Above a certain temperature known as the *equicohesive* temperature, which depends on the material in question, intercrystalline fracture occurs. For high stresses and short time to rupture, the favoured mode consists of grain boundary slip. The traces of this slip can be seen on the grain boundaries surface after separation. Simultaneously with this process, micro-craters form on those grain boundaries which are oriented at right angles to the direction of slip. At high temperatures and with low stresses, the formation of so-called creep voids is favoured. Grain boundary separation at elevated temperatures has been attributed to the presence of films of low melting-point phases and heavy metals.

Rupture in the pasty state

If parting occurs at solid-liquid phase boundaries, e.g. during the cooling of castings, then the resulting fracture surface will resemble the surface of shrinkage cavities with filament-like peaks of metal drawn out from it. It can often be found in the neighbourhood of shrinkage cavities.

2.2.3 Brittle damage

Transcrystalline brittle damage

One form of damage that results in unstable normal separation is quasi-cleavage fracture. Although this, admittedly shows clear features of ductile flow on a microscopic scale, on a macroscopic scale it shows very small deformation. The most distinctive form of transcrystalline normal fracture is represented by cleavage. In contrast to quasi-cleavage fracture, which is composed of curved or bowed facets and rosette surfaces having no orientation relationship with the underlying crystallographic planes, cleavage fracture proceeds along definite crystal planes. Figure 2.7(a) depicts the typical microscopic aspect of brittle fracture by cleavage.

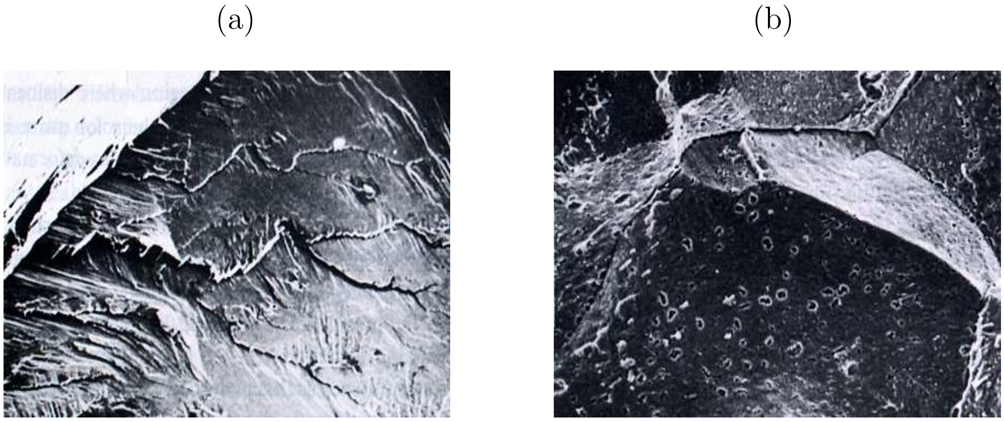

Figure 2.7: Brittle damage in metals. Microscopic aspect. (a) Brittle fracture by cleavage; (b) Intercrystalline brittle fracture (Lemaitre & Chaboche (1990)).

Intercrystalline brittle damage

Unstable normal fracture will propagate in an intercrystalline manner if the grain boundaries are embrittled by precipitates or impurity phases. Grain boundary carbides are often the cause of intercrystalline fracture in steels. If the carbides are large, their chemical composition can be indicated by x-ray microanalysis. In extreme cases of excessive carbon contents, the carbides can occupy so much of the micro-structure that their own brittleness determines the course of fracture. Figure 2.7(b) shows the typical microscopic aspect of intercrystalline brittle fracture.

Quenching cracks in steels are intercrystalline in that they follow the prior austenite grain boundaries. Here too, grain boundary impurities are responsible for the failure of grain boundaries. Intercrystalline failure can also be promoted by the presence of hydrogen and stress corrosion.

Remark 2.2 *In this chapter, some basic microscopic mechanisms associated with internal damage evolution in solids have been reviewed. It is clear that it involves a rheological process quite different from deformation. While damage manifests itself in the form of irreversible rupture of atomic bonds, deformation can be associated with reversible variations of interatomic spacing (in purely elastic processes) and movement and accumulation of dislocations (in permanent deformations of metals). Therefore, it should be expected that in order to describe the internal degradation of solids within the framework of the continuum mechanics theory, new variables intrinsically connected with the internal damage process will have to be introduced in addition to the standard variables (such as the strain tensor, plastic strain, etc.) employed in the description of deformation.*

Chapter 3

Continuum mechanics and thermodynamics

THE description of the physical structure, phenomena of deformation and damage that lead to fracture onset of metals, undertaken briefly in Chapter 2, can be macroscopically modelled by general principles. A well established approach, based on the response of the *representative volume element* [1], is known as the mechanics and thermodynamics of continuous media. This theory, provides powerful and effective tools to explain various phenomena successfully without detailed knowledge of the complexity of their microstructures. The macroscopic continuum scale both filter (average) and modulate (set the boundary conditions or driving forces for) the atomic-scale phenomena.

The phenomenological approach has been particularly successful in the field of solid mechanics. Numerous well established models of solids, such as classical elastoplasticity (Hill, 1950), have been developed on a purely phenomenological basis. This is the avenue that has been pursued in this thesis since the major concern is the description of essentially macroscopic behaviour.

Therefore, this chapter summarizes some basic concepts of mechanics and thermodynamics of continuous media. The definitions and notation introduced will be systematically employed throughout the subsequent chapters of this thesis. The general principles introduced are broadly widespread in the continuum mechanics literature and an effort has been made to follow the notation and nomenclature in use in standard textbooks (Truesdell & Noll, 1965; Spencer, 1980; Gurtin, 1981; Marsden & Hughes, 1983; Ogden, 1984).

---

[1] the element of matter large enough to be regarded as a homogeneous continuum.

3.1 Kinematics of deformation

This section is concerned with the description of *kinematics*. The study of motion and deformation is undertaken without reference to the cause.

3.1.1 Configurations and motions of continuum bodies

Let $\mathcal{B}$ be a *body* embedded in the three-dimensional euclidean space $\mathbb{R}^3$, with regular boundary represented by $\partial\mathcal{B}$, in its *reference* configuration. Here, for convenience, the reference configuration is assumed to coincide with the *initial* configuration. Therefore, each material particle is labelled by the coordinates $\boldsymbol{p}$, with respect to an orthogonal basis $\boldsymbol{E}_i$, at their original positions. In its *deformed* configuration, $\mathcal{B}$ occupies the region $\boldsymbol{\varphi}(\mathcal{B})$ with boundary $\boldsymbol{\varphi}(\partial\mathcal{B})$ defined through the deformation map $\boldsymbol{\varphi}$ (see Figure 3.1). The corresponding current position of a particle $\boldsymbol{p}$ of $\mathcal{B}$ in the deformed configuration is defined

$$\boldsymbol{x} = \boldsymbol{\varphi}(\boldsymbol{p}) \tag{3.1}$$

The vector field $\boldsymbol{u}(\boldsymbol{p})$, defined by:

$$\boldsymbol{u}(\boldsymbol{p}) = \boldsymbol{\varphi}(\boldsymbol{p}) - \boldsymbol{p}\,, \tag{3.2}$$

which is the *displacement* of $\boldsymbol{p}$. Thus, one may write

$$\boldsymbol{x} = \boldsymbol{p} + \boldsymbol{u}(\boldsymbol{p}). \tag{3.3}$$

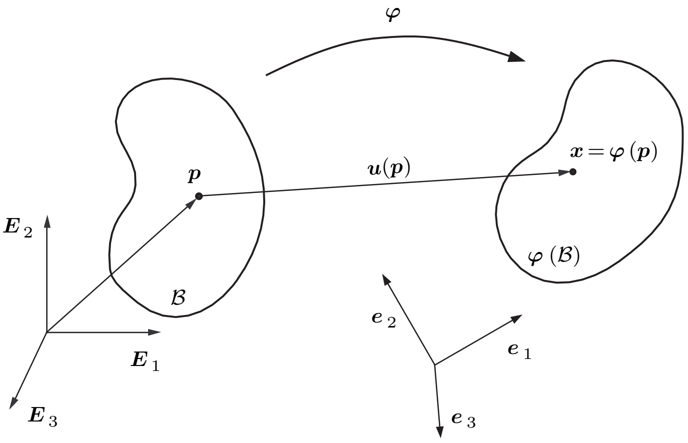
φ
$\boldsymbol{u}(\boldsymbol{p})$
$\boldsymbol{x} = \varphi\,(\boldsymbol{p})$
$\boldsymbol{p}$
$\boldsymbol{E}_2$
$\varphi\,(\mathcal{B})$
$\mathcal{B}$
$\boldsymbol{e}_2$
$\boldsymbol{e}_1$
$\boldsymbol{E}_1$
$\boldsymbol{E}_3$
$\boldsymbol{e}_3$

Figure 3.1: Configurations of a deformable body.

The above equations represent a mapping between the *undeformed* (initial) and *deformed* (current) body. As the body $\mathcal{B}$ moves in space from one instant to another, it occupies a continuous sequence of geometrical regions.

A time-dependent deformation of $\mathcal{B}$ is called a *motion* of $\mathcal{B}$. The motion is defined by a function $\boldsymbol{\varphi}$ so that for each time t, the map $\boldsymbol{\varphi}(\cdot, t)$ is a deformation of $\mathcal{B}$. During the motion $\boldsymbol{\varphi}$, the position $\boldsymbol{x}$ of a material particle $\boldsymbol{p}$ at time t is given by:

$$\boldsymbol{x} \;=\; \boldsymbol{\varphi}(\boldsymbol{p}, t)\,. \tag{3.4}$$

Similarly,

$$\boldsymbol{\varphi}(\mathcal{B}, t)$$

will denote the region of $\mathbb{R}^3$ occupied by the body $\mathcal{B}$ at time t. Generally the current positions of these particles are located, by the coordinates $\boldsymbol{x}$ with respect to an alternative Cartesian basis $\boldsymbol{e}_i$ (see Figure 3.1). In terms of the displacement field the motion is expressed as:

$$\boldsymbol{\varphi}(\boldsymbol{p}, t) \;=\; \boldsymbol{p} + \boldsymbol{u}(\boldsymbol{p}, t)\,. \tag{3.5}$$

Since at each time t the map $\boldsymbol{\varphi}(\cdot, t)$ is one-to-one (and hence invertible) by assumption, material points can be expressed in terms of the place they occupy at a time t as:

$$\boldsymbol{p} = \boldsymbol{\varphi}^{-1}(\boldsymbol{x}, t) = \boldsymbol{x} - \boldsymbol{u}(\boldsymbol{\varphi}^{-1}(\boldsymbol{x}, t), t). \tag{3.6}$$

The map $\boldsymbol{\varphi}^{-1}$ is called the *reference map*. In *finite deformation* analysis no assumption is made regarding the magnitude of the displacement $\boldsymbol{u}(\boldsymbol{p}, t)$, indeed it may even exceed the initial dimensions of the body as in the case, for instance, of metal forming. In *infinitesimal deformation* analysis the displacement $\boldsymbol{u}(\boldsymbol{p}, t)$ is assumed to be small in comparison with the dimensions of the body, and geometrical changes are ignored.

Time dependence

The dependency of the deformation $\boldsymbol{\varphi}(\boldsymbol{p}, t)$ on the time must be considered in many non-linear problems. During a motion $\boldsymbol{\varphi}$, the *velocity* and *acceleration* of a material particle $\boldsymbol{p}$ are defined by the first and second derivatives of the motion with respect to time (holding $\boldsymbol{p}$ fixed). We obtain

$$\dot{\boldsymbol{x}}(\boldsymbol{p}, t) = \frac{\partial \boldsymbol{\varphi}(\boldsymbol{p}, t)}{\partial t} \qquad \text{and} \qquad \ddot{\boldsymbol{x}}(\boldsymbol{p}, t) = \frac{\partial^2 \boldsymbol{\varphi}(\boldsymbol{p}, t)}{\partial^2 t}. \tag{3.7}$$

Using the reference map (3.6), one may define the functions:

$$\boldsymbol{v}(\boldsymbol{x}, t) \equiv \dot{\boldsymbol{x}}(\boldsymbol{\varphi}^{-1}(\boldsymbol{x}, t), t) \qquad \text{and} \qquad \boldsymbol{a}(\boldsymbol{x}, t) \equiv \ddot{\boldsymbol{x}}(\boldsymbol{\varphi}^{-1}(\boldsymbol{x}, t), t)\,, \tag{3.8}$$

where $\boldsymbol{v}$ and $\boldsymbol{a}$ denote the spatial description of the velocity field and acceleration field, respectively. They give the velocity and acceleration of the material particle positioned at $\boldsymbol{x}$ at time t.

3.1.2 Material and spatial descriptions

For finite deformations a judicious distinction has to be made between the coordinate systems that can be chosen to describe the behaviour of the body $\mathcal{B}$. Let us consider, for the sake of simplicity, a scalar time dependent quantity, α, defined over the body, $\mathcal{B}$.

(a) *Material description*: if the value of α is expressed as a function of material particles $\boldsymbol{p}$ (and time) with respect to the domain $\mathcal{B} \times \mathbb{R}^3$, then α is said to be a *material field*, defined by

$$\alpha_m(\boldsymbol{p}, t) \tag{3.9}$$

(b) *Spatial description*: On the other hand, if the value of α is expressed as a function of a spatial position $\boldsymbol{x}$ (and time) with respect to the domain $\boldsymbol{\varphi}_t(\mathcal{B}) \times \mathbb{R}^3$, then α is said to be a *spatial field*, defined by

$$\alpha_s(\boldsymbol{x}, t) \tag{3.10}$$

Of course, the previous descriptions also apply for both vector and tensor fields. The material and spatial descriptions are alternatively referred to as *Lagrangian* and *Eulerian* descriptions, respectively.

Material and spatial gradients, divergences and time derivatives

The *material* and *spatial gradients* of a scalar field α, denoted respectively $\nabla_p \alpha$ and $\nabla_x \alpha$, are defined as:

$$\nabla_p \alpha = \frac{\partial}{\partial \boldsymbol{p}} \alpha_m(\boldsymbol{p}, t), \qquad \nabla_x \alpha = \frac{\partial}{\partial \boldsymbol{x}} \alpha_s(\boldsymbol{x}, t)\,, \tag{3.11}$$

i.e, they are, respectively, the derivatives of α with respect to $\boldsymbol{p}$ and $\boldsymbol{x}$ holding t fixed. In addition, the *material* and *spatial divergence* of a vector field $\boldsymbol{r}$, are respectively, given by

$$\mathrm{div}_p \boldsymbol{r} = \mathrm{tr}(\nabla_p \boldsymbol{r}), \qquad \mathrm{div}_x \boldsymbol{r} = \mathrm{tr}(\nabla_x \boldsymbol{r}), \tag{3.12}$$

Furthermore, for a tensor field $\boldsymbol{T}$, the spatial and material divergence are given, in Cartesian components, by

$$(\mathrm{div}_p \boldsymbol{T})_i = \frac{\partial T_{ij}}{\partial p_j}, \qquad (\mathrm{div}_x \boldsymbol{T})_i = \frac{\partial T_{ij}}{\partial x_j}, \tag{3.13}$$

Similarly, the *material* and *spatial time derivatives* of α, denoted respectively $\dot{\alpha}_m$ and $\dot{\alpha}_s$, are defined by:

$$\dot{\alpha}_m = \frac{\partial}{\partial t} \alpha_m(\boldsymbol{p}, t), \qquad \dot{\alpha}_s = \frac{\partial}{\partial t} \alpha_s(\boldsymbol{x}, t)\,. \tag{3.14}$$

The material time derivative $\dot{\alpha}_m$ measures the rate of change of α at a *fixed material particle* $\boldsymbol{p}$. The spatial time derivative $\dot{\alpha}_s$, on the other hand, measures the rate of change of α observed at a *fixed spatial position* $\boldsymbol{x}$.

3.1.3 The deformation gradient

A key quantity in finite deformation analysis is the *deformation gradient* of the motion $\boldsymbol{\varphi}$. It relates quantities before deformation to corresponding quantities after (or during) deformation. This quantity is defined by a second order tensor, denoted by $\boldsymbol{F}$:

$$\boldsymbol{F}\,(\boldsymbol{p},t) \;=\; \nabla_p\boldsymbol{\varphi}(\boldsymbol{p},t) \;=\; \frac{\partial \boldsymbol{x}_t}{\partial \boldsymbol{p}}\,. \tag{3.15}$$

In view of (3.5) it can be written as

$$\boldsymbol{F} \;=\; \boldsymbol{I} + \nabla_p \boldsymbol{u}\,. \tag{3.16}$$

The cartesian components of $\boldsymbol{F}$ are given by:

$$F_{ij} = \frac{\partial x_i}{\partial p_j} = \delta_{ij} + \frac{\partial u_i}{\partial p_j}\,, \tag{3.17}$$

where x_i denote the components of $\boldsymbol{x}_t$. In terms of the reference map, the deformation gradient may be equivalently expressed as:

$$\boldsymbol{F}\,(\boldsymbol{x},t) = \left[\nabla_x \boldsymbol{\varphi}^{-1}(\boldsymbol{x},t)\right]^{-1} = [\boldsymbol{I} - \nabla_x \boldsymbol{u}]^{-1}\,. \tag{3.18}$$

Consider now the infinitesimal volume $\mathrm{d}V$ defined by the infinitesimal vectors $\mathrm{d}\boldsymbol{a}$, $\mathrm{d}\boldsymbol{b}$ and $\mathrm{d}\boldsymbol{c}$ emanating from the material particle $\boldsymbol{p}$ in the reference configuration (Figure 3.2). Trivially, one has:

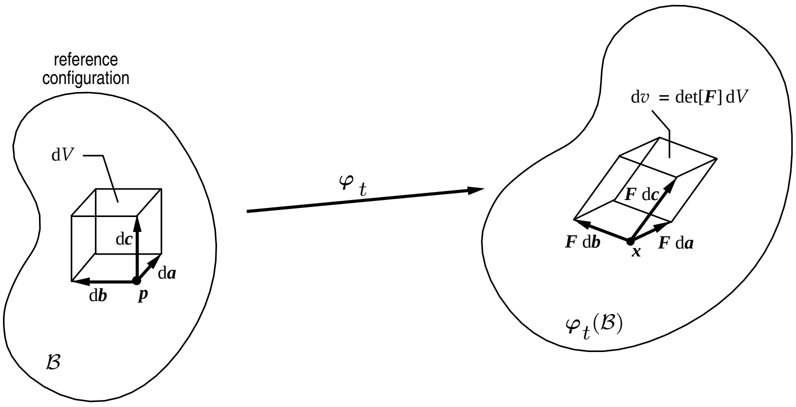

Figure 3.2: The determinant of the deformation gradient.

$$\mathrm{d}V = (\mathrm{d}\boldsymbol{a} \times \mathrm{d}\boldsymbol{b}) \cdot \mathrm{d}\boldsymbol{c}\,.$$

The deformation $\boldsymbol{\varphi}_t$ maps the infinitesimal vectors, respectively, into $\boldsymbol{F}\;\mathrm{d}\boldsymbol{a}$, $\boldsymbol{F}\;\mathrm{d}\boldsymbol{b}$ and $\boldsymbol{F}\;\mathrm{d}\boldsymbol{c}$, so that the deformed infinitesimal volume is given by:

$$\mathrm{d}v = (\boldsymbol{F}\;\mathrm{d}\boldsymbol{a} \times \boldsymbol{F}\;\mathrm{d}\boldsymbol{b}) \cdot \boldsymbol{F}\;\mathrm{d}\boldsymbol{c}\,.$$

By making use of tensor algebra, it follows that

$$\det \boldsymbol{F} = \frac{(\boldsymbol{F}\ \mathrm{d}\boldsymbol{a} \times \boldsymbol{F}\ \mathrm{d}\boldsymbol{b}) \cdot \boldsymbol{F}\ \mathrm{d}\boldsymbol{c}}{(\mathrm{d}\boldsymbol{a} \times \mathrm{d}\boldsymbol{b}) \cdot \mathrm{d}\boldsymbol{c}} = \frac{\mathrm{d}v}{\mathrm{d}V}\,, \tag{3.19}$$

i.e., the determinant of the deformation gradient represents, locally, the volume after deformation per unit reference volume. In what follows, J will be frequently employed to denote the determinant of $\boldsymbol{F}$:

$$J \equiv \det \boldsymbol{F}\ . \tag{3.20}$$

From (3.19) it follows that if $J = 0$ then the infinitesimal volume has collapsed into a material particle, which represents a physically unacceptable situation. At the reference configuration, $\boldsymbol{F} = \boldsymbol{I}$ and, consequently, $J = 1$. Thus, a configuration with $J < 0$ cannot be reached from the reference configuration without having, at some stage, $J = 0$. Therefore, in any deformed configuration of a body, J satisfies:

$$J > 0\,. \tag{3.21}$$

Isochoric/volumetric split of the deformation gradient

Any deformation can be locally decomposed as a purely volumetric deformation followed by an isochoric deformation or as an isochoric deformation followed by a pure volumetric deformation. To see this, note that the deformation gradient can always be multiplicatively split as:

$$\boldsymbol{F} = \boldsymbol{F}_{\mathrm{iso}}\, \boldsymbol{F}_{\mathrm{v}} = \boldsymbol{F}_{\mathrm{v}}\, \boldsymbol{F}_{\mathrm{iso}}\,, \tag{3.22}$$

where

$$\boldsymbol{F}_{\mathrm{v}} \equiv (\det \boldsymbol{F}\,)^{\frac{1}{3}}\, \boldsymbol{I} \tag{3.23}$$

is the *volumetric* component of $\boldsymbol{F}$ and

$$\boldsymbol{F}_{\mathrm{iso}} \equiv (\det \boldsymbol{F}\,)^{-\frac{1}{3}}\, \boldsymbol{F} \tag{3.24}$$

is the *isochoric* (*volume preserving* or *unimodular*) component. Note that, by construction, $\boldsymbol{F}_{\mathrm{v}}$ corresponds indeed to a purely volumetric deformation and, since

$$\det \boldsymbol{F}_{\mathrm{v}} = \left[(\det \boldsymbol{F}\,)^{\frac{1}{3}}\right]^3 \det \boldsymbol{F} = \det \boldsymbol{F}\ , \tag{3.25}$$

$\boldsymbol{F}_{\mathrm{v}}$ produces the same volume change as $\boldsymbol{F}$. The isochoric component in turn represents a volume preserving deformation, that is,

$$\det \boldsymbol{F}_{\mathrm{iso}} = \left[(\det \boldsymbol{F}\,)^{-\frac{1}{3}}\right]^3 \det \boldsymbol{F} = 1\,. \tag{3.26}$$

3.1.4 Polar decomposition. Stretches and rotation

The crucial role of $\boldsymbol{F}$ is further revealed in terms of its decomposition into *stretch* and *rotation* components. By applying the *polar decomposition* to the deformation gradient, one obtains:

$$\boldsymbol{F} = \boldsymbol{R}\boldsymbol{U} = \boldsymbol{V}\boldsymbol{R}, \tag{3.27}$$

where $\boldsymbol{U}$ is the *right* stretch tensor with a basis in the *reference configuration*, and $\boldsymbol{V}$ is the *left stretch tensor* which is an object in the *current configuration*. The proper orthogonal tensor $\boldsymbol{R}$ is the local *rotation tensor* which connects both configurations. The right and left stretch tensors are related by the rotation:

$$\boldsymbol{V} = \boldsymbol{R}\,\boldsymbol{U}\,\boldsymbol{R}^T. \tag{3.28}$$

As functions of $\boldsymbol{F}$, $\boldsymbol{U}$ and $\boldsymbol{V}$ are expressed by:

$$\boldsymbol{U} = \sqrt{\boldsymbol{C}}, \qquad \boldsymbol{V} = \sqrt{\boldsymbol{b}}, \tag{3.29}$$

where $\boldsymbol{C}$ and $\boldsymbol{b}$ are named, respectively, the *right* and *left Cauchy-Green tensors* defined as:

$$\boldsymbol{C} = \boldsymbol{U}^2 = \boldsymbol{F}^T\boldsymbol{F}, \qquad \boldsymbol{b} = \boldsymbol{V}^2 = \boldsymbol{F}\,\boldsymbol{F}^T. \tag{3.30}$$

Since $\boldsymbol{U}$ and $\boldsymbol{V}$ are symmetric, it follows from the *spectral theorem* (see Section A.2.1, page 248) that they admit the spectral decomposition:

$$\boldsymbol{U} = \sum_{i=1}^{3} \lambda_i\,\boldsymbol{N}_i \otimes \boldsymbol{N}_i, \qquad \boldsymbol{V} = \sum_{i=1}^{3} \lambda_i\,\boldsymbol{n}_i \otimes \boldsymbol{n}_i, \tag{3.31}$$

where $\{\lambda_1, \lambda_2, \lambda_3\}$ are the eigenvalues of $\boldsymbol{U}$ (and $\boldsymbol{V}$) named the *principal stretches*. The vectors $\boldsymbol{N}_i$ and $\boldsymbol{n}_i$ are unit eigenvectors of $\boldsymbol{U}$ and $\boldsymbol{V}$ respectively. The triads $\{\boldsymbol{N}_1, \boldsymbol{N}_2, \boldsymbol{N}_3\}$ and $\{\boldsymbol{n}_1, \boldsymbol{n}_2, \boldsymbol{n}_3\}$ form orthonormal bases for the space $\mathcal{U}$ of vectors in $\mathbb{R}^3$. They are called, respectively, the *Lagrangian* and *Eulerian triads* and define the *Lagrangian* and *Eulerian principal directions*.

Substitution of (3.28) into (3.31) gives the following relationship between the eigenvectors of $\boldsymbol{V}$ and $\boldsymbol{U}$:

$$\boldsymbol{N}_i = \boldsymbol{R}\,\boldsymbol{n}_i, \tag{3.32}$$

that is, each vector $\boldsymbol{n}_i$ differs from the corresponding $\boldsymbol{N}_i$ by a rotation $\boldsymbol{R}$.

The spectral decomposition of the right and left stretch tensors implies that in *any* deformation, the local stretching from a material particle can always be expressed as a superposition of stretches along three mutually orthogonal directions.

3.1.5 Strain Measures

In the previous section, within an infinitesimal neighbourhood of a generic material particle $\boldsymbol{p}$, pure rotations can be distinguished from pure stretching by means of the polar decomposition of the deformation gradient. Under the action of pure rotations, the distances between particles within this neighbourhood remain fixed. In this case, the difference between the deformed neighbourhood of $\boldsymbol{p}$ and its reference configuration is a *rigid deformation.*

Pure *stretching*, on the other hand, characterised by $\boldsymbol{U}$ or $\boldsymbol{V}$, changes the distance between material particles. To quantify straining, i.e., to evaluate how much $\boldsymbol{U}$ (or $\boldsymbol{V}$) departs from $\boldsymbol{I}$ (a rigid deformation), some kind of *strain measure* needs to be defined. In fact, the definition of a strain measure is somewhat arbitrary and a specific choice is usually dictated by mathematical and physical convenience. An important family of *Lagrangian strain tensors*, i.e., strain measures based on the Lagrangian triad, is defined by:

$$\boldsymbol{E}^{(m)} = \begin{cases} \frac{1}{m}(\boldsymbol{U}^m - \boldsymbol{I}) & m \neq 0 \\ \ln[\boldsymbol{U}] & m = 0 \end{cases} \tag{3.33}$$

where m is a real number and $\ln[\,\cdot\,]$ denotes the *tensor logarithm* of $[\,\cdot\,]$. Equivalently, in terms of its spectral decomposition, (3.33) may be rephrased as:

$$\boldsymbol{E}^{(m)} = \sum_{i=1}^{3} f(\lambda_{(i)})\ \boldsymbol{N}_{(i)} \otimes \boldsymbol{N}_{(i)}\,, \tag{3.34}$$

where

$$f(\lambda_{(i)}) = \begin{cases} \frac{1}{m}(\lambda_{(i)}^m - 1) & m \neq 0 \\ \ln \lambda_{(i)} & m = 0\,. \end{cases} \tag{3.35}$$

The Green-Lagrange strain tensor, $\boldsymbol{E}^{(2)}$, is a particular member of this family (with $m=2$). Other commonly used members of this family are the the Biot ($m = 1$), Hencky ($m = 0$) and Almansi ($m = -2$) strain tensors. Note that for any m, the associated strain tensor vanishes if and only if the deformation gradient represents, locally, a rigid deformation:

$$\boldsymbol{E}^{(m)} = \boldsymbol{0} \iff \boldsymbol{U} = \boldsymbol{I} \iff \boldsymbol{F} = \boldsymbol{R}\,.$$

Analogously to the strain measures discussed above, it is also possible to define tensors that measure strain along the principal *Eulerian* directions or, simply, *Eulerian strain tensors.* Based on the *left* stretch tensor, the Eulerian counterpart of the Lagrangian family of strain measures above is defined by:

$$\boldsymbol{\varepsilon}^{(m)} = \begin{cases} \frac{1}{m}(\boldsymbol{V}^m - \boldsymbol{I}) & m \neq 0 \\ \ln[\boldsymbol{V}] & m = 0\,, \end{cases} \tag{3.36}$$

or, using the Eulerian triad,

$$\boldsymbol{\varepsilon}^{(m)} = \sum_{i=1}^{3} f(\lambda_{(i)})\ \boldsymbol{n}_{(i)} \otimes \boldsymbol{n}_{(i)}\,. \tag{3.37}$$

Lagrangian and Eulerian strain tensors are related by:

$$\boldsymbol{\varepsilon}^{(m)} = \boldsymbol{R}\,\boldsymbol{E}^{(m)}\boldsymbol{R}^{T}\,, \tag{3.38}$$

that is, they differ by the local rotation $\boldsymbol{R}$.

3.1.6 The velocity gradient. Rate of deformation and spin

The velocity has been expressed in Equation $(3.8)_1$ as a function of the spatial coordinates as $\boldsymbol{v}(\boldsymbol{x}, t)$. The derivative of this expression with respect to spatial coordinates defines the *velocity gradient tensor* $\boldsymbol{l}$ as,

$$\boldsymbol{l} = \nabla_x \boldsymbol{v}\,,$$

Equivalently, with application of the chain rule one has:

$$\boldsymbol{l} = \frac{\partial}{\partial t}\left(\frac{\partial \boldsymbol{\varphi}}{\partial \boldsymbol{p}}\right)\frac{\partial \boldsymbol{p}}{\partial \boldsymbol{x}} = \dot{\boldsymbol{F}}\ \boldsymbol{F}^{-1}\,. \tag{3.39}$$

Two important tensors are obtained by splitting $\boldsymbol{l}$ into its symmetric and skew parts. Namely, the *rate of deformation* tensor (sometimes referred to as the *stretching* tensor), $\boldsymbol{d}$, and the *spin* tensor, $\boldsymbol{w}$, are defined by

$$\boldsymbol{d} = \operatorname{sym}(\boldsymbol{l})\,, \qquad \boldsymbol{w} = \operatorname{skew}(\boldsymbol{l})\,. \tag{3.40}$$

where the following notation has been used

$$\operatorname{sym}(\cdot) = \tfrac{1}{2}\left[(\cdot) + (\cdot)^T\right] \qquad \operatorname{skew}(\cdot) = \tfrac{1}{2}\left[(\cdot) - (\cdot)^T\right]. \tag{3.41}$$

3.1.7 Superimposed rigid body motions and objectivity

An important concept in non-linear continuum mechanics is the notion of *objectivity.* This concept can be understood by studying the effect of a rigid body motion superimposed on the *deformed* configuration. From the point of view of an observer attached to and rotating with a solid, many quantities describing the behaviour of the solid remain unchanged. Such quantities, like the distance between two particles or the state of stress in the body, amongst others are said to be objective (Holzapfel, 2000).

Although the intrinsic nature of these quantities remains unchanged, their *spatial* description may change. Let us consider an elemental vector $\mathrm{d}\boldsymbol{p}$ in the initial configuration that deforms to $\mathrm{d}\boldsymbol{x}$ and is subsequently rotated to $\mathrm{d}\breve{\boldsymbol{x}}$ as

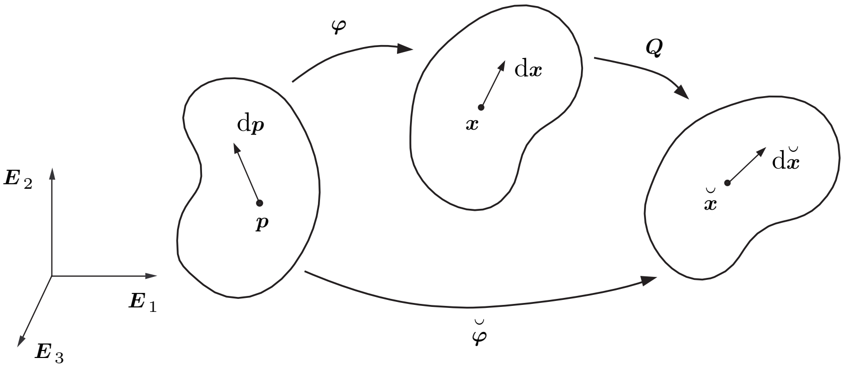

Figure 3.3: Superimposed rigid body motion.

shown in Figure 3.3. The relationship between these elemental vectors is given by

$$\mathrm{d}\breve{\boldsymbol{x}} = \boldsymbol{Q}\mathrm{d}\boldsymbol{x} = \boldsymbol{Q}\boldsymbol{F}\,\mathrm{d}\boldsymbol{p} \tag{3.42}$$

where $\boldsymbol{Q}$ is an orthogonal tensor describing the superimposed rigid body rotation. Even though the vector $\mathrm{d}\breve{\boldsymbol{x}}$ is different from $\mathrm{d}\boldsymbol{x}$, their magnitudes are obviously equal. In this sense it can be said that $\mathrm{d}\boldsymbol{x}$ is objective under rigid body motions. This definition is extended to any vector $\boldsymbol{a}$ that transforms according to $\boldsymbol{a} \longrightarrow \boldsymbol{Q}\boldsymbol{a}$.

From Equation (3.42) it is possible to note that the deformation gradients with respect to the current and rotated configurations are related as,

$$\boldsymbol{F} \longrightarrow \boldsymbol{Q}\boldsymbol{F} \tag{3.43}$$

The next step consists in extending the definition of objectivity to second-order tensors. Objective second order tensors, $\boldsymbol{G}$, transform as

$$\boldsymbol{G} \longrightarrow \boldsymbol{Q}\,\boldsymbol{G}\,\boldsymbol{Q}^T \tag{3.44}$$

Obviously, material tensors (defined in the reference configuration), such as $\boldsymbol{C}$ and $\boldsymbol{E}$, are unchanged under superimposed rigid body motions.

3.2 Stress and Equilibrium

This section will introduce the stresses and equilibrium concepts for a deformable body undergoing a finite motion. It should be noted that, so far, no reference has been made to *forces* and how they are transferred within continuum bodies. To describe surface forces mathematically, the concept of *stress* as well as the different ways of quantifying it are discussed in this section.

Crucial to the description of surface forces is *Cauchy's axiom* stated in what follows. Consider a body $\mathcal{B}$ in an arbitrarily deformed configuration (Figure 3.4). Let $\mathcal{S}$ be an oriented surface of $\mathcal{B}$ with unit normal vector $\boldsymbol{n}$

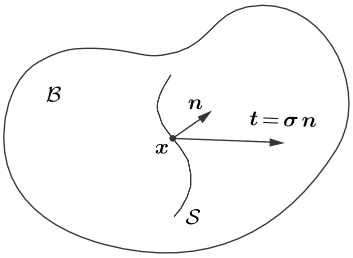

Figure 3.4: Surface forces. The Cauchy stress.

at a point $\boldsymbol{x}$. Cauchy's axiom states that: *At $\boldsymbol{x}$, the surface force, i.e., the force per unit area, exerted across $\mathcal{S}$ by the material on the side of $\mathcal{S}$ into which $\boldsymbol{n}$ is pointing upon the material on the other side of $\mathcal{S}$ depends on $\mathcal{S}$ only through its normal $\boldsymbol{n}$.* This means that identical forces are transmitted across *any* surfaces with normal $\boldsymbol{n}$ at $\boldsymbol{x}$. This force (per unit area) is called the *Cauchy stress vector* and will be denoted

$$\boldsymbol{t}(\boldsymbol{n}),$$

with dependence on $\boldsymbol{x}$ and time omitted for notational convenience. If $\mathcal{S}$ belongs to the boundary of $\mathcal{B}$ then the Cauchy stress vector represents the contact force exerted by the surrounding environment on $\mathcal{B}$.

3.2.1 The Cauchy stress tensor

The dependency of the surface force $\boldsymbol{t}$ on the normal $\boldsymbol{n}$ is *linear*. This implies that there exists a *tensor* field $\boldsymbol{\sigma}(\boldsymbol{x})$ such that the Cauchy stress vector is given by (Figure 3.4):

$$\boldsymbol{t}(\boldsymbol{x}, \boldsymbol{n}) \;=\; \boldsymbol{\sigma}(\boldsymbol{x})\,\boldsymbol{n}. \tag{3.45}$$

The tensor $\boldsymbol{\sigma}$ is *symmetric*:

$$\boldsymbol{\sigma} = \boldsymbol{\sigma}^T, \tag{3.46}$$

and is called the *Cauchy stress tensor*. It is often referred to as the *true stress tensor* or, simply, *stress tensor.*

Deviatoric and hydrostatic stresses

It is often convenient, particularly for the purpose of constitutive modelling, to split the stress tensor $\boldsymbol{\sigma}$ into the sum of a *spherical* and a *traceless* component:

$$\boldsymbol{\sigma} = \boldsymbol{s} + p\,\boldsymbol{I}, \tag{3.47}$$

where

$$p \equiv \tfrac{1}{3}\,\mathrm{tr}\,\boldsymbol{\sigma} \tag{3.48}$$

is the *hydrostatic pressure* (also referred to as *hydrostatic stress* or *mean normal pressure*), and the remainder:

$$\boldsymbol{s} \equiv \boldsymbol{\sigma} - p\,\boldsymbol{I} = \left[\mathsf{I} - \tfrac{1}{3}\,\boldsymbol{I} \otimes \boldsymbol{I}\right] : \boldsymbol{\sigma}\,, \tag{3.49}$$

is a traceless tensor named the *deviatoric stress* or *stress deviator*. The tensor:

$$p\,\boldsymbol{I} = \tfrac{1}{3}\,(\boldsymbol{I} \otimes \boldsymbol{I}) : \boldsymbol{\sigma} \tag{3.50}$$

is called the *spherical stress tensor*. Obviously, the hydrostatic pressure p is an invariant of the stress tensor.

Stress objectivity

Since the Cauchy stress tensor is of key importance to establish any equilibrium or constitutive equation, it is decisive to inquire whether $\boldsymbol{\sigma}$ is objective as defined in Section 3.1.7. Let us consider the transformations of the normal and traction vectors implied by the superimposed rigid body motion $\boldsymbol{Q}$ as:

$$\begin{aligned} \breve{\boldsymbol{t}}(\breve{\boldsymbol{n}}) &= \boldsymbol{Q}\,\boldsymbol{t}(\boldsymbol{n}) \\ \breve{\boldsymbol{n}} &= \boldsymbol{Q}\,\boldsymbol{n} \end{aligned} \tag{3.51}$$

with dependence on $\boldsymbol{x}$ and time omitted for notational convenience. Using the relationship between the traction vector and stress tensor, $\boldsymbol{t}(\boldsymbol{n}) = \boldsymbol{\sigma}\,\boldsymbol{n}$, in conjunction with the above quantities gives,

$$\boldsymbol{\sigma} \longrightarrow \boldsymbol{Q}\,\boldsymbol{\sigma}\,\boldsymbol{Q}^T \tag{3.52}$$

The rotation of $\boldsymbol{\sigma}$ given by the above equation conforms with the definition of objectivity for a second order tensor (see Equation 3.44).

3.2.2 Alternative stress tensors

Numerous definitions of stress tensors have been proposed in the literature. In the following we discuss stress tensors used for practical nonlinear analysis. Most of their components do not have a direct physical interpretation.

The Kirchhoff stress tensor Often it is convenient to work with the so-called *Kirchhoff stress tensor*, $\boldsymbol{\tau}$, which differs from the Cauchy by the volume ratio J, and is defined by:

$$\boldsymbol{\tau} = J\,\boldsymbol{\sigma}\,. \tag{3.53}$$

Due to the symmetry of $\boldsymbol{\sigma}$, the Kirchhoff stress is also *symmetric*.

The first Piola-Kirchhoff stress tensor The traction vector $\boldsymbol{t}$ of expression (3.45) measures the force exerted across a material surface per unit *deformed* area. Since in many situations the deformed configuration of $\mathcal{B}$ is not known in advance, it is convenient to define the *first Piola-Kirchhoff stress tensor*,

$$\boldsymbol{P} = J\,\boldsymbol{\sigma}\,\boldsymbol{F}^{-T}. \tag{3.54}$$

This definition derives from the counterpart vector $\bar{\boldsymbol{t}}$ of $\boldsymbol{t}$ that measures, at the point of interest, the current force per unit *reference* area. The tensor $\boldsymbol{P}$ is often referred to as the *nominal* or *engineering* stress. Note that in contrast to the Cauchy stress, $\boldsymbol{P}$ is generally *unsymmetric*.

The second Piola-Kirchhoff stress tensor It is possible to contrive a totally material symmetric stress tensor, known as the *second Piola-Kirchhoff stress tensor* $\boldsymbol{S}$, defined by:

$$\boldsymbol{S} = J\,\boldsymbol{F}^{-1}\boldsymbol{\sigma}\,\boldsymbol{F}^{-T}. \tag{3.55}$$

It often represents a very useful stress measure in computational mechanics and in the formulation of constitutive equations, in particular, for solids. In spite of the mathematical convenience, it does not admit a physical interpretation in terms of surface tractions.

3.3 Fundamental laws of thermodynamics

In order to state the fundamental laws of thermodynamics, it is necessary to introduce the scalar fields θ, e, s and r defined over $\mathcal{B}$ which represent, respectively, the *temperature*, *specific internal energy*, *specific entropy* and the *density of heat production*. In addition, $\boldsymbol{f}$ and $\boldsymbol{q}$ will denote the vector fields corresponding, respectively, to the *body force* (force per unit volume in the deformed configuration) and *heat flux*.

3.3.1 Conservation of mass

The postulate of conservation of mass requires that

$$\dot{\rho} + \rho\,\mathrm{div}_x\,\dot{\boldsymbol{u}} = 0\,, \tag{3.56}$$

where $\mathrm{div}_x[\cdot]$ (with subscript x) denotes the *spatial* divergence of $[\cdot]$.

3.3.2 Momentum balance

In its local form, the momentum balance can be expressed by the equations:

$$\begin{aligned} \mathrm{div}_x\,\boldsymbol{\sigma} + \boldsymbol{f} &= \rho\,\ddot{\boldsymbol{u}} && \text{in } \boldsymbol{\varphi}(\mathcal{B}) \\ \boldsymbol{t} &= \boldsymbol{\sigma}\,\boldsymbol{n} && \text{in } \boldsymbol{\varphi}(\partial\mathcal{B})\,, \end{aligned} \tag{3.57}$$

where $\boldsymbol{n}$ is the outward unit vector normal to the deformed boundary $\boldsymbol{\varphi}(\partial\mathcal{B})$ of $\mathcal{B}$, $\boldsymbol{t}$ is the boundary traction vector field on $\boldsymbol{\varphi}(\partial\mathcal{B})$.

The above momentum balance equations are formulated in the *spatial* (deformed) configuration. Equivalently, they may be expressed in the *reference* (or material) configuration of $\mathcal{B}$ in terms of the first Piola-Kirchhoff stress tensor as:

$$\begin{aligned} \operatorname{div}_p \boldsymbol{P} + \bar{\boldsymbol{f}} &= \bar{\rho}\,\ddot{\boldsymbol{u}} \quad \text{in } \mathcal{B} \\ \bar{\boldsymbol{t}} &= \boldsymbol{P}\boldsymbol{m} \qquad \text{in } \partial\mathcal{B}\,, \end{aligned} \tag{3.58}$$

where div_p (with subscript p) denotes the *material* divergence, $\bar{\boldsymbol{f}}$ is the body force measured per unit reference volume, $\bar{\rho}$ is the density in the reference configuration:

$$\bar{\rho} = J\,\rho\,, \tag{3.59}$$

$\bar{\boldsymbol{t}}$ is the boundary traction force per unit reference area and $\boldsymbol{m}$ is the outward normal to the boundary of $\mathcal{B}$ in its reference configuration.

3.3.3 The first principle

The first principle of thermodynamics postulates the *conservation of energy.* Before stating this principle, it is convenient to introduce the product:

$$\boldsymbol{\sigma} : \boldsymbol{d}\,, \tag{3.60}$$

which represents the *stress power* per unit volume in the deformed configuration of a body. The first principle of thermodynamics is mathematically expressed by the equation:

$$\rho\,\dot{e} = \boldsymbol{\sigma} : \boldsymbol{d} + \rho\,r - \operatorname{div}_x \boldsymbol{q}\,. \tag{3.61}$$

In words, the rate of internal energy per unit deformed volume must equal the sum of the stress power and heat production per unit deformed volume minus the spatial divergence of the heat flux.

3.3.4 The second principle

The second principle of thermodynamics postulates the *irreversibility of entropy production.* It is expressed by means of the inequality:

$$\rho\,\dot{s} \;+\; \operatorname{div}_x\!\left[\frac{\boldsymbol{q}}{\theta}\right] \;-\; \frac{\rho\,r}{\theta} \;\geq\; 0\,. \tag{3.62}$$

3.3.5 The Clausius-Duhem inequality

By combination of the first and second principles stated above, one easily obtains the fundamental inequality:

$$\rho\,\dot{s} \;+\; \operatorname{div}_x\!\left[\frac{\boldsymbol{q}}{\theta}\right] \;-\; \frac{1}{\theta}\,(\rho\,\dot{e} - \boldsymbol{\sigma} : \boldsymbol{d} + \operatorname{div}_x \boldsymbol{q}) \;\geq\; 0\,.$$

The introduction of the *specific free energy* ψ (also known as the *Helmholtz free energy per unit mass*), defined by

$$\psi = e - \theta\, s\,, \tag{3.63}$$

along with the identity:

$$\mathrm{div}_x\left[\frac{\boldsymbol{q}}{\theta}\right] \;=\; \frac{1}{\theta}\,\mathrm{div}_x\,\boldsymbol{q} - \frac{1}{\theta^2}\,\boldsymbol{q}\cdot\nabla_x\theta\,,$$

into the above fundamental inequality results in the *Clausius-Duhem inequality*:

$$\boldsymbol{\sigma} : \boldsymbol{d} - \rho\left(\dot{\psi} + s\,\dot{\theta}\right) - \frac{1}{\theta}\,\boldsymbol{q}\cdot\boldsymbol{g} \;\geq\; 0\,, \tag{3.64}$$

where we have defined $\boldsymbol{g} = \nabla_x\theta$.

3.4 Constitutive theory

The balance principles presented so far are valid for any continuum body, *regardless* of the material of which the body is made. In order to distinguish between different types of material, a *constitutive* model must be introduced. In this section, the use of internal variables to formulate constitutive models of dissipative materials is addressed.

3.4.1 Thermodynamics with internal variables

An effective alternative to describe the dissipative constitutive behaviour is the adoption of the so-called *thermodynamics with internal variables*. The starting point of the thermodynamics with internal variables is the hypothesis that at any instant of a thermodynamical process the thermodynamic state (defined by $\boldsymbol{\sigma}$, ψ, s and $\boldsymbol{q}$) at a given point $\boldsymbol{p}$ can be completely determined by the knowledge of a finite number of *state variables.* The thermodynamic state depends only on the *instantaneous* value of the state variables and not on their past history. This hypothesis is intimately connected with the assumption of the existence of a (fictitious) state of thermodynamic equilibrium known as the *local accompanying state* (Kestin & Bataille, 1977) described by the current value of the state variables. In other words, every process is considered to be a succession of equilibrium states. Therefore, despite the success of the internal variable approach in numerous fields of continuum physics, phenomena induced by very fast external actions (at time scales comparable to atomic vibrations) which involve states far from thermodynamic equilibrium are excluded from representation by internal variable theories.

The state variables

For the applications with which we are mostly concerned, it will be convenient to assume that at any time t, the thermodynamic state at a point is determined by the following set of *state variables*:

$$\{\boldsymbol{F},\, \theta,\, \boldsymbol{g},\, \boldsymbol{\alpha}\}\,,$$

where $\boldsymbol{F}$, θ and $\boldsymbol{g}$ are the *instantaneous* values of the deformation gradient, temperature and the temperature gradient and

$$\boldsymbol{\alpha} = \{\alpha_k\}$$

is a set of *internal variables* containing, in general, entities of scalar, vectorial and tensorial nature associated with dissipative mechanisms.

Thermodynamic potential. Stress constitutive equation

Following the above hypothesis, the specific free energy is assumed to have the form:

$$\psi \;=\; \psi(\boldsymbol{F},\, \theta,\, \boldsymbol{\alpha})\,, \tag{3.65}$$

so that its rate of change is given by:

$$\dot{\psi} \;=\; \frac{\partial \psi}{\partial \boldsymbol{F}} : \dot{\boldsymbol{F}} \;+\; \frac{\partial \psi}{\partial \theta}\,\dot{\theta} \;+\; \frac{\partial \psi}{\partial \alpha_k}\,\dot{\alpha}_k\,, \tag{3.66}$$

where summation over k is implied. In that case, using the connection:

$$\boldsymbol{\sigma} : \boldsymbol{d} = \boldsymbol{\sigma}\,\boldsymbol{F}^{-T} : \dot{\boldsymbol{F}}\,, \tag{3.67}$$

for the stress power, one obtains for the Clausius-Duhem inequality:

$$\left(\boldsymbol{\sigma}\,\boldsymbol{F}^{-T} - \rho\,\frac{\partial \psi}{\partial \boldsymbol{F}}\right) : \dot{\boldsymbol{F}} \;-\rho\left(s + \frac{\partial \psi}{\partial \theta}\right)\dot{\theta} - \rho\,\frac{\partial \psi}{\partial \alpha_k}\,\dot{\alpha}_k - \frac{1}{\theta}\,\boldsymbol{q}\cdot\boldsymbol{g} \geq 0\,. \tag{3.68}$$

Equivalently, in terms of power per unit *reference* volume, we have:

$$\left(\boldsymbol{P} - \bar{\rho}\,\frac{\partial \psi}{\partial \boldsymbol{F}}\right) : \dot{\boldsymbol{F}} \;-\bar{\rho}\left(s + \frac{\partial \psi}{\partial \theta}\right)\dot{\theta} - \bar{\rho}\,\frac{\partial \psi}{\partial \alpha_k}\,\dot{\alpha}_k - \frac{J}{\theta}\,\boldsymbol{q}\cdot\boldsymbol{g} \geq 0\,. \tag{3.69}$$

Equation (3.69) must remain valid for any pair of functions $\{\dot{\boldsymbol{F}}(t), \dot{\theta}(t)\}$. This implies the well known constitutive equations:

$$\boldsymbol{P} \;=\; \bar{\rho}\,\frac{\partial \psi}{\partial \boldsymbol{F}}\,, \qquad\qquad s \;=\; -\frac{\partial \psi}{\partial \theta}\,, \tag{3.70}$$

for the first Piola-Kirchhoff stress and entropy. Equation $(3.70)_1$ is equivalent to the following constitutive relations for the Cauchy and Kirchoff stress tensors:

$$\boldsymbol{\sigma} \;=\; \frac{1}{J}\,\bar{\rho}\,\frac{\partial \psi}{\partial \boldsymbol{F}}\,\boldsymbol{F}^{T}, \qquad\qquad \boldsymbol{\tau} \;=\; \bar{\rho}\,\frac{\partial \psi}{\partial \boldsymbol{F}}\,\boldsymbol{F}^{T}. \tag{3.71}$$

Thermodynamical forces

For each internal variable α_k of the set $\boldsymbol{\alpha}$, we define the *conjugate thermodynamical force*:

$$A_k \equiv \bar{\rho}\, \frac{\partial \psi}{\partial \alpha_k}\,. \tag{3.72}$$

With this definition and the identities (3.70), the Clausius-Duhem inequality can be rewritten as:

$$-\, A_k\, \dot{\alpha}_k \;-\; \frac{J}{\theta}\, \boldsymbol{q} \cdot \boldsymbol{g} \;\geq\; 0\,. \tag{3.73}$$

In what follows, we will adopt for convenience the notation:

$$\boldsymbol{A} \equiv \{A_k\} \tag{3.74}$$

for the set of thermodynamical forces.

Dissipation. Evolution of the internal variables

In order to completely characterise a constitutive model, complementary laws associated with the dissipative mechanisms are required. Namely, constitutive equations for the flux variables $\frac{1}{\theta}\boldsymbol{q}$ and $\dot{\boldsymbol{\alpha}}$ must be postulated. In the general case, we assume that the flux variables are given functions of the state variables. The following constitutive equations are then postulated:

$$\begin{aligned} \dot{\boldsymbol{\alpha}} &= f(\boldsymbol{F}, \theta, \boldsymbol{g}, \boldsymbol{\alpha}) \\ \tfrac{1}{\theta}\boldsymbol{q} &= h(\boldsymbol{F}, \theta, \boldsymbol{g}, \boldsymbol{\alpha})\,. \end{aligned} \tag{3.75}$$

The Clausius-Duhem inequality, now expressed by (3.73), must hold for any process. This requirement places restrictions on the possible forms of the general constitutive functions f and h in (3.75) [see Coleman & Gurtin (1967) and Truesdell (1969) for further details on this issue]. It is also important to mention that when internal variables of vectorial or tensorial nature are present, it is frequently convenient to re-formulate $(3.75)_1$ in terms of so-called *objective rates* rather than the standard material time derivative of $\boldsymbol{\alpha}$. Objective rates are insensitive to rigid body motions and may be essential in the definition of *frame invariant* evolution laws for variables representing physical states associated with material directions. Objective rates are discussed in Section 4.2 in the context of the hypoelastic-based formulation of plasticity models.

Dissipation potential. Normal dissipativity An effective way of ensuring that (3.73) is satisfied consists in postulating the existence of a scalar-valued *dissipation potential* of the form:

$$\Xi \;=\; \Xi(\boldsymbol{A}, \boldsymbol{g}; \boldsymbol{F}, \theta, \boldsymbol{\alpha})\,, \tag{3.76}$$

where the state variables $\boldsymbol{F}$, θ and $\boldsymbol{\alpha}$ appear as parameters. The potential Ξ is assumed convex with respect to each A_k and $\boldsymbol{g}$, non-negative and zero valued at the origin, $\{\boldsymbol{A}, \boldsymbol{g}\} = \{\boldsymbol{0}, \boldsymbol{0}\}$. In addition, the hypothesis of *normal dissipativity* is introduced, i.e, the flux variables are assumed to be determined by the laws:

$$\dot{\alpha}_k = -\frac{\partial \Xi}{\partial A_k}, \qquad \frac{1}{\theta}\boldsymbol{q} = -\frac{\partial \Xi}{\partial \boldsymbol{g}}\,. \tag{3.77}$$

A constitutive model defined by (3.65), (3.70) and (3.77) satisfies "a priori" the dissipation inequality. It should be noted, however, that the constitutive description by means of convex potentials as described above is *not* a consequence of thermodynamics but, rather, a tool for formulating constitutive equations without violating thermodynamics. Examples of constitutive models supported by experimental evidence which do not admit representation by means of dissipation potentials are discussed by Onat & Leckie (1988).

3.4.2 Phenomenological and micromechanical approaches

The success of a constitutive model intended to describe the behaviour of a particular material depends crucially on the choice of an appropriate set of internal variables. Since no plausible model will be general enough to describe the response of a material under all processes, we should have in mind that the choice of internal variables must be guided not only by the specific material in question but also the material process. In general, due to the difficulty involved in the identification of the underlying dissipative mechanisms, the choice of the appropriate set of internal variables is somewhat subtle and tends to be biased by the preferences and background of the investigator.

In simple terms, we can say that constitutive modelling by means of internal variables relies either on a *micromechanical* or on a *phenomenological* approach. The micromechanical approach involves the determination of mechanisms and related variables at the atomic, molecular or crystalline levels. In general, these variables are discrete quantities and their continuum (macroscopic) counterparts can be defined by means of homogenisation techniques. The phenomenological approach, on the other hand, is based on the study of the response of the *representative volume element*, i.e., the element of matter large enough to be regarded as a homogeneous continuum. The internal variables in this case will be directly associated with the dissipative behaviour observed at the *macroscopic* level in terms of continuum quantities (such as strain, stress, temperature, etc.). Despite the macroscopic nature of theories derived on the basis of the phenomenological methodology, it should be expected that "good" phenomenological internal variables will be somehow related to the underlying microscopic dissipation mechanisms [de Souza Neto *et al.* (2005a)].

3.4.3 The purely mechanical theory

Thermal effects are ignored in the constitutive theories addressed in this thesis. It is, therefore, convenient at this point to summarise the general internal variable-based constitutive equations in the purely mechanical case. By removing the thermally-related terms of the above theory, we end up with the following set of mechanical constitutive equations:

$$\begin{cases} \psi = \psi(\boldsymbol{F}, \boldsymbol{\alpha}) \\ \boldsymbol{P} = \bar{\rho}\, \dfrac{\partial \psi}{\partial \boldsymbol{F}} \\ \dot{\boldsymbol{\alpha}} = f(\boldsymbol{F}, \boldsymbol{\alpha}) \end{cases} \tag{3.78}$$

3.4.4 The constitutive initial value problem

Our basic constitutive problem is defined as follows: "*Given the history of the deformation gradient (and the history of temperature and temperature gradient, if thermal effects are considered), find the free-energy and stress (plus entropy and heat flux, in the thermomechanical case) according to the constitutive law*". If the internal variable approach is adopted in the formulation of the constitutive equations, the generic constitutive problem reduces to the following fundamental mechanical *initial value problem*.

Problem 3.4.1 (The mechanical constitutive initial value problem) *Given the initial values of the internal variables $\boldsymbol{\alpha}(t_0)$ and the history of the deformation gradient*

$$\boldsymbol{F}(t) \qquad t \in [t_0, \bar{t}],$$

find the functions $\boldsymbol{P}(t)$ and $\boldsymbol{\alpha}(t)$, for the first Piola-Kirchhoff stress and the set of internal variables, such that the constitutive equations:

$$\begin{cases} \boldsymbol{P}(t) = \bar{\rho}\, \left.\dfrac{\partial \psi}{\partial \boldsymbol{F}}\right|_t \\ \dot{\boldsymbol{\alpha}}(t) = f(\boldsymbol{F}(t), \boldsymbol{\alpha}(t)) \end{cases} \tag{3.79}$$

are satisfied for $t \in [t_0, \bar{t}]$.

3.5 Weak equilibrium. The principle of virtual work

The *strong* (point-wise, local or differential) forms of the momentum balance have been stated in Section 3.3 by expressions (3.57) and (3.58). In this section, we state the momentum balance equations in their corresponding *weak* (global or integral) forms. The weak equilibrium statement – the *Principle of Virtual*

Work – is fundamental to the definition of the basic initial boundary value problem and, is the starting point of finite element procedures.

Again, let us consider the body $\mathcal{B}$ which occupies the region $\mathcal{B} \subset \mathbb{R}^3$ with boundary $\partial\mathcal{B}$ in its reference configuration be subjected to body forces in its interior and surface tractions on its boundary. In its deformed configuration, $\mathcal{B}$ occupies the region $\boldsymbol{\varphi}(\mathcal{B})$ with boundary $\boldsymbol{\varphi}(\partial\mathcal{B})$ defined through the deformation map $\boldsymbol{\varphi}$.

3.5.1 The spatial version

The *spatial* version of the principle of virtual work states that "the body $\mathcal{B}$ is in *equilibrium* if and only if its Cauchy stress field, $\boldsymbol{\sigma}$, satisfies the equation:

$$\int_{\varphi(\mathcal{B})} [\boldsymbol{\sigma} : \nabla_x \boldsymbol{\eta} - (\boldsymbol{f} - \rho\, \ddot{\boldsymbol{u}}) \cdot \boldsymbol{\eta}]\, \mathrm{d}v - \int_{\varphi(\partial\mathcal{B})} \boldsymbol{t} \cdot \boldsymbol{\eta}\, \mathrm{d}a = 0 \qquad \forall\, \boldsymbol{\eta} \in \mathcal{V}\,, \tag{3.80}$$

where $\boldsymbol{f}$ and $\boldsymbol{t}$ are the body force per unit deformed volume and boundary traction per unit deformed area and $\mathcal{V}$ is the *space of virtual displacements* of $\mathcal{B}$, i.e., the space of sufficiently regular arbitrary displacements

$$\boldsymbol{\eta} : \boldsymbol{\varphi}(\mathcal{B}) \to \mathcal{U}\,."$$

3.5.2 The material version

The virtual work equation can be equivalently expressed in the *reference* configuration of $\mathcal{B}$. The corresponding *material* (or *reference*) version of the Principle of Virtual Work states that $\mathcal{B}$ is in equilibrium if and only if its first Piola-Kirchhoff stress field, $\boldsymbol{P}$, satisfies:

$$\int_{\mathcal{B}} [\boldsymbol{P} : \nabla_p \boldsymbol{\eta} - (\bar{\boldsymbol{f}} - \bar{\rho} \ddot{\boldsymbol{u}}) \cdot \boldsymbol{\eta}]\, \mathrm{d}v - \int_{\partial\mathcal{B}} \bar{\boldsymbol{t}} \cdot \boldsymbol{\eta}\, \mathrm{d}a = 0 \qquad \forall\, \boldsymbol{\eta} \in \mathcal{V}\,, \tag{3.81}$$

where $\bar{\boldsymbol{f}} = J\, \boldsymbol{f}$ is the reference body force and $\bar{\boldsymbol{t}}$ is the boundary traction per unit reference area. The space of virtual displacements, $\mathcal{V}$, is accordingly defined as the space of sufficiently regular arbitrary displacement fields:

$$\boldsymbol{\eta} : \mathcal{B} \to \mathcal{U}\,.$$

The material version of the virtual work equation is obtained by introducing, in its spatial counterpart, the identities:

$$\boldsymbol{\sigma} = \frac{1}{J} \boldsymbol{P} \boldsymbol{F}^{T} \qquad \nabla_x \boldsymbol{a} = \nabla_p \boldsymbol{a}\, \boldsymbol{F}^{-1}\,,$$

where the second expression holds for a generic vector field $\boldsymbol{a}$, and making use of the standard relation (Gurtin, 1981):

$$\int_{\varphi(\mathcal{B})} a(\boldsymbol{x})\, \mathrm{d}v = \int_{\mathcal{B}} J(\boldsymbol{p})\, a(\boldsymbol{\varphi}(\boldsymbol{p}))\, \mathrm{d}v\,,$$

valid for any scalar field a.

CHAPTER 4

FINITE ELEMENT MODELLING OF FINITE STRAIN PLASTICITY

THE great majority of metals and alloys, when subjected to high levels of stress fail to return to the initial undeformed configuration and instead permanent inelastic deformations are observed. Several constitutive theories and models such as plasticity, viscoplasticity and others are broadly used to describe such permanent effects. The mathematics of these material models is well understood in the *small strain* case and due to the underlying additive structure of infinitesimal plasticity, computational algorithms based on the *operator split* concept are especially suitable for the integration of small strain constitutive equations (Owen & Hinton, 1980; Simo & Hughes, 1987).

Despite the merit of these approaches, several applications of nonlinear continuous mechanics often include large permanent inelastic deformations and the *infinitesimal deformation* hypothesis cannot be introduced without significant loss of accuracy. Typical examples include the analysis of metal forming operations and crashworthiness problems where the underlying deformation processes are dominated by very large strains and rotations.

The present chapter is devoted to the theory and finite element implementation of *finite strain* elasto/visco-plasticity. In the theory and numerical algorithms discussed here, the effects of finite strains appear only at the kinematic level and are separated from the operations at the constitutive level. In both *implicit* and *explicit* time integrations schemes, the stress update procedure is specifically designed to enable small strain constitutive models to be directly employed. More details on the subject are provided in the book by de Souza Neto *et al.* (2005a), on which most of the following sections are based.

4.1 Finite strain elasto-plasticity. A brief review

The first papers devoted to the finite element implementation of *finite strain* elasto-plasticity were published in the 1970's. Initially, extension to the finite strain range (Hibbitt *et al.* , 1970; McMeeking & Rice, 1975; Argyris & Kleiber, 1977; Argyris *et al.* , 1978; Nagtegaal & de Jong, 1981) was obtained by an *ad doc* extension of the infinitesimal theory which relied on a *hypoelastic* characterization of the elastic response. During early stages of development, hypoelastic-based descriptions have been the subject of intense debate within the finite element community. Many controversial issues have arisen, ranging from the use of different objective stress rates in the formulation of the constitutive equations (Atluri, 1984; Nemat-Nasser, 1982; Perić, 1992) to fundamental drawbacks such as the possible lack of objectivity of (algorithmic) incremental constitutive laws (Hughes & Winget, 1980; Rubinstein & Atluri, 1983; Hughes, 1984) as well as observed oscillatory stress response under monotonic loading (Nagtegaal & de Jong, 1982) and dissipative behaviour within the 'elastic' range (Simo & Pister, 1984; Kojić & Bathe, 1987).

Therefore, *hyperelastic*-based formulations of finite plasticity have emerged (Simo, 1985; Simo & Ortiz, 1985). Based on the hyperelastic description of the reversible behaviour in conjunction with the multiplicative elasto-plastic split of the deformation gradient (Lee & Liu, 1967), such theories naturally by-pass the inherent drawbacks of hypoelastic-based approaches. Moreover, when the Hencky strain energy function is adopted to model the elastic behaviour, a small strain format return mapping-based stress updating procedure can be elegantly recovered with the use of a suitable exponential map-based integrator for the plastic flow equation (Eterovic & Bathe, 1990; Weber & Anand, 1990; Perić & Owen, 1991; Perić *et al.* , 1992; Simo & Miehe, 1992; Simo, 1992; Cuitiño & Ortiz, 1992). Throughout the last decade, the hyperelastic-based multiplicative approach has gained widespread acceptance and is currently adopted for large strain elasto-plastic analysis, soil plasticity, damage mechanics and anisotropic single crystal plasticity.

4.2 Hypoelastic-based plasticity models. Rate forms

The inelastic response of finitely deforming solids can be modelled by means of the so-called *hypoelastic-based* constitutive theories. The starting point of hypoelastic-based models is the formulation of the constitutive equations for stress in terms of objective (frame invariant) stress rates. Early formulations of finite strain plasticity have relied exclusively on the hypoelastic-based approach to provide ad-hoc finite strain extensions to existing infinitesimal models.

In spite of the conceptual simplicity of their formulations, hypoelastic-based plasticity models do not usually account for truly reversible behaviour, even in the absence of plastic flow. In other words, dissipative behaviour may be predicted even within what is meant to be an ‘elastic’ (reversible) domain. In addition, the formulation of incremental constitutive equations which preserve the objectivity (frame-invariance) of the rate (time-continuum) forms is not trivial and may, in some circumstances, result in rather cumbersome numerical procedures. In spite of the aforementioned objections, hypoelastic-based models remain widely used in many circles of the computational and applied mechanics community. This strategy is used, in this work, in conjunction with an explicit time integration scheme; therefore, this section is devoted to this class of constitutive models of plastic materials.

4.2.1 Objective stress rates

Crucial to the formulation of hypoelastic-based models of plasticity is the definition of *objective stress rates*. In section 3.1.7 objective tensors were defined by imposing that under rigid body motions they transform according to Equation (3.44) and in Section 3.2.1 it was shown that the Cauchy stress tensor satisfies this requirement.

A given *stress rate*, which we will be here denoted generically $\overset{\bullet}{\boldsymbol{\sigma}}$ (note the bold dot), is said to be *objective* if, under a change of observer, it transforms according to the same rule. That is, a stress rate $\overset{\bullet}{\boldsymbol{\sigma}}$ is objective only if it transforms as

$$\overset{\bullet}{\boldsymbol{\sigma}} \longrightarrow \boldsymbol{Q}\,\overset{\bullet}{\boldsymbol{\sigma}}\,\boldsymbol{Q}^T \tag{4.1}$$

for any change in observer. Note, for instance, that the material time derivative $\dot{\boldsymbol{\sigma}}$ of the Cauchy stress is *not* an objective stress rate. In this case, the transformation reads

$$\dot{\boldsymbol{\sigma}} \longrightarrow \boldsymbol{Q}\,\dot{\boldsymbol{\sigma}}\,\boldsymbol{Q}^T + \dot{\boldsymbol{Q}}\,\boldsymbol{\sigma}\,\boldsymbol{Q}^T + \boldsymbol{Q}\,\boldsymbol{\sigma}\,\dot{\boldsymbol{Q}}^T\,, \tag{4.2}$$

and satisfies (4.1) only for changes in observer with time-independent rotation ($\dot{\boldsymbol{Q}} = \boldsymbol{0}$). In order to ensure material objectivity in the formulation of finite strain constitutive laws directly in terms of *stress rates*, it is essential that the constitutive equation for the stress tensor be defined in terms of objective stress rates. Objective stress rates are usually defined by suitably modifying the material time derivative of the stress tensor to ensure that (4.1) is satisfied. Some of the most commonly used objective rates are reviewed in the following.

The Jaumann rate

The *Jaumann rate* of Cauchy stress, denoted $\overset{\triangledown}{\boldsymbol{\sigma}}$, is defined as:

$$\overset{\triangledown}{\boldsymbol{\sigma}} \equiv \dot{\boldsymbol{\sigma}} - \boldsymbol{w}\,\boldsymbol{\sigma} + \boldsymbol{\sigma}\,\boldsymbol{w}\,, \tag{4.3}$$

where $\boldsymbol{w}$ is the *spin* tensor:

$$\boldsymbol{w} \equiv \mathrm{skew}[\boldsymbol{l}]\,, \qquad \boldsymbol{l} \equiv \nabla_x \boldsymbol{v} = \dot{\boldsymbol{F}}\;\boldsymbol{F}^{-1}\,. \tag{4.4}$$

This rate is also frequently referred to as the *Jaumann-Zaremba* rate.

The Truesdell rate

The *Truesdell* rate of $\boldsymbol{\sigma}$ is defined as:

$$\overset{\circ}{\boldsymbol{\sigma}} \equiv \dot{\boldsymbol{\sigma}} - \boldsymbol{l}\,\boldsymbol{\sigma} - \boldsymbol{\sigma}\,\boldsymbol{l}^T + (\mathrm{tr}\,\boldsymbol{l})\,\boldsymbol{\sigma}\,. \tag{4.5}$$

The Green-Naghdi rate

The *Green-Naghdi* rate of $\boldsymbol{\sigma}$, here denoted $\overset{\diamond}{\boldsymbol{\sigma}}$, is obtained by rotating $\boldsymbol{\sigma}$ back to the reference configuration, taking the time material derivative of the rotated quantity and then rotating the resulting derivative forward to the deformed configuration. That is:

$$\overset{\diamond}{\boldsymbol{\sigma}} \equiv \boldsymbol{R}\left[\frac{\mathrm{d}}{\mathrm{d}t}(\boldsymbol{R}^T\boldsymbol{\sigma}\,\boldsymbol{R})\right]\boldsymbol{R}^T = \dot{\boldsymbol{\sigma}} - \boldsymbol{\Omega}\,\boldsymbol{\sigma} + \boldsymbol{\sigma}\,\boldsymbol{\Omega}\,, \tag{4.6}$$

where the skew-symmetric tensor:

$$\boldsymbol{\Omega} \equiv \dot{\boldsymbol{R}}\,\boldsymbol{R}^T\,, \tag{4.7}$$

is the spin of the Eulerian triad relative to the Lagrangian triad.

4.2.2 Hypoelastic-based plasticity models

The starting point in the formulation of hypoelastic-based plasticity models, is the decomposition of the strain measure into elastic and plastic parts. Motivated by the infinitesimal theory, the additive decomposition of the spatial rate of deformation into an elastic and plastic part is introduced:

$$\boldsymbol{d} = \boldsymbol{d}^e + \boldsymbol{d}^p\,, \tag{4.8}$$

where $\boldsymbol{d}$ is the usual stretching tensor, $\boldsymbol{d}^e$ and $\boldsymbol{d}^p$ are measures of rate of elastic and plastic deformation, respectively. Furthermore, it is postulated that the elastic response is governed by a *hypoelastic* rate constitutive law of the form:

$$\overset{\bullet}{\boldsymbol{\Sigma}} = \mathsf{D}^e : (\boldsymbol{d} - \boldsymbol{d}^p)\,, \tag{4.9}$$

where $\overset{\bullet}{\boldsymbol{\Sigma}}$ denotes some objective rate of some stress measure $\boldsymbol{\Sigma}$ and D^e is some suitably defined tangential elasticity operator related to the choice of the stress rate. Concerning the particular form of the hypoelastic constitutive Equation (4.9), the tangential operator D^e is typically assumed constant and isotropic with the same form as the standard *infinitesimal* isotropic elasticity tensor. The above rate equation is complemented by a constitutive law for $\boldsymbol{d}^p$ (a *plastic flow rule*) usually stated as:

$$\boldsymbol{d}^p = \dot{\gamma}\,\frac{\partial\Psi}{\partial\boldsymbol{\Sigma}}\,,$$

where $\Psi(\boldsymbol{\Sigma}, \boldsymbol{\alpha})$ is a flow potential, with $\boldsymbol{\alpha}$ denoting a set of internal variables whose evolution is governed by:

$$\dot{\boldsymbol{\alpha}} = \dot{\gamma}\, \boldsymbol{H}(\boldsymbol{\Sigma}, \boldsymbol{\alpha})\,,$$

where $\boldsymbol{H}$ is a given evolution function and the plastic multiplier, $\dot{\gamma}$, defines the load/unloading criterion through the usual complementarity condition:

$$\Phi \leq 0 \qquad \dot{\gamma} \geq 0 \qquad \dot{\gamma}\Phi = 0\,, \tag{4.10}$$

with $\Phi(\boldsymbol{\Sigma}, \boldsymbol{\alpha})$ denoting a yield function. The extension of a given infinitesimal model to the finite strain range is obtained by adopting in the above equations Ψ, Φ and $\boldsymbol{H}$ with the same functional format as those of the corresponding infinitesimal model. The overall model is summarized in Box 4.1.

Box 4.1: Ad Hoc phenomenological isotropic finite strain model

(i) Additive decomposition of the rate of deformation tensor

$$\boldsymbol{d} = \boldsymbol{d}^e + \boldsymbol{d}^p$$

(ii) Hypoelastic stress-strain relationship

$$\overset{\bullet}{\boldsymbol{\Sigma}} = \mathsf{D}^e : (\boldsymbol{d} - \boldsymbol{d}^p)\,,$$

(iii) Evolution equations for $\boldsymbol{d}^p$ and internal variable set $\boldsymbol{\alpha}$

$$\boldsymbol{d}^p = \dot{\gamma}\, \frac{\partial \Psi}{\partial \boldsymbol{\Sigma}}$$

$$\dot{\boldsymbol{\alpha}} = \dot{\gamma}\, \boldsymbol{H}(\boldsymbol{\Sigma}, \boldsymbol{\alpha})$$

(iv) Loading/unloading criterion

$$\Phi \leq 0 \qquad \dot{\gamma} \geq 0 \qquad \dot{\gamma}\Phi = 0$$

Criticism of hypoelastic-based models

Models of the type outlined above have been extensively used in the computational mechanical literature, particularly with reference to metal plasticity, in conjunction with the classical von Mises yield criterion (Pinsky *et al.* , 1983; Nagtegaal & de Jong, 1981; Nagtegaal, 1982). However, no matter what objective rate is chosen, fundamental drawbacks will be present in models defined on a purely *ad hoc* basis by simply choosing one particular objective stress rate and postulating an evolution law of the type (4.9) with constant and isotropic elasticity tensor D^e. It has been shown by Simo & Pister (1984) that models postulated as such fail to define an elastic material (even in the absence of plastic flow). That is, dissipation of energy will occur within closed (supposedly elastic) cycles. It should be emphasised, however, that such inconsistencies remain negligible in metal plasticity (where elastic strains are small).

4.2.3 Integration algorithms and incremental objectivity

From the numerical point of view, the central issue is the numerical integration of the constitutive model. In fact, it is by no means easy to formulate integration algorithms for rate-based finite plasticity models that preserve the property of material objectivity. The objectivity of incremental constitutive laws is usually referred to as *incremental objectivity*. If incremental objectivity is not satisfied, then spurious stress changes may be produced within increments with rigid incremental displacement fields.

Incrementally objective algorithms for rate-based models

The issue of incremental objectivity of integration algorithms for hypoelastic-based constitutive models has been investigated by many researchers (Hughes & Winget, 1980; Pinsky *et al.* , 1983; Rubinstein & Atluri, 1983; Flanagan & Taylor, 1987; Simo & Hughes, 1998). There are many possible alternatives in the formulation of incrementally objective algorithms. The underlying idea, however, is the same and comprises the following steps:

(i) Firstly, the original rate constitutive equation is mapped into a *rigid motion-insensitive* (or *rotation-neutralised*) local configuration.

(ii) Time discretisation is then performed over the resulting equation which involves only rigid motion-insensitive quantities.

(iii) Finally, the discretised equation is mapped back to the spatial configuration.

The reader is referred to Chapter 8 of Simo & Hughes (1998) for a detailed description of the general methodology. Here, we shall limit our discussion to the Green-Naghdi rate of the Kirchhoff stress combined with a midpoint rule-based algorithm, employed in this work.

4.2.4 Integration of Green-Naghdi rate-based model

According with the above strategy, the idea is to use a *rotation neutralised description* of the spatial evolution equations. To formalize this approach, let

$\boldsymbol{W}$ be *any* spatial, skew-symmetric, second order tensor. Consider the general initial value problem

$$\begin{cases} \dot{\boldsymbol{\Lambda}} = \boldsymbol{W}\,\boldsymbol{\Lambda} \\ \boldsymbol{\Lambda}|_{t=0} = \boldsymbol{I}\,, \end{cases} \tag{4.11}$$

where $\boldsymbol{\Lambda}$ is a proper orthogonal tensor. Let $\boldsymbol{\Sigma}$ be the *rotated Kirchhoff stress tensor* and $\boldsymbol{D}$ the *rotated stretching tensor*:

$$\boldsymbol{\Sigma} \equiv \boldsymbol{\Lambda}^T\,\boldsymbol{\tau}\,\boldsymbol{\Lambda} \qquad\qquad \boldsymbol{D} \equiv \boldsymbol{\Lambda}^T\,\boldsymbol{d}\,\boldsymbol{\Lambda}\,. \tag{4.12}$$

The material time derivative of the rotated Kirchhoff stress is given by:

$$\dot{\boldsymbol{\Sigma}} = \boldsymbol{\Lambda}^T\,\left[\dot{\boldsymbol{\tau}} + \boldsymbol{\tau}\boldsymbol{W} - \boldsymbol{W}\boldsymbol{\tau}\right]\boldsymbol{\Lambda}. \tag{4.13}$$

In particular, if $\boldsymbol{W} = \boldsymbol{\Omega}$ is defined as

$$\boldsymbol{\Omega} \equiv \dot{\boldsymbol{R}}\,\boldsymbol{R}^T\,,$$

with $\boldsymbol{R}$ being the rotation tensor resulting from the polar decomposition of the deformation gradient, $\boldsymbol{F} = \boldsymbol{R}\boldsymbol{U} = \boldsymbol{V}\boldsymbol{R}$, we obtain the Green-Naghdi stress rate. Trivially, the exact solution to problem (4.11) is

$$\boldsymbol{\Lambda} = \boldsymbol{R}\,. \tag{4.14}$$

Considering the ‘elastic’ regime, the first step [item (i) above] in the formulation of the present algorithm is to rotate both sides of the Green-Naghdi stress rate evolution law

$$\overset{\diamond}{\boldsymbol{\tau}} = \mathsf{D}^e : \boldsymbol{d} \tag{4.15}$$

with the rotation $\boldsymbol{R}^T$. This results in the following equivalent rate form defined in the local rotated configuration:

$$\dot{\boldsymbol{\Sigma}} = \mathsf{D}^e : \boldsymbol{D}\,. \tag{4.16}$$

In rotating the right hand side of (4.15) we have made use of the fact that D^e is isotropic. The above rate form of the constitutive equation for the stress is *rigid motion-insensitive*, in the sense that it involves only quantities which are not affected by superimposed rigid body motions.

Incrementally objective stress integration

The discretisation of the rotation-insensitive rate equation (4.16), corresponds to item (ii) listed in page 44. Let us consider the standard interval $[t_n, t_{n+1}]$ and start by approximating the midpoint velocity gradient as:

$$\boldsymbol{l}_{n+\frac{1}{2}} = \nabla_{n+\frac{1}{2}}\boldsymbol{v}_{n+\frac{1}{2}}\,, \tag{4.17}$$

where, the gradient $\nabla_{n+\frac{1}{2}}$ is taken with respect to the *midpoint configuration*, defined by the displacement field:

$$\boldsymbol{u}_{n+\frac{1}{2}} = \boldsymbol{u}_n + \tfrac{1}{2}\,\Delta\boldsymbol{u}\,. \tag{4.18}$$

The midpoint velocity field, $\boldsymbol{v}_{n+\frac{1}{2}}$ is computed according to

$$\boldsymbol{v}_{n+\frac{1}{2}} = \frac{\Delta\boldsymbol{u}}{\Delta t}\,. \tag{4.19}$$

With $\boldsymbol{l}_{n+\frac{1}{2}}$ computed as above, the midpoint stretching tensor is computed by:

$$\boldsymbol{d}_{n+\frac{1}{2}} = \mathrm{sym}[\boldsymbol{l}_{n+\frac{1}{2}}]\,.$$

By applying the midpoint rule to (4.16) the following update formula for the rotated stress $\boldsymbol{\Sigma}$ is obtained:

$$\boldsymbol{\Sigma}_{n+1} - \boldsymbol{\Sigma}_n = \Delta t\,\dot{\boldsymbol{\Sigma}}_{n+\frac{1}{2}} = \mathsf{D}^e : \Delta t\,\boldsymbol{D}_{n+\frac{1}{2}} \tag{4.20}$$

where $\boldsymbol{\Sigma}_n$ is given by

$$\boldsymbol{\Sigma}_n = \boldsymbol{R}_n^T\,\boldsymbol{\tau}_n\,\boldsymbol{R}_n. \tag{4.21}$$

The midpoint rotated stretching tensor, $\boldsymbol{D}_{n+\frac{1}{2}}$, is computed as:

$$\boldsymbol{D}_{n+\frac{1}{2}} = \boldsymbol{R}^T_{n+\frac{1}{2}}\,\boldsymbol{d}_{n+\frac{1}{2}}\,\boldsymbol{R}_{n+\frac{1}{2}}\,. \tag{4.22}$$

The midpoint rotation tensor, $\boldsymbol{R}_{n+\frac{1}{2}}$, is obtained through the polar decomposition of the deformation gradient at the midpoint configuration:

$$\boldsymbol{F}_{n+\frac{1}{2}} = \boldsymbol{I} + \tfrac{1}{2}\nabla_{n+\frac{1}{2}}(\Delta\boldsymbol{u}) \tag{4.23}$$

According with the previous relations, it is possible to express the mid point approximation of the strain increment by

$$\Delta\boldsymbol{\varepsilon} = \boldsymbol{R}^T_{n+\frac{1}{2}}\left(\Delta t\,\boldsymbol{d}_{n+\frac{1}{2}}\right)\boldsymbol{R}_{n+\frac{1}{2}} \tag{4.24}$$

Once all the above quantities have been evaluated, the next step consists in performing the standard small strain integration algorithm, denoted here by

$$\boldsymbol{\Sigma}_{n+1} = \hat{\boldsymbol{\Sigma}}\;(\boldsymbol{\Sigma}_n, \Delta\boldsymbol{\varepsilon}, \boldsymbol{\alpha}_n) \tag{4.25}$$

where $\boldsymbol{\alpha}_n$ denotes the transported set of internal variables, which may require to be rotated accordingly if tensorial variables are included.

Finally, with the updated rotated Kirchhoff stress computed by (4.20), the Kirchhoff stress tensor at t_{n+1} is then obtained by simply rotating $\boldsymbol{\Sigma}_{n+1}$ back to the spatial configuration [item (iii) listed in page 44]:

$$\boldsymbol{\tau}_{n+1} = \boldsymbol{R}_{n+1}\,\boldsymbol{\Sigma}_{n+1}\,\boldsymbol{R}^T_{n+1}\,, \tag{4.26}$$

where the rotation $\boldsymbol{R}_{n+1}$ is obtained by the standard polar decomposition. The overall incrementally objective algorithm for the Green-Naghdi rate-based finite plasticity model is summarised in Box 4.2.

Box 4.2: Incrementally objective integration algorithm for a general Green-Naghdi rate-based finite plasticity model

(i) Given the incremental displacement, $\Delta \boldsymbol{u}$, compute the deformation gradients

$$\boldsymbol{F}_{n+1} = \boldsymbol{I} + \nabla_n(\Delta \boldsymbol{u}) \qquad \text{and} \qquad \boldsymbol{F}_{n+\frac{1}{2}} = \boldsymbol{I} + \tfrac{1}{2}\nabla_{n+\frac{1}{2}}(\Delta \boldsymbol{u})$$

(ii) Perform polar decompositions to obtain the rotations

$$\boldsymbol{F}_{n+1} = \boldsymbol{R}_{n+1}\boldsymbol{U}_{n+1} \qquad \text{and} \qquad \boldsymbol{F}_{n+\frac{1}{2}} = \boldsymbol{R}_{n+\frac{1}{2}}\boldsymbol{U}_{n+\frac{1}{2}}$$

(iii) Mid point velocity gradient and stretching tensor

$$\boldsymbol{l}_{n+\frac{1}{2}} = \nabla_{n+\frac{1}{2}}\boldsymbol{v}_{n+\frac{1}{2}} \qquad \text{and} \qquad \boldsymbol{d}_{n+\frac{1}{2}} = \text{sym}[\boldsymbol{l}_{n+\frac{1}{2}}]$$

(iv) Mid point approximation of the strain increment

$$\Delta \boldsymbol{\varepsilon} = \boldsymbol{R}^T_{n+\frac{1}{2}} \left(\Delta t \, \boldsymbol{d}_{n+\frac{1}{2}}\right) \boldsymbol{R}_{n+\frac{1}{2}}$$

(v) Map the Kirchhoff stress tensor

$$\boldsymbol{\Sigma}_n = \boldsymbol{R}^T_n \, \boldsymbol{\tau} \, \boldsymbol{R}_n$$

(vi) Use the small strain format return mapping algorithm to compute $\boldsymbol{\Sigma}_{n+1}$ and $\boldsymbol{\alpha}_{n+1}$

$$\boldsymbol{\Sigma}_{n+1} = \hat{\boldsymbol{\Sigma}} \, (\boldsymbol{\Sigma}_n, \Delta \boldsymbol{\varepsilon}, \boldsymbol{\alpha}_n)$$

(vii) Rotate $\boldsymbol{\Sigma}_{n+1}$ back to the spatial configuration

$$\boldsymbol{\tau}_{n+1} = \boldsymbol{R}_{n+1} \, \boldsymbol{\Sigma}_{n+1} \, \boldsymbol{R}^T_{n+1}$$

4.3 Explicit dynamic finite element solution strategy

Over recent years, application of dynamic explicit time integration schemes to metal forming problems has increased, specially to those involving high nonlinearity, complex contact conditions and material failure. Explicit schemes are *conditionally stable* with the permissible time step governed by the Courant stability limit (Belytschko, 1983; Hughes, 1987; Bathe, 1996; Belytschko *et al.* , 2000), which may lead to longer computing times as compared with analogous implicit schemes. However, explicit transient dynamic procedures adopted in the simulation of forming operations rely on a simpler and more robust treatment of frictional contact. This usually allows explicit solutions to be attained in situations where the implicit method fails to converge. In addition, it is important to note that for problems characterised by very large numbers of degrees of freedom (typical of realistic industrial problems), the size of the underlying linear equation systems to be solved within the implicit iterative scheme often exceeds the current capacity of available hardware. These are the main reasons behind the frequent application of explicit procedures in the simulation of inherently quasi-static forming processes.

In the explicit solution procedure the bulk of the computation cost lies in the stress update algorithm at the integration points and in the contact search. This, coupled with stringent restrictions on increment size, has lead to a widespread use of relatively inexpensive and simple stress integration schemes. These schemes normally rely on the use of some variant of the rate form of the constitutive equation, as described previously in this section. Here, we provide the essential features of the explicit approach to finite element analysis employed in this work and refer to recent texts by Simo & Hughes (1998) and Belytschko *et al.* (2000) for further details.

4.3.1 The discretised dynamic equations

The point of departure for the explicit dynamic analysis is the weak form of the momentum balance, stated in its spatial version in Section 3.5.1 (page 38), as follows

$$\int_{\varphi(\mathcal{B})} [\boldsymbol{\sigma} : \nabla_x \boldsymbol{\eta} - (\boldsymbol{f} - \rho\, \ddot{\boldsymbol{u}}) \cdot \boldsymbol{\eta}]\, \mathrm{d}v - \int_{\varphi(\partial\mathcal{B})} \boldsymbol{t} \cdot \boldsymbol{\eta}\, \mathrm{d}a = 0 \qquad \forall\, \boldsymbol{\eta} \in \mathcal{V}\,. \tag{4.27}$$

In addition, let the motion be prescribed on a portion of the boundary so that at time t the set of *kinematically admissible* deformations of $\mathcal{B}$ is defined as

$$\mathcal{K} = \{\boldsymbol{u} : \mathcal{B} \to \mathcal{U} \,|\, \boldsymbol{u} = \bar{\boldsymbol{u}} \quad \text{on} \quad \partial\mathcal{B}_u\} \tag{4.28}$$

where $\bar{\boldsymbol{u}}$ is the prescribed boundary displacement.

Discretization in space: Several methods have been applied in different situations for the discretization in space of the above problem: finite differences, finite elements, finite volumes, boundary solutions and Galerkin methods (Hilber & Hughes, 1978). However, finite elements are by far the most commonly used. Standard textbooks that provide a detailed account of the finite element method are Oden (1972), Hughes (1987), Crisfield (1991, 1997), Bathe (1996), Belytschko *et al.* (2000), Zienkiewicz & Taylor (2000). In this section the main steps of the solution procedure based on the Galerkin finite element discretization, will be briefly reviewed.

In a conventional approach, approximations to the boundary value problem, can be obtained by replacing the functional sets $\mathcal{K}$ and $\mathcal{V}$ with their discrete counterparts $\mathcal{K}^h$ and $\mathcal{V}^h$. Let $N_A : \mathcal{B} \to \mathbb{R}$, $A = 1, .., n_{\text{node}}$ denote the prescribed n_{node} global finite element shape (interpolation) functions which, together with the associated nodal points $\boldsymbol{x}_A \in \boldsymbol{\varphi}(\mathcal{B})$, discretize the deformed configuration $\boldsymbol{\varphi}(\mathcal{B})$ of the body $\mathcal{B}$. The shape functions are subjected to the standard completeness condition $N_A(\boldsymbol{x}_B) = \delta_{AB}$, where δ_{AB} is the Kronecker symbol. In the Galerkin finite element formulation the finite dimensional subspaces $\mathcal{K}^h$ and $\mathcal{V}^h$ are defined, respectively, as:

$$\boldsymbol{u}^h = \sum_{A=1}^{n_{\text{node}}} N_A(\boldsymbol{x})\boldsymbol{u}_A, \quad \text{and} \quad \boldsymbol{\eta}^h = \sum_{A=1}^{n_{\text{node}}} N_A(\boldsymbol{x})\boldsymbol{\eta}_A, \qquad \forall \boldsymbol{x} \in \boldsymbol{\varphi}(\mathcal{B}), \tag{4.29}$$

where u_A is the nodal displacement. Inserting (4.29) into the weak form (4.27) leads to a set of semi-discrete equations:

$$\boldsymbol{M}\ddot{\boldsymbol{u}} + \mathbf{f}^{\text{int}}(\boldsymbol{u}) = \mathbf{f}^{\text{ext}} \tag{4.30}$$

where $\boldsymbol{u}$ are the nodal displacements, $\boldsymbol{M}$ denotes the mass matrix and $\mathbf{f}^{\text{int}}(\boldsymbol{u})$ represents the internal force contribution from the element stress field which satisfies the (non-linear) constitutive relations. The term $\mathbf{f}^{\text{ext}}$ represents the external forces arising from applied tractions and contact conditions.

Discretization in time: A wide range of techniques are available to solve the problem defined by equations (4.30). Modal analysis is traditionally used for systems dominated by low frequencies, whilst direct integration techniques are better suited for the transient response of systems with a wide spectrum of frequencies. In this work, the standard form of the explicit integration of

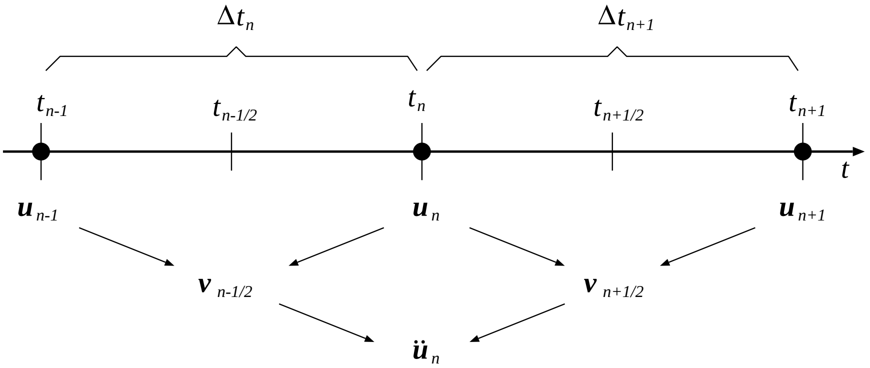

Figure 4.1: Central difference approximation.

equations (4.30) relies on the central difference approximation for the velocity and acceleration, as illustrated in Figure 4.1. After some simple manipulations and assuming, for simplicity, a constant time step increment $\Delta t = t_{n+1} - t_n = t_n - t_{n-1}$, the following recursive expressions for velocity and displacements may be obtained

$$\begin{aligned} \boldsymbol{v}_{n+\frac{1}{2}} &= \boldsymbol{v}_{n-\frac{1}{2}} + \Delta t\, \boldsymbol{M}^{-1} \left(\mathbf{f}_n^{\text{ext}} - \mathbf{f}_n^{\text{int}}\right) \\ \boldsymbol{u}_{n+1} &= \boldsymbol{u}_n + \Delta t\, \boldsymbol{v}_{n+\frac{1}{2}} \end{aligned} \tag{4.31}$$

The use of a diagonal lumped mass matrix $\boldsymbol{M}$ is highly desirable in order to de-couple the finite element equations and avoid the solution of the system of algebraic equations (4.31). The evaluation of displacement can then proceed on an individual nodal basis with inter nodal coupling occurring only throughout the calculation of the internal forces $\mathbf{f}^{\text{int}}$. This, makes explicit dynamic analysis an attractive solution approach for many industrially relevant problems.

Explicit time integration schemes are simple in logic and structure, but are *conditionally stable*, which constitutes a notable disadvantage. Numerical stability is governed by the time step increment, Δt_{cr}, which in turn, can be defined as a function of the maximum eigenvalue of the system, $\omega_{\max}$, as

$$\Delta t \leq \Delta t_{cr} = \frac{2}{\omega_{\max}}. \tag{4.32}$$

The present algorithm approximates the maximum eigenvalue of the *system* by the maximum *element* eigenvalue (Owen & Hinton, 1980). A practical measure of Δt_{cr} can be defined based on the wave propagation problem, which, for plane-strain problems and constant strain elements, is given by

$$\Delta t_{cr} = \frac{h_e}{Q + \sqrt{Q^2 + c^2}}, \tag{4.33}$$

where h_e is the characteristic length of the element, Q is a reduction factor related to the artificial viscosity,

$$Q = Q_l\, c + Q_q\, h_e\, \text{tr}[\dot{\boldsymbol{\varepsilon}}\,] \tag{4.34}$$

and c is the dilational wave speed associated with the element,

$$c = \sqrt{\frac{E(1-\nu)}{\rho(1+\nu)(1-2\nu)}}, \tag{4.35}$$

where $\text{tr}[\dot{\boldsymbol{\varepsilon}}\,]$ is the volumetric strain rate, Q_l and Q_q are the linear and quadratic bulk viscosity coefficients respectively, ν is the Poisson's ratio and E is the Young's modulus. Belytschko (1983) reports that, for central difference schemes, the critical time step should be further reduced to $\Delta t_{cr,c} = \Delta t_{cr}(\sqrt{1+\xi^2} - \xi)$, where ξ is a fraction of the critical damping in the maximum frequency.

In general, fine meshes require smaller time steps which increases the total computational time substantially. On the other hand, the majority of forming operations are sufficiently slow to be classified as quasi-static, with the material response being rate independent. Therefore in order to provide acceptable CPU times, the material density is artificially increased to achieve larger critical time steps. In addition, the punch velocity is usually raised to reduce the total number of time steps required to model forming process. Since increasing both the material density and punch velocity results in increased inertia forces, a sensible loading history must be designed to minimise the inertia effects.

Remark 4.1 *Considerable efforts have been made to improve the performance of explicit schemes (Zienkiewicz* et al. *, 1984; Thomas & Gladwell, 1988; Hoff & Taylor, 1990), and the developed versions have in general accuracy of order greater than or equal to two. However, this has resulted in either a reduced critical time step or a need for residual forces to be calculated more than once during each time step.*

4.4 Hyperelastic-based multiplicative finite plasticity

A rather general class of isotropic hyperelastic-based multiplicative plasticity models, formulated in the spatial configuration, is described in this section. The theory introduced forms the basis of the isotropic large strain plasticity framework whose finite element implementation is addressed in Section 4.5.

4.4.1 Multiplicative elasto-plasticity kinematics

The main hypothesis underlying the present approach to finite strain elasto-plasticity is the *multiplicative split* of the deformation gradient, $\boldsymbol{F}$, into elastic and plastic contributions:

$$\boldsymbol{F} = \boldsymbol{F}^{e}\boldsymbol{F}^{p}, \tag{4.36}$$

where $\boldsymbol{F}^{e}$ and $\boldsymbol{F}^{p}$ are named, respectively, the *elastic* and *plastic deformation gradients*. The multiplicative split of $\boldsymbol{F}$, introduced by Lee & Liu (1967) and Lee (1969), embodies the assumption of the existence of a local *unstressed intermediate configuration* defined by the plastic deformation gradient, $\boldsymbol{F}^{p}$. The concept is schematically illustrated in Figure 4.2. It must be emphasised that the unstressed intermediate configuration concept is valid only in the *local* (pointwise) sense.

Following the above multiplicative split of $\boldsymbol{F}$, the stretches and rotations associated with the elastic and plastic parts of the deformation gradient are obtained by performing the polar decompositions

$$\boldsymbol{F}^{e} = \boldsymbol{R}^{e}\boldsymbol{U}^{e} = \boldsymbol{V}^{e}\boldsymbol{R}^{e} \tag{4.37}$$

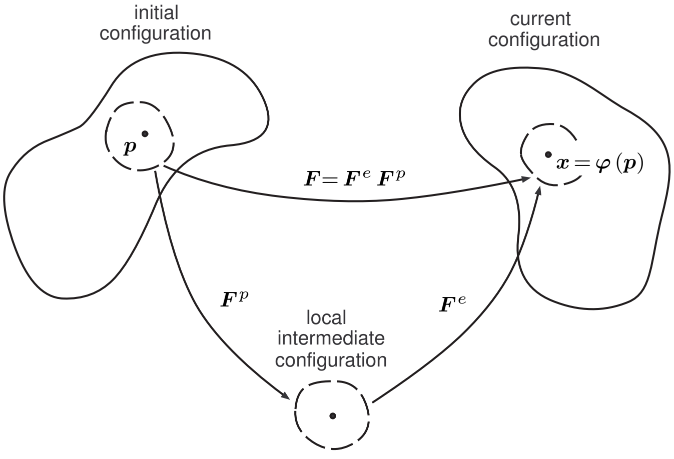
initial configuration
current configuration
$\boldsymbol{p}$
$\boldsymbol{F} = \boldsymbol{F}^e\,\boldsymbol{F}^p$
$\boldsymbol{x} = \boldsymbol{\varphi}\,(\boldsymbol{p})$
$\boldsymbol{F}^p$
$\boldsymbol{F}^e$
local intermediate configuration

Figure 4.2: Multiplicative decomposition of the deformation gradient.

and

$$\boldsymbol{F}^{\,p} = \boldsymbol{R}^p\,\boldsymbol{U}^p = \boldsymbol{V}^p\,\boldsymbol{R}^p \tag{4.38}$$

The resulting tensors $\boldsymbol{U}^e(\boldsymbol{U}^p)$, $\boldsymbol{V}^e(\boldsymbol{V}^p)$ and $\boldsymbol{R}^e(\boldsymbol{R}^p)$, are named, respectively, the *elastic* (*plastic*) right stretch tensor, the *elastic* (*plastic*) left stretch tensor and the *elastic* (*plastic*) rotation tensor.

Additive split of the velocity gradient, stretching and spin

As a consequence of the assumed multiplicative split of $\boldsymbol{F}$, the *velocity gradient* (refer to Section 3.1.6, page 27) defined by

$$\boldsymbol{l} \equiv \nabla_x \boldsymbol{v} = \dot{\boldsymbol{F}}\;\boldsymbol{F}^{\,-1}\,, \tag{4.39}$$

can be decomposed additively as:

$$\boldsymbol{l} = \boldsymbol{l}^e + \boldsymbol{l}^p\,, \tag{4.40}$$

where $\boldsymbol{l}^e$ and $\boldsymbol{l}^p$ are, respectively, the elastic and plastic contributions *defined* by

$$\boldsymbol{l}^e \equiv \dot{\boldsymbol{F}}^{\,e}(\boldsymbol{F}^{\,e})^{-1}\,, \qquad \boldsymbol{l}^p \equiv \boldsymbol{F}^{\,e}\dot{\boldsymbol{F}}^{\,p}(\boldsymbol{F}^{\,p})^{-1}(\boldsymbol{F}^{\,e})^{-1}\,. \tag{4.41}$$

Similarly, the *stretching* (or *rate of deformation*) tensor, $\boldsymbol{d}\equiv\mathrm{sym}[\boldsymbol{l}]$, can be decomposed as:

$$\boldsymbol{d} = \boldsymbol{d}^{\,e} + \boldsymbol{d}^{\,p}\,,$$

with the elastic and plastic stretchings given by

$$\boldsymbol{d}^{\,e} \equiv \mathrm{sym}[\boldsymbol{l}^e] \qquad\qquad \boldsymbol{d}^{p} \equiv \mathrm{sym}[\boldsymbol{l}^p]\;. \tag{4.42}$$

The same additive decomposition applies to the *spin tensor*, $\boldsymbol{w} \equiv \text{skew}[\boldsymbol{l}]$:

$$\boldsymbol{w} = \boldsymbol{w}^e + \boldsymbol{w}^p \,,$$

where the elastic and plastic spin tensors are defined by:

$$\boldsymbol{w}^e \equiv \text{skew}[\boldsymbol{l}^e] \qquad\qquad \boldsymbol{w}^p \equiv \text{skew}[\boldsymbol{l}^p] \;.$$

Spatially rotated plastic stretching

In the following, the *spatial* configuration will be used to formulate the general finite isotropic plasticity model. In this context, all kinematic quantities involved in the constitutive formulation will be expressed as spatial quantities (i.e., in the deformed configuration). It is thus convenient to define the following rotation of $\boldsymbol{d}^p$:

$$\tilde{\boldsymbol{d}}^p \equiv \boldsymbol{R}^e \, \boldsymbol{d}^p \, (\boldsymbol{R}^e)^T = \boldsymbol{R}^e \, \text{sym}\Big[\dot{\boldsymbol{F}}^p (\boldsymbol{F}^p)^{-1}\Big] \, (\boldsymbol{R}^e)^T \,. \tag{4.43}$$

The above tensor represents the rate of plastic stretching rotated (by the elastic rotation) to the spatial (or deformed) configuration and will be called the *spatial* plastic stretching (or rate of plastic deformation).

4.4.2 The logarithmic elastic strain measure

In Section 3.1.5 [page 26] Eulerian (or spatial) strain measures have been defined as functions of the left stretch tensor $\boldsymbol{V}$. Similarly, spatial *elastic* strain measures can be defined as functions of the *elastic* left stretch tensor, $\boldsymbol{V}^e$. As we shall notice, the use of the *logarithmic* (or *natural*) strain measure to describe the elastic behaviour is particularly convenient. The Eulerian logarithmic elastic strain is defined by:

$$\boldsymbol{\varepsilon}^e \equiv \ln \boldsymbol{V}^e = \tfrac{1}{2} \ln \boldsymbol{b}^e \,, \tag{4.44}$$

where $\ln(\cdot)$ above denotes the *tensor logarithm* of $(\cdot)$ and

$$\boldsymbol{b}^e = \boldsymbol{F}^e (\boldsymbol{F}^e)^T = (\boldsymbol{V}^e)^2$$

is the left elastic Cauchy-Green strain tensor.

Deviatoric and volumetric logarithmic strains

By performing the deviatoric/volumetric split of the elastic logarithmic strain we obtain:

$$\boldsymbol{\varepsilon}^e = \boldsymbol{\varepsilon}^e_d + \varepsilon^e_v \, \boldsymbol{I} \,, \tag{4.45}$$

where

$$\boldsymbol{\varepsilon}^e_d \equiv \boldsymbol{\varepsilon}^e - \tfrac{1}{3} \, \text{tr}[\boldsymbol{\varepsilon}^e] \boldsymbol{I} \,,$$

and the volumetric logarithmic elastic strain is given by

$$\varepsilon_v^e \equiv \mathrm{tr}[\boldsymbol{\varepsilon}^e] = \ln J^e \,,$$

with

$$J^e \equiv \det \boldsymbol{F}^{\,e} \,.$$

Due to the properties of the logarithmic strain measure, analogously to the infinitesimal theory, a traceless $\boldsymbol{\varepsilon}^e$ ($\varepsilon_v^e = 0$) corresponds to a finite volume preserving elastic deformation, i.e., a deformation with $\det \boldsymbol{F}^{\,e} = 1$.

4.4.3 A general isotropic large strain plasticity model

A rather general class of isotropic hyperelastic-based finite strain elasto-plastic constitutive models, formulated in the spatial configuration, is described below. The model is defined by the following assumptions.

Stress response. Hyperelastic relationship

The existence of a quadratic strain energy function $\psi^e(\boldsymbol{\varepsilon}^e)$ is assumed in the form of a scalar symmetric function of its stretches $\lambda_{(i)}^e$ (i) $(i = 1,\, 2,\, 3)$. In fact, it is generally accepted that a sufficiently general constitutive model with possibly wide range of applications, including metal plasticity, may be defined by employing the so-called Hencky strain energy function $\psi^e(\boldsymbol{\varepsilon}^e)$, which is given by:

$$\begin{aligned} \psi^e(\lambda_1^e, \lambda_2^e, \lambda_3^e) = G \left[(\ln\lambda_1^e)^2 + (\ln\lambda_2^e)^2 + (\ln\lambda_3^e)^2 \right] \\ + \tfrac{1}{2} \left(K + \tfrac{2}{3} G \right) \ln{(J^e)}^2 \,, \end{aligned} \tag{4.46}$$

where G and K are positive material constants and $J^e = \lambda_1^e\, \lambda_2^e\, \lambda_3^e$. The above strain-energy renders the following hyperelastic constitutive relationship between the Kirchhoff stress and the Eulerian logarithmic strain:

$$\boldsymbol{\tau} = \bar{\rho}\, \frac{\partial \psi}{\partial \boldsymbol{\varepsilon}^e} = \mathsf{D}^e : \boldsymbol{\varepsilon}^e \tag{4.47}$$

which has the same format as the infinitesimal linear elastic stress-strain relation. In Equation (4.47), D^e denotes the fourth-order isotropic constant elastic tensor.

The plastic flow rule

The evolution of the plastic deformation gradient – the plastic flow – is defined by the following constitutive equation for the rotated plastic stretching:

$$\tilde{\boldsymbol{d}}^p = \dot{\gamma}\, \frac{\partial \Psi}{\partial \boldsymbol{\tau}} \,, \tag{4.48}$$

where $\Psi(\boldsymbol{\tau}, \boldsymbol{A})$ is the *plastic flow potential*, expressed as a function of the *Kirchhoff* stress and the thermodynamical force set, $\boldsymbol{A}$. Equation (4.48) is complemented by postulating a null plastic spin:

$$\boldsymbol{w}^p = \boldsymbol{0}\,. \tag{4.49}$$

The two equations above completely define the evolution of $\boldsymbol{F}^{\,p}$. Indeed, the definition (4.43) of $\tilde{\boldsymbol{d}}^p$ together with the constitutive laws (4.48) and (4.49) are equivalent to the following evolution law for the plastic deformation gradient:

$$\dot{\boldsymbol{F}}^{\,p} = \dot{\gamma}\ (\boldsymbol{R}^e)^T \,\frac{\partial \Psi}{\partial \boldsymbol{\tau}}\, \boldsymbol{R}^e\, \boldsymbol{F}^{\,p}\,. \tag{4.50}$$

The elastic deformation gradient evolution equation corresponding to the above plastic flow equation within the multiplicative kinematics framework is given by

$$\dot{\boldsymbol{F}}^{e}(\boldsymbol{F}^{e})^{-1} = \dot{\boldsymbol{F}}\ (\boldsymbol{F})^{-1} - \dot{\gamma}\,\frac{\partial \Psi}{\partial \boldsymbol{\tau}}. \tag{4.51}$$

The evolution law for the internal variables assumes the standard format:

$$\dot{\boldsymbol{\alpha}} = -\dot{\gamma}\,\frac{\partial \Psi}{\partial \boldsymbol{A}}. \tag{4.52}$$

In the above, the *plastic multiplier*, $\dot{\gamma}$, is required to satisfy the standard complementarity relation:

$$\Phi \le 0 \qquad\qquad \dot{\gamma} \ge 0 \qquad\qquad \dot{\gamma}\Phi = 0\,. \tag{4.53}$$

with $\Phi(\boldsymbol{\tau}, \boldsymbol{A})$ denoting the *yield function*, expressed in terms of the *Kirchhoff* stress and the set $\boldsymbol{A}$ of conjugate thermodynamical forces.

The overall finite strain elasto-plastic constitutive model is completely defined by equations (4.47)– (4.53). The model is summarized in Box 4.3.

Finite strain extension to infinitesimal theories

Expression (4.47) as well as the adopted plastic flow rule (4.48) are completely analogous to their small strain counterparts. In the small strain limit, $\boldsymbol{\varepsilon}^e$ and $\tilde{\boldsymbol{d}}^p$ reduce, respectively, to the infinitesimal elastic strain tensor and plastic strain rate. Thus, the present approach allows a natural extension, to the finite strain range, of general isotropic infinitesimal models. Finite strain extensions obtained as such preserve some very important properties of the original small strain model (de Souza Neto *et al.* , 2005a):

- Volume preserving plastic deformations;
- Finite plastic incompressibility;
- Associativity and maximum plastic dissipation.

Box 4.3: General isotropic finite strain multiplicative elasto-plastic model

(i) Multiplicative decomposition of the deformation gradient

$$\boldsymbol{F} = \boldsymbol{F}^{e}\boldsymbol{F}^{p}$$

(ii) Isotropic hyperelastic law

$$\boldsymbol{\tau} = \bar{\rho}\,\frac{\partial\psi(\boldsymbol{\varepsilon}^e, \boldsymbol{\alpha})}{\partial\boldsymbol{\varepsilon}^e}$$

(iii) Evolution equations for $\boldsymbol{F}^{p}$ and internal variable set $\boldsymbol{\alpha}$

$$\begin{aligned} \dot{\boldsymbol{F}}^{p}(\boldsymbol{F}^{p})^{-1} &= \dot{\gamma}\,(\boldsymbol{R}^e)^T\,\frac{\partial\Psi}{\partial\boldsymbol{\tau}}\,\boldsymbol{R}^e \\ \dot{\boldsymbol{\alpha}} &= -\dot{\gamma}\,\frac{\partial\Psi}{\partial\boldsymbol{A}} \end{aligned}$$

(iv) Loading/unloading criterion

$$\Phi \leq 0 \qquad \dot{\gamma} \geq 0 \qquad \dot{\gamma}\Phi = 0$$

4.4.4 The general elastic predictor/return mapping algorithm

In any numerical scheme employed for the analysis of elasto-plastic problems it eventually becomes necessary to integrate the constitutive equations of the model. In this section, we show that an integration algorithm can be derived for the general finite multiplicative plasticity model based on analogous concepts of the elastic predictor/return mapping algorithms of the infinitesimal theory.

The incremental finite plasticity problem

The problem to be addressed, is that of updating the *known* state variables associated with a *converged* configuration at t_n into their corresponding updated values on the *updated* configuration at t_{n+1} in a manner consistent with the constitutive equations of Box 4.3. In this process, the incremental displacements, $\Delta\boldsymbol{u}$, defining the geometry update are assumed given.

In the present context, given $\boldsymbol{F}^{e}_{n}$ and the set $\boldsymbol{\alpha}_n$ of internal variables at the beginning of the interval $[t_n, t_{n+1}]$ and given the prescribed incremental deformation gradient, $\boldsymbol{F}_{\Delta}$, for this interval, solve the following system of algebraic equations

$$\begin{aligned} \boldsymbol{F}^{e}_{n+1} &= \boldsymbol{F}_{\Delta}\boldsymbol{F}^{e}_{n}\,\boldsymbol{R}^{e\,T}_{n+1}\,\exp\Big[-\Delta\gamma\;\frac{\partial\Psi}{\partial\boldsymbol{\tau}}\Big|_{n+1}\Big]\,\boldsymbol{R}^{e}_{n+1} \\ \boldsymbol{\alpha}_{n+1} &= \boldsymbol{\alpha}_{n} + \Delta\gamma\,\boldsymbol{H}_{n+1} \end{aligned} \tag{4.54}$$

for the unknowns $\boldsymbol{F}^{e}_{n+1}$, $\boldsymbol{\alpha}_{n+1}$ and $\Delta\gamma$, subjected to the constraints

$$\Delta\gamma > 0 \qquad \Phi(\boldsymbol{\tau}_{n+1}, \boldsymbol{A}_{n+1}) \leq 0 \qquad \Delta\gamma\,\Phi(\boldsymbol{\tau}_{n+1}, \boldsymbol{A}_{n+1}) = 0 \tag{4.55}$$

with

$$\boldsymbol{\tau}_{n+1} = \frac{\partial\psi}{\partial\boldsymbol{\varepsilon}^{e}}\bigg|_{n+1} \qquad \boldsymbol{A}_{n+1} = \frac{\partial\psi}{\partial\boldsymbol{\alpha}}\bigg|_{n+1} \tag{4.56}$$

and the kinematic relations

$$\begin{aligned} \boldsymbol{\varepsilon}^{e}_{n+1} &= \ln\boldsymbol{V}^{e}_{n+1} \\ \boldsymbol{V}^{e}_{n+1} &= \big[\boldsymbol{F}^{e}_{n+1}(\boldsymbol{F}^{e}_{n+1})^{T}\big]^{\frac{1}{2}} \\ \boldsymbol{R}^{e}_{n+1} &= \big[\boldsymbol{V}^{e}_{n+1}\big]^{-1}\boldsymbol{F}^{e}_{n+1}. \end{aligned} \tag{4.57}$$

After the solution of the above problem, the updated plastic strain can be promptly determined from the multiplicative elasto-plastic split as

$$\boldsymbol{F}^{p}_{n+1} = (\boldsymbol{F}^{e}_{n+1})^{-1}\,\boldsymbol{F}_{n+1}. \tag{4.58}$$

The elastic predictor/return mapping scheme

The operator split methodology results in an algorithm which consists of two basic steps: the *elastic predictor*, where the problem is assumed to be purely elastic between times t_n and t_{n+1} (no plastic flow or internal variable evolution), followed by a *plastic corrector*, where a discrete system of equations comprising the elasticity law, plastic flow, internal variables evolution and the loading/unloading criterion is solved with the results of the elastic predictor stage – the *elastic trial state* – as initial conditions. The general algorithm comprises the following steps:

(i) The *elastic predictor* step, obtained by solving (4.54) with $\Delta\gamma = 0$, gives the *elastic trial state*

$$\begin{aligned} \boldsymbol{F}^{e\,\text{trial}}_{n+1} &= \boldsymbol{F}_{\Delta}\boldsymbol{F}^{e}_{n} \\ \boldsymbol{\alpha}^{\text{trial}}_{n+1} &= \boldsymbol{\alpha}_{n}. \end{aligned} \tag{4.59}$$

where $\boldsymbol{F}^{e}_{n}$ is the elastic deformation gradient at t_n and $\boldsymbol{F}_{\Delta}$ denotes the *incremental deformation gradient*:

$$\boldsymbol{F}_{\Delta} \equiv \boldsymbol{F}_{n+1}(\boldsymbol{F}_{n})^{-1} = \boldsymbol{I} + \nabla_{x_n}[\Delta\boldsymbol{u}]\,, \tag{4.60}$$

with $\Delta\boldsymbol{u}$ denoting the incremental displacement field between times t_n and t_{n+1}. The corresponding elastic trial Kirchhoff stress and thermodynamical forces are given by the potential relations:

$$\boldsymbol{\tau}_{n+1}^{\text{trial}} = \bar{\rho}\,\frac{\partial\psi}{\partial\boldsymbol{\varepsilon}^e}\bigg|_{n+1}^{\text{trial}} \qquad\qquad \boldsymbol{A}_{n+1}^{\text{trial}} = \bar{\rho}\,\frac{\partial\psi}{\partial\boldsymbol{\alpha}}\bigg|_{n+1}^{\text{trial}} . \tag{4.61}$$

(ii) If the pair $\left\{\boldsymbol{\tau}_{n+1}^{\text{trial}}, \boldsymbol{A}_{n+1}^{\text{trial}}\right\}$, is plastically admissible, i.e, if

$$\Phi(\boldsymbol{\tau}_{n+1}^{\text{trial}}, \boldsymbol{A}_{n+1}^{\text{trial}}) \leq 0\,. \tag{4.62}$$

then the process is purely elastic within the interval $[t_n, t_{n+1}]$. The state is then updated as

$$(\cdot)_{n+1} = (\cdot)_{n+1}^{\text{trial}}\,.$$

(iii) Otherwise, plastic yielding occurs and we solve the *return mapping* equations

$$\begin{aligned} &\boldsymbol{F}_{n+1}^{e} = \boldsymbol{F}_{n+1}^{e\,\text{trial}}\,\boldsymbol{R}_{n+1}^{e\,T}\,\exp\Big[-\Delta\gamma\,\tfrac{\partial\Psi}{\partial\boldsymbol{\tau}}\big|_{n+1}\Big]\,\boldsymbol{R}_{n+1}^{e} \\ &\boldsymbol{\alpha}_{n+1} = \boldsymbol{\alpha}_{n}^{\text{trial}} + \Delta\gamma\,\boldsymbol{H}_{n+1} \\ &\Phi(\boldsymbol{\tau}_{n+1}, \boldsymbol{A}_{n+1}) = 0, \end{aligned} \tag{4.63}$$

for $\boldsymbol{F}_{n+1}^{e}$, $\boldsymbol{\alpha}_{n+1}$ and $\Delta\gamma$, which gives the numerical approximation to the state variables at time station t_{n+1}.

Logarithmic strains and the infinitesimal format return mapping

It is possible to simplify the return mapping equation $(4.63)_1$ by re-writing it in terms of the logarithmic elastic strain measure (rather than the elastic deformation gradient). The post-multiplication of both sides of $(4.63)_1$ by $\boldsymbol{R}_{n+1}^{e\,T}$ results in:

$$\boldsymbol{V}_{n+1}^{e} = \boldsymbol{F}_{n+1}^{e\,\text{trial}}\,\boldsymbol{R}_{n+1}^{e\,T}\,\exp\Big[-\Delta\gamma\,\tfrac{\partial\Psi}{\partial\boldsymbol{\tau}}\big|_{n+1}\Big]\,, \tag{4.64}$$

or, equivalently,

$$\boldsymbol{V}_{n+1}^{e}\,\exp\Big[\Delta\gamma\,\tfrac{\partial\Psi}{\partial\boldsymbol{\tau}}\big|_{n+1}\Big] = \boldsymbol{F}_{n+1}^{e\,\text{trial}}\,\boldsymbol{R}_{n+1}^{e\,T}\,. \tag{4.65}$$

Then, a further post-multiplication of each side by its transpose, gives:

$$\boldsymbol{V}_{n+1}^{e}\,\exp\Big[2\,\Delta\gamma\,\tfrac{\partial\Psi}{\partial\boldsymbol{\tau}}\big|_{n+1}\Big]\,\boldsymbol{V}_{n+1}^{e} = (\boldsymbol{V}_{n+1}^{e\,\text{trial}})^2\,. \tag{4.66}$$

Due to the assumed elastic isotropy, $\boldsymbol{V}^e$ and $\boldsymbol{\tau}$ commute. Then by rearranging the terms and taking the square root of both sides of expression (4.66) we obtain:

$$\boldsymbol{V}_{n+1}^{e} = \boldsymbol{V}_{n+1}^{e\,\text{trial}}\,\exp\Big[-\Delta\gamma\,\tfrac{\partial\Psi}{\partial\boldsymbol{\tau}}\big|_{n+1}\Big]\,. \tag{4.67}$$

Finally, by taking the tensor logarithm of both sides of (4.67), we obtain the much simpler formula in terms of logarithmic Eulerian strain tensors:

$$\boldsymbol{\varepsilon}^e_{n+1} = \boldsymbol{\varepsilon}^{e\ \mathrm{trial}}_{n+1} - \Delta\gamma\ \left.\frac{\partial\Psi}{\partial\boldsymbol{\tau}}\right|_{n+1}, \tag{4.68}$$

which has the same format as the update formula for the elastic strains of the standard *implicit* return mapping algorithms of the infinitesimal theory. For the elastic rotation, the above algorithm results in the following update formula:

$$\boldsymbol{R}^e_{n+1} = \boldsymbol{R}^{e\ \mathrm{trial}}_{n+1}. \tag{4.69}$$

To see this, note that by comparing (4.64) to (4.67), we find:

$$\boldsymbol{V}^{e\ \mathrm{trial}}_{n+1} = \boldsymbol{F}^{\ e\ \mathrm{trial}}_{\ n+1}\, \boldsymbol{R}^{e\ T}_{n+1} = \boldsymbol{V}^{e\ \mathrm{trial}}_{n+1}\, \boldsymbol{R}^{\ e\ \mathrm{trial}}_{n+1}\, \boldsymbol{R}^{e\ T}_{n+1}, \tag{4.70}$$

which leads to (4.69).

Computational implementation of the general algorithm

Since the elastic law is defined here in terms of the spatial elastic logarithmic strain, in the actual computational implementation of the above elastic predictor/return mapping procedure we shall take $\boldsymbol{\varepsilon}^e$ as the kinematic variable to be stored in the computer memory. Therefore, after retrieving the elastic logarithmic strain $\boldsymbol{\varepsilon}^e_n$ at t_n the elastic trial left Cauchy-Green tensor is computed by

$$\boldsymbol{b}^e_n = \exp[2\,\boldsymbol{\varepsilon}^e_n].$$

The following kinematic operations required for integration of the large strain elasto-plastic constitutive equations are summarized in Box 4.4.

Remark 4.2 *The operations carried out in Box 4.4 are related exclusively to the kinematics of finite strains. Due to the use of logarithmic strains to describe elasticity along with the implicit exponential approximation to the plastic flow rule, the essential material related stress updating procedure preserves the small strain format. It corresponds to the general elastic predictor/return mapping algorithm for infinitesimal plasticity. In computational terms, it means that all small strain elasto-plastic integration subroutines can be re-used in the finite strain range without modification.*

4.4.5 The incremental boundary value problem

The introduction of algorithmic constitutive function, $\hat{\boldsymbol{\sigma}}$, for the stress tensor

$$\hat{\boldsymbol{\sigma}}(\boldsymbol{\alpha}_n, \boldsymbol{F}_{n+1}) = \hat{\boldsymbol{\tau}}(\boldsymbol{\alpha}_n, \boldsymbol{F}_{n+1})/\det[\boldsymbol{F}_{n+1}] \tag{4.71}$$

Box 4.4: General integration algorithm for multiplicative finite strain elasto-plasticity

(i) Given incr.displ. $\Delta\boldsymbol{u}$, update the deformation gradient

$$\boldsymbol{F}_{\Delta} := \boldsymbol{I} + \nabla_n[\Delta\boldsymbol{u}] \qquad \boldsymbol{F}_{n+1} := \boldsymbol{F}_{\Delta}\,\boldsymbol{F}_{n}$$

(ii) Compute the elastic trial state

$$\begin{aligned}
\boldsymbol{b}_n^e &:= \exp[2\,\boldsymbol{\varepsilon}_n^e] \\
\boldsymbol{b}_{n+1}^{e\,\text{trial}} &:= \boldsymbol{F}_{\Delta}\,\boldsymbol{b}_n^e\,(\boldsymbol{F}_{\Delta})^T \\
\boldsymbol{\varepsilon}_{n+1}^{e\,\text{trial}} &:= \ln[\boldsymbol{V}_{n+1}^{e\,\text{trial}}] = \tfrac{1}{2}\ln[\boldsymbol{b}_{n+1}^{e\,\text{trial}}] \\
\boldsymbol{\alpha}_{n+1}^{\text{trial}} &:= \boldsymbol{\alpha}_n
\end{aligned}$$

(iii) Use the small strain algorithm to evaluate $\boldsymbol{\tau}_{n+1}$, $\boldsymbol{\varepsilon}_{n+1}^e$ and $\boldsymbol{\alpha}_{n+1}$

$$\boldsymbol{\tau}_{n+1} = \tilde{\boldsymbol{\tau}}\left(\boldsymbol{\alpha}_n, \boldsymbol{\varepsilon}_{n+1}^{e\,\text{trial}}\right).$$

(iv) Update the Cauchy stress

$$\boldsymbol{\sigma}_{n+1} := \det[\boldsymbol{F}_{n+1}]^{-1}\,\boldsymbol{\tau}_{n+1}$$

in the weak form of the equilibrium, stated in its spatial version in Section 3.5.1 (page 38), results in the *incremental boundary value problem* stated as follows:

Given the set $\boldsymbol{\alpha}_n$ *of internal variables at time* t_n*, and given the body forces* $\boldsymbol{f}_{n+1}$ *and surface traction* $\boldsymbol{t}_{n+1}$ *fields at* t_{n+1}*, find a kinematically admissible configuration* $\varphi_{n+1}(\mathcal{B}) \in \mathcal{K}_{n+1}$ *such that the the virtual work equation*

$$\int_{\varphi_{n+1}(\mathcal{B})} [\hat{\boldsymbol{\sigma}}(\boldsymbol{\alpha}_n, \boldsymbol{F}_{n+1}) : \nabla_x\boldsymbol{\eta} - \boldsymbol{f}_{n+1}\cdot\boldsymbol{\eta}]\,\mathrm{d}v - \int_{\varphi_{n+1}(\partial\mathcal{B})} \boldsymbol{t}_{n+1}\cdot\boldsymbol{\eta}\,\mathrm{d}a = 0, \quad (4.72)$$

is satisfied for any $\boldsymbol{\eta} \in \mathcal{V}$*, where* φ_{n+1} *is the deformation map at* t_{n+1}*. The set* $\mathcal{K}_{n+1}$ *is defined as*

$$\mathcal{K}_{n+1} = \{\boldsymbol{u} : \mathcal{B} \to \mathcal{U} \,|\, \boldsymbol{u} = \bar{\boldsymbol{u}}_{n+1} \quad \text{on} \quad \partial\mathcal{B}_u\} \qquad (4.73)$$

where $\bar{\boldsymbol{u}}_{n+1}$ *is the prescribed boundary displacement at* t_{n+1}*.*

It is important to remark that the weak form of the equilibrium, stated above, is restricted to *quasi-static* conditions, where inertia effects are ignored. Furthermore, due to the introduction of $\hat{\boldsymbol{\sigma}}$, the constitutive relations are satisfied only approximately.

The consistent spatial tangent modulus

In Appendix B, the exact linearization of the boundary value problem was carried out in the context of element technology. Here, the main concern is to derive a closed formula for the spatial tangent modulus a which takes part in the directional derivative of the internal work functional:

$$\mathrm{D}G^{\mathrm{int}}\,(\boldsymbol{u},\,\boldsymbol{\eta})\,[\boldsymbol{d}] = \int_{\varphi(\mathcal{B})} \nabla_x\,\boldsymbol{\eta} : \,\mathsf{a} : \,\nabla_x\,\boldsymbol{d}\,\mathrm{d}v \tag{4.74}$$

with cartesian derivatives given by

$$\mathsf{a}_{ijkl} = \frac{1}{J}\,\frac{\partial \boldsymbol{\tau}_{ij}}{\partial F_{kq}}\,F_{lq} - \sigma_{il}\,\delta_{jk}\,, \tag{4.75}$$

where $J = \det \boldsymbol{F}$. The term $\partial \boldsymbol{\tau}_{ij}/\partial F_{kq}$ taking part in (4.75) is the only term that depends on the particular constitutive model adopted. For the present model, in the small strain integration algorithm, the updated Kirchhoff stress, $\boldsymbol{\tau}_{n+1}$, is obtained as a function of internal variable set $\boldsymbol{\alpha}_n$, at t_n, and the elastic trial logarithmic strain [step (iii) of Box 4.4] of the form:

$$\boldsymbol{\tau}_{n+1} = \tilde{\boldsymbol{\tau}}\,(\boldsymbol{\alpha}_n, \boldsymbol{\varepsilon}^{e\ \mathrm{trial}}_{n+1})\,. \tag{4.76}$$

In the algorithm $\boldsymbol{\varepsilon}^{e\ \mathrm{trial}}_{n+1}$ is computed as a function of $\boldsymbol{b}^{e\ \mathrm{trial}}_{n+1}$ which, in turn, is a function of $\boldsymbol{F}^{\,p}_{n}$ and $\boldsymbol{F}_{n+1}$. The global operator split algorithm, defines an implicit function $\hat{\boldsymbol{\tau}}$, for the updated Kirchhoff stress, that can be generally expressed as:

$$\hat{\boldsymbol{\tau}}\,(\boldsymbol{\alpha}_n, \boldsymbol{F}_{n+1}) = \tilde{\boldsymbol{\tau}}\,(\boldsymbol{\alpha}_n, \boldsymbol{\varepsilon}^{e\ \mathrm{trial}}_{n+1}(\boldsymbol{b}^{e\ \mathrm{trial}}_{n+1}(\boldsymbol{F}^{\,p}_{n}, \boldsymbol{F}_{n+1})))\,. \tag{4.77}$$

In order to obtain the aforementioned derivative $\partial \boldsymbol{\tau}_{ij}/\partial F_{kq}$, we apply the chain rule to (4.77) and obtain

$$\frac{\partial \hat{\boldsymbol{\tau}}}{\partial \boldsymbol{F}_{n+1}} = \frac{\partial \tilde{\boldsymbol{\tau}}}{\partial \boldsymbol{\varepsilon}^{e\ \mathrm{trial}}_{n+1}} : \frac{\partial \boldsymbol{\varepsilon}^{e\ \mathrm{trial}}_{n+1}}{\partial \boldsymbol{b}^{e\ \mathrm{trial}}_{n+1}} : \frac{\partial \boldsymbol{b}^{e\ \mathrm{trial}}_{n+1}}{\partial \boldsymbol{F}_{n+1}}\,. \tag{4.78}$$

Substitution of this expression into (4.75) results, after straightforward manipulations, in the following closed formula for the components of the spatial tangent modulus consistent with the present operator split algorithm:

$$\mathsf{a}_{ijkl} \;=\; \frac{1}{2\,J}\,[\,\mathsf{D} : \mathsf{L} : \mathsf{B}\,]_{ijkl} \;-\; \sigma_{il}\,\delta_{jk}\,, \tag{4.79}$$

where D is the *small strain elastic or elasto-plastic consistent tangent operator*:

$$\mathsf{D} \;=\; \frac{\partial \tilde{\boldsymbol{\tau}}}{\partial \boldsymbol{\varepsilon}^{e\ \mathrm{trial}}_{n+1}}\,. \tag{4.80}$$

The fourth order tensor L is defined as:

$$\mathsf{L} = \frac{\partial \ln[\boldsymbol{b}^{e\ \mathrm{trial}}_{n+1}]}{\partial \boldsymbol{b}^{e\ \mathrm{trial}}_{n+1}}, \tag{4.81}$$

i.e., it is the derivative of the tensor logarithm function at $\boldsymbol{b}^{e\ \mathrm{trial}}_{n+1}$, which is a member of the class of isotropic tensor functions described in Appendix A. The fourth order tensor B is defined by the cartesian components:

$$\mathsf{B}_{ijkl} = \delta_{ik}\,(\boldsymbol{b}^{e\ \mathrm{trial}}_{n+1})_{jl} + \delta_{jk}\,(\boldsymbol{b}^{e\ \mathrm{trial}}_{n+1})_{il}\,. \tag{4.82}$$

Remark 4.3 *It should be noted that* D *is the* *only* *material related contribution to the spatial modulus* a*. All other terms taking part in its assemblage in (4.79) are related purely to the geometry of finite deformations and are completely independent of the particular material model adopted. The operator* D *has exactly the same functional format as the tangent consistent with the corresponding implicit integration algorithms for* *infinitesimal* *plasticity.*

4.5 Implicit quasi-static finite element solution strategy

The weak form of the momentum balance, the *principle of virtual work*, represents the starting point of displacement based finite element solution procedures (Hughes, 1987; Bathe, 1996; Zienkiewicz & Taylor, 2000). The standard finite element discretization, as described in Section 4.3.1, leads to a discrete version of the virtual work. This is obtained by inserting (4.29) into the weak form (4.72). The problem is then reduced to the following. Find the nodal displacement vector $\boldsymbol{u}_{n+1}$ at time t_{n+1} such that the following non-linear algebraic system:

$$\mathbf{r}(\mathbf{u}_{n+1}) \equiv \mathbf{f}^{\,\mathrm{int}}(\mathbf{u}_{n+1}) - \mathbf{f}^{\,\mathrm{ext}}_{n+1} = 0 \tag{4.83}$$

is satisfied, where $\mathbf{f}^{\,\mathrm{int}}(\mathbf{u}_{n+1})$ and $\mathbf{f}^{\,\mathrm{ext}}_{n+1}$ are, respectively, internal and external global force vectors resulting from the assemblage of the element vectors:

$$\mathbf{f}^{\,\mathrm{int}}_{(e)} = \int_{\boldsymbol{\varphi}(\mathcal{B}^{(e)})} \mathbf{B}^T \hat{\boldsymbol{\sigma}}\,(\boldsymbol{F}(\mathbf{u}_{n+1}), \boldsymbol{\alpha}_n)\,\mathrm{d}v \tag{4.84}$$

$$\mathbf{f}^{\,\mathrm{ext}}_{(e)} = \int_{\boldsymbol{\varphi}(\mathcal{B}^{(e)})} \mathbf{N}^T \boldsymbol{f}_{n+1}\,\mathrm{d}v + \int_{\partial\boldsymbol{\varphi}(\mathcal{B}^{(e)})} \mathbf{N}^T \boldsymbol{t}_{n+1}\,\mathrm{d}a \tag{4.85}$$

with $\mathbf{B}$ and $\mathbf{N}$ being, respectively, the standard discrete symmetric gradient operator and the interpolation matrix of the element (e) in the configuration defined by displacement $\mathbf{u}_{n+1}$ and $\hat{\boldsymbol{\sigma}}$ is the vector containing the Cauchy stress components delivered by the algorithmic function.

4.5.1 The Newton-Raphson scheme. Linearization

An effective and efficient way to find a solution $\mathbf{u}_{n+1}$ to the above non-linear system is to use the standard Newton-Raphson iterative procedure, obtained from the exact linearization of (4.83). During a typical Newton-Raphson iteration (k), the following linear system is solved for the iterative displacement $\Delta\mathbf{u}^{(k)}$:

$$\mathbf{K}(\mathbf{u}_{n+1}^{(k)})[\Delta\mathbf{u}^{(k)}] = -\mathbf{r}\,(\mathbf{u}_{n+1}^{(k)}) \tag{4.86}$$

and the new guess for the solution $\mathbf{u}_{n+1}$ is updated as:

$$\mathbf{u}_{n+1}^{(k+1)} = \mathbf{u}_{n+1}^{(k)} + \Delta\mathbf{u}^{(k)} \tag{4.87}$$

The *tangent stiffness* $\mathbf{K}$ is defined by the directional derivative formula:

$$\mathbf{K}(\mathbf{u})[\Delta\mathbf{u}] = \left.\frac{\mathrm{d}}{\mathrm{d}\,\varepsilon}\right|_{\varepsilon=0} \mathbf{r}\,(\mathbf{u} + \varepsilon\,\Delta\mathbf{u}) \tag{4.88}$$

If the external loads are assumed independent of $\mathbf{u}$, then the element tangent stiffness is given by the formula:

$$\mathbf{K}^{(e)} = \int_{\boldsymbol{\varphi}(\mathcal{B}^{(e)})} \mathbf{G}^T \mathbf{a} \mathbf{G}\,\mathrm{d}v \tag{4.89}$$

where $\mathbf{G}$ is the standard discrete spatial gradient operator and $\mathbf{a}$ denotes the matrix form of the *spatial elasticity tensor* $\mathbf{a}$ given, in Cartesian components, by:

$$\mathsf{a}_{ijkl} = \frac{1}{J}\,\frac{\partial \tau_{ij}}{\partial F_{km}}\,F_{lm} - \sigma_{il}\,\delta_{jk} \tag{4.90}$$

Note that, since the Kirchhoff stress tensor is the outcome of the algorithmic function (4.77), its derivative appearing in the expression above is, in fact, the derivative

$$\left.\frac{\partial \hat{\boldsymbol{\tau}}}{\partial \boldsymbol{F}}\right|_{(\boldsymbol{F}_{n+1}^{(k)},\,\boldsymbol{\alpha}_n)} \tag{4.91}$$

of the *incremental* (rather than the actual) constitutive functional. It is worth mentioning here that whenever more complex integration algorithms and/or material models (particularly in the finite strain range) are involved, *consistent tangent operators* may not be easily derived. Issues associated with consistent linearization aspects in finite multiplicative plasticity are discussed in detail by Simo & Miehe (1992) and Cuitiño & Ortiz (1992). As already mentioned in Section 1.1.4, consistent linearization is regarded as a crucial aspect of the formulations presented. The asymptotically quadratic rates of convergence more than justify the importance of this issue.

CHAPTER 5

DAMAGE CONSTITUTIVE MODELLING AND FAILURE IN DUCTILE METALS

THE gradual internal deterioration at the microscopic level which may, eventually, lead to the occurrence of macroscopic failure in ductile metals, undergoing plastic deformations, has been subjected to a detail study over the last two decades. In metal forming operations – our main area of interest – finite bulk deformations are almost invariably accompanied by large inelastic strains. As experimentally verified for many ductile polycrystalline metals, initially throughout metallographic observations (Hancock & Mackenzie, 1976; Le Roy *et al.* , 1981; Thomason, 1990), the nucleation and growth of voids and microcracks which accompany large plastic flow causes considerable reduction of stiffness, strength and is highly influenced by the triaxiality of the stress state (Lemaitre, 1984, 1985a). Close to material failure, the energy dissipation associated with such mechanisms has a dominant effect. A proper modelling of this phenomena at the mesoscale would strengthen the prediction of ductile failure in real life components and structures (i.e., the macroscale). Undoubtedly, the ability of the designer to anticipate mechanical breakdown is of crucial importance and accidental failure may have catastrophic effects, with consequences, far beyond purely economical issues.

The present chapter is devoted to computational continuum damage mechanics. Our intention here is to provide an introduction to this promising ramification of computational solid mechanics, which has been gaining widespread acceptance over the last three decades. This chapter is organised as follows. In Section 5.2 a brief historical review of *Continuum damage mechanics* is given and particular emphasis is given to the phenomenon of ductile plastic damage. The description of Lemaitre's elasto-plastic damage theory (Lemaitre, 1996), is undertaken in Section 5.3. The two following sections of this chapter, Sections 5.4 and 5.5, describe, respectively, a rate independent model for damage growth, which includes crack closure effects and a rate dependent version. In each of those sections, the computational implementation of the corresponding constitutive models is described in detail.

5.1 Introduction

In order to understand the material behaviour close to failure and improve the accuracy of inelastic constitutive relations, several approaches and theories have been proposed. The overall goal of one recent strategy is to construct well-defined, reliable connections between material microstructure and the macroscopic response of structural metals. The material structure is a collection of many features, such as chemical composition, atomic structure of the crystal lattice, precipitates and defects, dislocation structures within individual grains and subgrains, grain size and grain boundary deformations (see Section 2.1). With few exceptions, these features evolve during deformation and with time. Successful modelling of their role could suggest interventions on the micro-level, that would generate desirable behavior modifications on the macroscale. Such efforts involve modelling on many different size scales, and while much insight has been gained within the respective scales, connections between scales, especially those close to the opposite ends of the spectrum, remain often elusive and prevails an active area of research. This approach is strongly supported by the developments of experimental devices, like the high-resolution electron microscope, which allows the examination of defects at the atomic scale and the macroscopic response they engender [see Ortiz (1996) and Miehe *et al.* (1999), and references therein, for reviews of the computational approaches employed in this rapidly expanding field].

On the other hand, with the growing knowledge of the mechanisms of progressive internal damage that cause failure in a wide range of materials, it is becoming possible to formulate continuum constitutive models capable of accounting for the evolution of internal deterioration, in the analysis of large scale problems. It is often argued that the ultimate task of engineering research is to supply a rational predictive tool applicable in design. Such interest in the development of continuum theories for ductile damage may be attributed in part to the increasing industrial requirement for models capable of simulating the behaviour of metals under conditions in which internal damage plays a significant role. Therefore, a model intended to represent such phenomena should be simple enough to allow efficient numerical treatment and easy experimental verification of material parameters. At the same time its simplicity should not eliminate the essential features of the mechanical behaviour within the intended range of application.

5.2 Continuum damage mechanics

Since the pioneering work by Kachanov (1958), a considerable body of the literature on applied mechanics has been devoted to the formulation of constitutive models to describe internal degradation of solids within the framework of continuum mechanics. After over three decades of uninterrupted development, significant progress has been achieved and *Continuum damage mechanics* (CDM) has emerged as an alternative approach by introducing new state variables into the material constitutive model.

The material behaviour is modelled by constitutive equations taking into account its progressive deterioration. Such models are based on the assumption that the progressive internal deterioration observed prior to the onset of a macro-crack can be effectively represented by one or more internal variables of scalar, vectorial or tensorial nature. Such variable(s) named the damage variable(s) can be seen as phenomenological, averaged counterparts of microscopic measures of defects within a *representative volume element* (RVE). Their evolution must be defined by thermodynamically consistent constitutive relations, usually represented by a set of differential equations in time. In this context, we shall refer to as a *Continuum Damage Mechanics Model* any continuum constitutive model which features special internal variables representing, directly or indirectly, the density and/or distribution of the microscopic defects that characterise damage. The ultimate phase of the damage evolution is detected by a local criterion and corresponds to the failure of the RVE, and hence to a macro-crack initiation.

5.2.1 Original development. A brief review

Using the method of local state and internal variables, several continuum damage models, either phenomenological or micromechanically based, have been developed. The modern damage formulation can be traced back to the late fifties when Kachanov (1958), based on the concept the effective resisting surface, developed a model for creep rupture. A physical significance for the damage variable was given later by Rabotnov (1963) who proposed the reduction of the cross-sectional area due to microcracking as a suitable measure of the state of internal damage. A generalization of the basic definition assumes that the damage variable, D, physically represents the corrected area of cracks and cavities per unit surface cut by a plane perpendicular to a normal vector, $\boldsymbol{n}$, as

$$D = \frac{S - \tilde{S}}{S} \tag{5.1}$$

where S is the overall area of the element defined by its normal $\boldsymbol{n}$, $\tilde{S}$ is the effective resisting area and S_D is the total area of micro-cracks and cavities, as depicted in Figure 5.1. Rigorous formulation naturally leads to the definition of

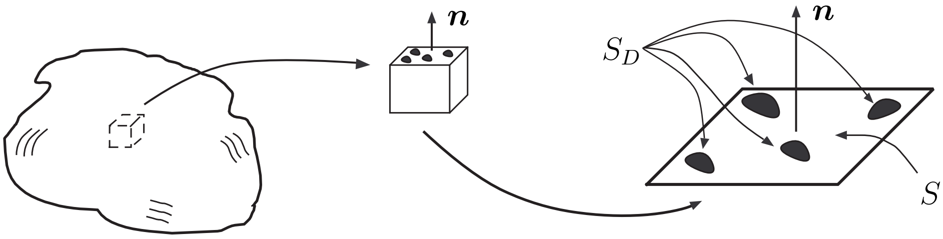

Figure 5.1: Damaged element.

a damage tensor, as proposed either by Chaboche (1984) or Murakami (1987) who have shown how large plastic flow is responsible for inducing anisotropy. In this case, the experimental identification of damage parameters becomes a very difficult and complicated task with very few examples in the published literature. However, assuming *isotropic* damage in many cases is not too far from reality, as a result of the random shapes and distribution of the included particles and precipitates that trigger damage initiation and growth. In this case, the damage variable, D, can assume values between $D=0$ corresponding to the virgin material and $D=1$ representing the total loss of load bearing capacity. In order to describe the strain rate increase which characterises tertiary creep, Kachanov has replaced the observed uniaxial stress σ with the *effective stress*:

$$\tilde{\sigma} = \frac{\sigma}{1-D} \tag{5.2}$$

in the standard Norton's Law for creep.

Despite its origin in the description of creep rupture, CDM was shown to provide an effective tool to describe the phenomenon of degradation in other areas of solid mechanics. Several different formulations for a variety of materials and processes have also been presented, such as elastic-brittle (Murakami, 1988, 1997), brittle (Krajčinović & Fonseka, 1981; Fonseka & Krajčinović, 1981; Krajčinović, 1983), creep (Leckie & Hayhurst, 1974; Chaboche, 1978, 1981; Murakami & Ohno, 1981; Chaboche, 1984; Krajčinović & Selvaraj, 1984; Chaboche, 1988; Saanouni *et al.* , 1989; Murakami, 1990), fatigue (Janson, 1978; Chaboche, 1988) and creep-fatigue (Lemaitre, 1987; Chaboche, 1988) amongst others. Further discussion on these models is provided by Lemaitre (1990) and Lemaitre (1996).

Remark 5.1 *Due to the diversity of forms in which internal damage manifests itself at the microscopic level, the definition of adequate damage variables is certainly not an easy task. During the development of CDM, briefly reviewed above, variables of different mathematical nature (scalars, vectors, tensors) possessing different physical meaning (reduction of load bearing area, loss of* *stiffness, distribution of voids) have been employed in the description of damage under various circumstances.*

Current methods of experimental identification of damage, comprising direct as well as indirect techniques, are described in detail by Lemaitre & Dufailly (1987). Such techniques range from the direct observation of microscopic pictures to the measurement of the degradation of the elastic moduli by means of ultrasonic emissions and micro-hardness tests. The potentialities and limitations of both micromechanical and phenomenological approaches to damage mechanics are discussed by Basista *et al.* (1992).

5.2.2 Ductile Plastic Damage

With applications to metal forming processes in mind, a detail study of different constitutive models proposed in the literature to describe the phenomenon of *ductile plastic damage* has been undertaken. Damage and plasticity are undoubtedly coupled, as the presence of internal deterioration introduces local stress concentrations which may in turn drive plastic deformation. Therefore, the evolution law of damage should reflect the nucleation and growth of voids and microcracks which accompany large plastic flow. In the nucleation phase, experimental evidence reveals that there is no noticeable effect on the mechanical properties, therefore a damage threshold is usually introduced to reflect this fact (Lemaitre, 1996).

Within the theory of elastoplasticity, Gurson (1977) has proposed a model for ductile damage where the (scalar) damage variable is obtained from the consideration of microscopic spherical voids embedded in an elasto-perfectly plastic matrix. Gurson's void theory was shown to be particularly suitable for the representation of the behaviour of porous materials. To improve this model, a mechanism of *damage nucleation*, whereby voids are nucleated depending on the strain history was latter incorporated. In this context, some nucleation laws have been proposed by Tvergaard (1982) and Tvergaard & Needleman (1984) whereby voids may nucleate in the absence of damage. Further acceleration in voids growth, intended to produce more realist response, can be relatively easily incorporated by introducing a modification into Gurson's macroscopic yield criterion as suggested by Tvergaard (1981, 1982) and Needleman & Tvergaard (1984). More recently, a number of finite element unit cell based micromechanical studies have been performed in order to correlate voids evolution and interaction with the resulting macroscale material yield function. Among others, Tvergaard & Niordoson (2004) investigated the role of smaller size voids in a ductile damage material. Schacht *et al.* (2003), used the 3D voided unit cell based approach to investigate the role and the effects associated with the crystallographic orientation of the matrix material, finding a substantial dependency of the growth and coalescence phase with the anisotropy of the material surrounding the voids.

A scalar damage variable was also considered by Lemaitre (1983) in the definition of a purely phenomenological model for ductile isotropic damage in metals. By appealing to the *hypothesis of strain equivalence* Lemaitre assumes that *"the strain associated with a damage state under the applied stress is equivalent to the strain associated with its undamaged state under the effective stress"*, this author postulates the following elastic constitutive law for a damaged material:

$$\tilde{\sigma} = \tilde{E}\,\varepsilon\,, \tag{5.3}$$

or, equivalently,

$$\sigma = E\,\varepsilon\,, \tag{5.4}$$

where $\tilde{E}$ and

$$E = (1-D)\tilde{E} \tag{5.5}$$

are the Young's moduli of the virgin (undamaged) and damaged materials, respectively. As a consequence, the standard definition of damage in terms of reduction of the (neither well defined nor easily measurable) load carrying area is replaced in Lemaitre's model by the reduction of the Young's modulus in the ideally isotropic case. The damage variable (5.1) is then redefined as:

$$D = \frac{E-\tilde{E}}{E}\,. \tag{5.6}$$

This theory was further elaborated by Lemaitre (1985a,b) and ageing effects were later incorporated by Marquis & Lemaitre (1988). More recently, the original isotropic model has been extended by Lemaitre *et al.* (2000) to account for the anisotropy of damage as well for partial closure of microcracks under compressive stresses. The damage variable in this case is a second order tensor whose evolution is linked to the principal directions of the plastic strain rate. Whitin the initial framework proposed by Lemaitre, several damage models, based on the use of special expressions for the damage dissipation potential, have been derived by different authors (Tai & Yang, 1986; Tai, 1990; Chandrakanth & Pandey, 1993). Also in the context of elastoplasticity Simo & Ju (1987) proposed a framework for the development of (generally anisotropic) strain and stress based damage models. In this case, the *equivalence* concept was extended by introducing the *hypothesis of stress equivalence*, in the formulation of models in stress and strain spaces. Recently, Brunig (2003) proposed an anisotropic CDM model using the porosity as a definition for the damage variable.

Remark 5.2 *As pointed out in Section 3.4.1 (see page 36), the appropriate definition of internal variables associated with a specific phenomenon is one of the most important factors determining the success or failure of the continuum model intended for its description. In this work, the final objective is the analysis of large scale problems for engineering design purposes. Therefore, a* *phenomenological approach is chosen together with a* scalar *damage variable to represent the internal degradation of ductile metals. The loss of microscopic information resulting from this approach is compensated for by the gain in analytical, experimental and computational control of the model.*

Computational aspects have been addressed by several authors, within the so-called *local* approach, and some of these contributions are mentioned below. Simo & Ju (1987) used the *operator split* methodology to derive algorithms for the numerical integration of the elastoplastic-damage equations of evolution. Doghri (1995), Johansson *et al.* (1999) and Lee & Fenves (2001) have numerically implemented damage kinetic equations, in a small strain format. De Souza Neto *et al.* (1994) presented a comprehensive finite-element formulation and error assessment for elastoplastic damage at finite strains, in which isotropic and kinematic hardening and Lemaitre's damage model were accounted for. Steinmann *et al.* (1994) formulate Lemaitre's and Gurson's isotropic damage models in the framework of finite multiplicative elastoplasticity, where issues on numerical implementation of the models were specially emphasised.

Remark 5.3 *By recognizing that the gradient effect is important when the characteristic dimension of the plastic deformation or damage is of the same order as the material intrinsic length scale, a number of so-called non-local theories have been proposed. The aforementioned local formulations lead to numerical stability problems, where the results are not independent of the adopted mesh. This dependency of the mesh manifests itself both relative to the mesh size and to the mesh orientation. As localization of deformations occurs in very small areas, which are usually much smaller than the typical element size, this mesh size imposes the size of the numerically obtained localization areas. Also, the mesh direction has an influence on the direction of the localized zones (de Borst & Pamin, 1996). In the literature, further details of this behaviour that include diagnostic and remedies, have been addressed in several works (Stein* et al. *, 1995; Peerlings* et al. *, 1996; Jirasek, 1998; Kuhl & Ramm, 1999; Nedjar, 2001; Geers* et al. *, 2001; de Borst, 2001), for instance.*

5.3 Lemaitre's elasto-plastic damage theory

The constitutive equations for small strain elasto-plasticity coupled with damage described in this section have been proposed by Lemaitre (1983, 1984, 1985a,b). Based on the concept of *effective stress* and the *hypothesis of strain equivalence* Lemaitre's model includes evolution of internal damage as well as non-linear isotropic and kinematic hardening in the description of the behaviour of ductile metals.

5.3.1 Original model

The description of Lemaitre's ductile damage model is presented in the following.

State variables

The starting point of the theory is the assumption that the free energy is a function of the set $\{\boldsymbol{\varepsilon}^e, \bar{\varepsilon}^{\mathrm{p}}, \boldsymbol{X}, D\}$ of state variables, i.e.,

$$\psi = \psi(\boldsymbol{\varepsilon}^e, \bar{\varepsilon}^{\mathrm{p}}, \boldsymbol{X}, D)\,, \tag{5.7}$$

where $\boldsymbol{\varepsilon}^e$ is the elastic strain tensor and $\bar{\varepsilon}^{\mathrm{p}}$ and D are the *scalar* internal variables associated, respectively, with *isotropic hardening* and *isotropic damage*. The second order tensor $\boldsymbol{X}$ is the internal variable related to *kinematic hardening*. Table 5.1 depicts the respective associated variables. The choice of internal variables depends on the physical phenomena under consideration.

Table 5.1: Internal variables.

Internal Variables		**Associated Variables**	
Isotropic hardening	$\bar{\varepsilon}^{\mathrm{p}}$	Radius of the yield surface	R
Kinematic hardening	$\boldsymbol{X}$	Backstress	$\boldsymbol{\beta}$
Isotropic damage	D	Strain energy release rate	Y

The continuum damage variable D, as discussed in Section 5.2.1, can be interpreted as an indirect measure of density of microvoids and microcracks (Leckie & Onat, 1981). In the present theory, such microscopic defects are assumed isotropically distributed and, as we shall see below, will be phenomenologically reflected in the degradation of the elastic modulus. A critical value for D_c, for the damage variable, is an experimentally determined parameter that defines the initiation of macrocracking (Lemaitre & Chaboche, 1990).

Under the hypothesis of decoupling between elasticity-damage and plastic hardening, the specific free energy is assumed to be given by the sum:

$$\psi = \psi^{ed}(\boldsymbol{\varepsilon}^e, D) + \psi^{p}(\bar{\varepsilon}^{\mathrm{p}}, \boldsymbol{X})\,, \tag{5.8}$$

where ψ^{ed} and ψ^{p} are, respectively, the elastic-damage and plastic contribution to the free energy.

The elastic-damage potential

In Lemaitre's theory the following form is postulated for the elastic-damage potential:

$$\bar{\rho}\,\psi^{ed}(\boldsymbol{\varepsilon}^e, D) = \tfrac{1}{2}\,\boldsymbol{\varepsilon}^e : (1-D)\mathsf{D}^e : \boldsymbol{\varepsilon}^e\,, \tag{5.9}$$

where D^e is the standard isotropic elasticity tensor. For this particular potential, the elasticity law is given by:

$$\boldsymbol{\sigma} = \bar{\rho}\,\frac{\partial \psi^{ed}}{\partial \boldsymbol{\varepsilon}^e} = (1-D)\mathsf{D}^e : \boldsymbol{\varepsilon}^e\,. \tag{5.10}$$

Equivalently, the above damaged elastic law can be written as:

$$\tilde{\boldsymbol{\sigma}} = \mathsf{D}^e : \boldsymbol{\varepsilon}^e\,, \tag{5.11}$$

where $\tilde{\boldsymbol{\sigma}}$ is the *effective stress tensor* that generalises the uniaxial effective stress of (5.2):

$$\tilde{\boldsymbol{\sigma}} \equiv \frac{1}{1-D}\,\boldsymbol{\sigma}\,. \tag{5.12}$$

The thermodynamical force conjugate to the damage internal variable is given by:

$$Y \equiv \bar{\rho}\,\frac{\partial \psi^{ed}}{\partial D} = -\tfrac{1}{2}\,\boldsymbol{\varepsilon}^e : \mathsf{D}^e : \boldsymbol{\varepsilon}^e\,, \tag{5.13}$$

or, using the inverse of the elastic stress/strain law,

$$\begin{aligned} Y &= \frac{-1}{2(1-D)^2}\,\boldsymbol{\sigma} : [\mathsf{D}^e]^{-1} : \boldsymbol{\sigma} \\ &= \frac{-1}{2E(1-D)^2}\left[(1+\nu)\,\boldsymbol{\sigma} : \boldsymbol{\sigma} - \nu\,(\mathrm{tr}\,\boldsymbol{\sigma})^2\right] \\ &= \frac{-q^2}{2E(1-D)^2}\left[\frac{2}{3}(1+\nu) + 3(1-2\nu)\left(\frac{p}{q}\right)^2\right] \\ &= \frac{-q^2}{6G\,(1-D)^2} - \frac{p^2}{2K\,(1-D)^2}\,, \end{aligned} \tag{5.14}$$

where E and ν are, respectively, the Young's modulus and Poisson ratio associated with G and K. In the above, p is the hydrostatic stress and q is the von Mises effective stress. Commonly known as the *damage energy release rate*, $-Y$ corresponds to the variation of internal energy density due to damage growth at constant stress. It is the continuum damage analogue of the J integral used in fracture mechanics (Rice, 1968). The product $-Y\dot{D}$ represents the power dissipated by the process of internal deterioration (mainly as decohesion of interatomic bonds).

Remark 5.4 *Stress-strain rule (5.10) has an important experimental consequence. With the elasticity-damage coupling introduced via the hypothesis of strain equivalence (stated in Section 5.2.1), the* effective *elastic modulus of the material, which can be measured from experiments, is given by:*

$$\tilde{\mathsf{D}} = (1-D)\mathsf{D}^e\,, \tag{5.15}$$

where the damage variable assumes values within the interval $[0,1]$. *In the absence of damage* ($D=0$)*, the effective modulus equals the modulus* D^e *of the virgin material. For a completely damaged state* ($D=1$)*,* $\tilde{\mathsf{D}}=\mathbf{0}$, *corresponding to a total loss of stiffness and load bearing capacity of the material. The identification of a generic damaged state, with* $D\in[0,1]$*, is then restricted to the measurement of the degradation of the current effective elastic modulus with respect to the virgin state* ($D=0$) *as described by Lemaitre (1985a) and Lemaitre & Chaboche (1990).*

Isotropic and kinematic hardening forces

The plastic contribution $\psi^p(\bar{\varepsilon}^{\mathrm{p}},\boldsymbol{X})$ to the free energy is chosen as a sum of an isotropic and a kinematic hardening-related term:

$$\bar{\rho}\,\psi^p(\bar{\varepsilon}^{\mathrm{p}},\boldsymbol{X})=\bar{\rho}\,\psi^I(\bar{\varepsilon}^{\mathrm{p}})+\frac{a}{2}\,\boldsymbol{X}:\boldsymbol{X}\,, \tag{5.16}$$

where a is a material constant and the isotropic hardening contribution, $\psi^I(\bar{\varepsilon}^{\mathrm{p}})$, is an arbitrary function of the single argument $\bar{\varepsilon}^{\mathrm{p}}$. The thermodynamical force associated to isotropic hardening is, then, defined as:

$$R\equiv\bar{\rho}\,\frac{\partial\psi^p(\bar{\varepsilon}^{\mathrm{p}},\boldsymbol{X})}{\partial\bar{\varepsilon}^{\mathrm{p}}}=\bar{\rho}\,\frac{\partial\psi^I(\bar{\varepsilon}^{\mathrm{p}})}{\partial\bar{\varepsilon}^{\mathrm{p}}}=R(\bar{\varepsilon}^{\mathrm{p}})\,. \tag{5.17}$$

From (5.16), it follows that the thermodynamic force associated with kinematic hardening – the *backstress tensor*, $\boldsymbol{\beta}$ – is given by:

$$\boldsymbol{\beta}\equiv\bar{\rho}\,\frac{\partial\psi}{\partial\boldsymbol{X}}=a\,\boldsymbol{X}. \tag{5.18}$$

The flow potential. Internal variables evolution

The evolution equation for internal variables can be derived by assuming the existence of a *flow potential*, Ψ, given by:

$$\Psi=\Phi+\frac{b}{2a}\boldsymbol{\beta}:\boldsymbol{\beta}+\frac{r}{(1-D)(s+1)}\left(\frac{-Y}{r}\right)^{s+1}, \tag{5.19}$$

where a, b, r and s are material constants and Φ is the *yield function* of von Mises type:

$$\Phi(\boldsymbol{\sigma},R,\boldsymbol{\beta},D)=\frac{\sqrt{3\,J_2(\boldsymbol{s}-\boldsymbol{\beta})}}{1-D}-\left[\sigma_{y_0}+R(\bar{\varepsilon}^{\mathrm{p}})\right], \tag{5.20}$$

where the material parameter σ_{y_0} is the initial uniaxial yield stress. The damage evolution constants r and s can be identified by integrating the damage evolution law for particular cases of (constant) stress triaxiality rate as described in Section 7.4 of Lemaitre & Chaboche (1990). The constants a and b, associated with kinematic hardening, are obtained from cyclic loading experiments (Lemaitre & Chaboche, 1990). The convexity of the flow potential Ψ with respect to the thermodynamical forces for positive constants a, b, r and s ensures that the dissipation inequality is satisfied 'a priori' by the present constitutive model. According to the hypothesis of generalised normality, the plastic flow is given by

$$\dot{\boldsymbol{\varepsilon}}^{p} = \dot{\gamma}\,\frac{\partial \Psi}{\partial \boldsymbol{\sigma}} = \dot{\gamma}\,\boldsymbol{N}, \tag{5.21}$$

where $\boldsymbol{N}$ represents the flow vector

$$\boldsymbol{N} \equiv \sqrt{\tfrac{3}{2}}\,\tfrac{\boldsymbol{s}-\boldsymbol{\beta}}{(1-D)\|\boldsymbol{s}-\boldsymbol{\beta}\|}. \tag{5.22}$$

The evolution law of the internal variables is

$$\begin{aligned}
\dot{\bar{\varepsilon}}^{\mathrm{p}} &= \dot{\gamma}\,\frac{\partial \Psi}{\partial R} = \dot{\gamma} \\
\dot{\boldsymbol{\beta}} &= \dot{\gamma}\,\frac{\partial \Psi}{\partial \boldsymbol{X}} = \dot{\gamma}\,(a\,\boldsymbol{N} - b\,\boldsymbol{\beta}) \\
\dot{D} &= \dot{\gamma}\,\frac{\partial \Psi}{\partial Y} = \dot{\gamma}\,\frac{1}{1-D}\left(\frac{-Y}{r}\right)^{s}
\end{aligned} \tag{5.23}$$

where $\dot{\gamma}$ is the *plastic multiplier*, which satisfies the standard complementary law of rate-independent plasticity:

$$\dot{\gamma} \geq 0, \qquad \Phi \leq 0, \qquad \dot{\gamma}\,\Phi = 0\,. \tag{5.24}$$

The constitutive equations of Lemaitre's ductile damage model are conveniently grouped in Box 5.1.

Damage threshold

At low values of accumulated plastic strain, $\bar{\varepsilon}^{p}$, which is related at microscopic level with the nucleation phase, the elastic modulus degradation can be hardly detected in experiments. Thus, we can assume that damage growth starts only at a critical value, denoted $\bar{\varepsilon}^{p}_{D}$. This critical value will be called the *damage threshold* and depends upon the loading, the fatigue limit and the ultimate stress (Lemaitre, 1996). Notwithstanding, in this work, for simplicity reasons, it is assumed that the threshold for damage evolution is a material property and can be included in the model by redefining the damage evolution law as:

$$\dot{D} = \dot{\gamma}\,\frac{H(\bar{\varepsilon}^{p} - \bar{\varepsilon}^{p}_{D})}{1-D}\left(\frac{-Y}{r}\right)^{s}, \tag{5.25}$$

where H here denotes the *heavyside step function* defined as:

$$H(a) \equiv \begin{cases} 1 & \text{if } a \geq 0 \\ 0 & \text{if } a < 0 \end{cases} \qquad \text{for any scalar } a. \tag{5.26}$$

Box 5.1: Lemaitre's standard ductile damage model

(i) Elasto-plastic split of the strain tensor

$$\boldsymbol{\varepsilon} = \boldsymbol{\varepsilon}^e + \boldsymbol{\varepsilon}^p$$

(ii) Coupled elastic-damage law

$$\boldsymbol{\sigma} = (1 - D)\mathsf{D}^e : \boldsymbol{\varepsilon}^e$$

(iii) Yield function

$$\Phi = \frac{\sqrt{3\, J_2(\boldsymbol{s}-\boldsymbol{\beta})}}{1-D} - [\sigma_{y_0} + R]$$

where $R = R\,(\bar{\varepsilon}^{\mathrm{p}})$.

(iv) Plastic flow and evolution equations for $\bar{\varepsilon}^{\mathrm{p}}$, $\boldsymbol{\beta}$ and D

$$\dot{\boldsymbol{\varepsilon}}^p = \dot{\gamma}\,\boldsymbol{N}$$

$$\dot{\bar{\varepsilon}}^{\mathrm{p}} = \dot{\gamma}$$

$$\dot{\boldsymbol{\beta}} = \dot{\gamma}\,(a\,\boldsymbol{N} - b\,\boldsymbol{\beta})$$

$$\dot{D} = \dot{\gamma}\,\frac{1}{1-D}\left(\frac{-Y}{r}\right)^s$$

with Y given by (5.14) and the flow vector:

$$\boldsymbol{N} \equiv \sqrt{\frac{3}{2}}\,\frac{\boldsymbol{s}-\boldsymbol{\beta}}{(1-D)\|\boldsymbol{s}-\boldsymbol{\beta}\|}$$

(v) Loading/unloading criterion

$$\Phi \leq 0 \qquad \dot{\gamma} \geq 0 \qquad \Phi\,\dot{\gamma} = 0$$

If such a threshold is adopted, then the evolution law for $\bar{\varepsilon}^p$ has to be defined for the model to be complete. From its definition we have:

$$\dot{\bar{\varepsilon}}^p = \sqrt{\frac{2}{3}}\,\|\dot{\boldsymbol{\varepsilon}}^p\|\,. \tag{5.27}$$

By taking the plastic flow rule for the present model into consideration, the above equation results in the following evolution law for the accumulated plastic strain:

$$\dot{\bar{\varepsilon}}^p = \frac{\dot{\gamma}}{1-D}\,. \tag{5.28}$$

Computational aspects

The numerical integration of Lemaitre's constitutive equations by means of a return mapping-type scheme has been originally proposed by Benallal *et al.* (1988) in the infinitesimal strain context and later exploited by several authors (de Souza Neto *et al.*, 1994; Steinmann *et al.* , 1994) with finite strain extensions of the model. A particularly efficient integration algorithm for a simplified version of the Lemaitre ductile damage model, that excludes kinematic hardening, has been recently proposed by de Souza Neto (2002). In this version, the return mapping stage requires the solution of only one scalar non-linear equation.

5.3.2 Improved model

Even though the model presented in the preceding section of this chapter is able to predict damage growth with reasonable accuracy over simple strain paths, increasing deviations from experimental observations should be expected as strain paths become more complex. In fact, this is true not only for damage models but for inelastic models of continua in general and, at present, it can be said that constitutive refinement in inelasticity remains largely an open issue (de Souza Neto *et al.*, 2005a).

One important feature of the original model is the fact that the state of stress triaxiality has a strong influence on the rate of damage growth. This experimentally observed phenomenon is accounted for through the definition of the damage energy release rate, Y, rewritten here:

$$Y = \frac{-q^2}{2E(1-D)^2}\left[\frac{2}{3}(1+\nu) + 3(1-2\nu)\left(\frac{p}{q}\right)^2\right], \tag{5.29}$$

which takes part in the damage evolution equation, $\dot{D}$:

$$\dot{D} = \dot{\gamma}\,\frac{H(\bar{\varepsilon}^p - \bar{\varepsilon}^p_D)}{1-D}\left(\frac{-Y}{r}\right)^s . \tag{5.30}$$

The inclusion of the hydrostatic component of $\boldsymbol{\sigma}$ in the definition of Y implies that $\dot{D}$ increases (decreases) with increasing (decreasing) triaxiality ratio. This is in sharp contrast with the standard von Mises plasticity model where only the stress deviator has an influence on the dissipative mechanisms.

However, one important aspect of damage growth is not considered by evolution law (5.30) and (5.29): the clear distinction between rates of damage growth observed for states of stress with identical triaxiality but stresses of opposite sign (tension and compression). Such a distinction stems from the fact that, under a compressive state, voids and micro-cracks that would grow under tension, will partially close and increase the load bearing area and stiffness, reducing (possibly dramatically) the damage growth rate.

This phenomenon can be crucially important in the simulation of forming operations, particularly under extreme strains (Andrade Pires *et al.* , 2004c). It is often the case that, in such operations, the solid (or parts of it) undergoes extreme compressive straining followed by extension or vice-versa. Under such conditions, it is obvious that the conventional model represented by (5.30) and (5.29) will not produce accurate predictions. To remedy the problem, we shall report here a refinement of the original theory, as introduced by Ladèveze (1983) and Ladevèze & Lemaitre (1984). The improved model is described in the following.

Crack closure effect, unilateral conditions

According to Lemaitre's elasto-plastic damage theory, the microscopic defects are assumed to be isotropically distributed, and described by a *scalar* damage variable. However, no distinction is made regarding the damage behaviour under tensile and compressive stress states. In order to introduce this feature, let us start by considering the uniaxial stress state case. For the original Lemaitre model discussed in Section 5.3.1, a material with damage D, has effective Young's modulus:

$$\tilde{E} = (1 - D)\, E\,, \tag{5.31}$$

where E is the Young's modulus of the virgin (undamaged) material. The uniaxial stress-strain constitutive equation for the damaged material is given by:

$$\sigma_1 = (1 - D)\, E\, \varepsilon \qquad \text{or} \qquad \tilde{\sigma}_1 = \frac{\sigma_1}{(1 - D)}\,. \tag{5.32}$$

When the stress normal to the crack is compressive, even though the cross section still contains physical cracks, the ability of the material to carry load increases. The crucial point in the definition of the crack closure model is the assumption that the above relationship is valid only under *tensile* stresses ($\sigma_1 \geq 0$). Under *compressive* stresses ($\sigma_1 < 0$), the uniaxial stress-strain relation is assumed to take the form:

$$\sigma_1 = (1 - h\, D)\, E\, \varepsilon \qquad \text{or} \qquad \tilde{\sigma}_1 = \frac{\sigma_1}{(1 - h\, D)}\,, \tag{5.33}$$

where h is an experimentally determined coeficient which satisfies:

$$0 \leq h \leq 1\,. \tag{5.34}$$

This coefficient characterizes the closure of microcracks and micro-cavities and depends upon the density and the shape of the defects. It is material dependent and, as a first approximation for simplicity, h is considered as constant. The effect of damage itself on closure is neglected. A value $h \approx 0.2$ is typically observed in many experiments (Lemaitre, 1996). Note that for $h = 1$, the behaviour of the original damage model, without crack closure effects is recovered, whereas the other extreme value, $h=0$, represents full crack closure with $\tilde{E}=E$ under compression. Any other value of h describes a partial crack closure effect.

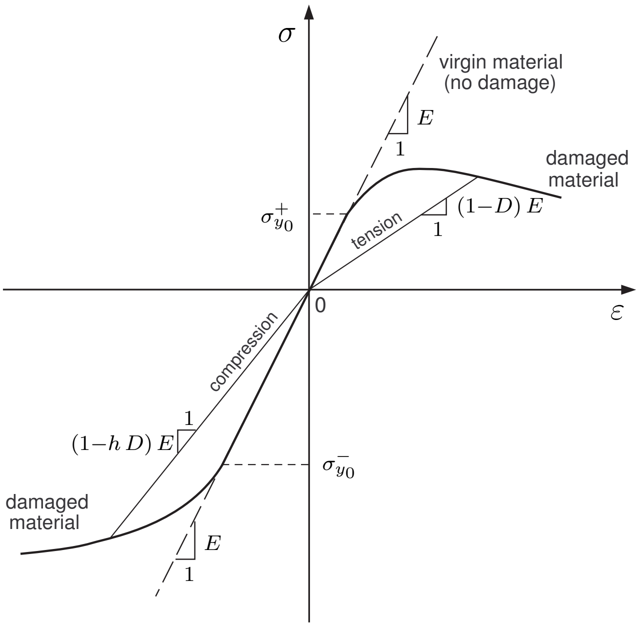

Figure 5.2: Uniaxial elastic model with damage and partial crack closure effect

In Figure 5.2, the effect of crack closure is schematically depicted by the uniaxial stress-strain diagram, for a general elastic material with different behaviour under tensile and compressive stresses. In particular, the compressive yield stress, $\left|\sigma^{-}_{y0}\right|$, is higher than the tensile one, $\left|\sigma^{+}_{y0}\right|$. It is possible to notice (see Figure 5.2) that the damage attained under tensile stress is manifested by the change of the elastic modulus after unloading, $(1-D)E$. Under a compressive stress the material can *heal*, which enables the increase of the elastic modulus, now given by $(1-h\,D)E$.

Tensile/compressive split of the stress tensor

As we have seen in the above, it is relatively easy to establish a piece-wise linear damaged elastic model capable of accounting for crack closure effects in the uniaxial case. The extension of such a simple model to the general three-dimensional situation, however, is not trivial.

In the present model, such a distinction is made on the basis of a *tensile/compressive split* of the stress tensor. That is, any stress tensor $\boldsymbol{\sigma}$ can be written as:

$$\boldsymbol{\sigma} = \sum_{i=1}^{3} \sigma_i \, \boldsymbol{e}_i \otimes \boldsymbol{e}_i \,, \tag{5.35}$$

where σ_i are the principal stresses and $\{\boldsymbol{e}_1, \boldsymbol{e}_2, \boldsymbol{e}_3\}$ is an orthonormal basis of vectors along the principal directions. The matrix representation of $\boldsymbol{\sigma}$ in this basis, reads:

$$[\boldsymbol{\sigma}] = \begin{bmatrix} \sigma_1 & 0 & 0 \\ 0 & \sigma_2 & 0 \\ 0 & 0 & \sigma_3 \end{bmatrix} . \tag{5.36}$$

The tensile/compressive split of the stress tensor consists in splitting $\boldsymbol{\sigma}$ additively as:

$$\boldsymbol{\sigma} = \boldsymbol{\sigma}_+ + \boldsymbol{\sigma}_- \,, \tag{5.37}$$

where $\boldsymbol{\sigma}_+$ and $\boldsymbol{\sigma}_-$ are, respectively, the *tensile* and *compressive component* of $\boldsymbol{\sigma}$ defined as:

$$\boldsymbol{\sigma}_+ = \sum_{i=1}^{3} \langle \sigma_i \rangle \; \boldsymbol{e}_i \otimes \boldsymbol{e}_i \tag{5.38}$$

and

$$\boldsymbol{\sigma}_- = -\sum_{i=1}^{3} \langle -\sigma_i \rangle \; \boldsymbol{e}_i \otimes \boldsymbol{e}_i \,. \tag{5.39}$$

The symbol $\langle \; \rangle$ represents the *Macauley bracket*, that is, for any scalar, a,

$$\langle a \rangle = \begin{cases} a & \text{if } \; a \geq 0 \\ 0 & \text{if } \; a < 0 \,, \end{cases} \tag{5.40}$$

and the matrix representation of $\boldsymbol{\sigma}_+$ and $\boldsymbol{\sigma}_-$ in principal stress basis reads:

$$[\boldsymbol{\sigma}_+] \equiv \begin{bmatrix} \langle \sigma_1 \rangle & 0 & 0 \\ 0 & \langle \sigma_2 \rangle & 0 \\ 0 & 0 & \langle \sigma_3 \rangle \end{bmatrix} \tag{5.41}$$

and

$$[\boldsymbol{\sigma}_-] \equiv - \begin{bmatrix} \langle -\sigma_1 \rangle & 0 & 0 \\ 0 & \langle -\sigma_2 \rangle & 0 \\ 0 & 0 & \langle -\sigma_3 \rangle \end{bmatrix} . \tag{5.42}$$

Note that, under uniaxial stresses, i.e., when only one of the principal stresses is non-zero, the above tensile/compressive split reduces to

$$\sigma_i = \sigma_+ + \sigma_- \,, \tag{5.43}$$

where

$$\sigma_+ = \langle \sigma_i \rangle \qquad \text{and} \qquad \sigma_- = -\langle -\sigma_i \rangle \; . \tag{5.44}$$

The three-dimensional damaged elasticity law

The definition of the multi-dimensional damaged elastic model with crack closure effects is obtained by modifying the standard three-dimensional linear stress-strain law. To do this, let us first recall the standard three-dimensional linear elastic stress-strain law (5.10) [page 72] of Lemaitre's damage model. Its inverse relation reads:

$$\begin{aligned} \boldsymbol{\varepsilon} &= \frac{1}{1-D} \mathsf{D}^{-1} : \boldsymbol{\sigma} \\ &= \frac{1}{1-D} \left[\frac{1+\nu}{2E} \boldsymbol{\sigma} - \frac{\nu}{2E} (\operatorname{tr} \boldsymbol{\sigma}) \boldsymbol{I} \right] \; . \end{aligned} \tag{5.45}$$

The three-dimensional generalisation of the damaged elastic model with the inclusion of the tensile/compressive split of the stress tensor is obtained by modifying the above rule as follows:

$$\boldsymbol{\varepsilon} = \frac{1+\nu}{2E} \left(\frac{\boldsymbol{\sigma}_+}{1-D} + \frac{\boldsymbol{\sigma}_-}{1-hD} \right) - \frac{\nu}{2E} \left(\frac{\langle \operatorname{tr} \boldsymbol{\sigma} \rangle}{1-D} - \frac{\langle -\operatorname{tr} \boldsymbol{\sigma} \rangle}{1-hD} \right) . \tag{5.46}$$

As remarked by de Souza Neto *et al.* (2005a), the stress-strain relation (5.46) remains isotropic ($\boldsymbol{\varepsilon}$ and $\boldsymbol{\sigma}$ share the same principal directions) but, is no longer linear. More precisely, the stress-strain relation is piece-wise linear with derivative discontinuities occurring when any of the principal stresses and/or the hydrostatic pressure vanishes.

The computational implementation of the above model within an implicit finite element environment has also been undertaken by the same authors (de Souza Neto *et al.*, 2005a). This solution is obtained by means of the Newton-Raphson algorithm where, due to definition of $\boldsymbol{\sigma}_+$ and $\boldsymbol{\sigma}_-$, it turns out convenient to re-write (5.46) in terms of principal stresses and strains. The basic ingredients of the implementation (stress updating procedure and the computation of the tangent operator associated) are discussed in detail.

Crack closure effects in damage evolution

The above model describes the effect of crack closure in damaged elastic materials that remain elastic, without evolution of damage. Crack closure effects can also have a strong influence on damage evolution. It is a well known fact that many materials have considerably higher strength in compression than in tension. The consideration of such an effect may be crucial under complex loading conditions and is relevant to many practical applications.

An alternative to describe this phenomenon is provided by the damage evolution law proposed by Ladevèze & Lemaitre (1984) [described by (Lemaitre, 1996) in more detail]. Their approach consists in modifying the damage energy release rate (5.14) of the original Lemaitre ductile damage model by including the tensile/compressive split of the stress tensor. Thus the original expression (5.14) is replaced with:

$$\begin{aligned} Y &= \frac{-1}{2E(1-D)^2}\left[(1+\nu)\,\boldsymbol{\sigma}_+ : \boldsymbol{\sigma}_+ - \nu\,\langle \mathrm{tr}\,\boldsymbol{\sigma}\rangle^2\right] \\ &\quad - \frac{h}{2E(1-hD)^2}\left[(1+\nu)\,\boldsymbol{\sigma}_- : \boldsymbol{\sigma}_- - \nu\,\langle -\mathrm{tr}\,\boldsymbol{\sigma}\rangle^2\right]\ , \end{aligned} \tag{5.47}$$

and the elasto-plastic damage evolution equation keeps the same format as in the original model:

$$\dot{D} = \dot{\gamma}\,\frac{1}{1-D}\left(\frac{-Y}{r}\right)^s . \tag{5.48}$$

The complete fully coupled elasto-plastic model for ductile damage is obtained by considering the above damage evolution equation together with the damaged isotropic elasticity law with crack closure effects (discussed in the previous section) and the standard plasticity equations of the original Lemaitre model. The constitutive equations of Lemaitre's improved ductile damage model are conveniently grouped in Box 5.2.

To the author's knowledge, the computational implementation of the above improved model has not been addressed. This is probably due to the fact that, if the fully coupled model is adopted, an increased degree of complexity will be introduced when compared with the original Lemaitre model, described in Section 5.3.1. Due to the non-linearity of the constitutive equations for both the elastic and plastic domains, the numerical integration by means of a return mapping-scheme would result in the solution of a large number of equations.

Remark 5.5 *The stress updating algorithm - which is applied at each Gauss integration point of the finite element mesh - makes simulations with this improved model substantially more expensive. The computational burden that results from this large number of equations is particularly noticeable in explicit transient dynamic finite element analysis, where the cost of Gauss point level operations has a greater impact on the overall computation time. Although to a lesser extent, the computational cost of implicit quasi-static finite element analysis is also increased when the solution of large systems of non-linear equations is required by the stress updating scheme. In order to reduce the computational cost and include the effect of crack closure on the material behaviour, the following model is proposed.*

Box 5.2: Lemaitre's improved ductile damage model

(i) Elasto-plastic split of the strain tensor

$$\boldsymbol{\varepsilon} = \boldsymbol{\varepsilon}^e + \boldsymbol{\varepsilon}^p$$

(ii) Coupled elastic-damage law

$$\boldsymbol{\varepsilon}^e = \tfrac{1+\nu}{2E}\left(\tfrac{\boldsymbol{\sigma}_+}{1-D} + \tfrac{\boldsymbol{\sigma}_-}{1-hD}\right) - \tfrac{\nu}{2E}\left(\tfrac{\langle \mathrm{tr}\,\boldsymbol{\sigma}\rangle}{1-D} - \tfrac{\langle -\mathrm{tr}\,\boldsymbol{\sigma}\rangle}{1-hD}\right)$$

(iii) Yield function

$$\Phi = \tfrac{\sqrt{3\,J_2(\boldsymbol{s}-\boldsymbol{\beta})}}{1-D} - [\sigma_{y_0} + R]$$

where $R = R\,(\bar{\varepsilon}^{\mathrm{p}})$.

(iv) Plastic flow and evolution equations for $\bar{\varepsilon}^{\mathrm{p}}$, $\boldsymbol{\beta}$ and D

$$\dot{\boldsymbol{\varepsilon}}^p = \dot{\gamma}\,\boldsymbol{N}$$

$$\dot{\bar{\varepsilon}}^{\mathrm{p}} = \dot{\gamma}$$

$$\dot{\boldsymbol{\beta}} = \dot{\gamma}\,(a\,\boldsymbol{N} - b\,\boldsymbol{\beta})$$

$$\dot{D} = \dot{\gamma}\,\tfrac{1}{1-D}\left(\tfrac{-Y}{r}\right)^s$$

with Y given by (5.47) and the flow vector:

$$\boldsymbol{N} \equiv \sqrt{\tfrac{3}{2}}\,\tfrac{\boldsymbol{s}-\boldsymbol{\beta}}{(1-D)\|\boldsymbol{s}-\boldsymbol{\beta}\|}$$

(v) Loading/unloading criterion

$$\Phi \leq 0 \qquad \dot{\gamma} \geq 0 \qquad \Phi\,\dot{\gamma} = 0$$

5.4 Elasto-plastic damage model with crack closure

The constitutive model proposed in this section, to describe the mechanism of internal damaging, was inspired in the model described in Section 5.3.2. In this model, elasticity and damage are assumed to be decoupled. This can be justified given the fact that the elastic strain remains truly infinitesimal in the family of processes addressed in this work. Also, by removing kinematic hardening from Lemaitre's improved ductile damage theory, we obtain a simplified version of the model whose numerical implementation assumes a simpler form. The use of such a simplified theory can be justified whenever the effects of kinematic hardening are not relevant, i.e., in any process where reverse plastic loading does not occur or has little influence on the overall evolution of damage and plastic flow.

Remark 5.6 *In the constitutive framework proposed by Lemaitre (see Section 5.3), the damage variable affects internal variables, such as strain, the yield condition and the standard complementary conditions as a result of the substitution of the stress tensor with the effective one.*

5.4.1 The constitutive model

The description of an elasto-plastic damage model, which includes the effect of crack closure in the damage evolution law, is presented in the following.

State variables

The free energy, is assumed to be a function of the set $\{\boldsymbol{\varepsilon}^e, \bar{\varepsilon}^{\mathrm{p}}\}$ of state variables, i.e.,

$$\psi = \psi(\boldsymbol{\varepsilon}^e, \bar{\varepsilon}^{\mathrm{p}}) \,, \tag{5.49}$$

where $\boldsymbol{\varepsilon}^e$ is the elastic strain tensor and $\bar{\varepsilon}^{\mathrm{p}}$ is the *scalar* internal variable associated, with *isotropic hardening.*

The free energy potential

Here, elasticity as well as the possibility of additional isotropic hardening or softening due to straining of the material are introduced and the free energy potential is assumed to be given by:

$$\psi = \psi(\boldsymbol{\varepsilon}^e, \bar{\varepsilon}^{\mathrm{p}}) = \psi^e(\boldsymbol{\varepsilon}^e) + \psi^p(\bar{\varepsilon}^{\mathrm{p}}) \,. \tag{5.50}$$

The elastic contribution ψ^e is taken as the standard quadratic strain-energy function:

$$\bar{\rho}\, \psi^e(\boldsymbol{\varepsilon}^e) = \tfrac{1}{2}\, \boldsymbol{\varepsilon}^e : \mathsf{D}^e : \boldsymbol{\varepsilon}^e \,, \tag{5.51}$$

yielding the standard linear elastic relation:

$$\boldsymbol{\sigma} = \bar{\rho}\, \frac{\partial \psi}{\partial \boldsymbol{\varepsilon}^e} = \mathsf{D}^e : \boldsymbol{\varepsilon}^e \,. \tag{5.52}$$

As in Lemaitre's model, the isotropic hardening contribution is left as an arbitrary function of a single argument, so that the thermodynamic force R associated with $\bar{\varepsilon}^{\mathrm{p}}$ is given by:

$$R = \bar{\rho}\, \frac{\partial \psi}{\partial \bar{\varepsilon}^{\mathrm{p}}} = \bar{\rho}\, \frac{\partial \psi^p}{\partial \bar{\varepsilon}^{\mathrm{p}}} = R(\bar{\varepsilon}^{\mathrm{p}}) \,. \tag{5.53}$$

Remark 5.7 *Note that, in contrast to Lemaitre's ductile damage model, the effect of internal damage on the elastic behaviour of the material is ignored in the present model. That is, the elasticity tensor is not a function of the damage variable.*

The flow potential. Internal variables evolution

The evolution equation for internal variables can be derived again by assuming the existence of a *flow potential*, Ψ, given by:

$$\Psi = \Phi + \frac{r}{(1-D)(s+1)} \left(\frac{-Y}{r} \right)^{s+1}, \tag{5.54}$$

where r and s are material constants and Φ is the *yield function.* At this point, it is important to remark that one of the underlying hypotheses in Lemaitre's formulation is that damage affects elastic strains only, therefore the substitution of the effective stress in the yield condition is questionable. As a matter of fact, the plastic flow response experimentally measured is the result of the concurrant action of both hardening and damage effects that cannot be separated in a test. In other words, it is not possible to measure directly the plastic flow curve for a material without damage.

Therefore, the effect of damage upon the plastic behaviour is accounted for by rewriting the *yield function* Φ in the following form:

$$\Phi(\boldsymbol{\sigma}, R, D) = \sqrt{3\, J_2(\boldsymbol{s})} - (1-D)\left[\sigma_{y_0} + R(\bar{\varepsilon}^{\mathrm{p}})\right]. \tag{5.55}$$

Here, the material parameter σ_{y_0} is the initial uniaxial yield stress of an undamaged and unstrained (or virgin) material, and R is the isotropic hardening thermodynamical force, assumed to be a function of a scalar hardening internal variable, $\bar{\varepsilon}^{\mathrm{p}}$ and D is the *damage variable.* It should be noted that (5.55) accounts for two competing effects: damaging, which shrinks (isotropically) the elastic domain (defined as the subset of stress space for which $\Phi \leq 0$) as D grows; and hardening, which expands the elastic domain (also isotropically) with the growth of R.

Remark 5.8 *As for Lemaitre's model the damage variable in the present case ranges between 0 and 1, with* $D=0$ *corresponding to the sound (undamaged) material and* $D=1$ *to the fully damaged state with complete loss of load carrying capacity. Note that damage growth induces softening, i.e., shrinkage of the yield surface defined by*

$$\Phi = 0\,.$$

For $D=0$ *the yield surface reduces to that of the (pressure insensitive) von Mises model. In the presence of damage, i.e., for* $D \neq 0$ *the yield surface shrinks and its size reduces to zero for* $D=1$.

According to the above definitions, the evolution law for the plastic flow rule of a damaged material should follow the standard *associative* plasticity theory without coupling with damage:

$$\dot{\boldsymbol{\varepsilon}}^{\,\mathrm{p}} = \dot{\gamma}\,\frac{\partial \Psi}{\partial \boldsymbol{\sigma}} = \dot{\gamma}\,\sqrt{\tfrac{3}{2}}\,\frac{\boldsymbol{s}}{\|\boldsymbol{s}\|}\,. \tag{5.56}$$

The evolution laws for the hardening internal variable, $\dot{\bar{\varepsilon}}^{\,\mathrm{p}}$, and damage, D, are given by

$$\begin{aligned} \dot{\bar{\varepsilon}}^{\mathrm{p}} &= \dot{\gamma}\,\frac{\partial \Psi}{\partial R} = \dot{\gamma} \\ \dot{D} &= \dot{\gamma}\,\frac{\partial \Psi}{\partial Y} = \dot{\gamma}\,\frac{1}{1-D}\left(\frac{-Y}{r}\right)^{s} \end{aligned} \tag{5.57}$$

where the coupling between effective accumulated plastic strain rate, $\dot{\bar{\varepsilon}}^{\mathrm{p}}$, and the damage rate, $\dot{D}$, is shown in Equation (5.57) throughout the definition of the plastic multiplier, $\dot{\gamma}$. The *plastic multiplier*, $\dot{\gamma}$, in (5.56–5.57) satisfies the standard complementarity law of rate-independent plasticity:

$$\dot{\gamma} \geq 0, \qquad \Phi \leq 0, \qquad \dot{\gamma}\,\Phi = 0\,. \tag{5.58}$$

Damage threshold

In addition, the evolution of the damage internal variable is redefined to include a threshold for damage evolution as:

$$\dot{D} = \begin{cases} 0 & \text{if } \bar{\varepsilon}^{\mathrm{p}} \leq \bar{\varepsilon}^{\mathrm{p}}_{D} \\ \dfrac{\dot{\gamma}}{1-D}\left(\dfrac{-Y}{r}\right)^{s} & \text{if } \bar{\varepsilon}^{\mathrm{p}} > \bar{\varepsilon}^{\mathrm{p}}_{D}\,, \end{cases} \tag{5.59}$$

where r, s and $\bar{\varepsilon}^{\mathrm{p}}_{D}$ are material constants. The constant $\bar{\varepsilon}^{\mathrm{p}}_{D}$ is the so-called *damage threshold*, i.e., the value of accumulated plastic strain below which no damage evolution is observed. The quantity, Y, introduced in Equation (5.47), and rewritten here,

$$\begin{aligned} Y \;=\; & \frac{-1}{2E(1-D)^2}\left[(1+\nu)\,\boldsymbol{\sigma}_{+} : \boldsymbol{\sigma}_{+} - \nu\,\langle \mathrm{tr}\,\boldsymbol{\sigma}\rangle^{2}\right] \\ & - \frac{h}{2E(1-hD)^2}\left[(1+\nu)\,\boldsymbol{\sigma}_{-} : \boldsymbol{\sigma}_{-} - \nu\,\langle -\mathrm{tr}\,\boldsymbol{\sigma}\rangle^{2}\right]\,, \end{aligned} \tag{5.60}$$

is the *damage energy release rate*, with E and ν denoting, respectively, the Young's modulus and the Poisson's ratio of the undamaged material.

The constitutive equations of the overall elasto-plastic damage model are conveniently summarized in Box 5.3.

Box 5.3: Proposed ductile damage model (isotropic hardening only)

(i) Elasto-plastic split of the strain tensor

$$\boldsymbol{\varepsilon} = \boldsymbol{\varepsilon}^{e} + \boldsymbol{\varepsilon}^{p}$$

(ii) Elastic law (uncoupled from damage)

$$\boldsymbol{\sigma} = \mathsf{D}^{e} : \boldsymbol{\varepsilon}^{e}$$

(iii) Yield function

$$\Phi = \sqrt{3\,J_2(\boldsymbol{s})} - (1 - D)\,[\sigma_{y_0} + R(\bar{\varepsilon}^{\mathrm{p}})]$$

(iv) Plastic flow and evolution equations for $\bar{\varepsilon}^{\mathrm{p}}$ and D

$$\begin{aligned} \dot{\boldsymbol{\varepsilon}}^{p} &= \dot{\gamma}\,\sqrt{\tfrac{3}{2}}\,\tfrac{\boldsymbol{s}}{\|\boldsymbol{s}\|} \\ \dot{\bar{\varepsilon}}^{\mathrm{p}} &= \dot{\gamma} \\ \dot{D} &= \dot{\gamma}\,\tfrac{1}{1-D}\left(\tfrac{-Y}{r}\right)^{s} \end{aligned}$$

with Y given by

$$\begin{aligned} Y \;=\; & -\tfrac{1}{2E(1-D)^2}\left[(1+\nu)\,\boldsymbol{\sigma}_{+}:\boldsymbol{\sigma}_{+} - \nu\,\langle \mathrm{tr}\,\boldsymbol{\sigma}\rangle^2\right] \\ & -\,\tfrac{h}{2E(1-hD)^2}\left[(1+\nu)\,\boldsymbol{\sigma}_{-}:\boldsymbol{\sigma}_{-} - \nu\,\langle -\mathrm{tr}\,\boldsymbol{\sigma}\rangle^2\right] \end{aligned}$$

(v) Loading/unloading criterion

$$\Phi \leq 0 \qquad \dot{\gamma} \geq 0 \qquad \Phi\,\dot{\gamma} = 0$$

It is important to remark here, that the choice of the accumulated plastic strain as the isotropic hardening internal variable is at variance with the original model proposed by Lemaitre (1984). In the present case, the original potential structure of the model is lost. However, this choice can be justified on experimental grounds since the measurement of accumulated plastic strain can be carried out experimentally in a straightforward manner allowing the determination of hardening and damage parameters from relatively simple micro-hardness measurements [refer to Arnold *et al.* (2002)]. A direct consequence of this assumption, is the fact that, the hardening and damage parameters calibrated for this model will, in general, be different from the ones employed in Lemaitre's theory.

An extension of that procedure, based on a finite element-based semi-inverse method, is currently under investigation. The method requires only relatively simple micro-hardness measurements in a tensile specimen and a severely compressed billet. The fine tuning of h is obtained by matching experimental measurements with results of the finite element simulation of the upsetting of the billet.

5.4.2 Integration algorithm

This section proceeds to describe an algorithm for the numerical integration of, the above described, elasto-plastic damage constitutive equations, including the effect of crack closure. Algorithms based on the so-called operator split concept, resulting in the standard *elastic predictor/plastic corrector* format, are widely used in computational plasticity [refer to Simo & Hughes (1998) for details of the procedure]. Here we shall focus only on the particularisation of the *fully implicit* elastic predictor/return mapping method to the above proposed model.

Let us consider what happens to a typical Gauss point of the finite element mesh within a (pseudo-) time interval $[t_n, t_{n+1}]$. Given the incremental strain:

$$\Delta\boldsymbol{\varepsilon} = \boldsymbol{\varepsilon}_{n+1} - \boldsymbol{\varepsilon}_n \,, \tag{5.61}$$

and the values $\boldsymbol{\sigma}_n$, $\boldsymbol{\varepsilon}^{\mathrm{p}}_n$, $\bar{\varepsilon}^{\mathrm{p}}_n$ and D_n at t_n, the numerical integration algorithm should obtain the updated values at the end of the interval, $\boldsymbol{\sigma}_{n+1}$, $\boldsymbol{\varepsilon}^{\mathrm{p}}_{n+1}$, $\bar{\varepsilon}^{\mathrm{p}}_{n+1}$, and D_{n+1} in a manner consistent with the constitutive equations of the model.

The elastic trial step

The first step in the algorithm is the evaluation of the *elastic trial state* where the increment is assumed purely elastic with no evolution of internal variables (internal variables *frozen* at t_n). The elastic trial strain and trial accumulated plastic strain are given by:

$$\boldsymbol{\varepsilon}^{\mathrm{e\,trial}} = \boldsymbol{\varepsilon}^{\mathrm{e}}_n + \Delta\boldsymbol{\varepsilon}; \qquad \bar{\varepsilon}^{\mathrm{p\,trial}} = \bar{\varepsilon}^{\mathrm{p}}_n. \tag{5.62}$$

The corresponding elastic trial stress tensor is computed:

$$\boldsymbol{\sigma}^{\mathrm{trial}} = \mathsf{D} : \boldsymbol{\varepsilon}^{\mathrm{e\,trial}} \,, \tag{5.63}$$

where D is the standard isotropic elasticity tensor. Equivalently, in terms of stress deviator and hydrostatic pressure, we have:

$$\boldsymbol{s}^{\mathrm{trial}} = 2G\,\boldsymbol{e}^{e\ \mathrm{trial}}, \qquad p^{\mathrm{trial}} = K\,v^{e\ \mathrm{trial}} \,, \tag{5.64}$$

where

$$\boldsymbol{e}^{e\ \mathrm{trial}} = \boldsymbol{e}^{e}_n + \Delta\boldsymbol{e}, \qquad v^{e\ \mathrm{trial}} = v^{e}_n + \Delta v \,. \tag{5.65}$$

The material constants G and K are, respectively, the shear and bulk moduli, $\boldsymbol{s}$ and p stand for the deviatoric and hydrostatic stresses. The strain deviator and the volumetric strain are denoted, respectively, by $\boldsymbol{e}$ and v. The trial yield stress is simply

$$\sigma_y^{\text{trial}} = \sigma_y(R_n). \tag{5.66}$$

The next step of the algorithm is to check whether $\boldsymbol{\sigma}^{\text{trial}}$ lies inside or outside of the trial yield surface. With variables $\bar{\varepsilon}^{\text{p}}$ and D frozen at time t_n we compute:

$$\begin{aligned} \Phi^{\text{trial}} &:= q^{\text{trial}} - (1 - D_n)\sigma_y(R_n) \\ &= \sqrt{\tfrac{3}{2}}\|\boldsymbol{s}^{\text{trial}}\| - (1 - D_n)\left[\sigma_{y_0} + R(\bar{\varepsilon}_n^{\text{p}})\right] . \end{aligned} \tag{5.67}$$

If $\Phi^{\text{trial}} \leq 0$, the process is indeed elastic within the interval and the elastic trial state coincides with the updated state at t_{n+1}. In other words, there is no plastic flow or damage evolution within the interval and

$$\begin{aligned} &\boldsymbol{\varepsilon}_{n+1}^{e} = \boldsymbol{\varepsilon}^{e\ \text{trial}}; \qquad \boldsymbol{\sigma}_{n+1} = \boldsymbol{\sigma}^{\text{trial}}; \qquad \bar{\varepsilon}_{n+1}^{\text{p}} = \bar{\varepsilon}^{\text{p trial}}; \\ &\sigma_{y\,n+1} = \sigma_y^{\text{trial}}; \qquad D_{n+1} = D^{\text{trial}}. \end{aligned} \tag{5.68}$$

Otherwise, it is necessary to apply the *plastic corrector* (or *return mapping* algorithm) whose step-by-step derivation is described in the following.

The plastic corrector step (or return mapping algorithm)

Following a straightforward specialisation of standard return mapping procedures (Simo & Hughes, 1998) for the present constitutive equations, leads to the numerical integration the evolution equations for $\boldsymbol{\varepsilon}^{\text{e}}$, $\bar{\varepsilon}_n^{\text{p}}$ and D having the trial state as the initial condition. The discrete counterparts of equations (5.56-5.59) read:

$$\begin{aligned} &\boldsymbol{\varepsilon}_{n+1}^{e} = \boldsymbol{\varepsilon}^{e\ \text{trial}} - \Delta\gamma\sqrt{\tfrac{3}{2}}\frac{\boldsymbol{s}_{n+1}}{\|\boldsymbol{s}_{n+1}\|} \\ &\bar{\varepsilon}_{n+1}^{\text{p}} = \bar{\varepsilon}_n^{\text{p}} + \Delta\gamma \\ &D_{n+1} = \begin{cases} 0 & \text{if } \bar{\varepsilon}_{n+1}^{\text{p}} \leq \bar{\varepsilon}_D^{\text{p}} \\ D_n + \frac{\Delta\gamma}{1-D_{n+1}}\left(\frac{-Y_{n+1}}{r}\right)^s & \text{if } \bar{\varepsilon}_{n+1}^{\text{p}} > \bar{\varepsilon}_D^{\text{p}}. \end{cases} \end{aligned} \tag{5.69}$$

The above equations must be complemented by the so-called *consistency condition* that guarantees that the stress state at the end of a plastic step lies on the updated yield surface:

$$\Phi_{n+1} = q_{n+1} - (1 - D_{n+1})\sigma_y(R_{n+1}) = 0. \tag{5.70}$$

The previous set of discrete evolution equations needs to be solved for the unknowns $\boldsymbol{\varepsilon}^e_{n+1}$, $\Delta\gamma$, $\bar{\varepsilon}^{\mathrm{p}}_{n+1}$ and D_{n+1}. After the solution of the above system, the plastic strain tensor can be updated according to the following formula:

$$\boldsymbol{\varepsilon}^p_{n+1} = \boldsymbol{\varepsilon}^p_n - \Delta\gamma\,\sqrt{\tfrac{3}{2}}\,\frac{\boldsymbol{s}_{n+1}}{\|\boldsymbol{s}_{n+1}\|} \tag{5.71}$$

As we shall see in what follows, analogously to what happens to the classical von Mises model, the above system can be reduced by means of simple algebraic substitutions to a *single* non-linear equation having the incremental plastic multiplier, $\Delta\gamma$, as a variable.

To start with let us consider the deviatoric/volumetric split of $(5.69)_1$. Since the plastic flow vector that multiplies $\Delta\gamma$ on the right hand side of $(5.69)_1$ is purely deviatoric, we have:

$$\begin{aligned} \boldsymbol{e}^e_{n+1} &= \boldsymbol{e}^{e\ \mathrm{trial}} - \Delta\gamma\,\sqrt{\tfrac{3}{2}}\,\frac{\boldsymbol{s}_{n+1}}{\|\boldsymbol{s}_{n+1}\|} \\ v^e_{n+1} &= v^{e\ \mathrm{trial}}\,. \end{aligned} \tag{5.72}$$

Expressions (5.72) together with the elastic law (5.63) gives the following updating relation for the stress deviator and hydrostatic pressure:

$$\begin{aligned} \boldsymbol{s}_{n+1} &= \boldsymbol{s}^{\mathrm{trial}} - \Delta\gamma\ 2G\,\sqrt{\tfrac{3}{2}}\,\frac{\boldsymbol{s}_{n+1}}{\|\boldsymbol{s}_{n+1}\|} \\ p_{n+1} &= p^{\mathrm{trial}}\,. \end{aligned} \tag{5.73}$$

The return mapping affects *only* the deviatoric stress component. The hydrostatic stress, p_{n+1}, remains unchanged and can, therefore, be eliminated from the system of equations. Further, simple inspection of $(5.73)_1$ shows that $\boldsymbol{s}_{n+1}$ is a scalar multiple of $\boldsymbol{s}^{\mathrm{trial}}$ so that, trivially, we have the identity:

$$\frac{\boldsymbol{s}_{n+1}}{\|\boldsymbol{s}_{n+1}\|} = \frac{\boldsymbol{s}^{\mathrm{trial}}}{\|\boldsymbol{s}^{\mathrm{trial}}\|}\,, \tag{5.74}$$

This indicates that the flow vectors at the trial and updated states coincide, which allows us to re-write $(5.73)_1$ as:

$$\boldsymbol{s}_{n+1} = \left(1 - \sqrt{\tfrac{3}{2}}\,\frac{\Delta\gamma\ 2G}{\|\boldsymbol{s}^{\mathrm{trial}}\|}\right)\boldsymbol{s}^{\mathrm{trial}} = \left(1 - \frac{\Delta\gamma\ 3G}{q^{\mathrm{trial}}}\right)\boldsymbol{s}^{\mathrm{trial}} \tag{5.75}$$

where q^{trial} is the elastic trial von Mises equivalent stress:

$$q^{\mathrm{trial}} = q(\boldsymbol{s}^{\mathrm{trial}}) = \sqrt{\tfrac{3}{2}}\,\|\boldsymbol{s}^{\mathrm{trial}}\|\,. \tag{5.76}$$

From equation (5.75) and the definition of the von Mises equivalent stress, results the following update formula for q:

$$q_{n+1} = q^{\mathrm{trial}} - 3G\,\Delta\gamma\,. \tag{5.77}$$

With the substitution of the above formula together with $(5.69)_2$ into the consistency equation (5.70), we obtain the following *scalar* non-linear equation for the incremental plastic multiplier $\Delta\gamma$:

$$\Phi_{n+1} = q^{\text{trial}} - 3G\,\Delta\gamma - (1 - D_{n+1})\sigma_y(R_{n+1}) = 0, \tag{5.78}$$

or, equivalently,

$$D_{n+1} = D(\Delta\gamma) \equiv 1 - \frac{\sqrt{\frac{3}{2}}\,\|\boldsymbol{s}^{\text{trial}}\| - 3G\,\Delta\gamma}{\sigma_{y_0} + R(\bar{\varepsilon}^{\text{p}}_n + \Delta\gamma)}\,, \tag{5.79}$$

which expresses D_{n+1} as an explicit function of $\Delta\gamma$.

One-equation return mapping We carry on here to show how the system (5.69) can be reduced leading to a computationally more efficient return mapping algorithm. By introducing the damage explicit function (5.79) into the discretised damage evolution equation $(5.69)_3$, the return mapping algorithm is reduced to the solution of a *single equation* for the unknown $\Delta\gamma$:

$$F(\Delta\gamma) \equiv \begin{cases} D(\Delta\gamma) = 0 & \text{if } \bar{\varepsilon}^{\text{p}}_{n+1} \leq \bar{\varepsilon}^{\text{p}}_D \\[2ex] D(\Delta\gamma) - D_n - \frac{\Delta\gamma}{1-D(\Delta\gamma)}\left(\frac{-Y(\Delta\gamma)}{r}\right)^s = 0 & \text{if } \bar{\varepsilon}^{\text{p}}_{n+1} > \bar{\varepsilon}^{\text{p}}_D\,. \end{cases} \tag{5.80}$$

In $(5.80)_2$, the dependency of Y on $\Delta\gamma$ originates from its dependency on the updated values of D and $\boldsymbol{\sigma}$ [clearly shown in definition (5.60)]. The updated stress tensor, $\boldsymbol{\sigma}_{n+1}$, whose tensile and compressive components take part in the calculation of Y_{n+1}, is obtained as:

$$\boldsymbol{\sigma}_{n+1} = \boldsymbol{s}_{n+1} + p_{n+1}\,\boldsymbol{I}\,, \tag{5.81}$$

where $\boldsymbol{I}$ is the second order identity tensor and $\boldsymbol{s}_{n+1}$ is obtained from the standard implicit von Mises return mapping as a function of $\Delta\gamma$ according to update formula (5.75):

$$\boldsymbol{s}_{n+1} = \left(1 - \frac{\Delta\gamma\,3G}{q^{\text{trial}}}\right)\boldsymbol{s}^{\text{trial}}; \qquad p_{n+1} = p^{\text{trial}}\,. \tag{5.82}$$

Equation (5.80) is then solved by the Newton-Raphson method and, once a solution $\Delta\gamma$ is found, the state variables are updated as follows:

$$\begin{aligned} \boldsymbol{s}_{n+1} &= \left(1 - \tfrac{\Delta\gamma\,3G}{q^{\text{trial}}}\right)\boldsymbol{s}^{\text{trial}}\,, \qquad p_{n+1} = p^{\text{trial}}\,, \\ \boldsymbol{\sigma}_{n+1} &= \boldsymbol{s}_{n+1} + p_{n+1}\,\boldsymbol{I}\,, \\ \boldsymbol{\varepsilon}^{\text{e}}_{n+1} &= [\mathsf{D}^e]^{-1} : \boldsymbol{\sigma}_{n+1} = \tfrac{1}{2G}\,\boldsymbol{s}_{n+1} + \tfrac{1}{3K}\,p_{n+1}\,\boldsymbol{I}\,, \\ \bar{\varepsilon}^{\text{p}}_{n+1} &= \bar{\varepsilon}^{\text{p}}_n + \Delta\gamma\,, \\ D_{n+1} &= 1 - \tfrac{\sqrt{\frac{3}{2}}\,\|\boldsymbol{s}^{\text{trial}}\| - 3G\,\Delta\gamma}{\sigma_{y_0} + R(\bar{\varepsilon}^{\text{p}}_n + \Delta\gamma)}\,. \end{aligned} \tag{5.83}$$

If required, the plastic strain tensor is updated by means of (5.71).

For convenience, the resulting algorithm for numerical integration of the elasto-plastic damage model with crack closure effects is listed in Box 5.4 in pseudo-code format.

Remark 5.9 (elasto-plastic solution) *The one equation return mapping (5.80) rigorously recovers the standard von Mises elasto-plastic model (rate-independent) when the damage exponent,* $s \rightarrow 0$ *and the damage denominator,* $r \rightarrow \infty$*. Evidently, in this case, the algorithm of Box 5.4 reproduces the conventional rate-independent elastoplastic numerical solution.*

Explicit implementation

The numerical integration of the proposed elasto-plastic damage model, whose constitutive equations are summarized in Box 5.3., has also been carried out within an *explicit* time integration scheme. In this case, due to the incremental nature of explicit schemes, the *elastic predictor* stage requires the following straightforward modification in the computation of the elastic trial stress tensor:

$$\boldsymbol{\sigma}^{\text{trial}} = \boldsymbol{\sigma}_n + \mathsf{D} : \Delta\boldsymbol{\varepsilon}, \tag{5.84}$$

where D is the standard isotropic elasticity tensor and $\Delta\boldsymbol{\varepsilon}$ the incremental strain. Equivalently, in terms of the deviatoric/hydrostatic split of $\boldsymbol{\sigma}$, we have

$$\boldsymbol{s}^{\text{trial}} = \boldsymbol{s}_n + 2G\,\Delta\boldsymbol{e} \qquad p^{\text{trial}} = p_n + K\,\Delta v. \tag{5.85}$$

The rest of the algorithm can be carried out without modification, as listed in Box 5.4 in pseudo-code format.

Remark 5.10 *The efficiency of numerical integration schemes for integration of the constitutive equations has a direct impact on the overall efficiency of the finite element framework. In this context, the use of more complex constitutive models can potentially incur a dramatic increase in analysis time. Here, the reduction of the return mapping to the solution of a* **single** *scalar equation is of crucial importance for the efficiency of the overall scheme and allows the introduction of crack closure effects in damage evolution with little impact on the overall analysis costs. It is also important to emphasise that this reduction would not be possible had damage with crack closure effects been considered also in the elastic law [as originally proposed by Lemaitre (1996)]. The consideration of such coupling under the present circumstances would result in a prohibitive increase in computational costs with little or no improvement in the predictive capability of the model.*

Box 5.4: Elastic predictor/return mapping algorithm for the elasto-plastic damage model with crack closure effect. Integration over $[t_n, t_{n+1}]$.

(i) *Elastic predictor.* Given the incremental strain, $\Delta\boldsymbol{\varepsilon}$, and the state variables at t_n, compute *elastic trial stresses*:

$$\begin{aligned}
\boldsymbol{\varepsilon}^{\mathrm{e\,trial}} &= \boldsymbol{\varepsilon}^{\mathrm{e}}_n + \Delta\boldsymbol{\varepsilon}; & \bar{\varepsilon}^{\mathrm{p\,trial}} &= \bar{\varepsilon}^{\mathrm{p}}_n;\\
\boldsymbol{s}^{\mathrm{trial}} &= 2G\,\boldsymbol{e}^{\mathrm{trial}}; & p^{\mathrm{trial}} &= K\,v^{\mathrm{trial}};\\
D^{\mathrm{trial}} &= D_n; & q^{\mathrm{trial}} &= \sqrt{\tfrac{3}{2}}\,\|\boldsymbol{s}^{\mathrm{trial}}\|,
\end{aligned}$$

(ii) *Plastic consistency check.* First compute:

$$\Phi^{\mathrm{trial}} = q^{\mathrm{trial}} - (1 - D_n)\,[\sigma_{y_0} + R(\bar{\varepsilon}^{\mathrm{p}}_n)]\,,$$

and then check:

- IF $\Phi^{\mathrm{trial}} \leq \varepsilon_{\mathrm{tol}}$ THEN the process is elastic,
  Update $(\cdot)_{n+1} = (\cdot)^{\mathrm{trial}}$ and EXIT
- ELSE GOTO (iii)

(iii) *Return mapping.* Find $\Delta\gamma$ such that:

$$F(\Delta\gamma) \equiv \begin{cases} D(\Delta\gamma) = 0 & \text{if } \bar{\varepsilon}^{\mathrm{p}}_{n+1} \leq \bar{\varepsilon}^{\mathrm{p}}_D \\ D(\Delta\gamma) - D_n - \frac{\Delta\gamma}{1 - D(\Delta\gamma)}\left(\frac{-Y(\Delta\gamma)}{r}\right)^s = 0 & \text{if } \bar{\varepsilon}^{\mathrm{p}}_{n+1} > \bar{\varepsilon}^{\mathrm{p}}_D \end{cases}$$

with $D(\Delta\gamma)$ defined by (5.79) and $Y(\Delta\gamma)$ defined through (5.60), (5.79) (5.81) and (5.82).

(iv) *Update the variables*:

$$\begin{aligned}
\boldsymbol{s}_{n+1} &= \left(1 - \frac{\Delta\gamma\,3G}{q^{\mathrm{trial}}}\right)\boldsymbol{s}^{\mathrm{trial}}; & p_{n+1} &= p^{\mathrm{trial}}\,;\\
\boldsymbol{\sigma}_{n+1} &= \boldsymbol{s}_{n+1} + p_{n+1}\,\boldsymbol{I}\,; & \bar{\varepsilon}^{\mathrm{p}}_{n+1} &= \bar{\varepsilon}^{\mathrm{p}}_n + \Delta\gamma\,;\\
\boldsymbol{\varepsilon}^{\mathrm{e}}_{n+1} &= \frac{1}{2G}\,\boldsymbol{s}_{n+1} + \frac{1}{3K}\,p_{n+1}\,\boldsymbol{I}\,; & D_{n+1} &= D(\Delta\gamma).
\end{aligned}$$

(v) EXIT

Accuracy and stability

Iso-error maps have long been accepted as an effective and reliable (if not the only) tool for assessing the accuracy of constitutive integration algorithms under realistic finite time/strain steps (Krieg & Krieg, 1977; Ortiz & Popov, 1985; Simo & Taylor, 1985). This section presents some iso-error maps obtained for the above described algorithm. The maps have been generated in the standard fashion. Using the three-dimensional implementation of the model, we start from a stress point at time t_n, $\boldsymbol{\sigma}_n$, lying on the yield surface (refer to Figure 5.3) and apply a sequence of strain increments (within the interval $[t_n, t_{n+1}]$), corresponding to linear combinations of trial stress increments of the form

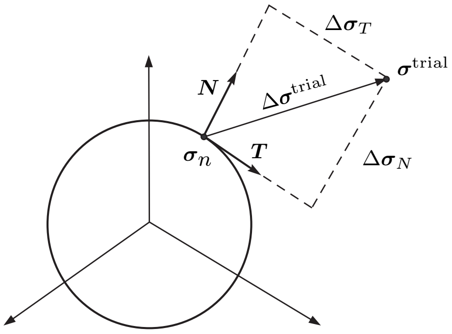

$\Delta\boldsymbol{\sigma}_T$
$\boldsymbol{\sigma}^{\text{trial}}$
$\boldsymbol{N}$
$\Delta\boldsymbol{\sigma}^{\text{trial}}$
$\boldsymbol{\sigma}_n$
$\boldsymbol{T}$
$\Delta\boldsymbol{\sigma}_N$

Figure 5.3: Isoerror map. Trial stress increment directions.

$$\Delta\boldsymbol{\sigma}^{\text{trial}} = \frac{\Delta\boldsymbol{\sigma}_T}{q}\boldsymbol{T} + \frac{\Delta\boldsymbol{\sigma}_N}{q}\boldsymbol{N}, \tag{5.86}$$

where $\boldsymbol{N}$ and $\boldsymbol{T}$ are, respectively, the unit normal and tangent vectors to the yield surface and q is the von Mises equivalent stress. For each increment of trial stress, we obtain a numerical solution, $\boldsymbol{\sigma}_{n+1}^{\text{num}}$, with the above described algorithm in one step. In addition, a solution assumed to be 'exact', $\boldsymbol{\sigma}_{n+1}^{\text{exact}}$, is obtained with the same algorithm by dividing the corresponding strain (and time) increment into 1000 sub-increments of equal size. For each point in which a numerical and 'exact' solution is obtained, the error is computed as:

$$\text{ERROR} = \frac{\|\boldsymbol{\sigma}_{n+1}^{\text{exact}} - \boldsymbol{\sigma}_{n+1}^{\text{num}}\|}{\|\boldsymbol{\sigma}_{n+1}^{\text{exact}}\|} \times 100\,.$$

The resulting iso-error map is the contour plot of the error field. A study of the finite step accuracy properties of the integration algorithm for the plane stress-projected implementation of Lemaitre's original model (see Section 5.3.1) has been carried out by de Souza Neto *et al.* (1994). The main conclusions are that the accuracy of the algorithm deteriorates as damage increases and the bowl of convergence of the local Newton algorithm shrinks. Also, at highly damaged states, the choice of an appropriate initial guess becomes crucial.

The material properties adopted in the present analysis, are listed in Table 5.1. These parameters were taken from Vaz Jr. & Owen (2001) for an aluminium alloy, except the value of the damage denominator, r. The value

Table 5.1: Material data for aluminium alloy.

Description	**Symbol**	**Value**
Elastic Modulus	E	69004 $[MN/m^2]$
Poisson's ratio	ν	0.3
Initial yield stress	σ_{y0}	80.559 $[MPa]$
Hardening curve	$\sigma_y(\bar{\varepsilon}^{\mathrm{p}})$	$589 \cdot (10^{-4} + \bar{\varepsilon}^{\mathrm{p}})^{0.216}$
Damage data (exponent)	s	1.0
Damage data (denominator)	r	2.8 $[MPa]$

of this material constant has been calibrated by performing several numerical tests with a single axisymmetric finite element, such that critical value of damage ($D = 1$) is attained, for the same applied displacement. The error maps obtained with isotropic hardening are shown in Figure 5.4. As dam-

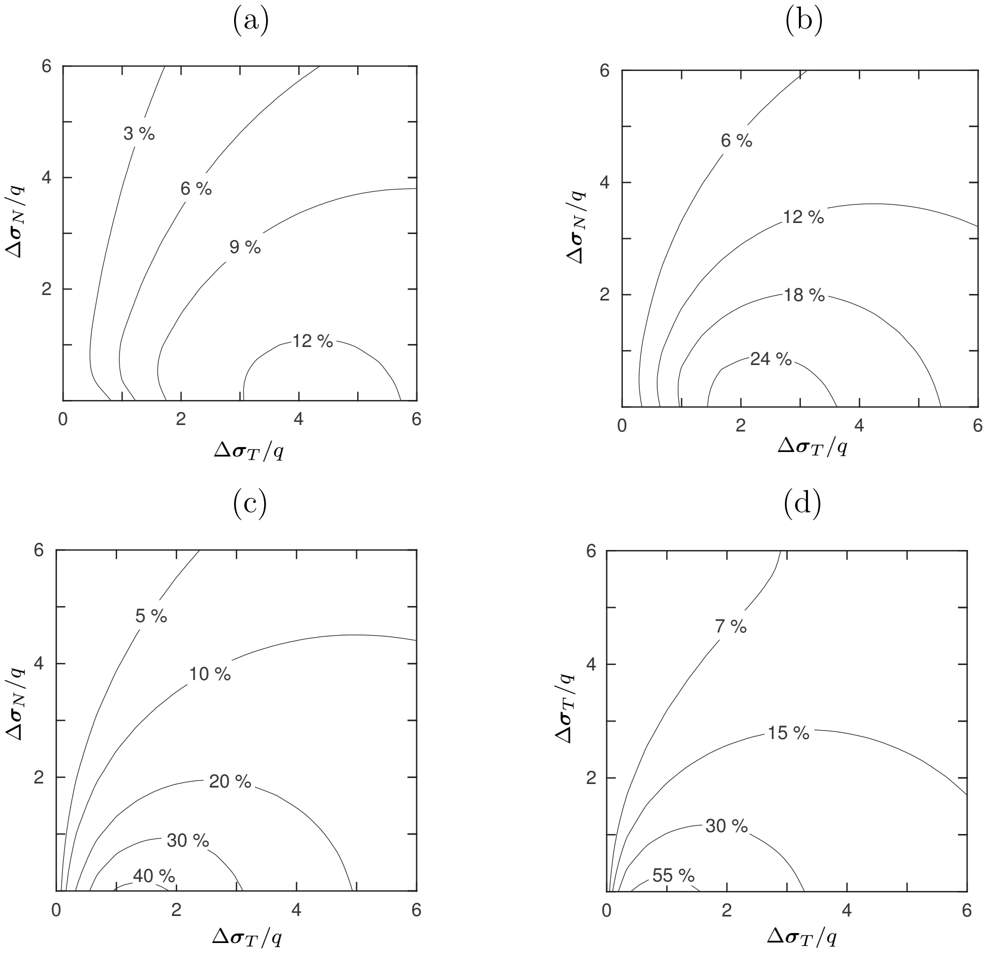

Figure 5.4: Iso-error maps for: (a) $D = 0\%$, $\bar{\varepsilon}^{\mathrm{p}} = 0$; (b) $D = 15\%$, $\bar{\varepsilon}^{\mathrm{p}} = 0.348$; (c) $D = 40\%$, $\bar{\varepsilon}^{\mathrm{p}} = 0.625$; (d) $D = 65\%$, $\bar{\varepsilon}^{\mathrm{p}} = 0.779$.

age increases the error maps obtained at different stages of damage evolution clearly show that the accuracy of the algorithm deteriorates. The integration error initially, Figure 5.4 (a), attains a higher value in the region where the increments on the tangential direction, $\boldsymbol{T}$, are greater combined with small increments on the normal direction, $\boldsymbol{N}$. As the initial damage is increased [see Figures 5.4 (b)–(d)], the location of the highest error moves toward the region where the increments on the tangential direction are smaller. In such circumstances, either the overall increment should be smaller or a substepping procedure should be included in the return mapping algorithm.

All the error maps, depicted in Figure 5.4, have been obtained with the crack closure constant set to zero. In spite of this fact, the integration error maps (not shown here) obtained for any value of the crack closure effect, $0 \leq h \leq 1$, are virtually the same as for the cases reported in Figures 5.4 (a)–(c).

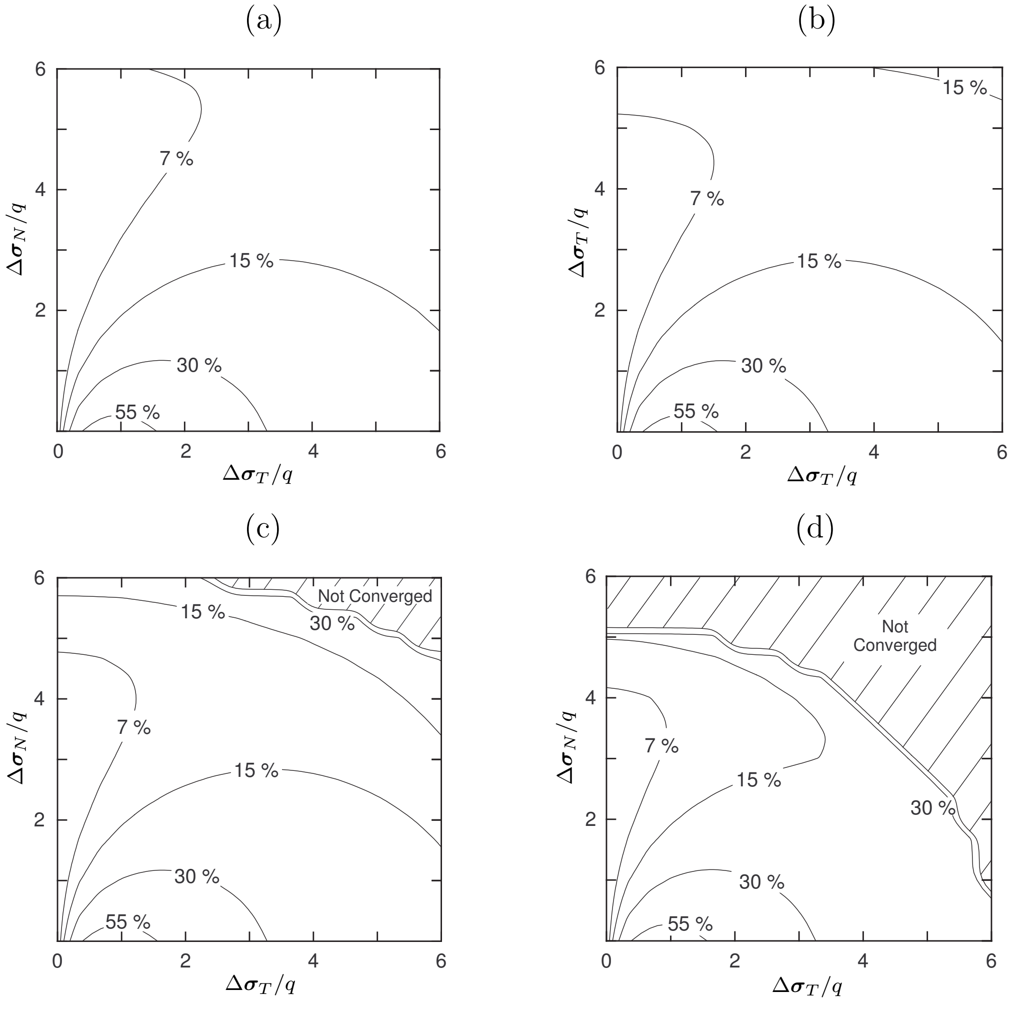

Figure 5.5: Iso-error maps for $D = 65\%$ and $\bar{\varepsilon}^{\mathrm{p}} = 0.779$. (a) $h = 0.7$; (b) $h = 0.9$; (c) $h = 0.95$; (d) $h = 1$.

When the initial value of damage is already significant, $D = 65\%$, the error map is clearly affected by the effect of crack closure. In Figure 5.5 several error maps are shown for different values of h. It can be observed that for values of h close to unity, it is not possible to obtain a converged solution, for large increments in both tangential and normal directions. With the aim of overcoming this problem, a different initial guess was used as suggested by de Souza Neto *et al.* (1994):

$$\Delta\gamma^{(0)} = \frac{q^{\text{trial}} - (1 - D_n)\, \sigma_y(R_n)}{3G}\,, \tag{5.87}$$

which corresponds to the perfectly plastic solution for the increment with *frozen* (damaged) yield surface at t_n. Although the number of iterations necessary to attain convergence was reduced, the Newton-Raphson scheme with the above initial guess also failed to converge at highly damaged states.

5.4.3 The tangent operator

If a full Newton-Raphson scheme is to be used in conjunction with the implicit finite element implementation of the present model, the tangent operator consistent with the above integration scheme is required in the assembly of the tangent stiffness matrix. In the elastic case, i.e., when the stress is inside the elastic domain ($\Phi < 0$) or if it is on the yield surface ($\Phi = 0$) and elastic unloading is assumed to occur, the *elastic consistent tangent* at t_{n+1} is simply the standard elasticity operator

$$\hat{\mathsf{D}} = \mathsf{D}^e = 2G\left[\mathsf{I} - \tfrac{1}{3}\boldsymbol{I}\otimes\boldsymbol{I}\right] + K\,\boldsymbol{I}\otimes\boldsymbol{I} \tag{5.88}$$

where I, is the fourth order identity tensor. In the elasto-plastic damage case, i.e., when it is assumed that plastic flow occurs within the step ($\Phi > 0$), the tangent operator is called the *elasto-plastic damage consistent tangent* and is denoted by $\hat{\mathsf{D}}^{ep}$. Thus, the consistent tangent operator

$$\hat{\mathsf{D}}^{ep} \equiv \frac{\mathrm{d}\hat{\boldsymbol{\sigma}}}{\mathrm{d}\boldsymbol{\varepsilon}_{n+1}} \tag{5.89}$$

is simply the *derivative of the implicit function* $\hat{\boldsymbol{\sigma}}$ for the updated stress defined by the return mapping procedure (Section 5.4.2). It follows the standard procedure for differentiation of implicit functions. The issue of consistent tangent operators and their derivation is thoroughly discussed elsewhere (Simo & Taylor, 1985; Simo & Hughes, 1998). In the present case it is possible to obtain a closed form expression for $\hat{\mathsf{D}}^{ep}$. Its derivation is relatively lengthy but follows only standard application of consistent linearisation concepts. The details of derivation will be omitted here and we shall limit ourselves to show only its final expression which is given by:

$$\mathsf{D}^{ep} = a_1\left[\mathsf{I} - \tfrac{1}{3}\boldsymbol{I}\otimes\boldsymbol{I}\right] + a_2\,\bar{\boldsymbol{s}}_{n+1}\otimes\bar{\boldsymbol{s}}_{n+1} + a_3\,\bar{\boldsymbol{s}}_{n+1}\otimes\boldsymbol{I} + K\,\boldsymbol{I}\otimes\boldsymbol{I}\,, \tag{5.90}$$

where $\bar{\boldsymbol{s}}_{n+1}$ is the normalised stress deviator:

$$\bar{\boldsymbol{s}}_{n+1} = \frac{\boldsymbol{s}_{n+1}}{\|\boldsymbol{s}_{n+1}\|}\,, \tag{5.91}$$

and the scalars a_1, a_2, a_3, are given by:

$$\begin{aligned} a_1 &= 2G\left(1 - \tfrac{\Delta\gamma\, 3G}{q^{\mathrm{trial}}}\right) \\ a_2 &= 6G^2\left[\tfrac{\Delta\gamma}{q^{\mathrm{trial}}} + \tfrac{\partial F}{\partial\,(q^{\mathrm{trial}})}\Big/\tfrac{\partial F}{\partial\,(\Delta\gamma)}\right] \\ a_3 &= 2G\sqrt{\tfrac{2}{3}}\,K\left[\tfrac{\partial F}{\partial\,(p^{\mathrm{trial}})}\Big/\tfrac{\partial F}{\partial\,(\Delta\gamma)}\right]. \end{aligned} \tag{5.92}$$

In the definition of constants a_2 and a_3, the scalars $\partial F/\partial\,(\Delta\gamma)$, $\partial F/\partial\,(q^{\mathrm{trial}})$ and $\partial F/\partial\,(p^{\mathrm{trial}})$, correspond to the derivatives of the return mapping residual function defined by (5.80):

$$\begin{aligned} \tfrac{\partial F}{\partial\,(\Delta\gamma)} &= \tfrac{\partial D}{\partial\,(\Delta\gamma)} + \tfrac{1}{1-D_{n+1}}\left(-\tfrac{Y_{n+1}}{r}\right)^{s} \\ &\qquad \left\{\left[-\tfrac{\partial D}{\partial\,(\Delta\gamma)}\big/{\scriptstyle (1-D_{n+1})} - s\,\tfrac{\partial Y}{\partial\,(\Delta\gamma)}\big/{\scriptstyle Y_{n+1}}\right]\Delta\gamma - 1\right\} \\ \tfrac{\partial F}{\partial\,(q^{\mathrm{trial}})} &= \tfrac{\partial D}{\partial\,(q^{\mathrm{trial}})} - {\scriptstyle \Delta\gamma}\tfrac{\partial D}{\partial\,(q^{\mathrm{trial}})}\big/{\scriptstyle (1-D_{n+1})^2}\left(-\tfrac{Y_{n+1}}{r}\right)^{s} \\ &\qquad - \tfrac{s\,\Delta\gamma}{r\,(1-D_{n+1})}\left(-\tfrac{Y_{n+1}}{r}\right)^{s-1}\tfrac{\partial Y}{\partial\,(q^{\mathrm{trial}})} \\ \tfrac{\partial F}{\partial\,(p^{\mathrm{trial}})} &= \tfrac{s\,\Delta\gamma}{r\,(1-D_{n+1})}\left(-\tfrac{Y_{n+1}}{r}\right)^{s}\tfrac{\partial Y}{\partial\,(p^{\mathrm{trial}})}. \end{aligned} \tag{5.93}$$

where the scalars $\partial Y/\partial\,(\Delta\gamma)$, $\partial Y/\partial\,(q^{\mathrm{trial}})$ and $\partial Y/\partial\,(p^{\mathrm{trial}})$, represent the derivatives of the energy release rate function, defined by (5.60):

$$\begin{aligned} \tfrac{\partial Y}{\partial\,(\Delta\gamma)} &= -\tfrac{\frac{\partial D}{\partial\,(\Delta\gamma)}}{E\,(1-D_{n+1})^3}\,b_+ + \tfrac{2G\sqrt{\frac{3}{2}}}{E\,(1-D_{n+1})^2}\,\boldsymbol{C}_+ : \bar{\boldsymbol{s}}_{n+1} - \tfrac{h^2\,\frac{\partial D}{\partial\,(\Delta\gamma)}}{E\,(1-h\,D_{n+1})^3}\,b_- \\ &\quad + \tfrac{2G\sqrt{\frac{3}{2}}\,h}{E\,(1-h\,D_{n+1})^2}\,\boldsymbol{C}_- : \bar{\boldsymbol{s}}_{n+1} \\ \tfrac{\partial Y}{\partial\,(q^{\mathrm{trial}})} &= -\tfrac{\frac{\partial D}{\partial\,(q^{\mathrm{trial}})}}{E\,(1-D_{n+1})^3}\,b_+ - \tfrac{\sqrt{\frac{2}{3}}}{E\,(1-D_{n+1})^2}\,\boldsymbol{C}_+ : \bar{\boldsymbol{s}}_{n+1} - \tfrac{h^2\,\frac{\partial D}{\partial\,(q^{\mathrm{trial}})}}{E\,(1-h\,D_{n+1})^3}\,b_- \\ &\quad + \tfrac{\sqrt{\frac{2}{3}}\,h}{E\,(1-h\,D_{n+1})^2}\,\boldsymbol{C}_- : \bar{\boldsymbol{s}}_{n+1} \\ \tfrac{\partial Y}{\partial\,(p^{\mathrm{trial}})} &= -\tfrac{1}{E\,(1-D_{n+1})^2}\,\boldsymbol{C}_+ : \boldsymbol{I} - \tfrac{h}{E\,(1-h\,D_{n+1})^2}\,\boldsymbol{C}_- : \boldsymbol{I} \end{aligned} \tag{5.94}$$

furthermore, the scalars b_+ and b_- and the second order tensors $\boldsymbol{C}_+$ and $\boldsymbol{C}_-$ introduced in (5.94), are given by

$$\begin{aligned} b_+ &= (1+\nu)\,\boldsymbol{\sigma}_+ : \boldsymbol{\sigma}_+ - \nu\,\langle \operatorname{tr}\boldsymbol{\sigma}\rangle^2 \\ b_- &= (1+\nu)\,\boldsymbol{\sigma}_- : \boldsymbol{\sigma}_- - \nu\,\langle -\operatorname{tr}\boldsymbol{\sigma}\rangle^2 \\ \boldsymbol{C}_+ &= (1+\nu)\,\tfrac{\partial\boldsymbol{\sigma}_+}{\partial\boldsymbol{\sigma}} : \boldsymbol{\sigma}_+ - \nu\,\langle \operatorname{tr}\boldsymbol{\sigma}\rangle\,\boldsymbol{I} \\ \boldsymbol{C}_- &= (1+\nu)\,\tfrac{\partial\boldsymbol{\sigma}_-}{\partial\boldsymbol{\sigma}} : \boldsymbol{\sigma}_- - \nu\,\langle -\operatorname{tr}\boldsymbol{\sigma}\rangle\,\boldsymbol{I} \end{aligned} \tag{5.95}$$

Here, one should note that, the tensors $\boldsymbol{C}_+$ and $\boldsymbol{C}_-$ defined in $(5.95)_3$ and $(5.95)_4$, respectively, contain the terms:

$$\frac{\partial\boldsymbol{\sigma}_+}{\partial\boldsymbol{\sigma}}, \qquad \text{and} \qquad \frac{\partial\boldsymbol{\sigma}_-}{\partial\boldsymbol{\sigma}}.$$

To compute such derivatives, we first note that (5.38) and (5.39) define $\boldsymbol{\sigma}_+$ and $\boldsymbol{\sigma}_-$ as *isotropic* tensor-valued functions of $\boldsymbol{\sigma}$. Such functions are particular cases of the families of functions discussed by Chadwick & Ogden (1971) and Carlson & Hoger (1986) and their derivatives are promptly available in closed form [see Appendix A].

To complete the definition of (5.93) it is necessary to define the scalars $\partial D/\partial\,(\Delta\gamma)$ and $\partial D/\partial\,(q^{\text{trial}})$, which are the outcome of the derivation of the damage function, defined by (5.79):

$$\begin{aligned} \tfrac{\partial D}{\partial\,(\Delta\gamma)} &= \tfrac{3G}{\sigma_y(R_{n+1})} + \tfrac{H(1-D_{n+1})}{\sigma_y(R_{n+1})} \\ \tfrac{\partial D}{\partial\,(q^{\text{trial}})} &= -\tfrac{1}{\sigma_y(R_{n+1})} \end{aligned} \tag{5.96}$$

In the above, H denotes the updated slope of the hardening curve at t_{n+1}:

$$H = \left.\frac{\mathrm{d}\sigma_y}{\mathrm{d}R}\right|_{R_{n+1}}. \tag{5.97}$$

Remark 5.11 *It is important to note that, as in Lemaitre's model, the resulting elasto-plastic tangent operator* D^{ep} *is generally unsymmetric so that, within the context of finite element computations, an unsymmetric solver is required in the global Newton-Raphson scheme.*

5.4.4 Numerical Examples

This section presents two examples aiming to illustrate basic aspects of the proposed one-equation integration algorithm described previously.

Tensile test

The simulation of crack initiation in a cylindrical pre-notched bar subjected to monotonic axial stretching, is used to illustrate the numerical performance of the proposed algorithm within an implicit quasi-static finite element environment. Tensile tests have been extensively used in both experimental and numerical analysis of ductile fracturing. On a microscope scale, nucleation, growth and coalescence of micro-voids are found to be the main mechanisms which cause fracture. This problem has been used by some authors (Benallal *et al.* , 1991; Cescotto & Zhu, 1995; Vaz Jr. & Owen, 2001; de Souza Neto, 2002) to assess the performance of different numerical formulations derived to model ductile plastic damage evolution. The geometry of the problem, boundary conditions and the finite element mesh adopted are given in Figure 5.6. A relatively fine discretisation is used in the region surrounding the smaller cross-section, in order to capture the necking pattern and damage evolution. The material properties adopted in the present analysis and other relevant simulation parameters are summarized in Table 5.1 [page 94]. The additional parameter h introduced in the model, does not have any influence, since the stress state is mainly tension. The loading consists of a prescribed vertical displacement, $u = 0.6[mm]$, (with free horizontal displacement) of the constrained edge. A total number of 329 four-noded axisymmetric *F-bar* quadrilaterals (de Souza Neto *et al.* , 1996) has been used in the discretisation amounting to a total of 367 nodes. The evolution of the damage variable field obtained in the finite element analysis is illustrated in the contour plots shown in Figure 5.7.

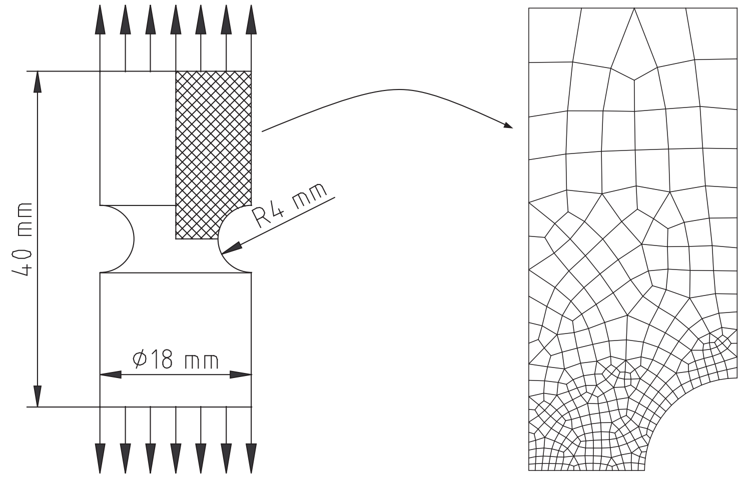

Figure 5.6: Axisymmetric notched bar. Geometry, boundary conditions and finite element mesh.

It can be seen that during the early stages of the loading process, maximum damage is detected near the root of the notch. As the specimen is progressively stretched, the maximum damage area moves gradually toward the centre of the

(a) $u = 0.21\,[mm]$ (b) $u = 0.36\,[mm]$

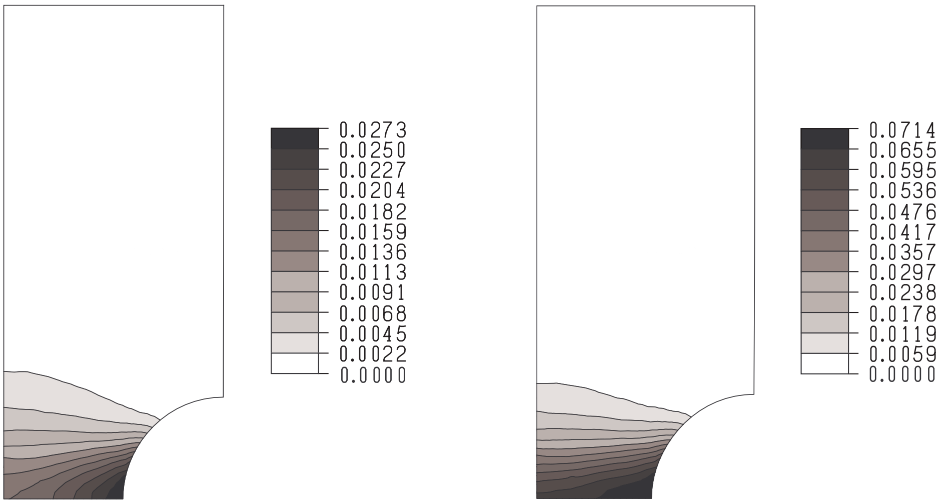

(c) $u = 0.45\,[mm]$ (d) $u = 0.6\,[mm]$

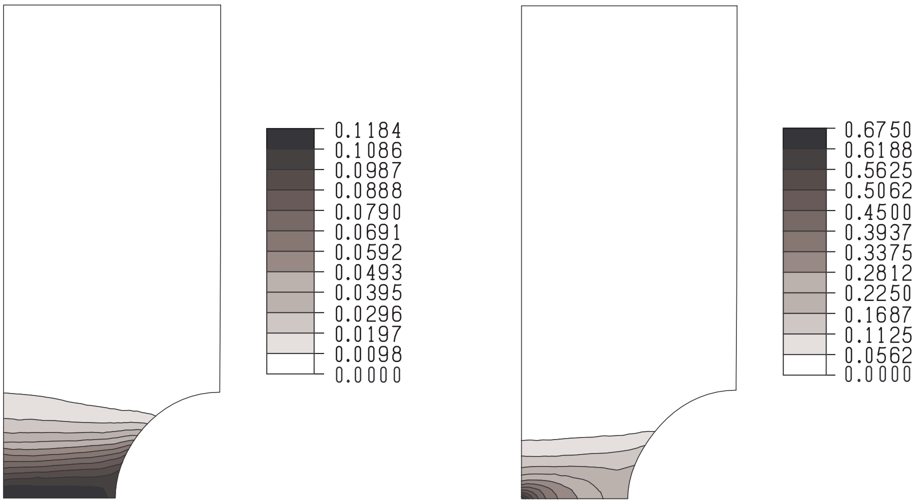

Figure 5.7: Axisymmetric notched bar. Damage contour plots.

specimen and localises there. At the final stage with $u = 0.6\,[mm]$ damage is highly localised around the centre. It is implied, therefore, that fracture initiation should be expected in that area. This prediction is in agreement with experimental observations by Hancock & Mackenzie (1976) and Cescotto & Zhu (1995) who show that for certain notched specimen configurations fracturing initiates at the centre of the specimen and propagates radially toward the notch.

The simulation results obtained using the present framework, are in close agreement, with the ones obtained by Vaz Jr. & Owen (2001), using an *explicit* *time integration scheme* but in conjunction with the standard Lemaitre fully coupled model (Lemaitre, 1983, 1985a) combined with the four node axisymmetric element with hourglass control proposed by Belytschko *et al.* (1984). In view of the use of the tangent operator described in the above section, convergence rates to equilibrium are quadratic. This is illustrated in Table 5.2 where the convergence of the relative residual of out-of-balance forces throughout the equilibrium Newton-Raphson iterations is shown for a typical load increment.

Table 5.2: Cylindrical notched bar. Convergence table.

Iteration number	**Relative residual (%)**
1	0.477462E+01
2	0.264637E+00
3	0.124162E−03
4	0.269092E−09

The evolution of the damage variable at the centre of the specimen is depicted in Figure 5.8(a) where the value of D computed at that point is plotted against the prescribed edge deflection. Prediction of ductile fracture onset in damaged materials usually adopts the damage variable itself as indicator by assuming that failure takes place when the damage variable attains a critical value, $D = D_{cr}$. Recent comparative analysis suggest that damage-based

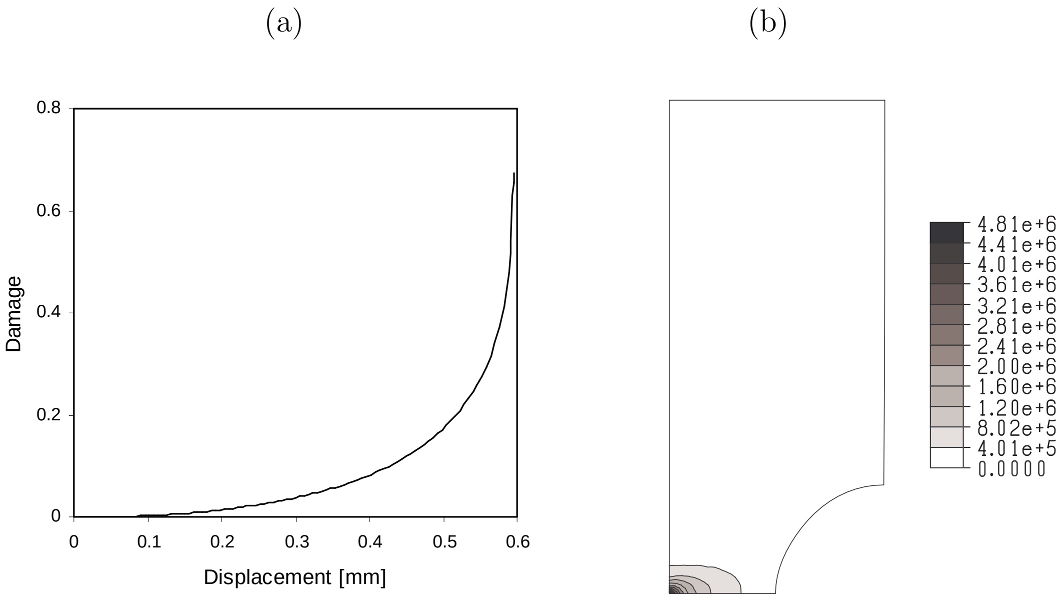

Figure 5.8: Cylindrical notched bar. (a) Damage variable evolution at the centre of the specimen, (b) Total damage work.

measures are more reliable in predicting the correct site of fracture initiation (Vaz Jr. & Owen, 2001) and the use of fracture criteria based on *total damage work*, generally defined as:

$$I_{\omega_D} = \int_0^t (-Y)\dot{D}\, dt = \int (-Y)\, dD, \tag{5.98}$$

offers a promising alternative, due to the high gradient exhibited by the indicator near the critical failure zone. It is possible to perceive [see Figure 5.8(b)] that the *total damage work* exhibits a better performance than the damage variable [see Figure 5.7(d)] due to the localised behaviour exhibited by the indicator near the critical zone.

Backward extrusion

In many forming processes the material is subjected to very high local strains that can lead to the nucleation and growth of micro-cracks with subsequent failure of the workpiece. Therefore, the prediction of damage in industrial forming processes can be of great interest for the optimisation of the design in order to avoid or restrict the initiation of defects induced by plastic deformation. The purpose of this example is to numerically assess the performance of the constitutive model proposed, which includes crack closure effects in damage evolution, in highly strained situations typically arising in back extrusion problems. The initial geometry of the problem is shown in Figure 5.9. The material is compressed by the tool on the right hand side and flows throughout the space between tool and die. An axisymmetric model of the problem is adopted in the simulation. The tool and die are assumed to be rigid bodies and the frictional contact condition at the tool/workpiece interface is modelled by the standard Coulomb friction law. In order to prevent unwanted

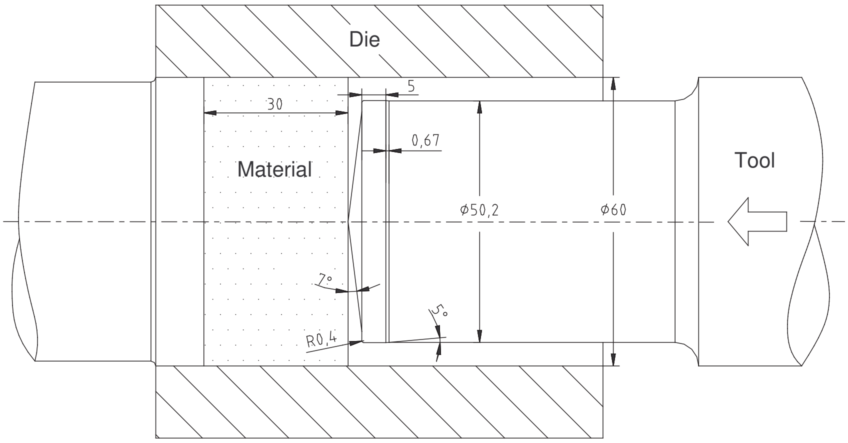

Figure 5.9: Backward extrusion. Problem geometry (dimensions in [mm]).

phenomena on the surface of the workpiece and to reduce the extrusion force, the tool and die are well lubricated. Therefore, the friction coefficient is reduced to a low value of $m = 0.08$. The contact impenetrability constraint is enforced by the classical penalty method. The selection of an appropriate penalty coefficient, in this context, is known to be essential for the successful application of the method. On one hand, if the penalty coefficient is too small large penetrations will occur, on the other hand, large penalty coefficients may compromise the stability of the solution. The normal and tangential penalty values employed in this simulation are, respectively, $P_n = 2 \times 10^5\,[N/mm]$ and $P_t = 1 \times 10^5\,[N/mm]$. A prescribed total displacement of $u = 24.8\,[mm]$ is applied to the tool.

The material used in this example is a 16 Mn Cr 5 steel. The identification of the material properties, including the damage evolution parameters, was undertaken by Arnold *et al.* (2002). The procedure used by these authors is based on micro-hardness measurements to identify ductile damage. In this application adaptive remeshing becomes an essential component of the finite element analysis. If remeshing is not included, many elements will be severely distorted producing unacceptably inaccurate solutions. The corresponding material properties and other simulation parameters employed in the adaptive process are listed in Table 5.3. The basic components of the adaptive procedure [1] employed in this simulation comprise (i) a criterion for mesh re-

Table 5.3: Material data for 16 Mn Cr 5 steel. Lemaitre's model parameters.

Description	**Symbol**	**Value**
Specific mass	ρ	7850 $[kg/m^3]$
Elastic Modulus	E	180 000 $[MN/m^2]$
Poisson's ratio	ν	0.3
Initial yield stress	σ_{y_0}	256 $[MPa]$
Yield stress	$\sigma_y(\bar{\varepsilon}^{\mathrm{p}})$	$\sigma_{y_0} + 255 \cdot [1 - \exp(-\bar{\varepsilon}^{\mathrm{p}}/0.066)] +$ $5282 \cdot [1 - \exp(-\bar{\varepsilon}^{\mathrm{p}}/24.1)]\ [MPa]$
Friction	m	0.08
Damage data (exponent)	s	1.0
Damage data (denominator)	r	11 $[MPa]$
Plastic threshold	$\bar{\varepsilon}^{\mathrm{p}}_D$	0.3
Error checking		200 time steps
Target error	η	5 %
Maximum element size	h_{max}	1.0 $[mm]$
Minimum element size	h_{min}	0.1 $[mm]$

---

[1] Further details on adaptive remeshing for history dependent problems in solid mechanics, including *error estimation* and *transfer operators*, are presented in Chapter 7.

finement based on the *rate of plastic work* (Perić *et al.* , 1994); (ii) a *transfer operator* that maps the primary unknowns using the shape functions from the nodes of the old mesh, to the nodes of the new mesh. The internal history dependent variables, including the damage variable, are mapped directly between gauss points of an old and new mesh by a weighted least-squares method using 8 sampling points; and (iii) an unstructured meshing approach based on the *Delaunay triangulation* is adopted.

Damage evolution without crack closure effects: Considering the nature of the process, the material is expected to undergo very large strains particularly around the neighborhood of the punch. The evolution of the damage variable field obtained in the numerical simulation is illustrated by the contour plots shown in Figure 5.10. Throughout the simulation of the process several

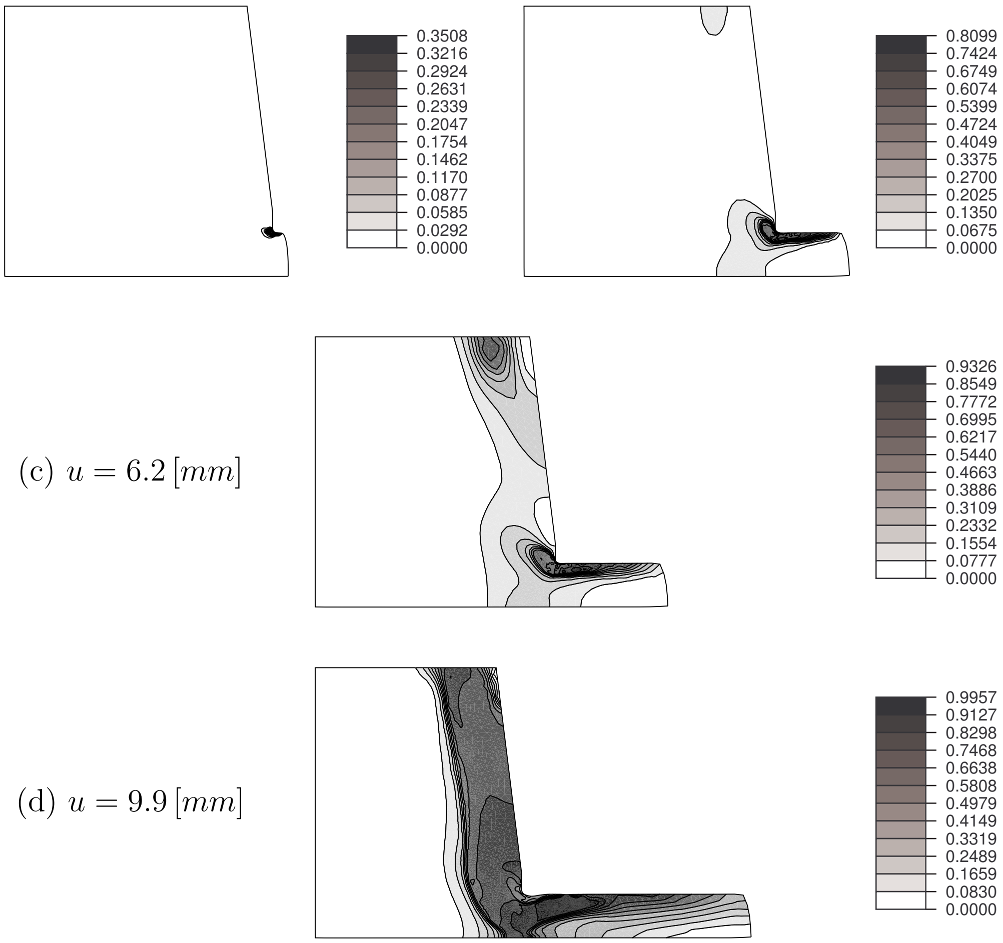

(a) $u = 3.1\,[mm]$ (b) $u = 5\,[mm]$

(c) $u = 6.2\,[mm]$

(d) $u = 9.9\,[mm]$

Figure 5.10: Standard model. Damage contour plots.

mesh adaptions were performed promoting a good aspect ratio of the finite element mesh and assuring a good quality of the solution. It can be seen that during the early stages of the loading process, maximum damage is detected near the edge of the punch [Figure 5.10 (a)]. As the material is progressively compressed, the damaged area develops through the material surrounding the corner of the punch [Figure 5.10(b)]. At this stage of the process, the maximum damage value attained is already extremely high. This result indicates that the microscopic deterioration of a representative volume element (RVE) modelled by the damage variable at macro-scale is close to failure, and hence to a macro-crack initiation. In the latter stages of the simulation [Figure 5.10(c) and (d)] the damaged area spreads almost over the entire contact zone between the punch and material, attaining values, in some places, close to unity.

The numerical prediction of material degradation, based on the damage model without crack closure effects, is not in agreement with experimental evidence, which shows that only a relatively small damage accumulation results from the process. The reason for the erroneous prediction obtained with the model without crack closure effects lies in the law (5.30) and (5.29) which imply fast damage growth rates under states of high stress triaxiality, regardless of the sign (tension or compression) of the dominating stresses.

Inclusion of crack closure effects in the damage evolution: The lack of accuracy of the above prediction is addressed here by adopting the damage model with crack closure effects described in Section 5.4. The additional material constant, h (the *crack closure parameter*) is chosen as $h = 0.01$. This choice implies a substantial reduction in damaging rates under compressive dominant stress. Figure 5.11 shows the spatial evolution of the damage variable field obtained by finite element analysis, for various stages of the process. It can be seen that throughout the extrusion, the maximum damage is observed at the surface of the workpiece that is in contact with the tool. The critical area is located near the corner of the punch, where the material is submitted to complex strain paths. This result is in agreement with experimental evidence, that suggests that defects are observed in this region.

We remark that, the damage evolution observed in Figure 5.11, is substantially different from the evolution obtained by the model without crack closure effects (see Figure 5.10). The numerical value of the damage variable remains below $D \leq 0.3$, throughout the simulation. The material at the centre of the workpiece does not suffer any damage and only beyond a critical radius near the external surface does the damage variable increase substantially. In order to obtain extruded workpieces of good quality, it is necessary to reduce the ductile damage within the material.

(a) $u = 6.2\,[mm]$

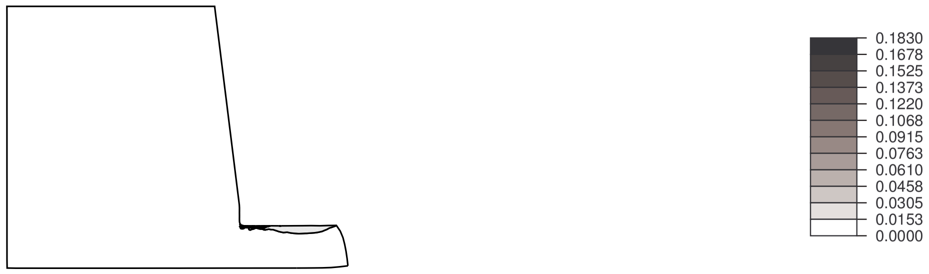

(b) $u = 12.4\,[mm]$

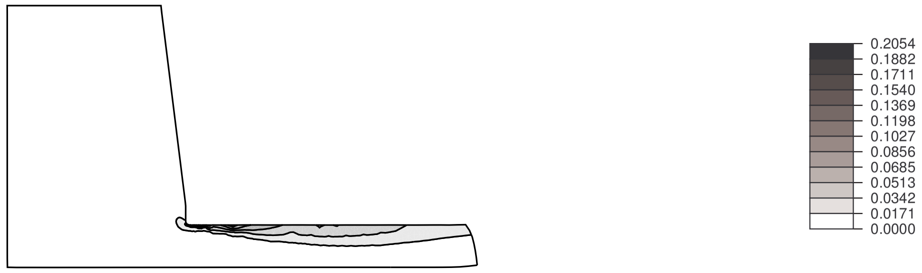

(c) $u = 18.6\,[mm]$

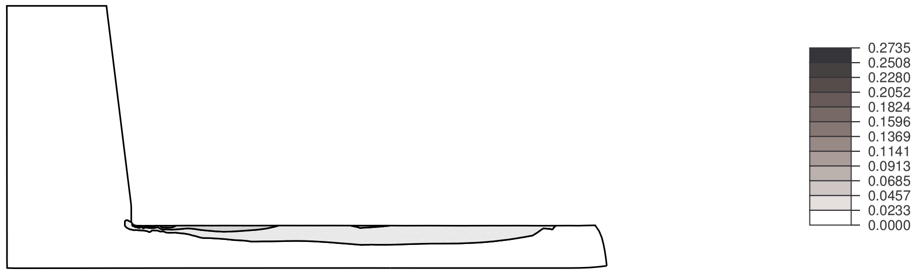

(d) $u = 24.8\,[mm]$

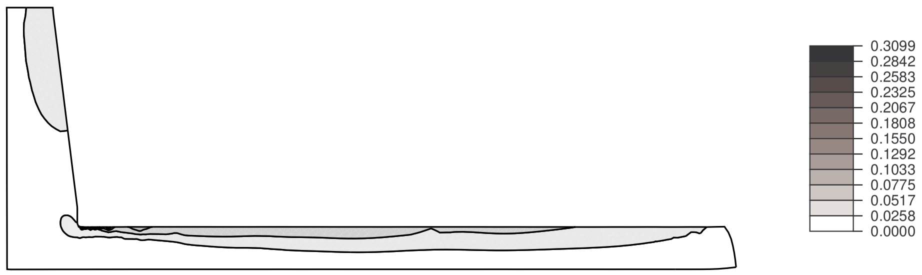

Figure 5.11: Improved model. Damage contour plots.

5.5 Elasto-viscoplastic damage model with crack closure

The elasto-plastic damage model presented in Section 5.4 of this chapter is classified as *rate-independent* or *time-independent.* That is, the material response is regarded as independent of the rate of application of the load and/or the time scale of the problems considered. However, the experimental behaviour of real materials suggests that the amount of microcracking(damage) at a particular strain level exhibits *rate sensitivity* to the applied rate of loading. That is, the stress response always depend on the time scale considered and/or the rate of loading. The extent of such dependence may or may not be significant according to the physical conditions of the problem. Rate-dependence effects are described by means of so-called *visco-plasticity* (or *rate-dependent plasticity*) models, to which the present section is devoted.

5.5.1 The constitutive model

A generic von Mises type power law elasto-viscoplastic damage model with crack closure effects and isotropic strain hardening can be defined by the following set of constitutive equations:

1. Linear elastic relation between the stress tensor, $\boldsymbol{\sigma}$, and the elastic strain, $\boldsymbol{\varepsilon}^e$:

   $$\boldsymbol{\sigma} = \mathbf{D} : \boldsymbol{\varepsilon}^e \tag{5.99}$$

   where $\mathbf{D}$ is the standard isotropic elasticity fourth order tensor and the symbol : denotes double contraction.

2. Additive split of the total strain rate, $\dot{\boldsymbol{\varepsilon}}$, into an elastic contribution, $\dot{\boldsymbol{\varepsilon}}^e$, and an inelastic contribution, $\dot{\boldsymbol{\varepsilon}}^p$:

   $$\dot{\boldsymbol{\varepsilon}} = \dot{\boldsymbol{\varepsilon}}^e + \dot{\boldsymbol{\varepsilon}}^p \tag{5.100}$$

3. An associative plastic flow rule:

   $$\dot{\boldsymbol{\varepsilon}}^p = \dot{\gamma}\,\frac{\partial \Phi}{\partial \boldsymbol{\sigma}}\,. \tag{5.101}$$

   where $\dot{\gamma}$ is the plastic multiplier whose expression is defined later.

4. In the above, Φ is the yield function where the effect of damage on the viscoplastic behaviour can be accounted for rewriting the *yield function* Φ in the following form:

   $$\Phi(\boldsymbol{\sigma}, R, D) \equiv q - (1-D)\,\sigma_y \;= \sqrt{3\,J_2(\boldsymbol{s})} - (1-D)\,\sigma_y, \tag{5.102}$$

where $\boldsymbol{s} \equiv \boldsymbol{\sigma} - \frac{1}{3}\,(\mathrm{tr}\boldsymbol{\sigma})\,\boldsymbol{I}$, with $\boldsymbol{I}$ the identity tensor, is the stress deviator, and

$$\sigma_y = \sigma_y(\bar{\varepsilon}^p) \tag{5.103}$$

is the stress-like variable associated with isotropic hardening. In the present case (isotropic *strain* hardening), σ_y is an experimentally determined function of the equivalent plastic strain, $\bar{\varepsilon}^p$, whose evolution is defined by the rate equation:

$$\dot{\bar{\varepsilon}}^p = \sqrt{\tfrac{2}{3}}\,\|\dot{\boldsymbol{\varepsilon}}^p\|\,. \tag{5.104}$$

5. An evolution law for the damage internal variable, governed by the relation (5.59), rewritten here

$$\dot{D} = \begin{cases} 0 & \text{if } \bar{\varepsilon}^{\mathrm{p}} \leq \bar{\varepsilon}^{\mathrm{p}}_D \\ \dfrac{\dot{\gamma}}{1-D}\left(\dfrac{-Y}{r}\right)^s & \text{if } \bar{\varepsilon}^{\mathrm{p}} > \bar{\varepsilon}^{\mathrm{p}}_D\,, \end{cases} \tag{5.105}$$

where r, s and $\bar{\varepsilon}^{\mathrm{p}}_D$ are material constants. The quantity, Y is the damage energy release rate [see Equation (5.60)], given by

$$\begin{aligned} Y \;=\; & \frac{-1}{2E(1-D)^2}\left[(1+\nu)\,\boldsymbol{\sigma}_+ : \boldsymbol{\sigma}_+ - \nu\,\langle \mathrm{tr}\,\boldsymbol{\sigma}\rangle^2\right] \\ & - \frac{h}{2E(1-hD)^2}\left[(1+\nu)\,\boldsymbol{\sigma}_- : \boldsymbol{\sigma}_- - \nu\,\langle -\mathrm{tr}\,\boldsymbol{\sigma}\rangle^2\right]\,. \end{aligned} \tag{5.106}$$

The viscoplasticity power law coupled with damage The viscoplasticity model is completely characterised with the definition of a constitutive law for $\dot{\gamma}$. Several possibilities exist in the definition of $\dot{\gamma}$. In the present thesis our attention will be focussed on the power-type law discussed by Perić (1993), which is here coupled with damage:

$$\dot{\gamma} = \begin{cases} \dfrac{1}{\mu}\left[\left(\dfrac{q}{(1-D)\,\sigma_y}\right)^{1/\epsilon} - 1\right] & \text{if} \quad \Phi(\boldsymbol{\sigma}, R, D) > 0 \\ 0 & \text{if} \quad \Phi(\boldsymbol{\sigma}, R, D) \leq 0\,, \end{cases} \tag{5.107}$$

where the strictly positive material constants μ and ϵ are, respectively, the *viscosity* and *rate-sensitivity* parameters. According to the above law, the function Φ defines an *elastic domain*, i.e., a region of stress space where the material behaves as purely elastic with no plastic flow ($\dot{\gamma} = 0 \Rightarrow \dot{\boldsymbol{\varepsilon}}^p = 0$).

Remark 5.12 *One important aspect of the visco-plastic model defined by (5.99)–(5.107) is that the standard rate-independent von Mises elasto-plastic model is rigorously recovered as a limiting case [refer to Perić (1993)] when $\mu \longrightarrow 0$ (no viscosity) and/or $\epsilon \longrightarrow 0$ (no rate-sensitivity). At such limits, $\sigma_{yp}(\bar{\varepsilon}^p)$ is identified with the usual hardening curve obtained from uniaxial tensile experiments for the rate-independent von Mises model.*

5.5.2 Integration algorithm

In this section the derivation of an integration algorithm for the elasto-visco-plastic damage constitutive model, described in the previous section is carried out in detail. Operator split algorithms are particularly suitable for numerical integration of constitutive equations and are widely used in the context of elasto-plasticity and also elasto-viscoplasticity (Simo & Taylor, 1985; Ortiz & Simo, 1986; Simo & Govindjee, 1991; Perić, 1993; Crisfield, 1997).

Let us consider a typical time step over the time interval $[t_n, t_{n+1}]$, where the time and strain increments are defined in the usual way as

$$\Delta t = t_{n+1} + t_n, \qquad \Delta \boldsymbol{\varepsilon} \equiv \boldsymbol{\varepsilon}_{n+1} - \boldsymbol{\varepsilon}_n \,. \tag{5.108}$$

In addition all variables of the problem, given by the set $\{\boldsymbol{\sigma}_n, \boldsymbol{\varepsilon}^e_n, \boldsymbol{\varepsilon}^p_n, \bar{\varepsilon}^p_n, D_n\}$, are assumed to be known at t_n. The operator split algorithm should obtain the updated set $\{\boldsymbol{\sigma}_{n+1}, \boldsymbol{\varepsilon}^e_{n+1}, \boldsymbol{\varepsilon}^p_{n+1}, \bar{\varepsilon}^p_{n+1}, D_{n+1}\}$ of variables at t_{n+1} consistently with the evolution equations of the model. The algorithm comprises the standard *elastic predictor* and the *visco-plastic return mapping* which, for the present model, has the following format.

Elastic predictor

The material is assumed to behave purely elastically within the time interval $[t_n, t_{n+1}]$. An *elastic trial* state is then obtained as:

$$\begin{aligned} \boldsymbol{\varepsilon}^{e\ \mathrm{trial}} &= \boldsymbol{\varepsilon}^e_n + \Delta\boldsymbol{\varepsilon}\,, & \boldsymbol{\varepsilon}^{p\ \mathrm{trial}} &= \boldsymbol{\varepsilon}^p_n\,, \\ \boldsymbol{\sigma}^{\mathrm{trial}} &= \mathbf{D} : \boldsymbol{\varepsilon}^{e\ \mathrm{trial}}\,, & \bar{\varepsilon}^{p\ \mathrm{trial}} &= \bar{\varepsilon}^p_n\,, \\ \sigma_y^{\mathrm{trial}} &= \sigma_{y\,n}\,, & D^{\mathrm{trial}} &= D_n\,. \end{aligned} \tag{5.109}$$

If $\Phi^{\mathrm{trial}} \leq 0$, then the process is indeed elastic within the interval and no viscoplastic flow takes place within the considered time step. In this case, the variables at t_{n+1} are assigned the values of the trial variables. Otherwise, we apply the viscoplastic corrector algorithm described in the following.

Visco-plastic corrector (or return mapping algorithm)

At this stage, we solve the evolution equations of the model with the elastic trial state as the initial condition. With the adoption of a backward Euler discretisation, the viscoplastic corrector is given by the following set of algebraic equations:

$$
\begin{aligned}
&\boldsymbol{\sigma}_{n+1} = \boldsymbol{\sigma}^{\text{trial}} - \Delta\gamma \; \mathsf{D} : \left.\frac{\partial \Phi}{\partial \boldsymbol{\sigma}}\right|_{n+1} \\
&\bar{\varepsilon}^{p}_{n+1} = \bar{\varepsilon}^{p}_{n} + \Delta\gamma \\
&D_{n+1} = \begin{cases} 0 & \text{if } \bar{\varepsilon}^{\mathrm{p}}_{n+1} \leq \bar{\varepsilon}^{\mathrm{p}}_{D} \\ D_n + \frac{\Delta\gamma}{1-D_{n+1}} \left(\frac{-Y_{n+1}}{r}\right)^{s} & \text{if } \bar{\varepsilon}^{\mathrm{p}}_{n+1} > \bar{\varepsilon}^{\mathrm{p}}_{D}\,, \end{cases}
\end{aligned}
\tag{5.110}
$$

where the *incremental multiplier*, $\Delta\gamma$, is given by:

$$
\Delta\gamma = \frac{\Delta t}{\mu} \left\{ \left[\frac{q(\boldsymbol{\sigma}_{n+1})}{(1 - D_{n+1})\, \sigma_y(R_{n+1})} \right]^{1/\epsilon} - 1 \right\}, \tag{5.111}
$$

with Δt denoting the time increment within the considered interval. After solving (5.110), we can update:

$$
\boldsymbol{\varepsilon}^{p}_{n+1} = \boldsymbol{\varepsilon}^{p}_{n} + \Delta\gamma \left.\frac{\partial \Phi}{\partial \boldsymbol{\sigma}}\right|_{n+1} \qquad \boldsymbol{\varepsilon}^{e}_{n+1} = \boldsymbol{\varepsilon}^{e\ \text{trial}} - \Delta\gamma \left.\frac{\partial \Phi}{\partial \boldsymbol{\sigma}}\right|_{n+1}. \tag{5.112}
$$

The visco-plastic corrector can be more efficiently implemented by reducing (5.110) to a *single* non-linear equation for the incremental multiplier $\Delta\gamma$.

Single-equation corrector The situation here is completely analogous to that of the elasto-plastic damage (rate-independent) model described in Section 5.4.2 (page 88). For the sake of completeness, the main steps leading to the system reduction are repeated here. Firstly, we observe that the plastic flow vector:

$$
\frac{\partial \Phi}{\partial \boldsymbol{\sigma}} = \sqrt{\tfrac{3}{2}}\, \frac{\boldsymbol{s}}{\|\boldsymbol{s}\|} \tag{5.113}
$$

is deviatoric. The stress update equation $(5.110)_1$ can then be split as:

$$
\begin{aligned}
&\boldsymbol{s}_{n+1} = \boldsymbol{s}^{\text{trial}} - \Delta\gamma \; 2G \sqrt{\tfrac{3}{2}}\, \tfrac{\boldsymbol{s}_{n+1}}{\|\boldsymbol{s}_{n+1}\|} \\
&p_{n+1} = p^{\text{trial}}\,,
\end{aligned}
\tag{5.114}
$$

where p denotes the hydrostatic pressure and G is the shear modulus. Further, simple inspection of $(5.114)_1$ shows that $\boldsymbol{s}_{n+1}$ is a scalar multiple of $\boldsymbol{s}^{\text{trial}}$ so that, trivially, we have the identity:

$$
\frac{\boldsymbol{s}_{n+1}}{\|\boldsymbol{s}_{n+1}\|} = \frac{\boldsymbol{s}^{\text{trial}}}{\|\boldsymbol{s}^{\text{trial}}\|}\,, \tag{5.115}
$$

which allows us to re-write $(5.114)_1$ as:

$$\boldsymbol{s}_{n+1} = \left(1 - \sqrt{\tfrac{3}{2}}\,\frac{\Delta\gamma\; 2G}{\|\boldsymbol{s}^{\text{trial}}\|}\right)\boldsymbol{s}^{\text{trial}} = \left(1 - \frac{\Delta\gamma\; 3G}{q^{\text{trial}}}\right)\boldsymbol{s}^{\text{trial}} \tag{5.116}$$

where q^{trial} is the elastic trial von Mises equivalent stress:

$$q^{\text{trial}} = q(\boldsymbol{s}^{\text{trial}}) = \sqrt{\tfrac{3}{2}}\,\|\boldsymbol{s}^{\text{trial}}\|\,. \tag{5.117}$$

Equation (5.116) results in the following update formula for q:

$$q_{n+1} = q^{\text{trial}} - 3G\,\Delta\gamma\,. \tag{5.118}$$

With the substitution of the above formula together with $(5.110)_2$ into (5.111) we obtain the following scalar algebraic equation for the incremental multiplier, $\Delta\gamma$:

$$\Delta\gamma - \frac{\Delta t}{\mu}\left\{\left[\frac{q^{\text{trial}} - 3G\,\Delta\gamma}{(1-D_{n+1})\,\sigma_y(R_{n+1})}\right]^{1/\epsilon} - 1\right\} = 0\,, \tag{5.119}$$

or, equivalently, after a straightforward rearrangement,

$$D_{n+1} = D(\Delta\gamma) \equiv 1 - \frac{\sqrt{\frac{3}{2}}\,\|\boldsymbol{s}^{\text{trial}}\| - 3G\,\Delta\gamma}{\sigma_{y_0} + R(\bar{\varepsilon}^{\text{p}}_n + \Delta\gamma)}\left(\frac{\Delta t}{\mu\,\Delta\gamma + \Delta t}\right)^{\epsilon}, \tag{5.120}$$

which expresses D_{n+1} as an explicit function of $\Delta\gamma$. Finally, by introducing the damage explicit function (5.120) into the discretised damage evolution equation $(5.110)_3$, the viscoplastic corrector is reduced to the solution of a *single* algebraic equation for the incremental multiplier, $\Delta\gamma$:

$$G(\Delta\gamma) \equiv \begin{cases} D(\Delta\gamma) = 0 & \text{if } \bar{\varepsilon}^{\text{p}}_{n+1} \le \bar{\varepsilon}^{\text{p}}_D \\[2ex] D(\Delta\gamma) - D_n - \frac{\Delta\gamma}{1-D(\Delta\gamma)}\left(\frac{-Y(\Delta\gamma)}{r}\right)^{s} = 0 & \text{if } \bar{\varepsilon}^{\text{p}}_{n+1} > \bar{\varepsilon}^{\text{p}}_D\,. \end{cases} \tag{5.121}$$

The single-equation viscoplastic corrector comprises the solution of the above equation for $\Delta\gamma$, followed by the straightforward update of the relevant variables:

$$\begin{aligned}
&\boldsymbol{s}_{n+1} = \left(1 - \tfrac{\Delta\gamma\; 3G}{q^{\text{trial}}}\right)\boldsymbol{s}^{\text{trial}}\,, \qquad p_{n+1} = p^{\text{trial}}\,,\\
&\boldsymbol{\sigma}_{n+1} = \boldsymbol{s}_{n+1} + p_{n+1}\,\boldsymbol{I}\,,\\
&\boldsymbol{\varepsilon}^{\text{e}}_{n+1} = [\mathsf{D}^e]^{-1} : \boldsymbol{\sigma}_{n+1} = \tfrac{1}{2G}\,\boldsymbol{s}_{n+1} + \tfrac{1}{3K}\,p_{n+1}\,\boldsymbol{I}\,,\\
&\bar{\varepsilon}^{\text{p}}_{n+1} = \bar{\varepsilon}^{\text{p}}_n + \Delta\gamma\,,\\
&D_{n+1} = 1 - \tfrac{\sqrt{\frac{3}{2}}\,\|\boldsymbol{s}^{\text{trial}}\| - 3G\,\Delta\gamma}{\sigma_{y_0} + R(\bar{\varepsilon}^{\text{p}}_n + \Delta\gamma)}\left(\tfrac{\Delta t}{\mu\,\Delta\gamma + \Delta t}\right)^{\epsilon}\,.
\end{aligned} \tag{5.122}$$

Box 5.5: Elastic predictor/visco-plastic return mapping integration algorithm for the elasto-viscoplastic damage model with crack closure effect (over time interval $[t_n, t_{n+1}]$).

(i) *Elastic predictor*. Given $\Delta\boldsymbol{\varepsilon}$, Δt and the state variables at t_n, compute the *elastic trial state*:

$$\begin{aligned}
&\boldsymbol{\varepsilon}^{\mathrm{e\,trial}} = \boldsymbol{\varepsilon}^{\mathrm{e}}_n + \Delta\boldsymbol{\varepsilon}; \quad && \boldsymbol{e}^{\mathrm{trial}} = \mathrm{dev}[\boldsymbol{\varepsilon}^{\mathrm{e\,trial}}]; \quad v^{\mathrm{trial}} = \mathrm{tr}[\boldsymbol{\varepsilon}^{\mathrm{e\,trial}}] \\
&\bar{\varepsilon}^{\mathrm{p\,trial}} = \bar{\varepsilon}^{\mathrm{p}}_n; && D^{\mathrm{trial}} = D_n \\
&\boldsymbol{s}^{\mathrm{trial}} = 2G\,\boldsymbol{e}^{\mathrm{trial}}; && p^{\mathrm{trial}} = K\,v^{\mathrm{trial}} \\
&q^{\mathrm{trial}} = \sqrt{\tfrac{3}{2}}\,\|\boldsymbol{s}^{\mathrm{trial}}\|,
\end{aligned}$$

(ii) Check for viscoplastic flow. First compute:

$$\Phi^{\mathrm{trial}} = q^{\mathrm{trial}} - (1 - D_n)\left[\sigma_{y_0} + R(\bar{\varepsilon}^{\mathrm{p}}_n)\right],$$

IF $\Phi^{\mathrm{trial}} \leq \varepsilon_{\mathrm{tol}}$ THEN (elastic step)
    Update $(\cdot)_{n+1} = (\cdot)^{\mathrm{trial}}$ and EXIT
ELSE GOTO (iii)

(iii) *Visco-plastic corrector*. Solve the return mapping equation

$$G(\Delta\gamma) \equiv \begin{cases} D(\Delta\gamma) = 0 & \text{if } \bar{\varepsilon}^{\mathrm{p}}_{n+1} \leq \bar{\varepsilon}^{\mathrm{p}}_D \\ D(\Delta\gamma) - D_n - \frac{\Delta\gamma}{1 - D(\Delta\gamma)}\left(\frac{-Y(\Delta\gamma)}{r}\right)^s = 0 & \text{if } \bar{\varepsilon}^{\mathrm{p}}_{n+1} > \bar{\varepsilon}^{\mathrm{p}}_D \end{cases}$$

with $D(\Delta\gamma)$ defined by (5.120) and $Y(\Delta\gamma)$ defined through (5.60), (5.120) (5.81) and (5.82).

(iv) *Update the variables*:

$$\begin{aligned}
&\boldsymbol{s}_{n+1} = \left(1 - \frac{\Delta\gamma\,3G}{q^{\mathrm{trial}}}\right)\boldsymbol{s}^{\mathrm{trial}}; \quad && p_{n+1} = p^{\mathrm{trial}}; \\
&\boldsymbol{\sigma}_{n+1} = \boldsymbol{s}_{n+1} + p_{n+1}\,\boldsymbol{I}; && \bar{\varepsilon}^{\mathrm{p}}_{n+1} = \bar{\varepsilon}^{\mathrm{p}}_n + \Delta\gamma; \\
&\boldsymbol{\varepsilon}^{\mathrm{e}}_{n+1} = \frac{1}{2G}\,\boldsymbol{s}_{n+1} + \frac{1}{3K}\,p_{n+1}\,\boldsymbol{I}; && D_{n+1} = D(\Delta\gamma).
\end{aligned}$$

(v) EXIT

The solution of the equation for $\Delta\gamma$ is, as usual, undertaken by the Newton-Raphson iterative scheme. The overall algorithm for the numerical integration of the elasto-viscoplastic damage model, which includes the effect of crack closure, is summarised in Box 5.5 in pseudo-code format.

Remark 5.13 (rate-independent limit) *Note that, as one should expect, equation (5.121) rigorously recovers its elasto-plastic damage (rate-independent) counterpart (5.80) [refer to page 90] when* $\mu \to 0$ *(no viscosity),* $\epsilon \to 0$ *(no rate-sensitivity) or* $\Delta t \to \infty$ *(infinitely slow straining). Obviously, in such cases, the algorithm of Box 5.5 reproduces the rate-independent elastoplastic numerical solution.*

Remark 5.14 (computational implementation aspects) *In the computer implementation of the model (as shown in Box 5.5), it is important to specify the damage function* $D(\Delta\gamma)$*, as expressed in equation (5.120). The reason for this lies in the fact that, for low rate-sensitivity, i.e., small values of* ϵ*, the Newton-Raphson scheme for solution of (5.119) becomes unstable as its convergence bowl is sharply reduced with decreasing* ϵ*. The reduction of the convergence bowl stems from the fact that large exponents* $1/\epsilon$ *can easily produce numbers which are computationally intractable. This fact has been recognised by Perić* et al. *(1993) in the context of a more general visco-plastic algorithm. In equation (5.120), on the other hand, the term to the power* ϵ *on the left hand side can only assume values within the interval* $[0, 1]$ *and causes no numerical problems within practical ranges of material constants.*

Iso-error maps

To illustrate the accuracy of the above integration algorithm in practical situations, this section presents some isoerror maps, produced with material constants covering a range of high rate-sensitivity to rate-independency. The maps have been generated in the standard fashion as described in Section 5.4.2 [refer to Figure 5.3, page 93]. Using the three-dimensional implementation of the model, we start from a stress point at time t_n, with $\boldsymbol{\sigma}_n$ lying on the yield surface, and apply a sequence of strain increments, corresponding to linear combinations of trial stress increments in the direction normal and tangential [directions of the unit tensors $\boldsymbol{N}$ and $\boldsymbol{T}$ of Figure 5.3, respectively] to the von Mises circle in the deviatoric plane.

The material properties adopted for the present analysis are exactly the same as the rate-independent case and are listed in Table 5.1 [page 94]. To preserve the constant rate of total strain $\Delta\boldsymbol{\varepsilon}/\Delta t$ for the iso-error map under consideration, the time increment Δt is appropriately scaled. Figure 5.12 shows iso-error maps obtained at low and high strain rates with the non-dimensional rate

$$\mu \, \|\dot{\boldsymbol{\varepsilon}}\|$$

set respectively to 1 and 1000. For each non-dimensional rate, three values of rate-sensitivity parameter,ϵ, have been used: 10^0, 10^{-1} and 0. For $\epsilon = 0$

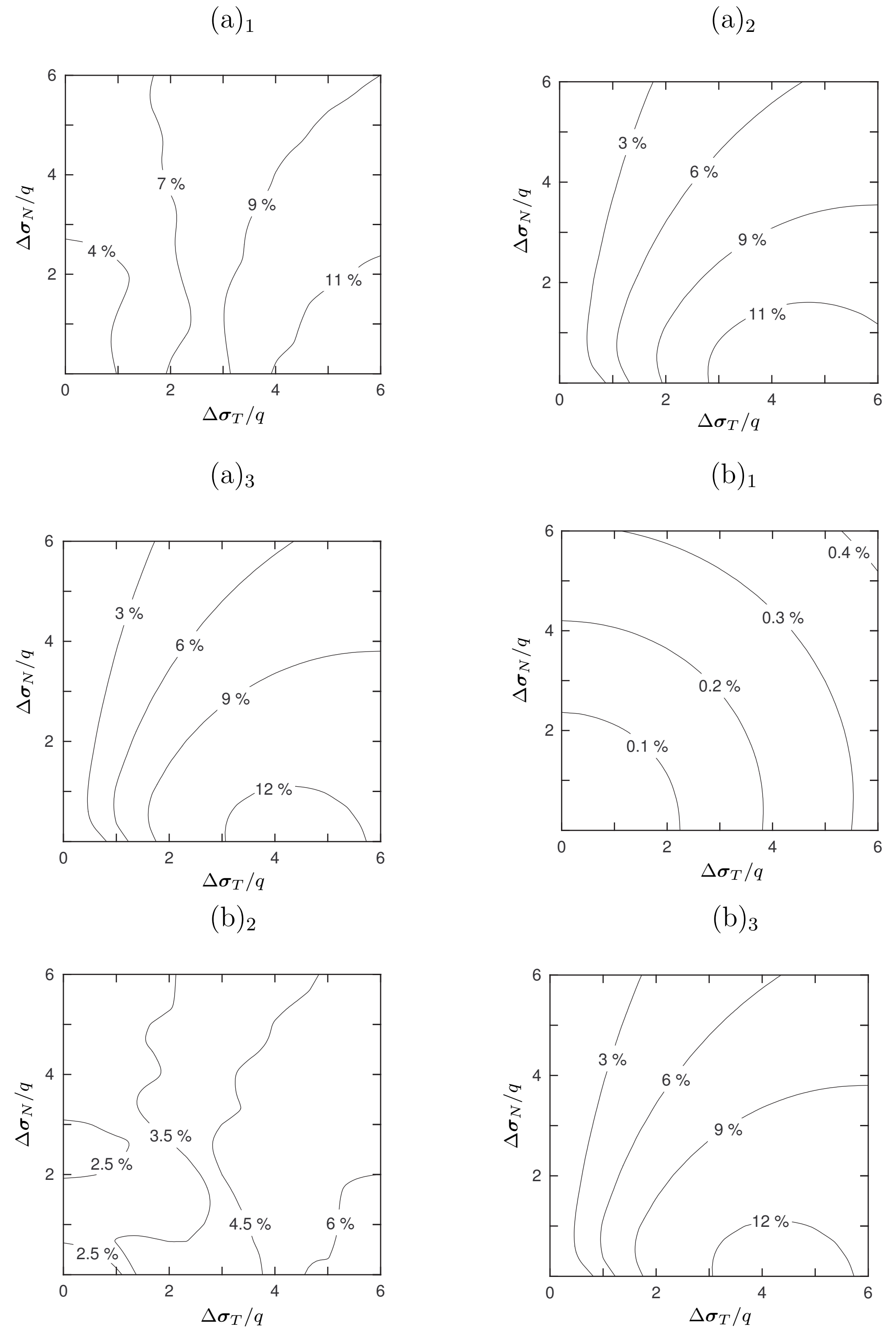

(a)$_1$ (a)$_2$ (a)$_3$ (b)$_1$ (b)$_2$ (b)$_3$

Figure 5.12: Iso-error maps for $D = 0\%$ and $\bar{\varepsilon}^{\mathrm{p}} = 0$: (a)$_1$ $\mu\,\|\dot{\boldsymbol{\varepsilon}}\| = 1$, $\epsilon = 10^0$; (a)$_2$ $\mu\,\|\dot{\boldsymbol{\varepsilon}}\| = 1$, $\epsilon = 10^{-1}$; (a)$_3$ $\mu\,\|\dot{\boldsymbol{\varepsilon}}\| = 1$, $\epsilon = 0$; (b)$_1$ $\mu\,\|\dot{\boldsymbol{\varepsilon}}\| = 10^3$, $\epsilon = 10^0$; (b)$_2$ $\mu\,\|\dot{\boldsymbol{\varepsilon}}\| = 10^3$, $\epsilon = 10^{-1}$ and (b)$_3$ $\mu\,\|\dot{\boldsymbol{\varepsilon}}\| = 10^3$, $\epsilon = 0$.

virtually identical maps are obtained for the two rates [see Figure 5.12 (a)$_3$ and 5.12 (b)$_3$] and the algorithm recovers the rate-independent solution depicted in Figure 5.4 (a). In Figure 5.13 the error map of the algorithm is depicted at a different stage of damage evolution.

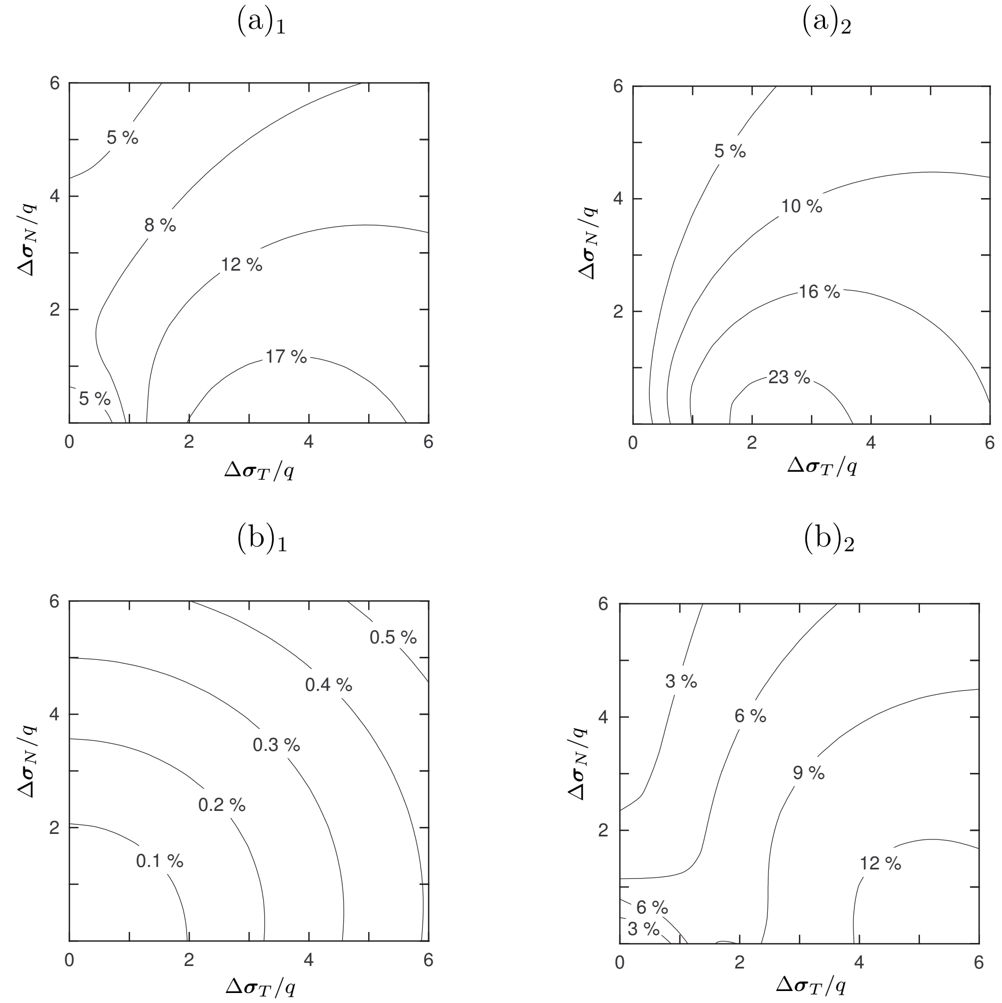

Figure 5.13: Iso-error maps for $D = 15\%$ and $\bar{\varepsilon}^{\mathrm{p}} = 0.348$: (a)$_1$ $\mu\,\|\dot{\boldsymbol{\varepsilon}}\| = 1$, $\epsilon = 10^0$; (a)$_2$ $\mu\,\|\dot{\boldsymbol{\varepsilon}}\| = 1$, $\epsilon = 10^{-1}$; (b)$_1$ $\mu\,\|\dot{\boldsymbol{\varepsilon}}\| = 10^3$, $\epsilon = 10^0$; and (b)$_2$ $\mu\,\|\dot{\boldsymbol{\varepsilon}}\| = 10^3$, $\epsilon = 10^{-1}$.

Again, the iso-error maps are obtained at low and high strain rates with the non-dimensional rate, $\mu\,\|\dot{\boldsymbol{\varepsilon}}\|$, set respectively to 1 and 1000. For each non-dimensional rate, two values of rate-sensitivity parameter, ϵ, have been used: 10^0 and 10^{-1}. Once more for $\epsilon = 0$, the algorithm reproduces the rate-independent solution shown in Figure 5.4 (b). By comparing Figures 5.12 and 5.13, the dependency of the algorithm accuracy on the state of internal damage is made clear. The more damaged the material is, the more restricted an increment of trial stress must be to maintain the integration error within a prescribed limit. In other words, the accuracy of the algorithm deteriorates as damage increases. It is also possible to conclude that, in general, increasing (decreasing) rate-sensitivity and/or increasing (decreasing) strain rates tend to produce decreasing (increasing) integration errors. The largest errors are expected in the rate-independent limit.

5.5.3 Consistent tangent operator

To obtain the consistent tangent operator for the case of a strain-driven problem, all variables of the problem are considered as functions of the strain $\boldsymbol{\varepsilon}$. The exact linearization of the algorithm described in Box 5.5 is performed by a systematic application of the concept of directional derivative.

In the elastic case, the *elastic consistent tangent* at t_{n+1}, is simply the standard elasticity operator

$$\hat{\mathsf{D}} = \mathsf{D}^e = 2G\left[\mathsf{I} - \tfrac{1}{3}\boldsymbol{I}\otimes\boldsymbol{I}\right] + K\,\boldsymbol{I}\otimes\boldsymbol{I} \tag{5.123}$$

where I, is the fourth order identity tensor.

In the elasto-viscoplastic damage case, i.e., when it is assumed that viscoplastic flow occurs within the step, the tangent operator is called the *elasto-viscoplastic damage consistent tangent* and is denoted by $\hat{\mathsf{D}}^{vp}$. For the present model it is possible to obtain a closed form expression for the tangent operator. The details of derivation, which is rather lengthy, will be omitted here and we shall limit ourselves to show only its final expression which is given by:

$$\mathsf{D}^{vp} = a_1\left[\mathsf{I} - \tfrac{1}{3}\boldsymbol{I}\otimes\boldsymbol{I}\right] + a_2\,\bar{\boldsymbol{s}}_{n+1}\otimes\bar{\boldsymbol{s}}_{n+1} + a_3\,\bar{\boldsymbol{s}}_{n+1}\otimes\boldsymbol{I} + K\,\boldsymbol{I}\otimes\boldsymbol{I}\,, \tag{5.124}$$

where $\bar{\boldsymbol{s}}_{n+1}$ is the normalised stress deviator:

$$\bar{\boldsymbol{s}}_{n+1} = \frac{\boldsymbol{s}_{n+1}}{\|\boldsymbol{s}_{n+1}\|}\,, \tag{5.125}$$

and the scalars a_1, a_2, a_3, are given by:

$$\begin{aligned} a_1 &= 2G\left(1 - \tfrac{\Delta\gamma\,3G}{q^{\text{trial}}}\right) \\ a_2 &= 6G^2\left[\tfrac{\Delta\gamma}{q^{\text{trial}}} + \tfrac{\partial G}{\partial\left(q^{\text{trial}}\right)}\Big/\tfrac{\partial G}{\partial\left(\Delta\gamma\right)}\right] \\ a_3 &= 2G\sqrt{\tfrac{2}{3}}\,K\left[\tfrac{\partial G}{\partial\left(p^{\text{trial}}\right)}\Big/\tfrac{\partial G}{\partial\left(\Delta\gamma\right)}\right]. \end{aligned} \tag{5.126}$$

In the definition of constants a_2 and a_3, the scalars $\partial G/\partial\left(\Delta\gamma\right)$, $\partial G/\partial\left(q^{\text{trial}}\right)$ and $\partial G/\partial\left(p^{\text{trial}}\right)$, correspond to the derivatives of the return mapping residual function defined by (5.121):

$$\begin{aligned}
\frac{\partial G}{\partial\,(\Delta\gamma)} &= \frac{\partial D}{\partial\,(\Delta\gamma)} + \frac{1}{1-D_{n+1}}\left(-\frac{Y_{n+1}}{r}\right)^{s} \\
&\qquad\qquad \left\{\left[-\frac{\partial D}{\partial\,(\Delta\gamma)}\Big/(1-D_{n+1}) - s\,\frac{\partial Y}{\partial\,(\Delta\gamma)}\Big/Y_{n+1}\right]\Delta\gamma - 1\right\} \\
\frac{\partial G}{\partial\,(q^{\mathrm{trial}})} &= \frac{\partial D}{\partial\,(q^{\mathrm{trial}})} - \Delta\gamma\frac{\partial D}{\partial\,(q^{\mathrm{trial}})}\Big/(1-D_{n+1})^{2}\left(-\frac{Y_{n+1}}{r}\right)^{s} \\
&\qquad\qquad - \frac{s\,\Delta\gamma}{r\,(1-D_{n+1})}\left(-\frac{Y_{n+1}}{r}\right)^{s-1}\frac{\partial Y}{\partial\,(q^{\mathrm{trial}})} \\
\frac{\partial G}{\partial\,(p^{\mathrm{trial}})} &= \frac{s\,\Delta\gamma}{r\,(1-D_{n+1})}\left(-\frac{Y_{n+1}}{r}\right)^{s}\frac{\partial Y}{\partial\,(p^{\mathrm{trial}})}.
\end{aligned} \tag{5.127}$$

where the scalars $\partial Y/\partial\,(\Delta\gamma)$, $\partial Y/\partial\,(q^{\mathrm{trial}})$ and $\partial Y/\partial\,(p^{\mathrm{trial}})$, represent the derivatives of the energy release rate function already outlined in expressions (5.94) and also (5.95).

Finally, the scalars $\partial D/\partial\,(\Delta\gamma)$ and $\partial D/\partial\,(q^{\mathrm{trial}})$, which are the outcome of the derivation of the damage function (5.120) are defined by

$$\begin{aligned}
\frac{\partial D}{\partial\,(\Delta\gamma)} &= \left(\frac{\Delta t}{\mu\,\Delta\gamma+\Delta t}\right)^{\epsilon}\left[\frac{3G}{\sigma_y(R_{n+1})} + \frac{H(q^{\mathrm{trial}}-3G\Delta\gamma)}{\sigma_y(R_{n+1})^{2}} + \frac{\mu\epsilon}{\mu\,\Delta\gamma+\Delta t}\left(\frac{q^{\mathrm{trial}}-3G\Delta\gamma}{\sigma_y(R_{n+1})}\right)\right] \\
\frac{\partial D}{\partial\,(q^{\mathrm{trial}})} &= -\frac{1}{\sigma_y(R_{n+1})}\left(\frac{\Delta t}{\mu\,\Delta\gamma+\Delta t}\right)^{\epsilon}
\end{aligned} \tag{5.128}$$

In the above, H denotes the derivative of the hardening function evaluated at R_{n+1}.

5.6 Concluding remarks

The prediction of damage growth and fracture initiation in finitely deforming ductile solids has been addressed in this chapter. With the coupling between damaging and material behaviour accounted for within the framework of *Continuum Damage Mechanics*, the material presented is of particular relevance to the simulation of industrial forming operations characterised by the presence of extreme deformations and strains, often resulting in localised material deterioration and possible fracture nucleation and growth.

In particular, the need for consideration of micro-crack closure effects in the damage evolution was specially emphasised. The introduction of the coupled constitutive equations did not affect appreciably the performance of the models, enabling the efficient simulation of the effects of material deterioration in large scale computations. This was due to the fact that the return mapping integration algorithm was reduced to a non-linear *single equation*. A closed formula for the tangent operator consistent with the integration algorithm has also been presented. The formula is useful for those seeking ductile damage simulation within an implicit finite element framework.

An assessment of the accuracy and stability of the elastic predictor-plastic corrector algorithm for integration of the constitutive equations has been carried out relying on the analysis of iso-error maps. Numerical simulations have illustrated the performance the algorithms in the presence of combined tensile/compressive stress states, which may have important consequences in failure analysis of metal forming processes. Finally, it is remarked that the extension to the finite strain range can be promptly obtained by means of the framework described in Chapter 4.

CHAPTER 6

FINITE ELEMENT TECHNOLOGY FOR FINITE NEARLY ISOCHORIC DEFORMATION

ONE of the most challenging tasks in finite element research is the development of low order elements for the solution of solid mechanics problems involving nearly-incompressible materials. As the incompressible limit is approached, elements with low order shape functions are known to perform poorly, showing the typical *volumetric locking* behaviour which, in many circumstances, completely invalidates the finite element solution. Problems of practical engineering interest for which incompressibility plays a crucial role include the analysis of rubbery solids, typically modelled as incompressible hyperelastic materials, as well as elastoplastic simulations under plastic dominant deformations and the assumption of isochoric plastic flow, such as in metal plasticity models. In such situations, spurious *locking*, i.e., overstiff solutions, frequently occur as a consequence of the inability of low order interpolation polynomials to adequately represent general volume preserving displacement fields. The problem can be remedied by simply adopting elements of sufficiently high order.

However, low order elements are often preferred due to their inherent simplicity. This is particularly true in large scale simulations where a number of complex interacting phenomena, such as frictional contact, high strains and progressive material fracturing, may be present. In many cases, the computational treatment of the problem, which may require the incorporation of adaptive mesh refinement techniques, is far simpler when lower order elements are adopted.

The present chapter is concerned with special finite element techniques for the analysis of large deformations of nearly incompressible solids. The material presented here is divided into five sections. In Section 6.1 a brief review of the numerical treatment of incompressibility for low order elements is presented. The description of the so-called *F-bar* methodology for finite strain analysis of nearly incompressible solids, is undertaken in Section 6.2. The next section of this chapter, Section 6.3, presents an assessment of the performance of formulations based on the volumetric nodal averaging concept proposed by Bonet & Burton (1998) in the context of explicit dynamics. In Section 6.4 we introduce a new methodology which extends the so-called *F-bar* procedure (de Souza Neto *et al.* , 1996) so as to accommodate the use of two- and three-dimensional simplex finite elements. The computational implementation of the new simplex finite elements within an implicit quasi-static and explicit dynamic finite element environment is described in detail.

6.1 Introduction

In order to allow the use of low order elements near the incompressible limit under finite strains, different approaches have been proposed in the computational literature. Within the context of the geometrically linear theory, the class of assumed enhanced strain *(EAS)* methods described by Simo & Rifai (1990), which incorporates popular procedures such as the classical incompatible modes formulation (Taylor *et al.* , 1976) and B-bar methods (Hughes, 1980), is well established and is employed with success in a number of existing commercial finite element codes.

Under infinitesimal kinematics, the use of *underintegrated* standard finite elements can provide simple and satisfactory solutions near the incompressible limit. In the geometrically non-linear regime, however, the enforcement of incompressibility is substantially more demanding and the development of robust and efficient low order finite elements is by no means trivial. To tackle such a problem, different approaches have been proposed in the computational literature. Among others, the class of mixed variational methods developed by Simo *et al.* (1985), the mixed *u/p* formulation proposed by Sussman & Bathe (1987), the geometrically non-linear extension of the B-bar methodology adopted by Moran *et al.* (1990), the family of enhanced elements of Simo & Armero (1992), the co-rotational incompatible modes of Crisfield & Moita (1996) and the geometrically non-linear selective reduced integration scheme of Doll *et al.* (2000) are possible alternatives.

Such formulations have produced families of elements for finite near- incompressibility whose lowest order members are the bi-linear (4-noded) quadrilateral in 2-D and the tri-linear (8-noded) hexahedron in 3-D. In some situations, however, the use of even lower order elements – the simplex (3-noded) triangle in 2-D and (4-noded) tetrahedron in 3-D – is far more desirable. A typical example is the three-dimensional analysis of bodies with complex geometry. The lack of robustness of currently available hexahedral mesh generators may impose severe limitations on the use of such elements in this context. The ideal alternative then would be the development of simplex elements with added special techniques to handle finite nearly isochoric deformations. Some methods to adapt simplex elements to this class of problems have been recently proposed. Among others, the elements proposed by Zienkiewicz *et al.* (1998), Bonet & Burton (1998) and Bonet *et al.* (2001) in the context of explicit dynamics and the mixed-enhanced 4-noded tetrahedron developed by Taylor (2000) for implicit computations are pertinent approaches.

One aspect that should be observed here is that, in addition to handling incompressibility, robust formulations should also be able to cope with the extra requirements that different problems may present. For instance, in applications such as the prediction of failure in metal forming processes, the ability to capture strain localisation phenomena becomes crucial; in problems involving extremely large strains, frequently encountered in the analysis of rubbery materials and metal forming simulations, it is not unusual that a solution can be obtained only if adaptive mesh refinement is employed. Thus, since a single formulation is normally not sufficiently robust to produce an optimal performance under a very wide range of conditions, the design of low order finite elements for large strain analysis of quasi-incompressible materials remains an open issue.

6.2 F-bar methodology

This section describes the development of a 4-node quadrilateral and a 8-node hexahedron for finite strain analysis of nearly incompressible solids. The elements, termed *F-bar* elements, are based on the concept of multiplicative isochoric/volumetric split in conjunction with the replacement of the compatible deformation gradient field with an assumed modified counterpart.

The basic idea behind the *F-bar* (De Souza Neto *et al.*, 1996) procedure is simple: an *F-bar* element is obtained from the corresponding standard (displacement-based) finite element by simply adopting a suitably modified deformation gradient in the computation of the stress tensor. To avoid incompressibility *locking*, the modified deformation gradient is constructed such that the incompressibility constraint can be enforced in an approximate average (not point-wise) sense throughout the element.

6.2.1 Stress computation

Consider an ordinary displacement-based 4-node quadrilateral and an 8-node hexahedron, with local coordinates denoted $\boldsymbol{\xi}$, as illustrated in Figure 6.1. Typically, the numerical integration of the element internal force vector requires the computation of the stresses at a prescribed number of gauss points and, for geometrically non-linear problems, the stresses are obtained from the deformation gradient by means of constitutive functionals. For elastic materials, the Cauchy stress is a given function of the current deformation gradient, $\boldsymbol{F}$ for Gauss point i (with coordinate $\boldsymbol{\xi}_i$, indicated in Figure 6.1) at t_{n+1}:

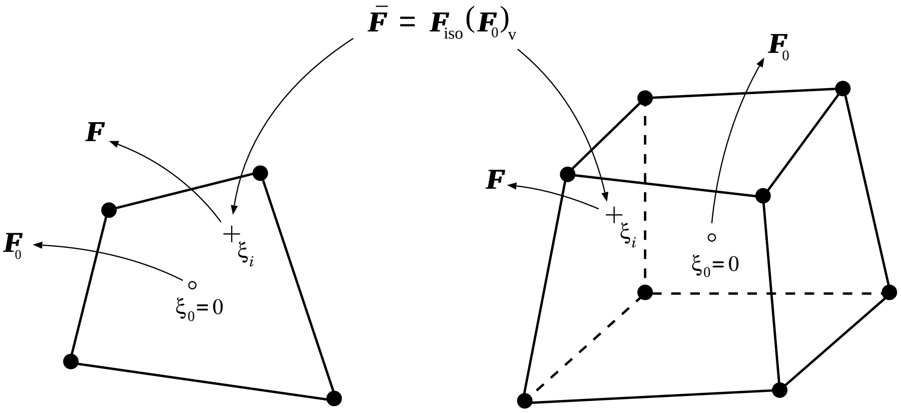

Figure 6.1: The *F-bar* 4-node quadrilateral and 8-node hexahedron.

$$\boldsymbol{\sigma} = \hat{\boldsymbol{\sigma}}(\boldsymbol{F}).$$

For inelastic materials, within the context of an incremental finite element procedure, the Cauchy stress is generally defined by an incremental constitutive function resulting from a suitable algorithm for numerical integration of the constitutive equations of the model. A typical example of such is the return mapping-based stress updating algorithm adopted in finite elasto-plasticity presented in Chapter 4. Within the typical time interval $[t_n, t_{n+1}]$, the stress $\boldsymbol{\sigma}$ at t_{n+1} is a function of the deformation gradient, $\boldsymbol{F}$, at t_{n+1} and the known set $\boldsymbol{\alpha}_n$ of internal state variables at t_n. This relation can be symbolically expressed as:

$$\boldsymbol{\sigma} = \hat{\boldsymbol{\sigma}}(\boldsymbol{F}, \boldsymbol{\alpha}_n), \tag{6.1}$$

where $\hat{\boldsymbol{\sigma}}$ here denotes the (generally implicit) incremental constitutive function defined by the underlying numerical integration algorithm. For conventional (or standard) finite elements, the deformation gradient $\boldsymbol{F}$ is computed directly from the standard interpolation (bi-linear for the quadrilateral and tri-linear for the hexahedron) of the displacement field at the integration point i.

The isochoric/volumetric split of the deformation gradient

Central to the developments presented below is the concept of multiplicative split of the deformation gradient, $\boldsymbol{F}$, into an isochoric (volume preserving) and a volumetric (purely dilatational) contribution. This concept has been introduced in Section 3.1.3 [page 24]. It has been exploited by many authors [Hughes *et al.* (1975), Simo *et al.* (1985), Moran *et al.* (1990) and Simo & Taylor (1991)] in the treatment of the incompressibility constraint in finite deformation problems. Essentially, $\boldsymbol{F}$ is split according to:

$$\boldsymbol{F} = \boldsymbol{F}_{\rm iso}\, \boldsymbol{F}_{\rm v}\,, \tag{6.2}$$

where

$$\boldsymbol{F}_{\rm iso} = (\det \boldsymbol{F})^{-1/3}\, \boldsymbol{F} \qquad \text{and} \qquad \boldsymbol{F}_{\rm v} = (\det \boldsymbol{F})^{1/3}\, \boldsymbol{I} \tag{6.3}$$

denote, respectively, the *isochoric* and *volumetric* components of $\boldsymbol{F}$.

6.2.2 The modified F-bar deformation gradient

The key idea of the *F-bar* method is to simply replace the conventional $\boldsymbol{F}$ with a modified counterpart, which we will denote $\bar{\boldsymbol{F}}$ (the *F-bar* deformation gradient), in (6.1) in order to circumvent the spurious volumetric *locking* exhibited by standard low order elements near the incompressible limit. To construct the *F-bar* deformation gradient the isochoric/volumetric split (6.3) is firstly applied to the conventional deformation gradient $\boldsymbol{F}$ at the Gauss point of interest as well as to the deformation gradient $\boldsymbol{F}_0$ that results from the conventional displacement interpolation at the *centroid* of the element, $\boldsymbol{\xi} = \boldsymbol{\xi}_0$ (Figure 6.1 illustrates the procedure for the 4-noded quadrilateral and 8-noded hexahedron):

$$\begin{aligned} \boldsymbol{F} &= \boldsymbol{F}_{\rm iso}\, \boldsymbol{F}_{\rm v}\,, \\ \boldsymbol{F}_0 &= (\boldsymbol{F}_0)_{\rm iso}\, (\boldsymbol{F}_0)_{\rm v}\,. \end{aligned} \tag{6.4}$$

The *F-bar* deformation gradient is then defined as the product of the isochoric component of $\boldsymbol{F}$ with the volumetric component of $\boldsymbol{F}_0$, i.e., we compute:

$$\bar{\boldsymbol{F}} = \boldsymbol{F}_{\rm iso}\, (\boldsymbol{F}_0)_{\rm v} = \left(\frac{\det \boldsymbol{F}_0}{\det \boldsymbol{F}} \right)^{1/3} \boldsymbol{F}\,. \tag{6.5}$$

Having defined the modified deformation gradient, the *F-bar* 4- and 8-noded elements are obtained by simply replacing $\boldsymbol{F}$ with $\bar{\boldsymbol{F}}$ in (6.1). That is, for the present elements, the Cauchy stress at each Gauss point is computed as:

$$\boldsymbol{\sigma}_{n+1} = \hat{\boldsymbol{\sigma}}(\boldsymbol{\alpha}_n, \bar{\boldsymbol{F}})\,. \tag{6.6}$$

Remark 6.1 *By construction of* $\bar{\boldsymbol{F}}$, *the isochoric/volumetric split of the modified deformation gradient gives:*

$$\left\{\begin{array}{l} \bar{\boldsymbol{F}}_{\text{iso}} = (\det \boldsymbol{F})^{-1/3} \boldsymbol{F} = \boldsymbol{F}_{\text{iso}} \\ \bar{\boldsymbol{F}}_{\text{v}} = (\det \boldsymbol{F}_0)^{1/3} \boldsymbol{I} = (\boldsymbol{F}_0)_{\text{v}} \end{array}\right. \tag{6.7}$$

i.e., the isochoric component of $\bar{\boldsymbol{F}}$ *coincides with the current (integration point) isochoric deformation gradient (as obtained from the conventional interpolation functions) while its volumetric part corresponds to the dilatation at the centroid of the element. In view of (6.6), this implies that, for materials whose deviatoric and volumetric constitutive responses are* ***decoupled****, the present formulation results in constant pressure throughout one element.*

The constitutive (near-)incompressibility constraint in this case is enforced only at the centroid of the element and not point-wise as in the conventional displacement-based finite element method. The constraint relaxation resulting from the above procedure has been shown (de Souza Neto *et al.*, 1996) to effectively overcome volumetric locking and produces excellent results in practical large strain hyperelasticity and plasticity problems. The resulting formulation can be used regardless of the material model adopted. In addition, the strain driven format of the algorithms for integration of the inelastic constitutive equations of the purely kinematic formulation is maintained. It has a particularly simple structure so that existing codes that support the conventional 4-node displacement based quadrilateral (or 8-node hexahedron, if 3-D analysis is sought) can be easily adapted to incorporate these elements.

Remark 6.2 *The basic difference between the* F-bar *method and the geometrically non-linear B-bar extension (Hughes* et al. *, 1975; Moran* et al. *, 1990) is the following. While in the* F-bar *method the conventional deformation gradient is replaced with its modified counterpart* ***in the computation of the stress tensor****, the non-linear B-bar procedure introduces this replacement in the corresponding* ***internal potential energy functional****, before the internal force vector is obtained from the first variation of the energy functional.*

6.3 Nodal average volume technique

The purpose of this section is to assess the performance of formulations based on the volumetric nodal averaging concept proposed by Bonet & Burton (1998) in the context of explicit dynamics. This investigation is motivated by the appearance of spurious pressure fluctuations in the original explicit tetrahedral nodal average pressure (ANP) formulation. This fact, prevents the successful use of the technique in situations where an accurate prediction of hydrostatic pressure is required. Such situations arise typically when strongly pressure-dependent constitutive equations, such as the ductile damage models reported in Chapter 5, are used.

Therefore, an implicit version of the original formulation is derived here by re-casting the original idea in terms of average nodal volume change ratio within the framework of the *F-bar* method proposed by de Souza Neto *et al.* (1996). In this context, an average nodal volume *F-bar* triangle for implicit plane strain and axisymmetric analysis of nearly incompressible solids is obtained.

6.3.1 The average nodal volume change ratio

Crucial to the derivation of the present element is the definition of the *average nodal volume change ratio* introduced by Bonet & Burton (1998). Let us consider a typical mesh of 3-noded triangular elements in its initial configuration and let a be an arbitrary node of the mesh. We define $\mathcal{A}$ as the set of all elements sharing node a. The initial volume, V_a, of all elements sharing node a can then be written as:

$$V_a = \sum_{e \in \mathcal{A}} V^{(e)}\,, \tag{6.8}$$

where $V^{(e)}$ denotes the volume of the generic element e in its initial configuration. The *nodal initial volume* assigned to node a is then defined as:

$$\bar{V}_a \equiv \tfrac{1}{3}\, V_a = \sum_{e \in \mathcal{A}} \tfrac{1}{3}\, V^{(e)}\,, \tag{6.9}$$

that is, each element sharing a generic node of a mesh contributes with one third of its volume to the nodal average volume assigned to that node. These definitions are entirely analogous to the well-known mass-lumping procedure used in dynamic analysis.

Similar quantities can be defined in the *deformed configuration* of the finite element mesh. With $v^{(e)}$ denoting the deformed volume of the generic element e, we define v_a as the total deformed volume of all elements sharing node a:

$$v_a \equiv \sum_{e \in \mathcal{A}} v^{(e)}\,, \tag{6.10}$$

and $\bar{v}_a$ as the *nodal deformed volume* associated with node a:

$$\bar{v}_a \equiv \tfrac{1}{3}\, v_a = \sum_{e \in \mathcal{A}} \tfrac{1}{3}\, v^{(e)}\,. \tag{6.11}$$

With the above nodal volumes at hand, we can now define the *nodal volume change ratio* for node a as:

$$\bar{J}_a \equiv \frac{\bar{v}_a}{\bar{V}_a} = \frac{v_a}{V_a}\,. \tag{6.12}$$

Within an arbitrary element e, with nodes i, j and k, the *average nodal volume change ratio* is defined as:

$$\bar{J}^{(e)} \equiv \frac{1}{3}\left(\bar{J}_i + \bar{J}_j + \bar{J}_k\right) = \frac{1}{3}\left(\frac{v_i}{V_i} + \frac{v_j}{V_j} + \frac{v_k}{V_k}\right). \tag{6.13}$$

6.3.2 F-bar based average nodal volume triangle

The original average nodal pressure triangle of Bonet & Burton (1998) was derived in the context of explicit dynamics by replacing the volume change ratio obtained from the standard isoparametric displacement interpolation with the above defined average nodal volume ratio in the elastic potential energy functional. The corresponding finite element internal force vector was then obtained by taking the first variation of the energy functional. When used in conjunction with a volumetric strain-energy function quadratic in the volume change ratio (Bonet & Burton, 1998), the procedure results in an average nodal *pressure* formulation.

Here, based on the same definition of average nodal volume change ratio, we derive an implicit version of the original element by means of the *F-bar* methodology proposed by de Souza Neto *et al.* (1996). This is described in the following.

The average nodal volume F-bar triangle

Here, the assumed modified deformation gradient, $\bar{\boldsymbol{F}}^{(e)}$, for a generic element e, is defined as:

$$\bar{\boldsymbol{F}}^{(e)} = \left(\frac{\bar{J}^{(e)}}{J^{(e)}}\right)^{\frac{1}{3}} \boldsymbol{F}^{(e)}, \tag{6.14}$$

where $\boldsymbol{F}^{(e)}$ is the deformation gradient obtained from the standard isoparametric interpolation of the displacement field within element e and

$$J^{(e)} \equiv \det \boldsymbol{F}^{(e)}. \tag{6.15}$$

The above definition implies that the volumetric component of the modified deformation gradient coincides with the average nodal volume change ratio:

$$\det \bar{\boldsymbol{F}}^{(e)} = \bar{J}^{(e)}, \tag{6.16}$$

whereas the isochoric component, $\bar{\boldsymbol{F}}^{(e)}_{\text{iso}}$, of $\bar{\boldsymbol{F}}^{(e)}$ coincides with the isochoric component of the standard deformation gradient:

$$\bar{\boldsymbol{F}}^{(e)}_{\text{iso}} \equiv \left(\det \bar{\boldsymbol{F}}^{(e)}\right)^{-\frac{1}{3}} \bar{\boldsymbol{F}}^{(e)} = \boldsymbol{F}^{(e)}_{\text{iso}} \equiv \left(\det \boldsymbol{F}^{(e)}\right)^{-\frac{1}{3}} \boldsymbol{F}^{(e)}. \tag{6.17}$$

The internal force of the F-bar-based average nodal volume linear triangle is calculated by simply adopting definition (6.14) in the computation of the Cauchy stress tensor according to (6.1).

The tangent stiffness matrix

The use of the exact tangent stiffness in the global Newton equilibrium iterations is highly desirable in view of the quadratic rates of convergence of the full Newton method. The high rates of convergence achieved result usually in higher overall efficiency of the finite element analysis procedure. A closed form expression for the exact tangent stiffness for the present element can be derived by consistently linearising the discrete equilibrium equations. The linearisation procedure in the present case is quite lengthy. Thus, we limit ourselves here to showing only its final expression.

Before presenting the formula, however, it is important to note that the modified deformation gradient used in the computation of the Cauchy stress for an average nodal volume element e depends on the displacement field of element e as well as, quite unconventionally, on the displacement fields of all elements neighbouring element e. This implies that the element internal force vector for an element e in the present case is a function of the nodal displacements of element e and all its neighbouring elements. This gives rise to the following contributions of element e to the global stiffness matrix:

- The tangent relation between the internal force vector of element e and the degrees of freedom of element e itself. This contribution will be denoted $\mathbf{K}_{ee}$. Its assembly into the global stiffness follows the same procedure of conventional finite elements;

- The tangent relationships between the internal force vector of element e and the degrees of freedom of each element s neighbouring e. These contributions will be denoted $\mathbf{K}_{es}$. We remark that their assembly into the global stiffness requires modifications in the standard procedure used for conventional elements.

Considering a typical element e with nodes i, j and k and neighbouring elements s, the exact expressions for the tangent stiffnesses can be written as:

$$\mathbf{K}_{ee} = \int_{\varphi(\Omega_{(e)})} \mathbf{G}_e^T \, \mathbf{a} \, \mathbf{G}_e \, \mathrm{d}v + \left[\frac{v^{(e)} \, (V_i V_j + V_j V_k + V_i V_k)}{3 \, \bar{J}^{(e)} \, V_i V_j V_k} - 1 \right] \int_{\varphi(\Omega_{(e)})} \mathbf{G}_e^T \, \mathbf{q} \, \mathbf{G}_e \, \mathrm{d}v \, , \tag{6.18}$$

$$\mathbf{K}_{es} = \frac{N_{es} \, v^{(s)}}{3 \, \bar{J}^{(e)} \, V_i V_j V_k} \int_{\varphi(\Omega_{(e)})} \mathbf{G}_e^T \, \mathbf{q} \, \mathbf{G}_s \, \mathrm{d}v \, , \tag{6.19}$$

where matrices $\mathbf{G}_e$ and $\mathbf{G}_s$ are the discrete (full) spatial gradient operators of elements e and s, respectively, and N_{es} is the number of nodes common to elements e and s. Matrix $\mathbf{a}$ is the finite element (matrix) representation of the fourth order *spatial elasticity tensor*:

$$a_{ijkl} = \frac{1}{\det \boldsymbol{F}} \, F_{jp} \, F_{tq} \, A_{ipkq} \, , \tag{6.20}$$

with A_{ipkq} denoting the Cartesian components of the *first elasticity tensor* (Marsden & Hughes, 1983) defined as:

$$A_{ipkq} = \frac{\partial P_{ip}}{\partial F_{kq}} . \tag{6.21}$$

In the above expression, P_{ip} are the components of the first Piola-Kirchhoff stress tensor:

$$\boldsymbol{P} = (\det \boldsymbol{F})\, \boldsymbol{\sigma}\, \boldsymbol{F}^{-T} . \tag{6.22}$$

Matrix $\mathbf{q}$ is the finite element (matrix) representation of the tensor:

$$\mathsf{q} = \tfrac{1}{3}\, \mathsf{a} : (\boldsymbol{I} \otimes \boldsymbol{I}) - \tfrac{2}{3}\, (\boldsymbol{\sigma} \otimes \boldsymbol{I}) . \tag{6.23}$$

All quantities in the above expressions are computed at $\boldsymbol{F} = \bar{\boldsymbol{F}}$. We remark here that the resulting stiffness matrix is generally *unsymmetric* regardless of the underlying material model.

Axisymmetric problems

To illustrate the simplicity of the extra stiffness term, the explicit form of the matrices involved in its computation is shown here for the axisymmetric case. Since the evaluation of the discrete gradient is standard, only the terms required for computation of $\mathbf{q}$ are presented below. Adopting the usual finite element convention, in which the matrix format indices $\{1, 2, 3, 4, 5\}$ correspond to the fourth order counterparts $\{11, 21, 12, 22, 33\}$, the matrix form of the term $\mathsf{a} : (\boldsymbol{I} \otimes \boldsymbol{I})$ that takes part in the definition (6.23) of q is given by:

$$[\mathsf{a} : (\boldsymbol{I} \otimes \boldsymbol{I})] = \begin{bmatrix} a_{11}+a_{14}+a_{15} & 0 & 0 & a_{11}+a_{14}+a_{15} & a_{11}+a_{14}+a_{15} \\ a_{21}+a_{24}+a_{25} & 0 & 0 & a_{21}+a_{24}+a_{25} & a_{21}+a_{24}+a_{25} \\ a_{31}+a_{34}+a_{35} & 0 & 0 & a_{31}+a_{34}+a_{35} & a_{31}+a_{34}+a_{35} \\ a_{41}+a_{44}+a_{45} & 0 & 0 & a_{41}+a_{44}+a_{45} & a_{41}+a_{44}+a_{45} \\ a_{51}+a_{54}+a_{55} & 0 & 0 & a_{51}+a_{54}+a_{55} & a_{51}+a_{54}+a_{55} \end{bmatrix} \tag{6.24}$$

where a_{ij} are the components of the spatial tangent modulus matrix $\mathbf{a}$. The matrix form of the remaining term $\boldsymbol{\sigma} \otimes \boldsymbol{I}$ appearing in (6.23) is simply given by:

$$[\boldsymbol{\sigma} \otimes \boldsymbol{I}] = \begin{bmatrix} \sigma_{11} & 0 & 0 & \sigma_{11} & \sigma_{11} \\ \sigma_{12} & 0 & 0 & \sigma_{12} & \sigma_{12} \\ \sigma_{12} & 0 & 0 & \sigma_{12} & \sigma_{12} \\ \sigma_{22} & 0 & 0 & \sigma_{22} & \sigma_{22} \\ \sigma_{33} & 0 & 0 & \sigma_{33} & \sigma_{33} \end{bmatrix} \tag{6.25}$$

In the expressions above, the matrix index 5 (or tensorial index 33) represents the circumferential direction, other indices correspond to the in-plane components.

Plane strain problems

Under plane strain, to ensure that the modified *F-bar* deformation gradient represents a plane deformation, we re-define (de Souza Neto *et al.*, 1996):

$$\bar{\boldsymbol{F}}^{(e)} = \left[\begin{array}{cc|c} \multicolumn{2}{c|}{\bar{\boldsymbol{F}}^{(e)}_{\text{plane}}} & \begin{array}{c} 0 \\ 0 \end{array} \\ \hline 0 & 0 & 1 \end{array} \right] , \tag{6.26}$$

where $\bar{\boldsymbol{F}}^{(e)}_{\text{plane}}$ is the assumed modified counterpart of the *in-plane component*, $\boldsymbol{F}^{(e)}_{\text{plane}}$, of the deformation gradient of element e , defined by:

$$\bar{\boldsymbol{F}}^{(e)}_{\text{plane}} = \left(\frac{\bar{J}^{(e)}}{J^{(e)}} \right)^{\frac{1}{2}} \boldsymbol{F}^{(e)}_{\text{plane}} \, . \tag{6.27}$$

In this case, in the calculation of the tangent stiffnesses, the tensor q of expression (6.23) is re-defined as:

$$\mathsf{q} = \tfrac{1}{2}\, \mathsf{a} : (\boldsymbol{I} \otimes \boldsymbol{I}) - \tfrac{1}{2}\, (\boldsymbol{\sigma} \otimes \boldsymbol{I}) \, . \tag{6.28}$$

The explicit form of the matrices $[\mathsf{a} : (\boldsymbol{I} \otimes \boldsymbol{I})]$ and $[\boldsymbol{\sigma} \otimes \boldsymbol{I}]$, in this case, is obtained from expressions (6.24) and (6.25) by simply deleting all components related to the circumferential direction. That is, we have:

$$[\mathsf{a} : (\boldsymbol{I} \otimes \boldsymbol{I})] = \begin{bmatrix} a_{11}+a_{14} & 0 & 0 & a_{11}+a_{14} \\ a_{21}+a_{24} & 0 & 0 & a_{21}+a_{24} \\ a_{31}+a_{34} & 0 & 0 & a_{31}+a_{34} \\ a_{41}+a_{44} & 0 & 0 & a_{41}+a_{44} \end{bmatrix} \tag{6.29}$$

and

$$[\boldsymbol{\sigma} \otimes \boldsymbol{I}] = \begin{bmatrix} \sigma_{11} & 0 & 0 & \sigma_{11} \\ \sigma_{12} & 0 & 0 & \sigma_{12} \\ \sigma_{12} & 0 & 0 & \sigma_{12} \\ \sigma_{22} & 0 & 0 & \sigma_{22} \end{bmatrix} \tag{6.30}$$

6.3.3 Numerical assessment

The performance of the nodal average volume linear triangle for implicit finite element analysis is assessed in this section by means of numerical examples. It should be noted that the hyperelastic simulations are dealt with within the context of finite elasticity set on the spatial configuration as described by de Souza Neto *et al.* (1995). In the elastoplastic problems, the framework for treatment of finite multiplicative plasticity based on logarithmic strains described by Perić *et al.* (1992) is adopted.

Cook's membrane

This example is frequently used to assess the convergence properties of finite elements near the incompressible limit under a mixture of shear and bending strains [Simo & Rifai (1990), de Souza Neto *et al.* (1996), Korelc & Wriggers (1996) and Glaser & Armero (1997)]. The problem consists of a tapered and swept panel of unit thickness, illustrated in Figure 6.2(a), with fully constrained displacements on its left vertical edge and subjected to a distributed shearing load, $F = 6.25$ (per unit length), applied to the opposite edge (amounting to a total vertical resultant force of intensity 100). Plane strain condition is assumed and a regularised neo-Hookean material with shear modulus $\mu = 80.1938$ and bulk modulus $k = 40.0942 \times 10^4$ is adopted. Note that near incompressibility is achieved with the high ratio k/μ, of order 10^4. Several meshes are considered, so that the convergence of the solution with mesh refinement can be assessed. A mesh of four elements per side is depicted in Figure 6.2 (a). The results are shown in Figure 6.2(b) where the final vertical

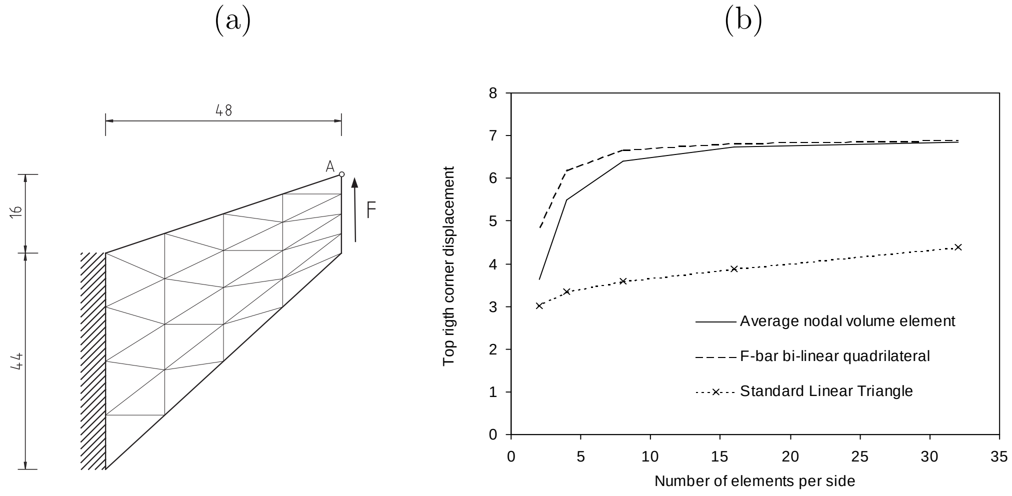

Figure 6.2: Cook's membrane. (a) Geometry and boundary conditions; and (b) Solution convergence with mesh refinement.

displacement obtained at the upper right corner of the panel [point A of Figure 6.2(a)] is plotted against the number of elements per side. Solutions obtained with the standard isoparametric three-noded triangle and the 4-noded *F-bar* quadrilateral (de Souza Neto *et al.* , 1996) are also plotted for comparison.

The convergence of the nodal average volumetric strain element is slightly slower than that of the 4-noded *F-bar* quadrilateral, but produces quite reasonable solutions with relatively coarse meshes. Note that the conventional isoparametric linear triangle exhibits severe *locking* in this case, producing a markedly over-stiff response, even with very fine meshes. The present results indicate that the nodal averaging procedure has considerably relaxed the volumetric over-constraint. In order to fully assess the performance of the present element in this benchmarking problem, we plot in Figure 6.3, the distributions of hydrostatic stress:

$$p \equiv \tfrac{1}{3}\,\mathrm{tr}\,\boldsymbol{\sigma}\,,$$

obtained at the load level $F = 100$ with the 8×8 element meshes of average nodal volume strain triangles and 4-node *F-bar* quadrilaterals.

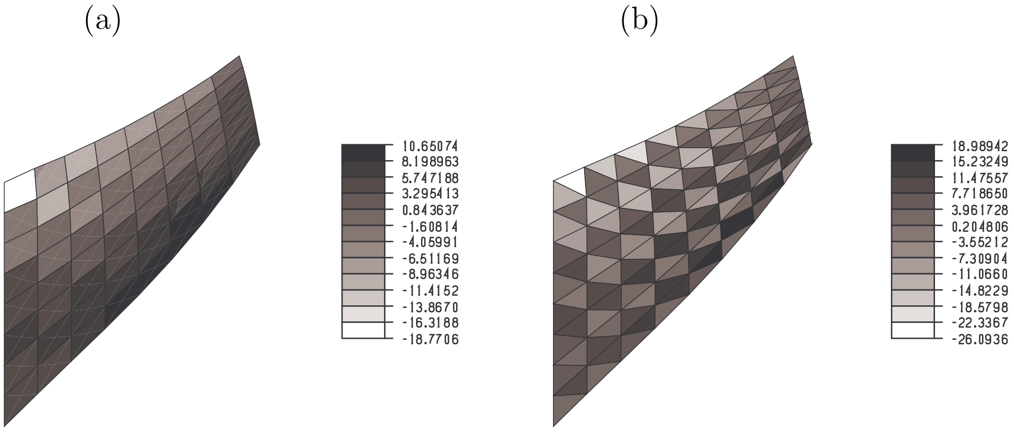

Figure 6.3: Cook's membrane. Hydrostatic pressure distributions at $F = 100$ on deformed meshes.(a) 4-noded *F-bar* quadrilateral; (b)Average nodal volume triangle.

The plots show that the average nodal volume element produces significant *checkerboard*-type pressure fluctuations. In spite of the considerable constraint relaxation resulting from the nodal averaging of volumetric strains, the spurious pressure modes detected in the present example point to limitations on the range of applicability of the present element.

Indentation of a rubber block

The problem here consists of the plane strain analysis of a rubber block of rectangular cross-section indented by a frictionless rigid indenter also of rectangular cross-section. This example has been considered by Crisfield *et al.*

(1995) to investigate a range of lower-order element formulations for elastic and elasto-plastic large strain problems under high compressive strains. The geometry of the problem as well as the boundary conditions are shown in Figure 6.4(a).

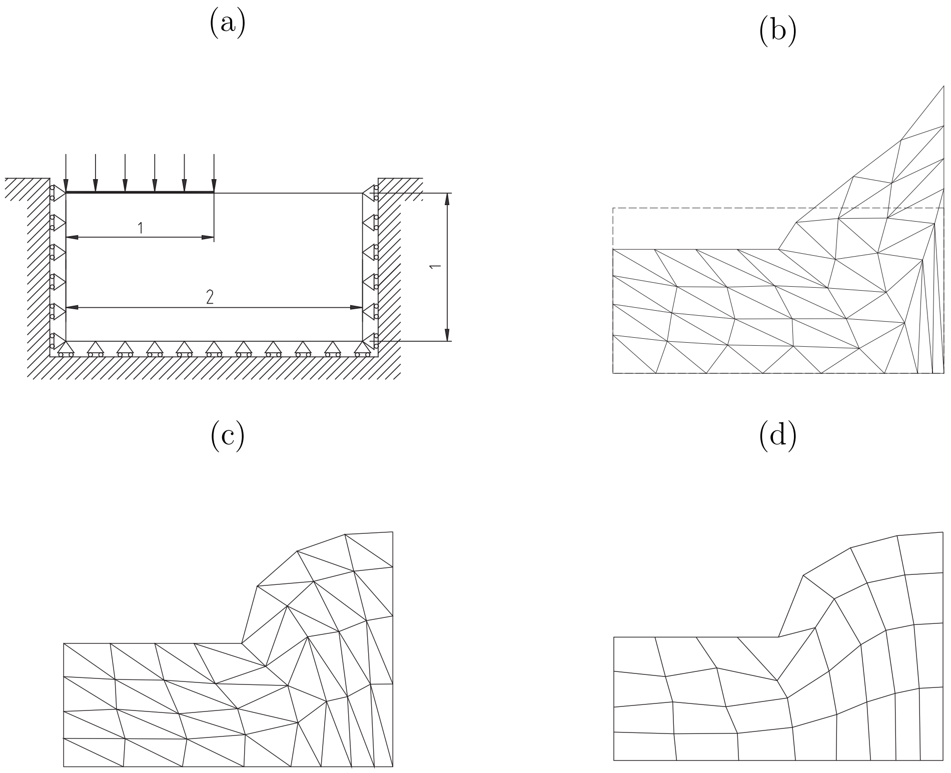

Figure 6.4: Indentation of a rubber block. (a) Problem definition; Deformed meshes at 25% compression; (b) Standard isoparametric 3-noded triangle; (c) Average nodal volume triangle; (d) 4-noded *F-bar* quadrilateral.

A regularised Mooney-Rivlin material model is adopted to describe the behaviour of the rubber block. The corresponding strain-energy function is given by:

$$\psi = C_1\,(I_1^* - 3) + C_2\,(I_2^* - 3) + \tfrac{1}{2}\,k\,(\ln J)^2\,,$$

where I_1^* and I_2^* are the first and second principal invariants of the isochoric component of the Cauchy-Green strain tensor [refer, for instance, to Ogden (1984)] and J denotes the volumetric change ratio. The constants C_1, C_2 and k are chosen as:

$$C_1 = 1.5; \qquad C_2 = 0.5; \qquad k = 10^5.$$

Again, a high value of the bulk modulus k is used to enforce (near-) incompressibility. The loading programme here consists of the incremental prescription of the vertical displacement [suggested by the arrows in Figure 6.4(a)] under the area in contact with the rigid plate. The horizontal displacements are left free in that area. A total displacement corresponding to 25% compression under the plate is prescribed.

The final deformed mesh obtained with a (coarse) mesh of 128 standard isoparametric 3-noded triangles is shown in Figure 6.4(b). The severe volumetric *locking* in this case is clearly illustrated by the unreasonable deformed shape predicted. Figure 6.4 (c) shows the deformed mesh obtained with average nodal volume triangles. It is clear that volumetric locking has been substantially alleviated by the nodal averaging volume technique allowing the prediction of a reasonable deformed shape with a rather coarse mesh. For comparison, the result of a similar simulation with 4-noded *F-bar* quadrilaterals, which also predict a reasonable deformed shape with a coarse mesh, is presented in Figure 6.4(d).

Double notched specimen

This example considers the plane strain simulation of the stretching of a double notched elastoplastic specimen. This classical test was introduced by Nagtegaal *et al.* (1974) in the infinitesimal strain context and illustrates the need for appropriate treatment of the incompressibility constraint to allow an accurate prediction of limit loads. Here, we consider the geometrically non-linear version of this problem to assess the performance of the average nodal volume element. The geometry of the problem is illustrated in Figure 6.5(a). Only one symmetric quarter of the specimen, discretised by the mesh of 300 elements shown in Figure 6.5(a), is used in the simulation. The material is modelled within the context of hyperelastic-based multiplicative plasticity and is assumed elastic-perfectly plastic with von Mises yield surface and Prandtl-Reuss flow rule. The yield stress is assumed:

$$\sigma_y = 0.45\,[GPa]\,.$$

The elastic behavior is defined by a Hencky (logarithmic strain-based) model with Young's modulus $E = 206.9\,[GPa]$ and Poisson ratio $\nu = 0.29$. This corresponds to the shear and bulk moduli:

$$\mu = 80.1938\,[GPa], \qquad\qquad k = 164.21\,[GPa]\,.$$

We remark that even though perfectly plastic response is assumed, no analytical solution for the limit load is available in the finite strain regime. A vertical displacement is applied to the top nodes of the mesh up to a total displacement $u = 0.3\,[mm]$. The simulation is carried out here using the average nodal volume triangular element as well as the 4-noded *F-bar* quadrilateral (de Souza Neto *et al.* , 1996) and the standard isoparametric 3-noded triangle. The total edge reactions per unit thickness obtained for each computation is plotted

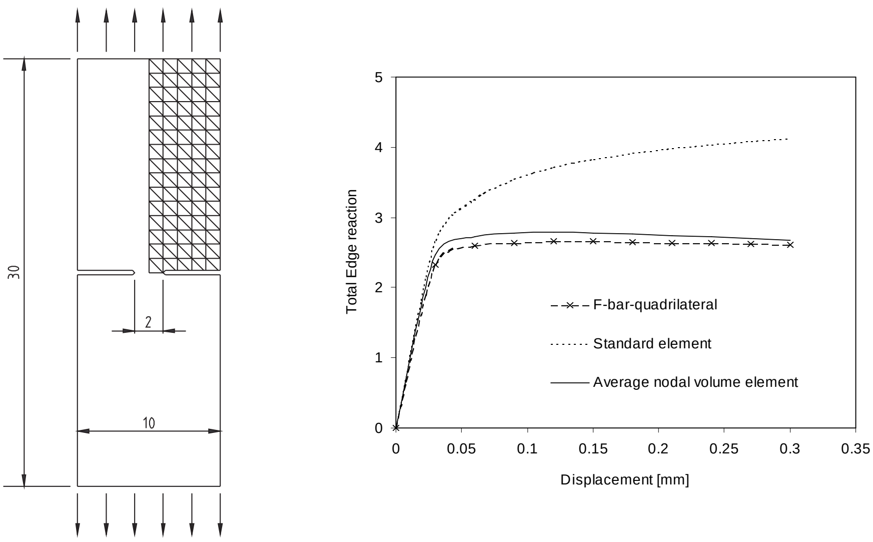
(a) (b)

Figure 6.5: Stretching of a double notched elastoplastic specimen. (a) Geometry and finite element discretisation; and (b) Reaction-displacement diagram.

versus the prescribed displacement in Figure 6.5(b). It is apparent from these results that the standard linear isoparametric element does not exhibit a limit load, in sharp contrast with the response exhibited by the present element. The force-displacement curve predicted by the present formulation is in close agreement with the one obtained with the F-*bar* quadrilateral.

Plane strain localisation

The present example assesses the performance of the nodal average volume triangle in strain localisation problems under plane strain condition. Owing to spurious locking, conventional linear triangles are unable to capture such phenomena. The problem here consists of the simulation of the stretching of a rectangular bar, with geometry shown in Figure 6.6. As in the previous example, the material of the bar is described by a hyperelastic-based multiplicative finite plasticity model with a von Mises yield surface and Prandtl-Reuss flow rule. Here, isotropic strain hardening is assumed with the following hardening/softening law:

$$\sigma_y(R) = \sigma_0 + (\sigma_\infty - \sigma_0)[1 - \exp(-\delta R)] + HR,$$

with constants:

$$\sigma_0 = 0.45\,[GPa], \;\; \sigma_\infty = 0.715\,[GPa], \;\; \delta = 16.93, \;\; H = -0.012924\,[GPa].$$

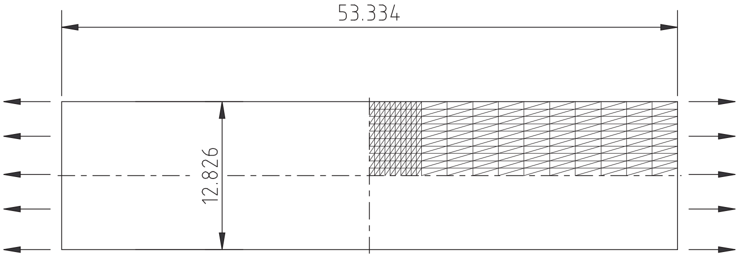

Figure 6.6: Plane strain localisation. Initial geometry and finite element mesh (dimensions in $[mm]$).

In the above law, σ_y denotes the uniaxial yield stress and R the accumulated plastic strain. The elastic constants are the same as in the previous example. This problem can be regarded a severe benchmark test and has been employed by many authors (Tvergaard *et al.* , 1981; Simo & Armero, 1992; de Souza Neto *et al.* , 1996) to assess the performance of finite elements under large isochoric plastic strains. Due to symmetry, only one quarter of the bar is discretised by the mesh shown in Figure 6.6 with appropriate boundary conditions imposed along the symmetry lines. To trigger strain localisation, we introduce an initial geometric imperfection in the form of a 1.8% width reduction at the transversal symmetry line. The width is then interpolated linearly along the half-length of the bar and achieves its nominal value (without reduction) at the leftmost boundary. The reaction force on the constrained edge of the bar obtained in the finite element simulation is plotted in Figure 6.7 versus the prescribed edge displacement. The reaction-displacement diagrams obtained with the standard

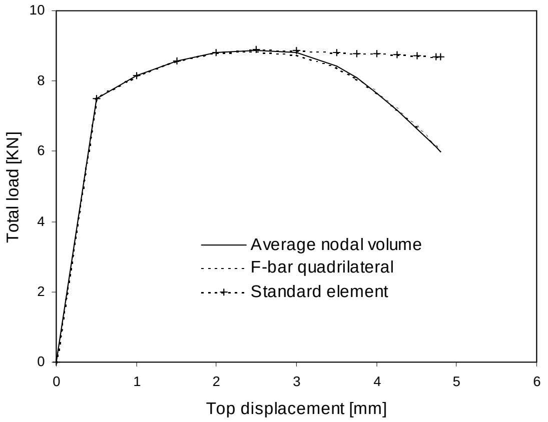

Figure 6.7: Plane strain localisation. Force-displacement diagrams.

isoparametric linear triangle and the 4-noded *F-bar* quadrilateral (de Souza Neto *et al.* , 1996) (whose performance in the present example is regarded as excellent) are also plotted for comparison. The global softening behaviour that characterises the strain localisation is clearly captured by the present element, whose curve is practically indistinguishable from that obtained with the *F-bar* quadrilateral. Note that the standard isoparametric triangle *locks* in the present case and the corresponding edge reactions remain high at the later stages of loading.

The deformed mesh obtained at $u = 4.5\,[mm]$ with the present element is shown in Figure 6.8. For comparison, the deformed mesh obtained with the *F-bar* quadrilateral is also shown. Clearly, the present element is able to capture the shear band that characterises strain localisation in the present problem. The deformed mesh is in very close agreement with that predicted by the *F-bar* quadrilateral. To fully assess the performance of the present element, the discrete (non-smoothed) hydrostatic pressure distributions obtained in both cases are also shown. While the *F-bar* quadrilateral predicts a relatively smooth pressure field, the average nodal volume element shows spurious checkerboard-type pressure oscillations, particularly in the localisation zone.

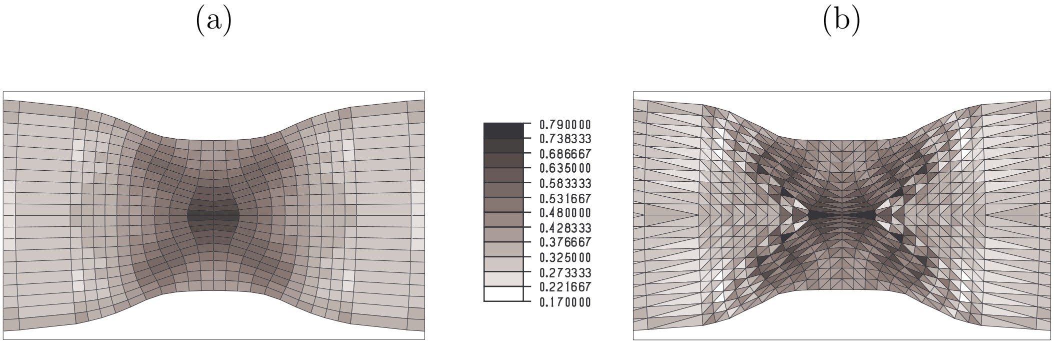

Figure 6.8: Plane strain localisation. Discrete pressure distribution $[GPa]$ at $u = 4.5\,[mm]$: (a) 4-noded F-*bar* quadrilateral;(b) Present average nodal volume triangle.

In conclusion, the nodal averaging procedure has substantially alleviated the volumetric locking tendency of the triangular element. This is made evident by the global softening behaviour and shear band formation captured by the present element. However, the observed pressure fluctuations will impose restrictions on the use of the present element under large isochoric plastic strains.

Necking of a cylindrical bar

This example tests the axisymmetric version of the nodal average volume triangle. It consists of the simulation of the necking of a cylindrical metal bar, with diameter of 12.826 $[mm]$ and length of 53.334 $[mm]$, in a tensile test. This problem has been used by some authors (Simo & Armero, 1992; de Souza Neto *et al.* , 1996) to assess the performance of specially treated axisymmetric and three-dimensional elements in large strain localisation problems under plastic incompressibility. The material model adopted to describe the bar is the same as in the previous example. All material constants are identical except for the hardening modulus, H, which is here taken as:

$$H = 0.12924\,[GPa].$$

Only one quarter of the longitudinal cross-section of the bar is discretised with the appropriate boundary conditions being imposed on the symmetry lines. Figure 6.9 shows the initial configuration of the finite element mesh used. A geometric imperfection of 1.8% radius reduction is introduced at the centre of the bar and linearly extended to the leftmost boundary to trigger the necking. A vertical displacement $u = 7.0[mm]$ is imposed incrementally at the leftmost boundary of the bar. The reaction forces on the constrained edge of the bar obtained in the simulation is plotted in Figure 6.10 against the corresponding imposed edge displacement. The results obtained with the 4-noded *F-bar* quadrilateral are also plotted for comparison. The reactions obtained with

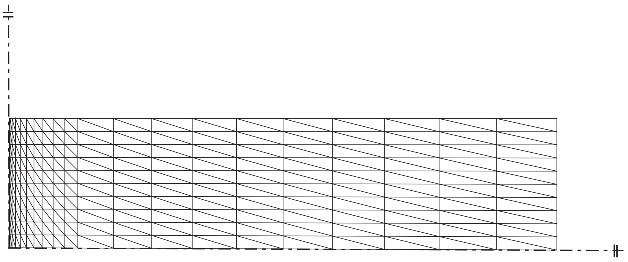

Figure 6.9: Axisymmetric necking. Initial finite element mesh.

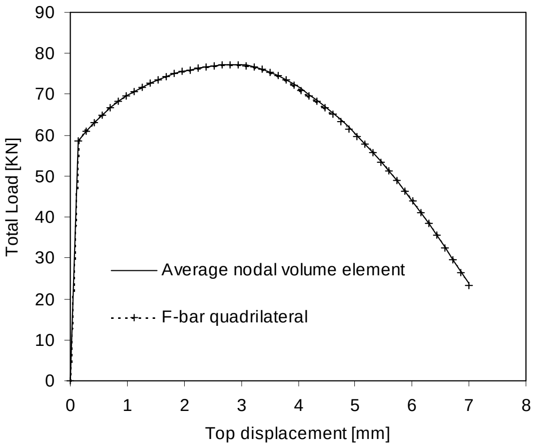

Figure 6.10: Axisymmetric necking. Force-displacement curves.

the present element are in very close agreement with those obtained with the 4-noded *F-bar* quadrilateral. We remark that, in this case, the conventional 3-noded triangle *locks* and does not capture the necking phenomenon. The corresponding reaction-displacement curve (not shown here) does not represent the softening branch that follows the onset of localisation at approximately $u = 3\,[mm]$.

The final deformed mesh obtained with the present element is shown in Figure 6.11 together with the deformed mesh obtained with the 4-noded *F-bar* quadrilateral (de Souza Neto *et al.* , 1996). For both elements, the (non-smoothed) hydrostatic pressure distribution is also shown for comparison. Clearly both elements are capable of capturing the strain localisation in this case and produce similar deformed shapes. The nodal average volume element exhibits a greater cross-section reduction in the necking zone. However, this element presents significant checkerboard-type pressure fluctuations. This shows that the pathology identified in the previous plane strain examples is also present in the axisymmetric version of the average nodal volume element.

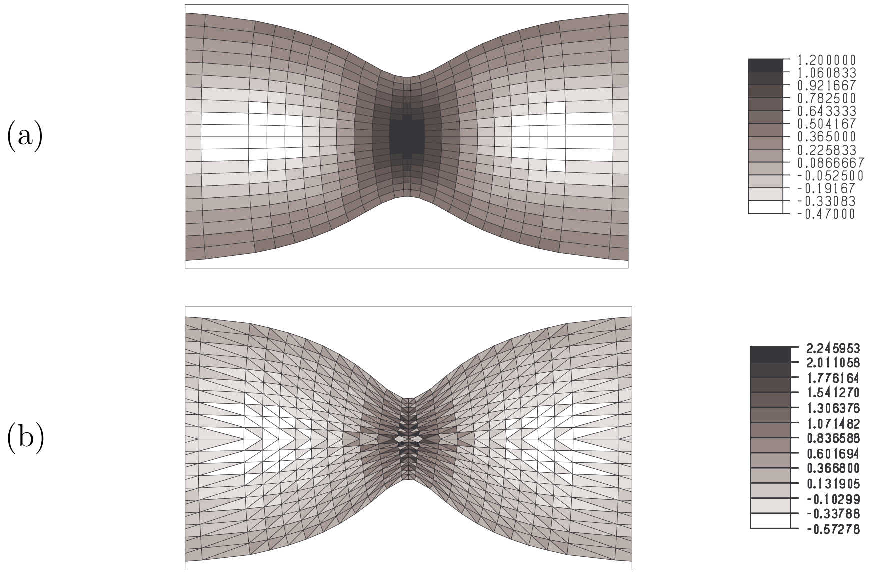
(a)
1.200000
1.060833
0.921667
0.782500
0.643333
0.504167
0.365000
0.225833
0.0866667
-0.052500
-0.19167
-0.33083
-0.47000
(b)
2.245953
2.011058
1.776164
1.541270
1.306376
1.071482
0.836588
0.601694
0.366800
0.131905
-0.10299
-0.33788
-0.57278

Figure 6.11: Axisymmetric necking. Deformed meshes and discrete pressure distribution $[GPa]$ at $u = 7.0\,[mm]$.(a) 4-noded F-*bar* quadrilateral; (b) Present average nodal volume element.

6.3.4 Closing remarks

A thorough assessment of the volumetric nodal average concept (Bonet & Burton, 1998) has been presented. The assessment has been carried out based on an implict version of the formulation obtained within the framework of the *F-bar* methodology (de Souza Neto *et al.* , 1996). In this context, a linear triangle for implicit plane strain and axisymmetric analysis of nearly incompressible solids has been devised. A comprehensive set of numerical examples has been presented. The examples have shown that the nodal averaging technique substantially reduces the locking tendency of the linear triangle and produces quite reasonable predictions of deformed shapes as well as reaction forces, including limit loads and strain localisation patterns in elasto-plastic analysis, near the incompressible limit.

However, in spite of the substantial reduction in locking tendency, the examples have also shown that the element can produce considerable checkerboard – type hydrostatic pressure fluctuations. This fact, which appears not to have been noticed in the literature, prevents the successful use of the average nodal volume technique in situations where an accurate prediction of hydrostatic pressure is required. Nevertheless, the use of the average nodal volume formulation can be recommended, with caution, in applications (typically encountered in metal forming simulation) where only final deformed shapes and, possibly, reaction forces are of interest to the analyst.

6.4 F-bar patch method

The purpose of this section is to introduce a new methodology which extends the so-called *F-bar* procedure (de Souza Neto *et al.* , 1996) so as to accommodate simplex elements. The underlying idea is simple: It relies essentially on the relaxation of the excessive volumetric constraint typical of low order elements by enforcing the incompressibility constraint over a *patch* of simplex elements. This idea has some conceptual similarities with the procedures proposed by Guo *et al.* (2000) and Thoutireddy *et al.* (2002) who developed *composite* triangular and tetrahedral elements.

6.4.1 The proposed F-bar-patch method

Unfortunately, the original *F-bar* procedure described in Section 6.2 cannot be applied directly to linear simplex elements (linear triangles in 2-D and linear tetrahedra in 3-D). The reason for this is that the deformation gradient computed from the displacement field of a linear simplex element is constant within the element so that:

$$\boldsymbol{F} = \boldsymbol{F}_0 \,.$$

In view of definition (6.5), this implies that, for such elements, the modified gradient, $\bar{\boldsymbol{F}}$, coincides with the standard deformation gradient, $\boldsymbol{F}$. Obviously, in this case, the adoption of the original *F-bar* methodology would have no effect in relaxing the excessive constraints associated with material incompressibility. An alternative then could be to redefine the *F-bar* gradient in a manner that will allow sufficient relaxation of incompressibility constraints.

This is the basic principle behind the new elements proposed in this section and is described in the following.

6.4.2 The modified F-bar deformation gradient defined for a patch of elements

The key idea to allow the use of simplex elements with the *F-bar* methodology is rather simple. Instead of working within an individual element, we now consider a *patch* of simplex elements. A typical patch is illustrated in Figure 6.12 (drawn in solid lines). Let $\mathcal{P}$ denote the set of elements forming a pre-defined patch. For each element $e \in \mathcal{P}$, the modified deformation gradient, $\bar{\boldsymbol{F}}_e$, is defined as:

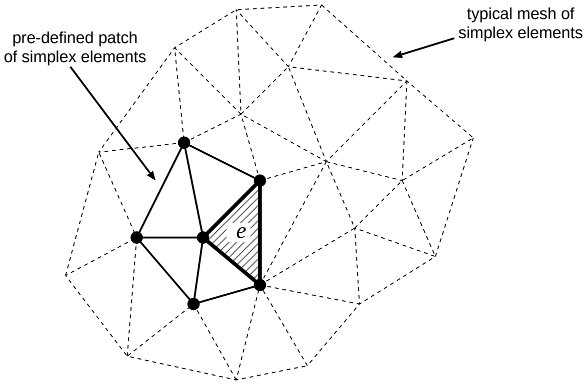

Figure 6.12: Definition of a patch of simplex elements.

$$\bar{\boldsymbol{F}}_e = \left[\frac{v_{\text{patch}}}{V_{\text{patch}} \, (\det \boldsymbol{F}_e)} \right]^{\frac{1}{3}} \boldsymbol{F}_e \,, \tag{6.31}$$

where $\boldsymbol{F}_e$ is the deformation gradient obtained from the standard linear displacement interpolation within element e and v_{patch} and V_{patch} denote, respectively, the deformed and reference (undeformed) volume of patch $\mathcal{P}$:

$$v_{\text{patch}} = \sum_{i \in \mathcal{P}} v_i \,, \qquad V_{\text{patch}} = \sum_{i \in \mathcal{P}} V_i. \tag{6.32}$$

In the above, v_i and V_i are, respectively, the deformed and reference (undeformed) volume of the generic element i of patch $\mathcal{P}$.

Remark 6.3 *The above definition implies that the determinant of the modified deformation gradient is identical for all elements e of patch $\mathcal{P}$ and is given by:*

$$\bar{J}_e \equiv \det \bar{\boldsymbol{F}}_e = \frac{v_{\text{patch}}}{V_{\text{patch}}} \,, \tag{6.33}$$

that is, det$\bar{\boldsymbol{F}}_e$ *is the ratio between the current (deformed) and the undeformed volume of the pre-defined* patch $\mathcal{P}$ *of elements. Thus, the use of the above defined* $\bar{\boldsymbol{F}}$ *in the calculation of the stress components for an incompressible constitutive model will require that the* patch $\mathcal{P}$ *of elements preserves its volume, even though individual elements of the patch may suffer volume changes during deformation. This is in contrast to conventional linear isoparametric elements where the incompressibility constraint is enforced within each element of a mesh. Clearly, the use of the above defined assumed modified deformation gradient will reduce the number of constraints associated with material incompressibility within the patch of simplex elements.*

Finally, the application of the new methodology to a problem defined by an arbitrary mesh of simplex elements requires that the mesh be split into a number of *non-overlapping* patches of elements. Within a patch, the modified deformation gradient to be used in the stress computation is calculated for each element according to (6.31). It is important to emphasise here that, as in the original *F-bar* method, the actual constitutive function (or *incremental* constitutive function in the case of dissipative materials) for the stress tensor is the *same* as we would use were the analysis to be carried out with conventional isoparametric elements. That is, the standard strain-driven format of the associated constitutive functions is preserved in the present formulation. In computational terms, it means that conventional stress updating routines already in use with standard isoparametric elements can be used in the present context without modification.

Remark 6.4 *Following the comments made in Remark 6.3, the more elements in each patch, the greater the constraint relaxation achieved. In defining such patches it is then crucial to consider that excessive constraint relaxation (too many elements in the patch) may lead to well-known spurious zero-energy mechanisms. On the other hand, insufficient constraint relaxation (too few elements in the patch) may result in incompressibility locking. Patches with appropriate number of elements for two- and three-dimensional analysis have been determined by the author by means of extensive numerical experiments. The examples presented in Section 6.4.6 adopt patches found by the authors to produce sufficient constraint relaxation to avoid locking without allowing for spurious mechanisms.*

6.4.3 Plane strain problems

As in the original *F-bar* procedure (de Souza Neto *et al.* , 1996), in the *plane strain* case, the modified deformation gradient of expression (6.31) is re-defined as:

$$\bar{\boldsymbol{F}}_e = \left[\begin{array}{cc|c} \multicolumn{2}{c|}{\bar{\boldsymbol{F}}_e^{\text{plane}}} & \begin{array}{c}0\\0\end{array} \\ \hline 0 \quad 0 & & 1 \end{array}\right] , \tag{6.34}$$

where $\bar{\boldsymbol{F}}_e^{\text{plane}}$ is the assumed modified counterpart of the *in-plane component*, $\boldsymbol{F}_e^{\text{plane}}$, of the deformation gradient at element $e \in \mathcal{P}$, defined by:

$$\bar{\boldsymbol{F}}_e^{\text{plane}} = \left[\frac{a_{\text{patch}}}{A_{\text{patch}}\left(\det \boldsymbol{F}_e^{\text{plane}}\right)}\right]^{\frac{1}{2}} \boldsymbol{F}_e^{\text{plane}} , \tag{6.35}$$

with a_{patch} and A_{patch} denoting, respectively, the *area* of patch $\mathcal{P}$ in its current and deformed configurations:

$$a_{\text{patch}} = \sum_{i \in \mathcal{P}} a_i , \qquad A_{\text{patch}} = \sum_{i \in \mathcal{P}} A_i . \tag{6.36}$$

In the above expression, a_i and A_i denote, respectively, the area of element i in its current and deformed configurations. This re-definition of $\bar{\boldsymbol{F}}$ is needed to ensure that the assumed modified deformation gradient represents a state of plane strain. If definition (6.31) were adopted instead, the resulting formulation would have generally non-vanishing out-of-plane strains. This would require an axisymmetric-type stress updating procedure, making the plane strain element implementation rather cumbersome within a conventional finite element code. It should be noted, also, that the above definition and definition (6.31) give identical results under uniform states of strain within the element. For generic states in practical applications, numerical experiments show a maximum stress component relative difference of order 0.15% between the two possible approaches (converging to identical results with mesh refinement).

6.4.4 Element tangent stiffness matrix

A crucial component needed in the implicit implementation of the proposed class of elements is the element tangent stiffness. The use of the exact tangent stiffness in the Newton iterative scheme to solve the non-linear equilibrium equations ensures quadratic rates of asymptotic convergence which normally result in higher code efficiency. For a *conventional* displacement-based finite element e (and also for an *F-bar* element following the original formulation discussed in Section 6.2) the tangent stiffness matrix is defined as the derivative of the element internal force vector, $\mathbf{f}_e^{\text{int}}$, with respect to the element vector of nodal displacements, $\mathbf{u}_e$:

$$\mathbf{K}_e = \frac{\partial \mathbf{f}_e^{\text{int}}}{\partial \mathbf{u}_e} . \tag{6.37}$$

Trivially, the tangent stiffness $\mathbf{K}_e$ of an element with n_{dof} degrees of freedom in this case is a square matrix of dimension $n_{\mathrm{dof}} \times n_{\mathrm{dof}}$. Its general form, in spatial (deformed configuration) representation, can be expressed as:

$$\mathbf{K}_e = \int_{\varphi(\Omega_e)} \mathbf{G}_e^T \, \mathbf{a} \, \mathbf{G}_e \, \mathrm{d}v \tag{6.38}$$

where $\varphi(\Omega_e)$ denotes the deformed domain of element e, $\mathbf{G}_e$ is the standard discrete spatial gradient operator of element e and $\mathbf{a}$ is the matrix form of the fourth order *spatial elasticity tensor*:

$$a_{ijkl} = \frac{1}{\det \boldsymbol{F}} \, F_{jp} \, F_{tq} \, A_{ipkq} \,, \tag{6.39}$$

with A_{ipkq} denoting the cartesian components of the *first elasticity tensor* (Marsden & Hughes, 1983) defined as:

$$A_{ipkq} = \frac{\partial P_{ip}}{\partial F_{kq}} \,. \tag{6.40}$$

In the above expression, P_{ip} are the components of the first Piola-Kirchhoff stress tensor:

$$\boldsymbol{P} = (\det \boldsymbol{F}) \, \boldsymbol{\sigma} \, \boldsymbol{F}^{-T} \,. \tag{6.41}$$

The tangent stiffness of an F-bar-Patch element

In sharp contrast to the above conventional case, the internal force vector of an *F-bar-Patch* element depends not only on the degrees of freedom of the element itself, but also on the degrees of freedom of all other elements belonging to its patch. Such a dependency stems from the use of the modified deformation gradient defined by (6.31) in the computation of the stress tensor components used to assemble the force vector. Note in (6.31) that volumetric changes in any element of a patch (produced by variations of any nodal displacements in a patch of elements) affects the *F-bar* gradient for all elements of the patch which, in turn, changes the stress state and the internal force vector of all elements of the patch. As a result, the tangent stiffness in the present case has a non-conventional structure. Let us then consider an *F-bar-Patch* element e, belonging to a patch $\mathcal{P}$. The internal force vector of element e depends on the vector:

$$\mathbf{u}_e$$

of nodal displacements of element e, as well as on the vectors:

$$\mathbf{u}_s \,, \qquad s \in \mathcal{P} \,; \; s \neq e \,,$$

of nodal displacements of the other elements of the patch. The application of a lengthy but standard exact linearisation procedure (the main steps of which are shown in the Appendix B) to the internal force vector of element e gives rise to the following element tangent stiffnesses:

$$\mathbf{K}_{ee} = \int_{\varphi(\Omega_e)} \mathbf{G}_e^T \, \mathbf{a} \, \mathbf{G}_e \, \mathrm{d}v + \left(\frac{v_e}{v_{\text{patch}}} - 1 \right) \int_{\varphi(\Omega_e)} \mathbf{G}_e^T \, \mathbf{q} \, \mathbf{G}_e \, \mathrm{d}v \tag{6.42}$$

$$\mathbf{K}_{es} = \frac{v_e}{v_{\text{patch}}} \int_{\varphi(\Omega_e)} \mathbf{G}_e^T \, \mathbf{q} \, \mathbf{G}_s \, \mathrm{d}v \,, \qquad s \in \mathcal{P} \,; \; s \neq e \,, \tag{6.43}$$

where $\mathbf{a}$ is the matrix form of the fourth order spatial elasticity tensor now evaluated at $\boldsymbol{F} = \bar{\boldsymbol{F}}$, $\mathbf{G}_i$ denotes the conventional discrete (full) gradient operator of a generic element i and $\mathbf{q}$ is the matrix form of the fourth order tensor defined by:

$$\mathsf{q} = \tfrac{1}{3} \, \mathsf{a} : (\boldsymbol{I} \otimes \boldsymbol{I}) - \tfrac{2}{3} (\boldsymbol{\sigma} \otimes \boldsymbol{I}) \;, \tag{6.44}$$

also computed at $\boldsymbol{F} = \bar{\boldsymbol{F}}$ (the matrix form of q suitable for computational implementation is shown in Section 6.3.2). Expression (6.44) is valid for the three-dimensional and axisymmetric cases. In plane strain, due to the redefinition (6.35) of the assumed modified deformation gradient, $\mathbf{q}$ is given by:

$$\mathsf{q} = \tfrac{1}{2} \, \mathsf{a} : (\boldsymbol{I} \otimes \boldsymbol{I}) - \tfrac{1}{2} (\boldsymbol{\sigma} \otimes \boldsymbol{I}) \;. \tag{6.45}$$

We remark that both $\mathbf{K}_{ee}$ and $\mathbf{K}_{es}$ are generally *unsymmetric*, regardless of the material model adopted.

Remark 6.5 (The structure of the tangent stiffness) *The stiffness contribution given in (6.42) represents the tangent relation between the internal force components and nodal displacements of element e. Its rows and columns are associated with the degrees of freedom of element e only – as in conventional isoparametric elements – and its formula is very similar to that of the stiffness of the original* F-bar *element (de Souza Neto* et al. *, 1996). The additional contributions (6.43), on the other hand, are the tangent relations between the internal force components of element e and nodal displacements of the* other *elements s of the patch. Their rows are associated with the degrees of freedom of element e and and their columns are associated with the degrees of freedom of the other elements s of the patch. The global tangent stiffness required in the solution of the equilibrium problem is obtained by adding, for each element e of the mesh, the contributions of $\mathbf{K}_{ee}$ and $\mathbf{K}_{es}$ ($s \in \mathcal{P}$; $s \neq e$) to the appropriate global stiffness matrix position.*

Remark 6.6 *As in the original* F-bar *method (de Souza Neto* et al. *, 1996), the general lack of symmetry of the element stiffness in the present case stems from the fact that the assumed modified deformation gradient has been introduced only in the computation of the stress in the assembly of the element* *internal force vector. This is in contrast with variationally-based methods, such as that of Hughes* et al. *(1975); Moran* et al. *(1990), where an assumed modified deformation gradient is introduced in the corresponding potential energy functional instead. At this point, we should remark that numerical tests reported by Srikanth & Zabaras (2001) with the original* F-bar *quadrilateral show a superior coarse mesh performance of this element over a variationally-based counterpart, justifying its use despite the potential lack of symmetry. In addition, it should be noted that lack of symmetry is almost invariably present in realistic large scale industrial problems which, typically, involve frictional contact and/or non-associative plasticity models. Under such conditions, the additional lack of symmetry resulting from the present technique will not have a significant effect on the overall computational costs. The extra computational effort required will be related mostly to the increase in stiffness bandwidth (as compared to conventional isoparametric simplex elements) due to the cross contributions* $\mathbf{K}_{es}$*. Note that the global tangent stiffness, in the present case, remains structurally symmetric.*

6.4.5 Computational implementation aspects

The most important aspects of the computational implementation of a finite element within an implicit code are: (i) The computation of the element internal force vector, and; (ii) The computation of the element tangent stiffness matrix. Practical aspects of the calculation of the internal force vector and tangent stiffness for the class of elements proposed are discussed below.

Internal force vector

As far as the internal force vector is concerned, the implementation of the methodology proposed here is relatively straightforward. The computation of the internal force vector for the new elements requires only simple modifications to the conventional displacement-based simplex element routines. Essentially, it requires the calculation of the modified deformation gradient according to (6.31) [or (6.35) in plane strain]. This is obtained by simply scaling the conventional deformation gradient by a factor involving the (undeformed and deformed) volumes/areas of the elements of the corresponding patch. For convenience, an algorithm for computation of the internal force vector of an *F-bar-Patch* simplex element is listed in Box 6.1 in pseudo-code format.

Tangent stiffness

Due to its unconventional structure, the computation of the tangent stiffness for *F-bar-Patch* elements requires some more substantial changes to existing

Box 6.1: Internal force vector computation for a generic simplex *F-bar-Patch* element, $e \in \mathcal{P}$.

```
(i) Compute the volume of patch $\mathcal{P}$ to which element $e$ belongs:
        $v_{patch} = \sum_{i \in \mathcal{P}} v_i$
(ii) Evaluate $\bar{J} = \det \bar{\boldsymbol{F}} = \frac{v_{patch}}{V_{patch}}$
(iii) Set the Gauss integration weight $w$ and compute the element
      jacobian determinant $j$
(iv) For element $e$:
    • compute the standard gradient matrix $\mathbf{G}$
    • $\boldsymbol{F} := \boldsymbol{I} + \mathbf{G}\mathbf{u}$ (standard deformation gradient)
    • $\bar{\boldsymbol{F}} := \left( \frac{\det \bar{\boldsymbol{F}}}{\det \boldsymbol{F}} \right)^{\frac{1}{3}} \boldsymbol{F}$ (modified deformation gradient)
    • $\boldsymbol{\sigma} := \hat{\boldsymbol{\sigma}}(\boldsymbol{\alpha}_n, \bar{\boldsymbol{F}})$ (call stress update routine)
    • compute the standard $\mathbf{B}$ matrix
    • $\mathbf{f}^{\rm int}_{(e)} := w \, j \, \mathbf{B}^{\rm T} \boldsymbol{\sigma}$ (element internal force vector)
(vi) RETURN
```

finite element codes which already support standard simplex displacement-based elements. The calculation of $\mathbf{K}_{ee}$ given by (6.42) is simple. Note that the first term on the right hand side of (6.42) has the same format as the stiffness of conventional elements. Its computation is straightforward. The second term on the right hand side of (6.42) is also simple. The basic extra requirement here is the calculation of matrix $\mathbf{q}$ according to (6.44) [or (6.45) under plane strain]. Computation of the matrices $\mathbf{K}_{es}$ is also straightforward. However, since their rows are associated with degrees of freedom of element e and their columns with degrees of freedom of the other elements s of the patch, the addition of their contributions to the global stiffness requires appropriate changes in the conventional routines for global stiffness assembly. The overall procedure is summarised in Box 6.2 in pseudo-code format.

Remark 6.7 *The methodology just outlined, implicitly assumes that the geom-*

Box 6.2: Stiffness matrix computation for one *F-bar-Patch* element.

(i) Compute the volume of patch $\mathcal{P}$ to which element e belongs:

$$v_{patch} = \sum_{i \in \mathcal{P}} v_i$$

(ii) Evaluate $\bar{J} = \det \bar{\boldsymbol{F}} = \dfrac{v_{patch}}{V_{patch}}$

(iii) Set the Gauss integration weight w and compute the element jacobian determinant j

(iv) For the element e:

- compute the standard gradient matrix $\mathbf{G}_e$
- $\boldsymbol{F} := \boldsymbol{I} + \mathbf{G}_e \mathbf{u}$ (standard deformation gradient)
- $\bar{\boldsymbol{F}} := \left(\dfrac{\det \bar{\boldsymbol{F}}}{\det \boldsymbol{F}} \right)^{\frac{1}{3}} \boldsymbol{F}$ (modified deformation gradient)
- $\mathbf{a} := \hat{\mathbf{a}}(\bar{\boldsymbol{F}})$ (tangent modulus computation routine)
- $\mathbf{K}_{ee} := w\, j\, \mathbf{G}_e^{\mathrm{T}} \mathbf{a}\, \mathbf{G}_e$
- compute $\mathsf{q} := \frac{1}{3} \mathsf{a} : (\boldsymbol{I} \otimes \boldsymbol{I}) - \frac{2}{3} (\boldsymbol{\sigma} \otimes \boldsymbol{I})$ at $\boldsymbol{F} = \bar{\boldsymbol{F}}$
- $\mathbf{K}_{ee} := \mathbf{K}_{ee} + w\, j \left(\dfrac{v_e}{v_{patch}} - 1 \right) \mathbf{G}_e^{\mathrm{T}} \mathbf{q}\, \mathbf{G}_e$

(v) For elements $s \in \mathcal{P}$, $s \neq e$ (all elements of the patch, except element e):

- compute the standard gradient matrix $\mathbf{G}_s$
- $\mathbf{K}_{es} := w\, j \left(\dfrac{v_s}{v_{patch}} \right) \mathbf{G}_e^{\mathrm{T}} \mathbf{q}\, \mathbf{G}_s$

(vi) Add contributions $\mathbf{K}_{ee}$ and all $\mathbf{K}_{es}$ to the global stiffness matrix

(vii) RETURN

etry of the problem, defined by a finite element mesh of simplex elements, is split into a number of non-overlapping patches. Additionally, it requires that information regarding the elements that compose each patch is promptly available. Therefore, whenever the mesh that represents the problem at hand is *created (or regenerated), the algorithm is compelled to create (or update) the list of elements that belong to each patch to preserve the integrity of the overall implementation.*

6.4.6 Numerical examples

The performance of the proposed *F-bar-Patch* methodology is assessed in this section by means of numerical examples. Some of the examples presented are well accepted benchmark tests and have been extensively used in the literature to assess finite element techniques for incompressible/nearly-incompressible problems. The examples comprise simulations with hyperelastic as well as hyperelastic-based multiplicative elasto-plastic underlying material models.

Cook's membrane

This example is frequently used to assess the convergence properties of finite elements near the incompressible limit under a mixture of shear and bending strains (Simo & Rifai, 1990; de Souza Neto *et al.* , 1996; Korelc & Wriggers, 1996; Glaser & Armero, 1997). The geometry, boundary conditions and material properties have already been described in Section 6.3.3.

The proposed method is tested here with patches of two three-noded triangular elements. Several meshes are considered, so that the convergence of the solution with mesh refinement can be assessed. For all meshes considered the total load is applied in 5 increments. The results are shown in Figure 6.13 where the final vertical displacement obtained at the upper right corner of the panel (point A of Figure 6.2) is plotted against the number of elements per

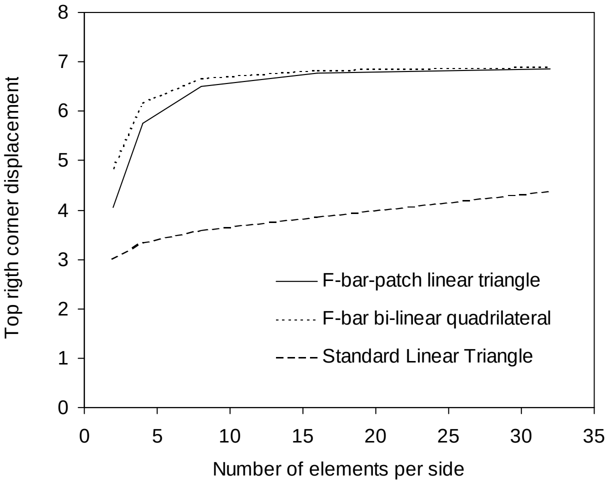

Figure 6.13: Cook's membrane. Solution convergence with mesh refinement.

side. Solutions obtained with the standard isoparametric three-noded element and the 4-noded *F-bar* quadrilateral (de Souza Neto *et al.* , 1996) are also plotted for comparison. For convenience, the results are also presented in tabular form in Table 6.1. This should be useful to researchers working in element development wishing to have the present problem as a benchmark.

Table 6.1: Cook's membrane. Solution convergence with mesh refinement.

No. of elements	Vertical displacement at point A		
per side	Standard triangle	*F-bar-Patch* triangle	*F-bar* quadrilateral
2	3.00905	4.06054	4.84713
4	3.35032	5.75040	6.17328
8	3.59242	6.50343	6.67370
16	3.86886	6.77039	6.83357
32	4.38168	6.86695	6.89150

The behavior of the proposed method is similar to that of the *F-bar* quadrilaterals which produce good solutions without the need for an excessively large number of elements. In this case, conventional isoparametric linear triangles present severe *locking*. This is illustrated by the over-stiff response shown in Figure 6.13. Convergence with mesh refinement is extremely slow in this case. The adoption of the new procedure with patches of only two elements effectively overcame the locking response that characterises the conventional linear triangle in this case. In order to fully assess the performance of the present element in this benchmarking problem, we plot in Figure 6.14 the distributions

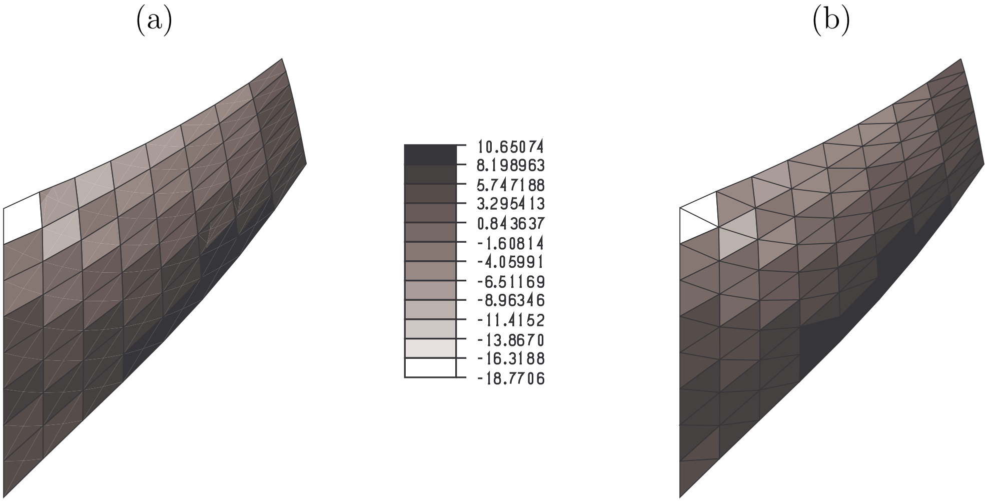
(a)
(b)

Figure 6.14: Cook's membrane. Hydrostatic pressure distributions at $F = 100$ on deformed meshes. (a) 4-noded *F-bar* quadrilateral; (b) 3-noded *F-bar-Patch* triangle with patches of 2 elements.

of hydrostatic stress:

$$p = \tfrac{1}{3}\,\mathrm{tr}\,\boldsymbol{\sigma}\,,$$

obtained at the load level $F = 100$ with meshes of 3-noded *F-bar-Patch* triangles and 4-node *F-bar* quadrilaterals (both with 8 elements per side). The plots show that the results produced by the present element are in very good agreement with those produced by the *F-bar* quadrilateral. The pressure distribution is quite smooth and, in particular, does not present the typical checkerboard-type fluctuations associated with locking elements.

Finally, as expected, the use of the exact tangent stiffness obtained from the consistent linearisation of the problem results in a quadratic rate of asymptotic convergence of the Newton-Raphson iterations employed in the solution of the finite element equilibrium equations. This is confirmed in Table 6.2 which shows the evolution of the Euclidean norm of the residual (normalised out-of-balance forces) over the iterations of a typical load increment with the present element.

Table 6.2: Cook's membrane. Evolution of residual Euclidean norm.

iteration number	relative residual (%)
1	0.116740E+05
2	0.298047E+02
3	0.156810E+02
4	0.717017E−02
5	0.854556E−06

Indentation of a rubber block

The problem here consists of the plane strain analysis of a rubber block of rectangular cross-section indented by a frictionless rigid indenter also of rectangular cross-section. The geometry, boundary conditions and material properties have already been described in Section 6.3.3. The final deformed mesh obtained with a (coarse) mesh of 64 standard isoparametric 3-noded triangles was already shown in Figure 6.4(b)[page 132]. Figure 6.15(a) shows the deformed configuration obtained for the same mesh with the proposed *F-bar-Patch* technique. As in the previous example, patches of two 3-noded triangles have been used.

It is clear that volumetric locking tendency of the conventional 3-noded triangle has been alleviated by the present technique allowing the prediction of a reasonable deformed shape with a rather coarse mesh. We remark that, in addition, the deformed shapes obtained with the present technique do not show the spurious hourglass patterns which have been associated with early enhanced assumed strain elements under high compressive strains (Wriggers &

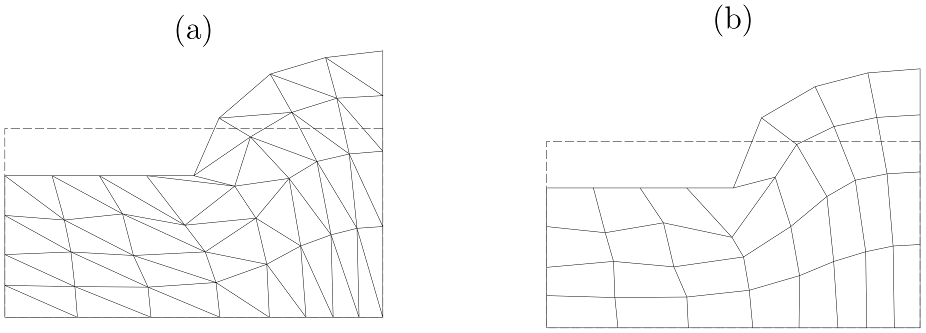

Figure 6.15: Indentation of a rubber block. (a) *F-bar-Patch* 3-noded triangle with patches of two elements; (b) 4-noded *F-bar* quadrilateral.

Reese, 1996). For comparison, the result of a similar simulation with 4-noded *F-bar* quadrilaterals (and a 32 element mesh), which also predict a reasonable coarse mesh deformed shape, is presented in Figure 6.15(b).

Rubber cylinder pressed between two plates

The numerical simulation of the compression of a rubber cylinder pressed between two frictionless rigid plates is carried out in this example. This problem was analysed in detail by Sussman & Bathe (1987) who made a careful comparison with existing analytical and experimental results within the context of the u/p formulation. Simo & Taylor (1991) and de Souza Neto *et al.* (1996) also employed the same example to illustrate, respectively, the performance of a mixed low order formulation in conjunction with an augmented Lagrangian procedure and the *F-bar* technique near the incompressible limit. The geometry of the problem and boundary conditions are illustrated in Figure 6.16(a).

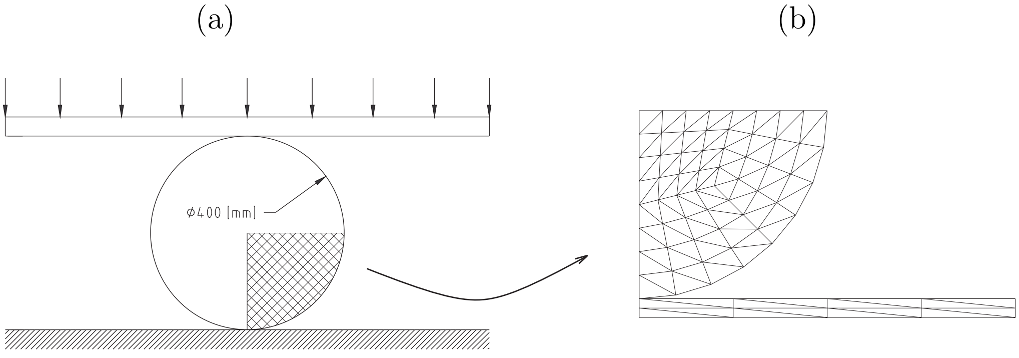

Figure 6.16: Rubber cylinder. (a) Geometry and boundary conditions; and (b) Initial finite element mesh.

Following Sussman & Bathe (1987) the cylinder made out of rubber is idealised using a regularised Mooney-Rivlin description (as in the previous example), with $C_1 = 0.293\,[MPa]$, $C_2 = 0.177\,[MPa]$ and bulk modulus $k =$

1410 $[MPa]$. Again, a high bulk modulus (as compared to the constants C_1 and C_2) enforces (near-)incompressibility. Plane strain state is assumed and, for symmetry reasons, only one quarter of the cylinder cross section is modelled. The symmetric quarter is initially discretised with a mesh of 48 quadrilaterals. To employ the present formulation, each quadrilateral of the original mesh is split into a patch of two *F-bar-Patch* triangles, resulting in the mesh of 96 triangles shown in Figure 6.16(b). The contact constraint is enforced by means of the classical penalty method (Perić & Owen, 1992). The final deformed configuration obtained with a prescribed displacement $u = 250\,[mm]$ of the plate is depicted in Figure 6.17(a).

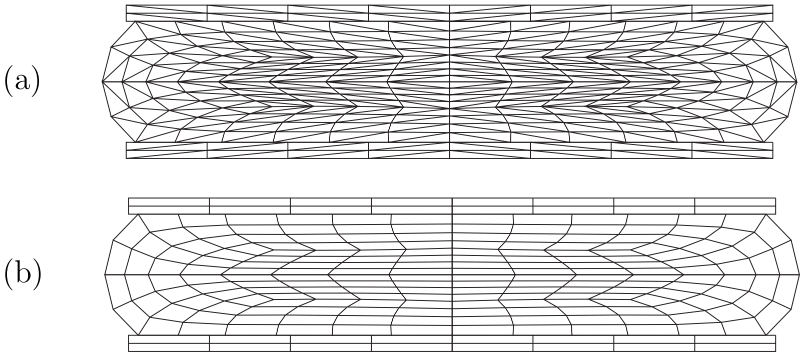

Figure 6.17: Rubber cylinder. Deformed mesh at u=250 $[mm]$.(a) *F-bar-Patch* method with patches of 2 linear triangles; (b) *F-bar* bi-linear quadrilateral.

The deformed mesh of the symmetric cross-section quarter has been mirrored into the remaining three quadrants. Again, for comparison, the result obtained with the *F-bar* quadrilateral is shown in Figure 6.17(b). There is a good qualitative agreement between the two deformed meshes. The reaction forces per unit thickness on the plate, for the Mooney-Rivlin model, are plotted in Figure 6.18 against the plate deflection. The curves are plotted up to $u = 200\,[mm]$. Also shown in Figure 6.18 is a force-deflection curve obtained using the regularised 3-term Ogden material model with the constants given in Table 6.3 (and same bulk modulus adopted with the Mooney-Rivlin material).

Table 6.3: Rubber cylinder. Material constants for Ogden model.

$\mu_i\,[MPa]$	α_i
0.746	1.748
-0.306	-1.656
6.609x10^{-5}	7.671

These coefficients were chosen to fit the same experimental data as the Mooney-Rivlin model. For both constitutive models there is an excellent agree-

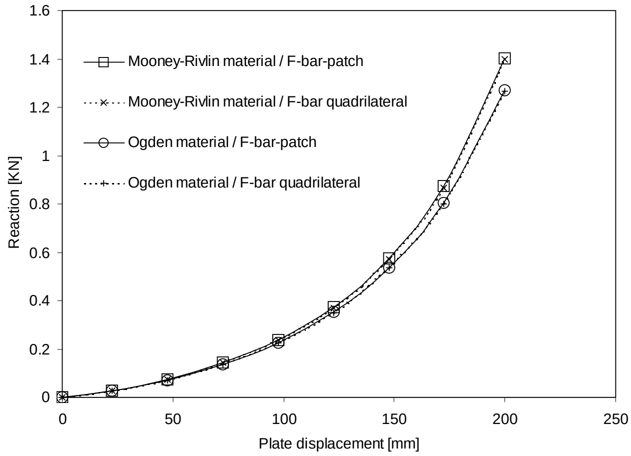

Figure 6.18: Rubber cylinder. Force-deflection curves.

ment between the reactions predicted by the present element and the 4-noded *F-bar* quadrilateral.

Elastomeric bead compression

The simulation of the compression of an elastomeric axisymmetric bead is carried out in this example. In reference (de Souza Neto *et al.* , 1996), this problem has been used to study the performance of the axisymmetric version of the 4-node quadrilateral F-bar element and the axisymmetric enhanced element Q1/E5 under high compressive strains. Here we use this example to assess the performance of the axisymmetric *F-bar-Patch* linear triangle. The bead – a circular ring with trapezoidal cross section – is schematically represented in Figure 6.19. The bead provides sealing when the plate, which contacts its top

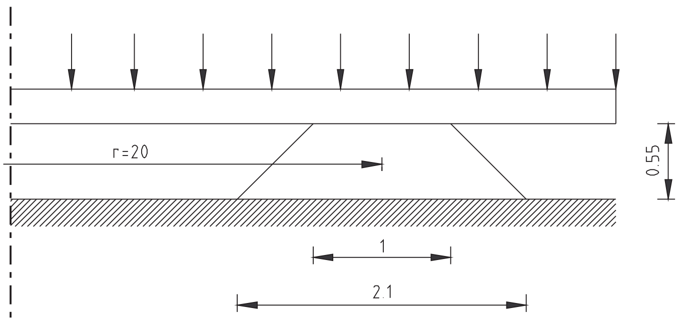

Figure 6.19: Elastomeric bead compression. Initial geometry and boundary conditions (dimensions in $[mm]$).

surface, is pressed downwards. In the finite element simulation, the bottom surface of the ring seal is assumed clamped to a flat rigid base and both plate and base are idealised as rigid bodies with frictionless contact condition on the boundaries. The bead is modelled as a regularised neo-Hookean material with shear modulus μ=5 $[MPa]$ and bulk modulus k=1000 $[MPa]$. A mesh of 520 quadrilateral elements is first generated and then each quadrilateral is split into a patch of 2 *F-bar-Patch* triangles, making up a total of 1040 triangles. Figure 6.20 (a) shows the mesh in its initial configuration. The compression of the bead is simulated here with both the axisymmetric version of the 3-node triangle proposed and the 4-noded axisymmetric *F-bar* quadrilateral. A total vertical displacement u =0.25$[mm]$ is applied to the plate. This corresponds to a 45% compression of the bead. Deformed meshes obtained at different stages of the compression process are depicted in Figure 6.20.

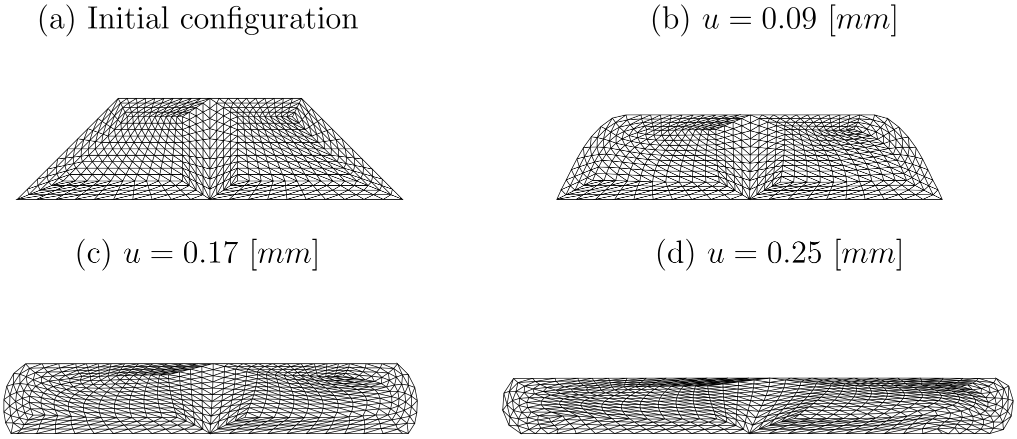
(a) Initial configuration
(b) $u = 0.09$ $[mm]$
(c) $u = 0.17$ $[mm]$
(d) $u = 0.25$ $[mm]$

Figure 6.20: Elastomeric bead compression. Finite element discretization on the initial configuration and deformed meshes obtained with the present element.

At the early stage shown in Figure 6.20(b), the lateral surfaces of the bead make contact only with the top of the plate. The contact constraint is enforced with the penalty method. Here a nodal penalty approach is adopted with penalty factor $p_N = 3 \times 10^5$ $[N/mm]$. At the later stages of Figure 6.20(c) and (d), contact also occurs with the rigid base. The reaction-displacement curve obtained is plotted in Figure 6.21.

There is an an excellent agreement between the reactions predicted by the *F-bar-Patch* axisymmetric triangle and the 4-noded *F-bar* axisymmetric quadrilateral. For comparison, the deformed meshes obtained with the original *F-bar* quadrilateral element are shown in Figure 6.22. These are in very good agreement with the deformed meshes shown in Figure 6.20 for the present element.

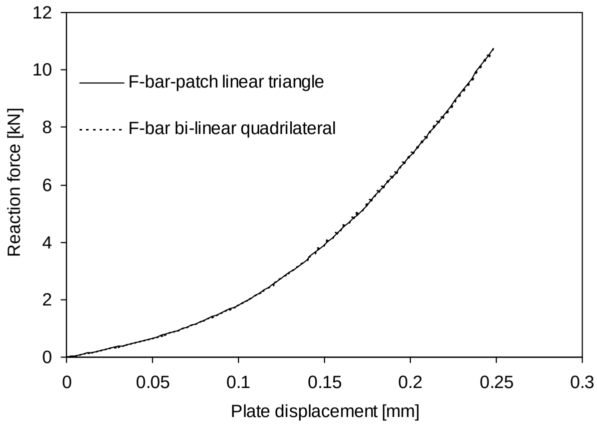

Figure 6.21: Elastomeric bead compression. Displacement-reaction diagram.

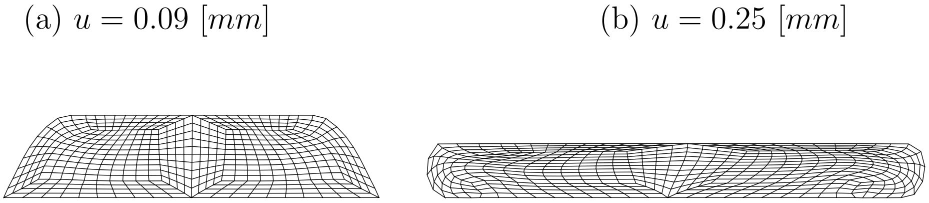

Figure 6.22: Elastomeric bead compression. Deformed meshes obtained with the *F-bar* bi-linear axisymmetric element.

Stretching of a double notched specimen

This example considers the plane strain simulation of the stretching of a double notched elastoplastic specimen. The geometry, boundary conditions and material properties have already been described in Section 6.3.3. The geometry of the problem is illustrated in Figure 6.5(a) [page 134]. Only one symmetric quarter of the specimen, discretised by the 150 element mesh shown in Figure 6.5(a), is also used in the simulation. Again, patches of 2 *F-bar-Patch* triangles are used (each patch making up one square in this case). The loading programme consists of prescribing the vertical displacement of the top nodes of the mesh [indicated by the arrows in Figure 6.5(a)] incrementally up to a total displacement $u = 0.3\,[\text{mm}]$. The total edge reactions per unit thickness obtained in the simulation is plotted versus the prescribed displacement in Figure 6.23.

The results obtained with the standard isoparametric linear triangle as well as the 4-noded *F-bar* quadrilateral are also plotted for comparison. It is apparent from these results that the displacement formulation does not exhibit a limit load. This is in sharp contrast with the response exhibited by

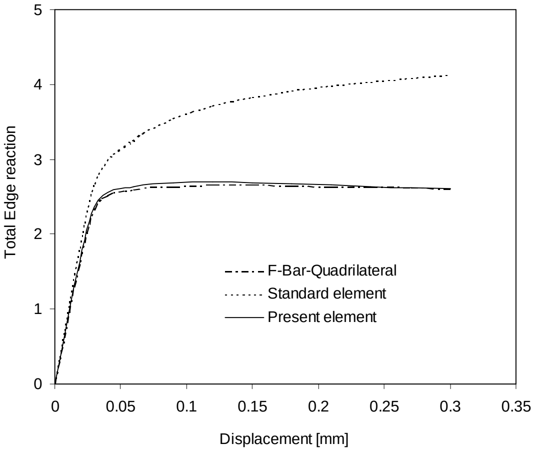

Figure 6.23: Stretching of a double notched specimen. Reaction-displacement diagram (reactions in $[KN]$).

the present element and the *F-bar* quadrilateral which, clearly, capture a limit load. The reaction-displacement curve predicted by the present formulation is very close to the one obtained with the *F-bar* quadrilateral.

Unconstrained elastoplastic test

The purpose of this test is to give an insight into the adequacy of a finite element to capture strain localisation phenomena in large strain elasto-plastic problems under plane strain. It has been used by Simo & Armero (1992) to

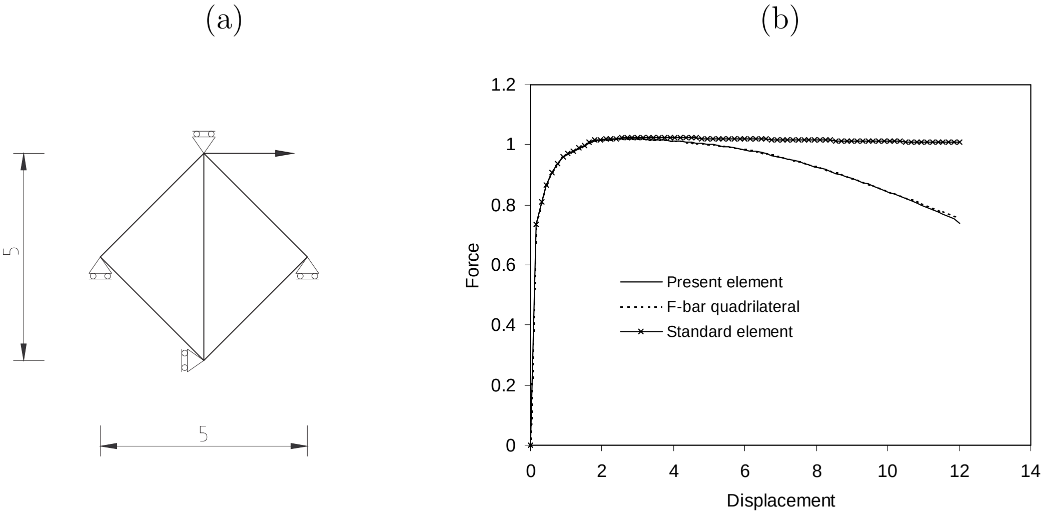

Figure 6.24: Unconstrained elastoplastic test. (a) Geometry and boundary conditions; (b) Force-displacement curve.

study the performance of the enhanced strain element Q1/E4 and in reference (de Souza Neto *et al.* , 1996) to assess the 4-noded *F-bar* quadrilateral. Here, this benchmarking test is carried out for the proposed 3-noded *F-bar-Patch* element. The results are compared to similar computations with the 4-noded *F-bar* element. The problem is schematically represented in Figure 6.24(a). In its original form (Simo & Armero, 1992; de Souza Neto *et al.* , 1996) a single 4-noded quadrilateral element is used. Here, a patch of 2 *F-bar-Patch* triangles, as shown in Figure 6.24(a), is tested. The kinematic constraints are also indicated in Figure 6.24(a). The loading consists of a prescribed horizontal displacement, u, applied to the top node. The material model adopted is identical to the one of the previous example except that the perfect plasticity assumption is replaced here with an isotropic hardening/softening law where the yield stress is given as a function of the equivalent plastic strain, R, as:

$$\sigma_y(R) = \sigma_0 + (\sigma_\infty - \sigma_0)[1 - \exp(-\delta R)] + HR,$$

with constants:

$$\sigma_0 = 0.45\,[GPa],\ \ \sigma_\infty = 0.715\,[GPa],\ \ \delta = 16.93,\ \ H = -0.012924\,[GPa].$$

The corresponding force per unit thickness, P, obtained in the numerical simulation is plotted in Figure 6.24(b). It can be seen that both the proposed element and the *F-bar* quadrilateral, are able to capture the global softening that characterises strain localisation. This indicates a possible suitability of the *F-bar-Patch* triangle for localisation problems. The results obtained with the standard 3-node triangle are also plotted and show that, for this element, no softening occurs. The deformed configurations, at u=10.5 [mm], of each of these elements discussed are depicted in Figure 6.25. The final deformed

(a) Present element (b) *F-bar* quadrilateral

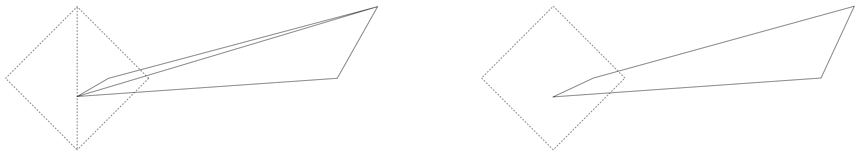

(c) Standard element

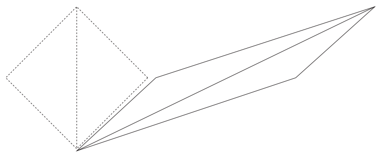

Figure 6.25: Unconstrained elastoplastic test. Final configurations at u=10.5 [mm].

configuration obtained with the patch of 2 *F-bar-Patch* triangles is very similar to that of the *F-bar* quadrilateral. In contrast, severe locking is exhibited by the standard triangle as a consequence of the element-wise enforcement of the plastic incompressibility constraint.

Plane strain localisation

This example illustrates the performance of the proposed 3-noded F-bar-Patch triangle in a full plane strain elasto-plastic boundary value problem involving strain localisation. The geometry, boundary conditions and material properties have already been described in Section 6.3.3 [page 134]. It simulates the occurrence of shear bands during the finite stretching of an elastoplastic rectangular bar. The bar is schematically illustrated in Figure 6.6 [page 135]. In references (Tvergaard *et al.* , 1981; Simo & Armero, 1992; de Souza Neto *et al.* , 1996), meshes of 4-noded quadrilaterals have been used. Here, the adopted mesh has been obtained by splitting each quadrilateral of the mesh of reference (de Souza Neto *et al.* , 1996) into a patch of 2 *F-bar-Patch* triangles.

The present element exhibited an excellent performance in capturing strain localisation in this problem. This can be seen in Figure 6.26, where deformed meshes for two stages of the simulation are presented. The figure shows in detail the deformed meshes in the central region of the bar obtained with the proposed *F-bar-Patch* method and the *F-bar* quadrilateral (whose behaviour is

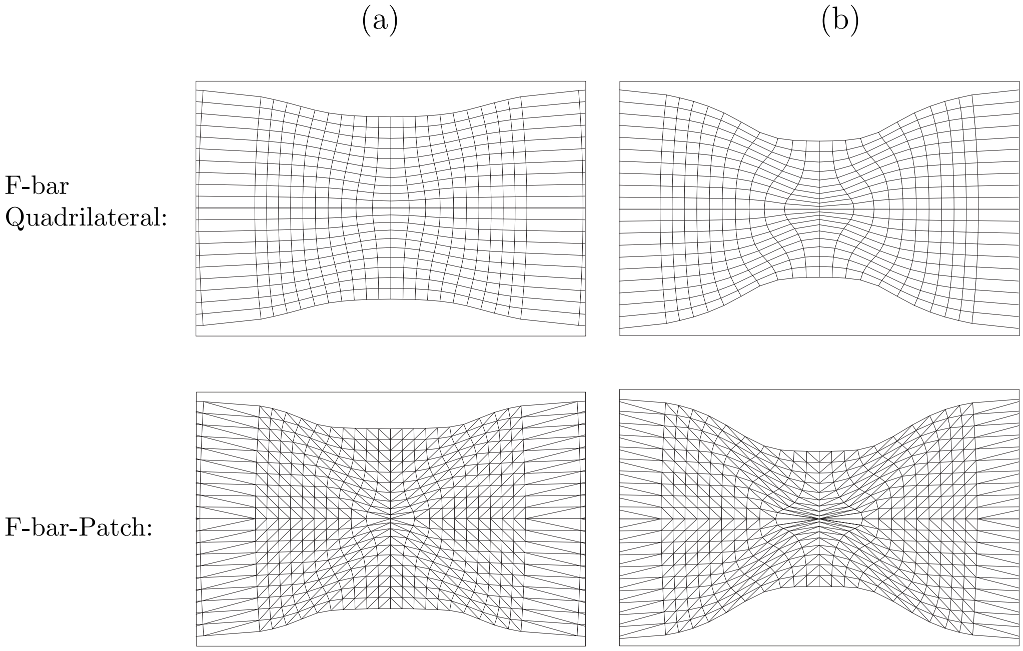

Figure 6.26: Plane strain localisation. Deformed configurations at two stages of imposed displacement: (a) $u = 4.0\,[mm]$; (b) $u = 4.9\,[mm]$.

regarded as excellent for such problems). In the initial stage of the deformation process, the specimen is maintained in an essentially homogeneous state of deformation. Subsequently, when the reaction load at the constrained edges reaches its peak value, a diffuse necking starts to develop, as seen in Figure 6.26(a). Finally, at a further stage depicted in Figure 6.26(b), the deformation mode changes to a pattern involving shear bands forming 45 degrees with the axial direction of loading. The distribution of effective plastic strain in the shear band zone during the different stages of the deformation process is depicted in Figure 6.27. The development of localised plastic strains within the characteristic shear bands can be clearly seen.

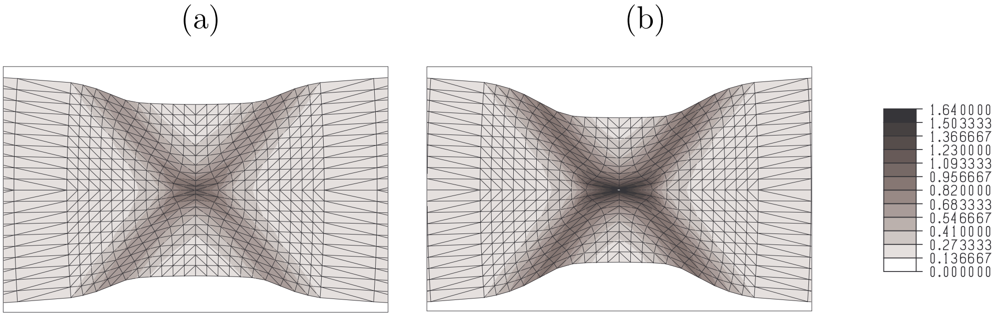

Figure 6.27: Plane strain localisation. Effective plastic strain distribution in the necking region at different stages: (a) $u = 4.0\,[mm]$; (b) $u = 4.5\,[mm]$.

The reaction force obtained on the constrained edge is plotted in the diagram of Figure 6.28 against the prescribed edge displacement. The results obtained with the *F-bar* quadrilateral and the conventional isoparametric linear triangle are also plotted. The reactions obtained with the present formulation

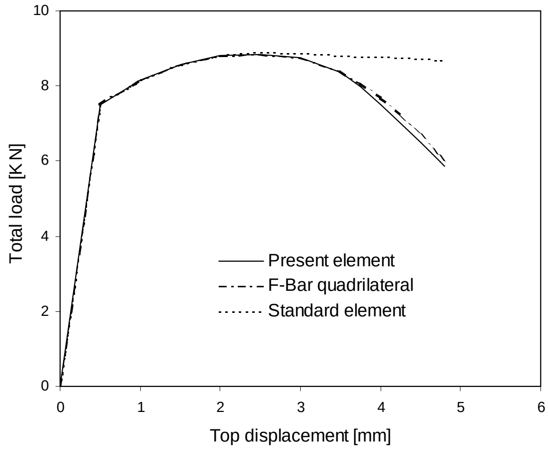

Figure 6.28: Plane strain localisation. Force-displacement diagrams.

follow very closely those obtained with the *F-bar* quadrilateral. The substantial decrease in the reaction forces occurring near $u = 3.0\,[mm]$ corresponds to the onset of shear band formation. For the conventional triangle, localisation does not occur and the reaction force remains high even at the later stages of loading. Figure 6.29 shows the discrete (non-smoothed) distribution of hydrostatic pressure obtained with the proposed element and the *F-bar* quadrilateral. The pressure distribution obtained with the present scheme is similar to that obtained by the *F-bar* quadrilateral. In particular, it is quite smooth and, very importantly, does not exhibit the checkerboard pattern typically associated with volumetric locking.

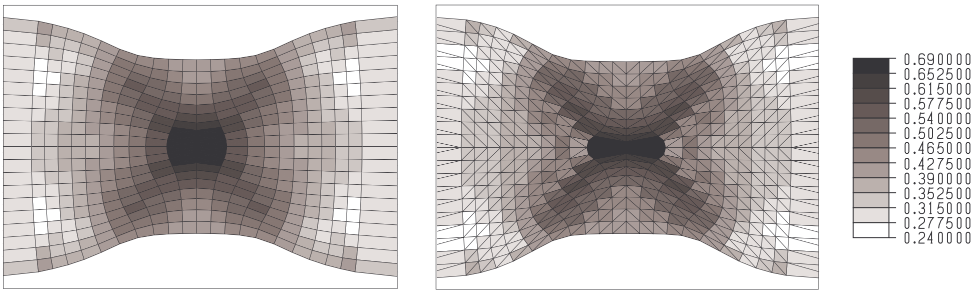
(a) (b)

Figure 6.29: Plane strain localisation. Discrete pressure distribution for $u = 4.5\,[mm]$: (a) *F-bar* quadrilateral; (b) *F-bar-Patch* triangle.

Necking of a cylindrical bar

This example is concerned with the simulation of the necking of a cylindrical metal bar, with diameter of $12.826\,[mm]$ and length of $53.334\,[mm]$, in a tensile test. This problem has been used to assess the nodal average volume technique in Section 6.3.3 [page 136] and is a well known benchmark (Simo & Armero, 1992; de Souza Neto *et al.* , 1996) to investigate the performance of the specially treated axisymmetric and three-dimensional elements in large strain localisation problems under plastic incompressibility. The material is assumed to be elastoplastic, modelled by J_2-flow theory with the isotropic hardening/softening given by:

$$\sigma_y(R) = \sigma_0 + (\sigma_\infty - \sigma_0)[1 - \exp(-\delta R)] + HR,$$

with constants

$$\sigma_0 = 0.45, \quad \sigma_\infty = 0.715, \quad \delta = 16.93, \quad H = 0.12924.$$

The resulting law is strictly hardening (without softening).

Axisymmetric analysis The problem is firstly analysed using the 2-D axisymmetric model. Therefore, only one quarter of the longitudinal cross-section of the bar is discretised with the appropriate boundary conditions being imposed on the symmetry lines. A geometric imperfection of 1.8% radius reduction is introduced at the centre of the bar and linearly extended to the leftmost boundary to trigger the necking. In order to improve the necking patterns at high levels of deformation the finite element mesh has 16 uniform divisions through the bar radius, while 24 divisions in the axial direction are approximately obtained by geometric progression from the center to the leftmost boundary of the bar. The mesh of 48x32 3-node axisymmetric elements, with initial geometry shown in Figure 6.30, is used.

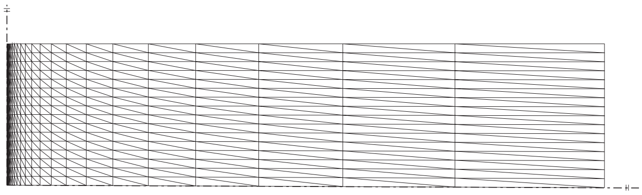

Figure 6.30: Necking of a cylindrical bar. Initial finite element mesh for axisymmetric analysis.

A vertical displacement $u = 7.0\,[mm]$ is imposed incrementally at the leftmost boundary of the bar. The final deformed mesh, in which the development of necking in the central zone can be clearly seen, is plotted in Figure 6.31(b). For comparison, the deformed mesh obtained with the 4-noded *F-bar* quadrilateral is plotted alongside in Figure 6.31(b). The deformed geometries obtained with both elements are in very close agreement. The hydrostatic pressure distribution obtained with the axisymmetric version of the proposed element is

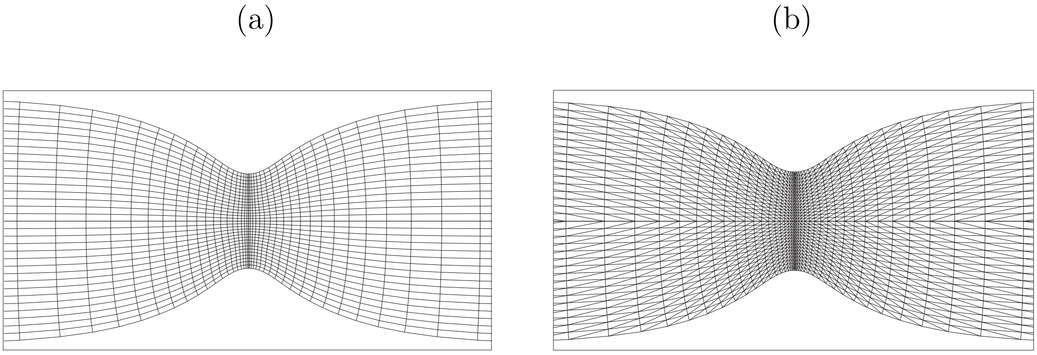

Figure 6.31: Necking of a cylindrical bar. Axisymmetric analysis. Deformed mesh with imposed displacement $u = 7.0\,[mm]$ (a) *F-bar* bi-linear quadrilateral; (b) *F-bar-Patch* method with patches of 2 linear triangles.

also in close agreement with the pattern obtained with the *F-bar* quadrilateral. This can be observed in Figure 6.32, where the discrete (non-smoothed) pressure contour plot obtained with both elements is shown.

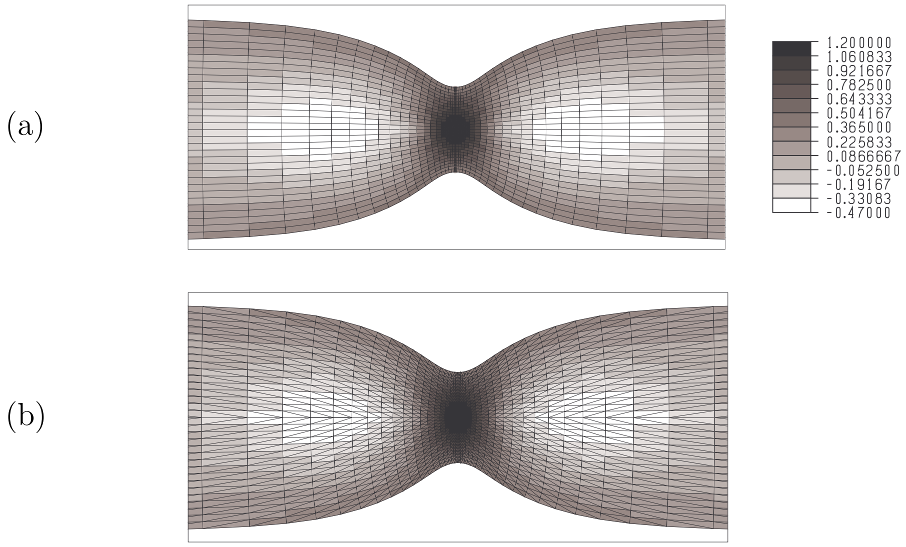
(a)
(b)
1.200000
1.060833
0.921667
0.782500
0.643333
0.504167
0.365000
0.225833
0.0866667
-0.052500
-0.19167
-0.33083
-0.47000

Figure 6.32: Necking of a cylindrical bar. Axisymmetric analysis. Discrete pressure distribution for $u = 7.0\,[mm]$: (a) *F-bar* quadrilateral; (b) *F-bar-Patch* triangle.

Figure 6.33 shows that the reaction-displacement curve obtained with the present element is also in close agreement with the result obtained with the *F-bar* quadrilateral.

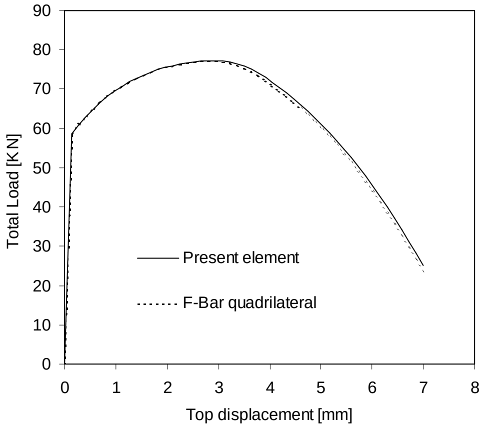

Figure 6.33: Necking of a cylindrical bar. Axisymmetric analysis. Force-displacement curves.

Three-dimensional analysis In order to assess the performance of the *F-bar-Patch* 4-noded tetrahedron, a three-dimensional analysis of the necking problem is carried out here. To permit a direct comparison with existing hexahedral elements each of the example problems uses a regular block of six tetrahedral elements to form a dodecahedron. This topology has appropriate symmetry between opposing faces which permits use of simple block generation routines to generate conforming meshes. Two different meshes, of 5760 and 14400 three-dimensional elements, shown in Figure 6.34 are used to discretize the symmetric octant of the specimen, with the appropriate boundary conditions imposed at the symmetry planes.

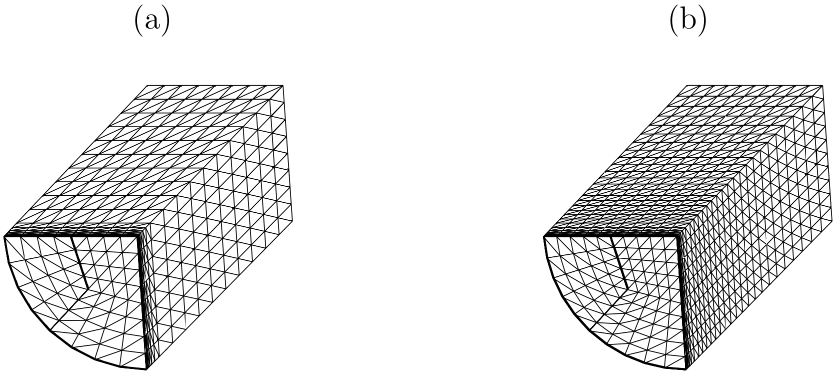

Figure 6.34: Three-dimensional necking of a cylindrical bar. (a) Initial mesh with 5760 elements; (b) Initial mesh with 14400 elements.

The final deformed configurations (corresponding to u=7.0 [mm]) obtained for both meshes are shown in Figure 6.35. It can be seen that the two meshes

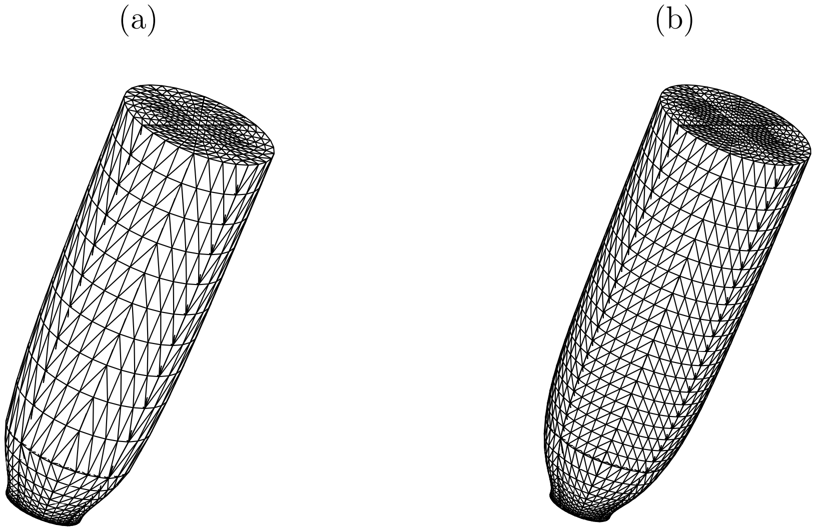

Figure 6.35: Three-dimensional necking of a cylindrical bar. Deformed configurations at u=7.0 [mm].(a) Mesh with 5760 elements; (b) Mesh with 14400 elements.

are able to predict correctly the necking phenomenon. This illustrates the suitability of the proposed *F-bar-Patch* for problems involving strain localization. We remark that the final shape resulting from the simulation with 14400 four-node tetrahedra is virtually identical to that predicted by the simulation where 768 axisymmetric three-noded triangular *F-bar-Patch* elements (with patches of 2 elements) has been employed. The force-displacement curves obtained for the 3-D simulations are plotted in Figure 6.36 along with the results of the axisymmetric analysis. The results for the finer 3-D mesh are almost undistinguishable from those obtained from the axisymmetric simulation.

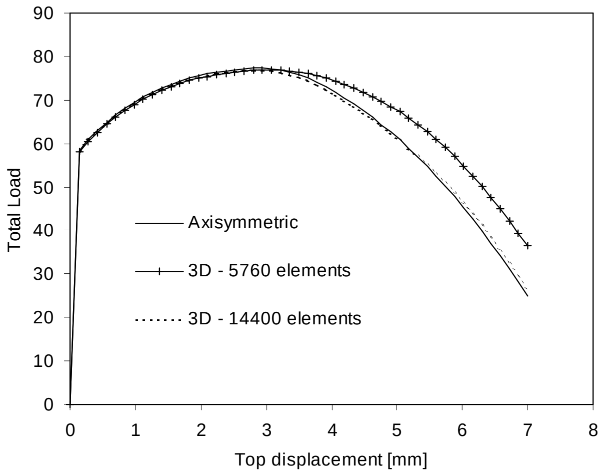

Figure 6.36: Axisymmetric and 3-D necking. Force-displacement diagrams.

This same problem is used to investigate the *F-bar-Patch* method with each patch composed of eight linear tetrahedra. In this case, an unstructured mesh generator is used. The following procedure is applied. An initial finite element mesh of ten noded tetrahedra is initially generated. Once this step is completed each element is split into 8 linear tetrahedral elements. The initial and final deformed configurations (corresponding to u=7.0 [mm]) obtained using this strategy are shown in Figure 6.37. In order to improve the computational necking pattern at high levels of deformation the finite element mesh is very fine in the necking region with a total of 15000 four-noded tetrahedral elements.

We remark that the final shape resulting from the simulation with 14400 four-node tetrahedra with each patch composed of six linear tetrahedra [see Figure 6.35(b)] is virtually identical to that predicted by the simulation with 15000 four-node tetrahedra with each patch composed of eight linear tetrahedra [see Figure 6.35(b)]. The force-displacement curves obtained for the 3-D simulations are plotted in Figure 6.38 along with the results of the 3-D version of the standard tetrahedral element. The results for the 3-D simulations of the *F-bar-Patch* method with each patch composed of eight linear tetrahedra

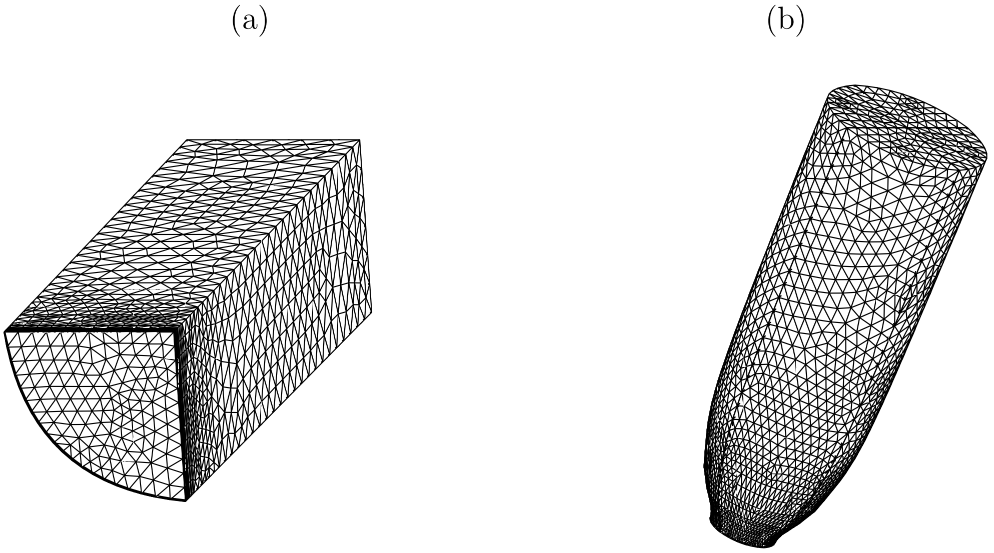

Figure 6.37: Three-dimensional necking of a cylindrical bar. (a) Initial configuration; (b) Deformed configuration at u=7.0 [mm].

are almost undistinguishable from those obtained with each patch composed of six linear tetrahedra. It is important to note that with a mesh of 15000 four-node standard displacement tetrahedra elements, the occurrence of severe locking has been observed. This is clearly illustrated in Figure 6.38 by the high reaction force observed at the late stages of loading.

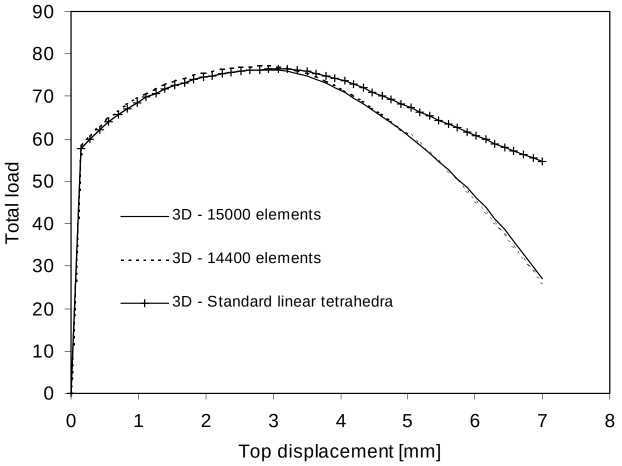

Figure 6.38: Axisymmetric and 3-D necking. Force-displacement diagrams.

This result indicates that the proposed methodology circumvents the volumetric locking response that characterises conventional linear simplex elements. This new method using each patch composed of eight linear tetrahedra allows the use of an unstructured mesh generator. This type of mesh generator is currently very robust and is able to handle complex geometry.

Upsetting of a cylindrical billet

The purpose of this example is to assess numerically the performance of the three-dimensional *F-bar-Patch* under investigation in highly strained situations arising in compression problems. The three-dimensional simulation described below corresponds to the upsetting of a cylindrical elastoplastic billet. The billet, with radius 9 $[mm]$ and height 30 $[mm]$ is compressed between two flat tools (assumed rigid) subjected to sticking contact on the interface. A J_2 elastoplastic material is assumed, but a linear hardening rule is adopted:

$$\sigma_y(R) = \sigma_{yo} + HR,$$

with $\sigma_{yo} = 0.45$ and the hardening modulus H=0.7 $[MPa]$. The Young's modulus and Poisson ratio are, respectively, E=200.0 $[GPa]$ and ν=0.3, corresponding to:

$$\mu = 76.92\,[GPa], \qquad\qquad k = 166.67\,[GPa].$$

The initial tool/workpiece configuration is schematically illustrated in Figure 6.39(a). Due to obvious symmetry considerations, only a quarter of the specimen needs to be considered.

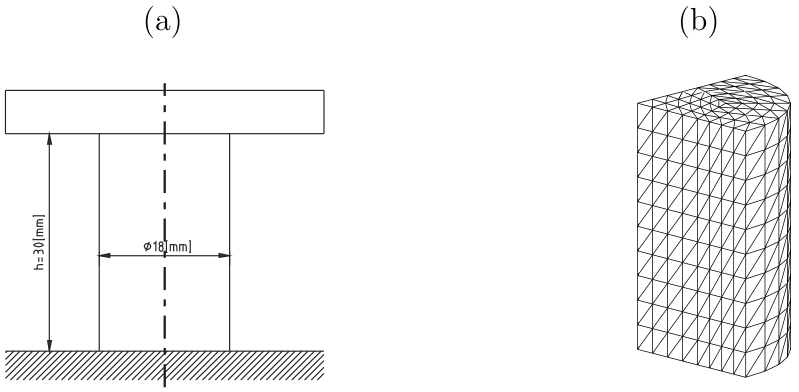
(a)
(b)

Figure 6.39: Upsetting of a cylindrical billet. (a) Initial tool/workpiece configuration; (b) Initial mesh.

The initial finite element mesh, shown in Figure 6.39(b), consists of a total of 2880 elements. The contact condition that takes place at high compressive strains between the planes defined by the upper and lower base and the lateral surface of the specimen is enforced via a conventional nodal penalty formulation. We note that the isochoric character of the plastic flow together with the very large plastic deformations result in a nearly incompressible response of the specimen. Figure 6.40 depicts the solution obtained with the proposed element.

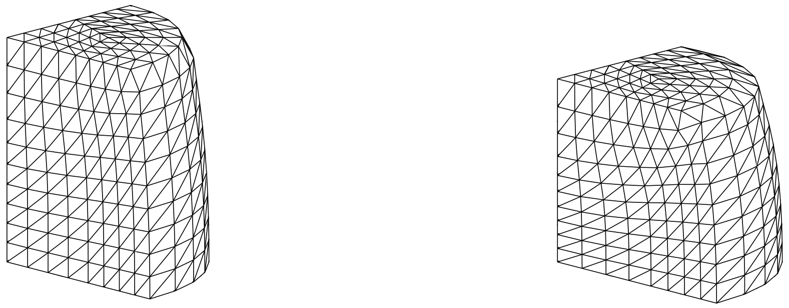

(a) 20 % compression (b) 35 % compression

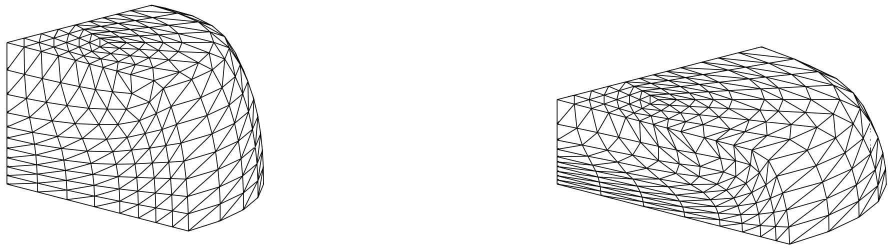

(c) 50 % compression (d) 70 % compression

Figure 6.40: Upsetting of a cylindrical billet. Deformed configurations at different reductions for the proposed element.

The results demonstrate that a good performance should be expected from this element in highly strained compressive situations. In Figure 6.41 the reaction force versus the cylinder reduction is plotted for the proposed three-dimensional element and the *F-bar* hexahedron. Inspection of this result reveals an overall agreement between the reactions obtained by the two elements. Nevertheless, a slight difference becomes noticeable when the contact constraint is enforced between the exterior elements and the top rigid surface.

For comparison, the deformed meshes obtained with the original *F-bar* hexahedron, in the latter stages of compression, are shown in Figure 6.42.

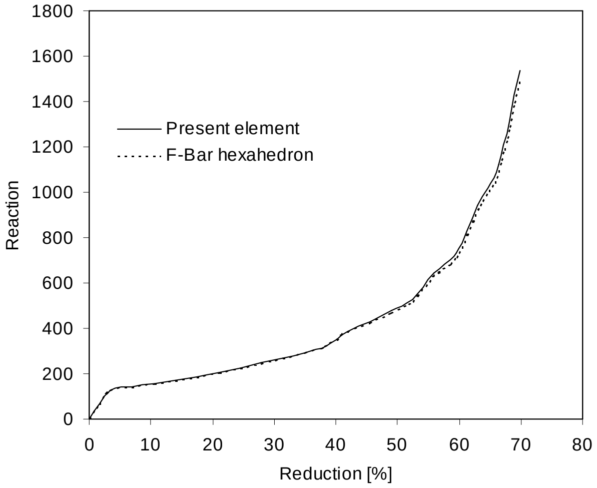

Figure 6.41: Upsetting of a cylindrical billet. Load versus reduction curves obtained with different elements.

There is a good qualitative agreement with the deformed meshes shown in Figure 6.40(c) and (d) for the present element.

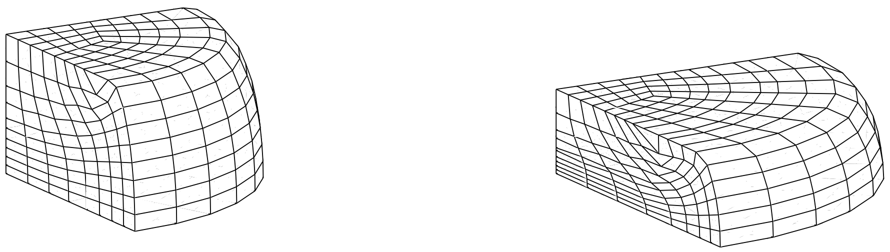
(a) (b)

Figure 6.42: Upsetting of a cylindrical billet. Deformed configurations at different reductions for the *F-bar* hexahedron. (a) deformed mesh at 50% compression; and (b) deformed mesh at 70% compression.

6.4.7 Explicit implementation

Despite the recent remarkable advance of implicit solution techniques, contact detection in a multi-fracture environment constitutes a major obstacle to use of implicit schemes to simulate problems such as metal cutting operations. In the simulation of fracturing of ductile materials where crack advance is typically preceded by nearly isochoric strains, conventional simplex elements are known to produce unacceptably inaccurate solutions due to the phenomenon of *volumetric locking*. Therefore, we adapt the above concepts for use within an explicit transient dynamic finite element environment. In the context of metal plasticity – our main area of interest – plastic flow is typically isochoric and the hydrostatic stress is a function of the total volumetric strain. This observation allows the derivation of a straightforward procedure whereby, before the stress update is carried out, say, with the Green-Naghdi based algorithm of Box 4.2, the volumetric component of the incremental strain is re-computed in a simple manner following the *F-bar-Patch* concept. The implementation of the procedure requires nothing more than a simple pre-processing operation on $\Delta\boldsymbol{\varepsilon}$ before the application of the conventional stress updating algorithm.

We start by assuming a hydrostatic pressure constitutive equation of the form:

$$p = K\,(\bar{J} - 1)\,, \tag{6.46}$$

where $\bar{J}$ is the volumetric ratio of the patch $\mathcal{P}$ of simplex elements. Now, considering the typical time interval $[t_n, t_{n+1}]$, we perform all operations of items (i)–(iii) of Box 4.2, without modification. The pre-processing is then carried out just before the small strain algorithm is called, from item (vi) of Box 4.2. The extra operations are as follows:

1. Retrieve the hydrostatic pressure of time t_n (beginning of the current step):

$$p_n := \tfrac{1}{3}\,\mathrm{tr}\,\boldsymbol{\sigma}_n \tag{6.47}$$

2. Retrieve the modified volumetric ratio $\bar{J}$ at t_n using constitutive law (6.46):

$$\bar{J}_n := \frac{p_n}{K} + 1 \tag{6.48}$$

3. Compute the incremental modified volumetric ratio, $\bar{J}_\Delta$, according to:

$$\bar{J}_\Delta := \frac{\sum_{k\in\mathcal{P}} v^k_{n+1}}{\sum_{k\in\mathcal{P}} v^k_n}\,, \tag{6.49}$$

   where v^k_n and v^k_{n+1} are the deformed volumes of element k, respectively, at times t_n and t_{n+1}.

4. Compute the current total modified volumetric ratio, $\bar{J}_{n+1}$:

$$\bar{J}_{n+1} := \bar{J}_n \bar{J}_\Delta\,. \tag{6.50}$$

   Note that $\bar{J}_{n+1}$ represents the ratio between the undeformed and deformed (at t_{n+1}) volume of the patch $\mathcal{P}$.

5. Compute the modified incremental strain, $\Delta\bar{\varepsilon}$, according to the expression:

$$\Delta\bar{\boldsymbol{\varepsilon}} := \Delta\boldsymbol{\varepsilon} + [(\bar{J}_{n+1} - \bar{J}_n) - \operatorname{tr}\Delta\boldsymbol{\varepsilon}]\,\boldsymbol{I}\,. \tag{6.51}$$

Finally, the above modified incremental strain is passed on to the procedure of Box 4.2 where the stress updating (integration of constitutive equations) is carried out without modification. Note that, following the procedure of Box 4.2, the hydrostatic component of the update stress tensor will satisfy:

$$p_{n+1} = p_n + K\operatorname{tr}\Delta\bar{\boldsymbol{\varepsilon}} = p_n + K\,(\bar{J}_{n+1} - \bar{J}_n) = K\,(\bar{J}_{n+1} - 1)\,. \tag{6.52}$$

The hydrostatic pressure is identical for all elements $k \in \mathcal{P}$.

6.4.8 Numerical examples

The performance of the proposed *F-bar-Patch* methodology for an explicit transient dynamic finite element environment is assessed in this section by means of two numerical examples. The first example evaluates the performance of the technique under extremely large deformation and the second investigates the element behaviour when combined with a pressure sensitive constitutive model.

Impact of a cylinder against a rigid wall

The first example studied is that of an impact with a rigid surface of a cylindrical copper bar moving with a relatively high speed. This well known example is a classical benchmark (Zhu & Cescotto, 1995; Zienkiewicz *et al.* , 1998; Bonet & Burton, 1998) usually employed to calibrate numerical algorithms. Here, it is used to illustrate the performance of the element formulation, proposed in Section 6.4.7, under extremely large deformation.

The bar of initial length of 32.4 $[mm]$ and initial radius of 3.2 $[mm]$ impacts a rigid, frictionless wall at 227 $[m/s]$. The material is elasto-plastic (von Mises yield surface with linear isotropic hardening) and the properties of the copper are defined in Table 6.4.

Table 6.4: Copper bar material properties.

Description	**Symbol**	**Value**
Specific mass	ρ	8930 $[kg/m^3]$
Elastic Modulus	E	117 $[GPa]$
Poisson's ratio	ν	0.35
Initial yield stress	σ_{Y0}	400 $[MPa]$
Hardening modulus	H	100 $[MPa]$

The deformation of the projectile has to be computed up to a time of $t{=}80\,[\mu s]$, at which almost all the kinetic energy has been transformed into plastic deformation.

Axisymmetric analysis The problem is firstly analysed using the 2-D axisymmetric model. Therefore, only one half of the bar is discretised with the appropriate boundary conditions being imposed on the symmetry line. The finite element mesh employed has 6 uniform divisions through the bar radius, with 72 divisions in the axial direction. The initial and final deformed shapes obtained using different formulations are shown in Figure 6.43. The

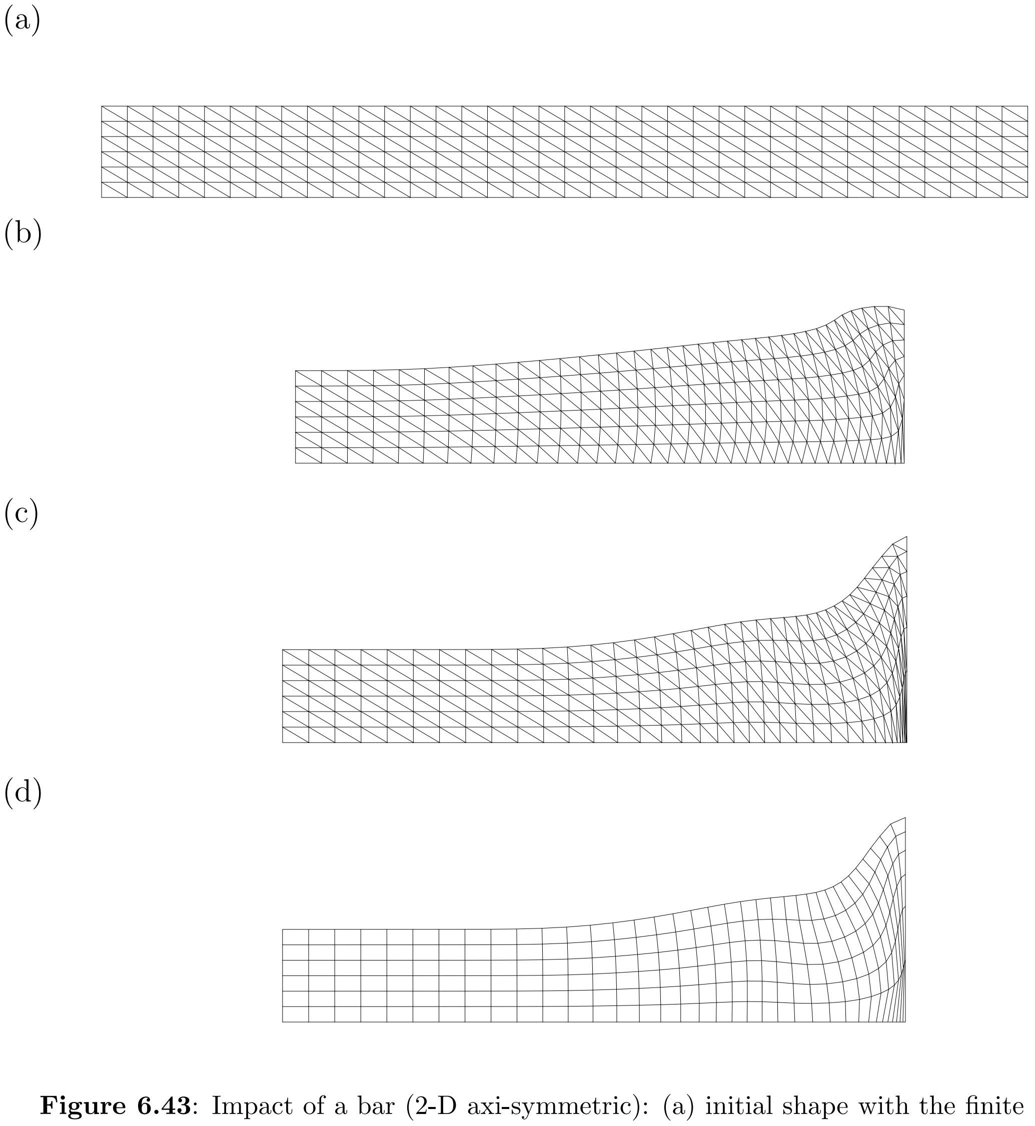

Figure 6.43: Impact of a bar (2-D axi-symmetric): (a) initial shape with the finite element discretization; (b) standard element; (c) *F-bar-Patch* triangle; (d) quadrilateral (Belytschko & Bindeman, 1991).

problem was initially analysed using the standard triangle and then with the new *F-bar-Patch* formulation. Deformed shapes for both cases are shown in Figure 6.43(b),(c). Comparing these results with those obtained with the quadrilateral element (Belytschko & Bindeman, 1991), volumetric locking is clearly observed for the standard element. In contrast, the deformed shape obtained with the new triangle compares very well with those obtained from the quadrilateral element.

Three-dimensional analysis In order to assess the performance of the *F-bar-Patch* 4-noded tetrahedron, a three-dimensional analysis of the impact problem is carried out here. The final deformed shapes obtained using different element formulations are shown in Figure 6.44. The cylindrical bar has been discretized with 972 hexahedral elements and 5932 tetrahedral elements.

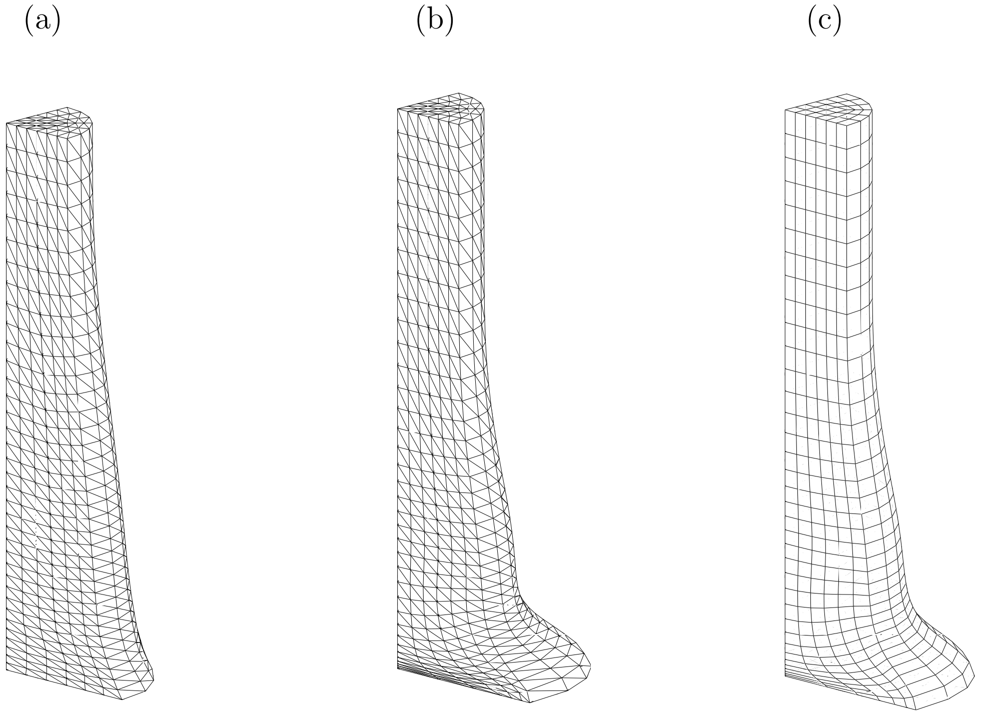

Figure 6.44: Impact of a bar: (a) standard element; (b) *F-bar-Patch* tetrahedron; (c) hexahedron (Belytschko & Bindeman, 1991).

Again, by comparing these results, volumetric locking is clearly observed for the standard element. In contrast, the deformed shape obtained with the new tetrahedron compare well with those obtained from the hexahedron element.

Tensile test

The classical tensile test of an axisymmetric notched specimen, is used to illustrate the performance of the element formulation when combined with a pressure sensitive constitutive model. The geometry, boundary conditions and material properties have already been described in Section 5.4.4 [page 99]. The initial finite element mesh used, for two-dimensional and three-dimensional cases, is depicted in Figure 6.45. A relatively fine discretisation is used in the region surrounding the smaller cross-section, in order to capture the necking pattern and damage evolution.

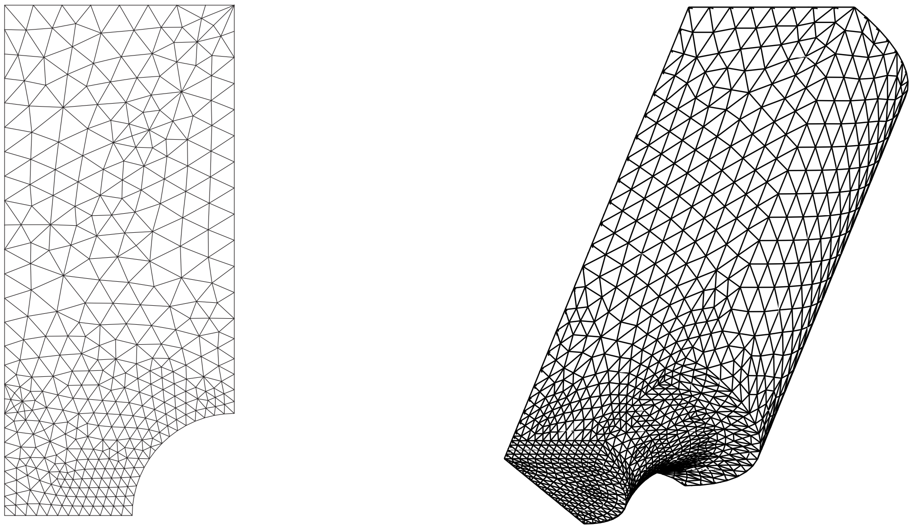

(a) Two dimensions (b) Three dimensions

Figure 6.45: Axisymmetric notched bar.Initial finite element mesh.

Axisymmetric analysis The problem is firstly analysed using the 2-D axisymmetric model. So, only one quarter of the longitudinal cross section of the notched specimen is discretised [see Figure 6.45 (a)] with the appropriate boundary conditions being imposed on the symmetry lines. The loading consists of a prescribed vertical displacement (with free horizontal displacement) of the constrained edge. A total number of 724 three-noded axisymmetric triangles has been used in the discretisation amounting to a total of 403 nodes. The analysis undertaken here, employs the damage algorithm proposed in Chapter 5. The evolution of the damage variable field obtained in the finite element analysis is illustrated in the contour plots shown in Figure 6.46.

It can be seen that during the early stages of the loading process, maximum damage is detected near the root of the notch. As the specimen is progressively stretched, the maximum damage area moves gradually toward the centre of the specimen and localises there. At the final stage with $u = 0.6\,[mm]$ damage is highly localised around the centre.The simulation results obtained using the present framework, are in close agreement, with the ones obtained in Section

(a) $u = 0.21\,[mm]$ (b) $u = 0.36\,[mm]$

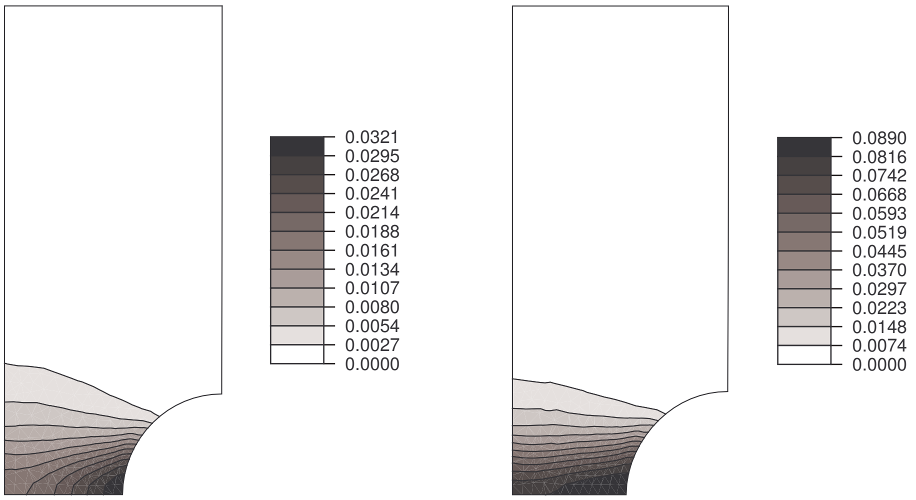

(c) $u = 0.45\,[mm]$ (d) $u = 0.6\,[mm]$

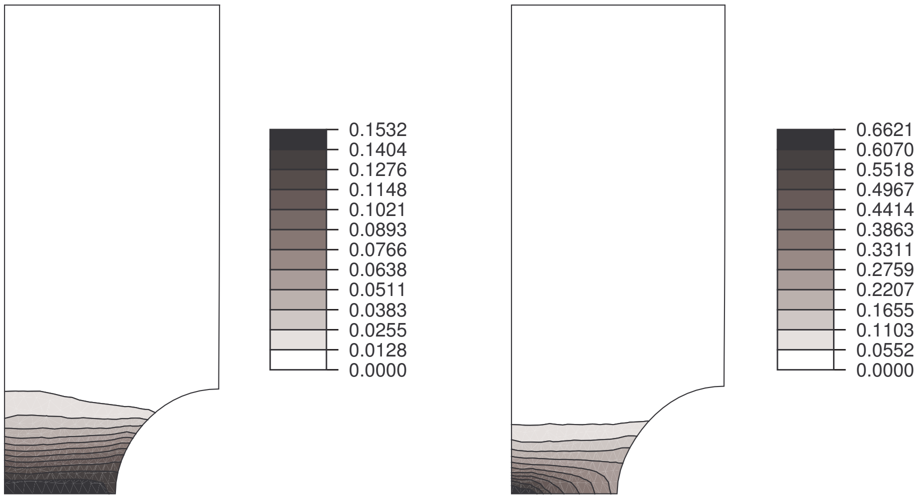

Figure 6.46: Axisymmetric notched bar. Damage contour plots.

5.4.4 [page 99] but using an *implicit time integration scheme*. In this example, the standard three-noded displacement based isoparametric triangle promotes a completely erroneous prediction (not shown here) of the failure location. The severe volumetric *locking* that characterises this element completely invalidates the finite element solution.

Three-dimensional analysis In order to assess the performance of the proposed 4-node tetrahedron, a three-dimensional analysis of the above problem is carried out here. Patches of 8 tetrahedra are used. Such a choice is motivated by the fact that 8-element patches can be easily generated by unstructured tetrahedral mesh generators regardless of the complexity of the geometry considered. Only one symmetric octant of the bar is discretised (see Figure 6.45 (b)) with the appropriate boundary conditions being imposed on the symmetry planes. A total number of 17,216 four-noded tetrahedra have been used in the discretisation amounting to a total of 3,718 nodes. The evolution of the damage variable field obtained in the finite element analysis is illustrated in the contour plots shown in Figure 6.47.

(a) $u = 0.21\,[mm]$ (b) $u = 0.36\,[mm]$

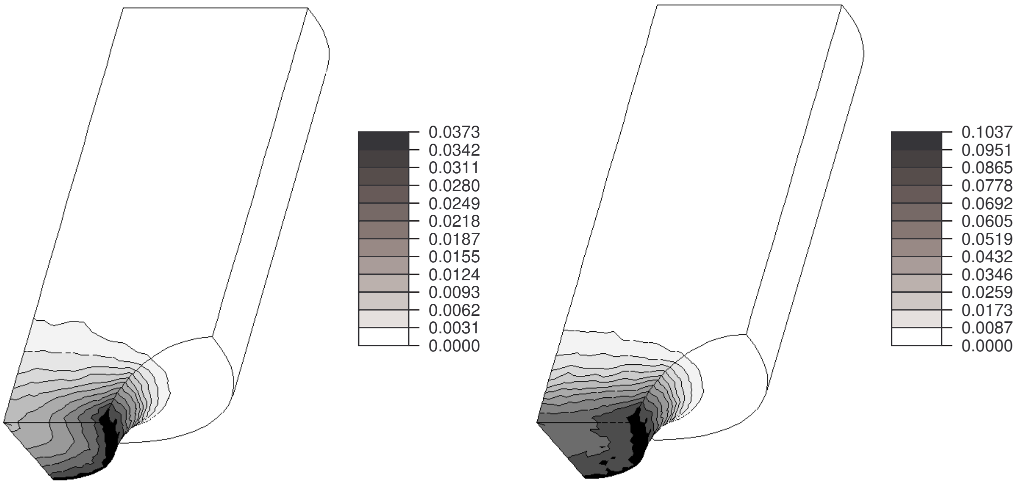

(c) $u = 0.45\,[mm]$ (d) $u = 0.6\,[mm]$

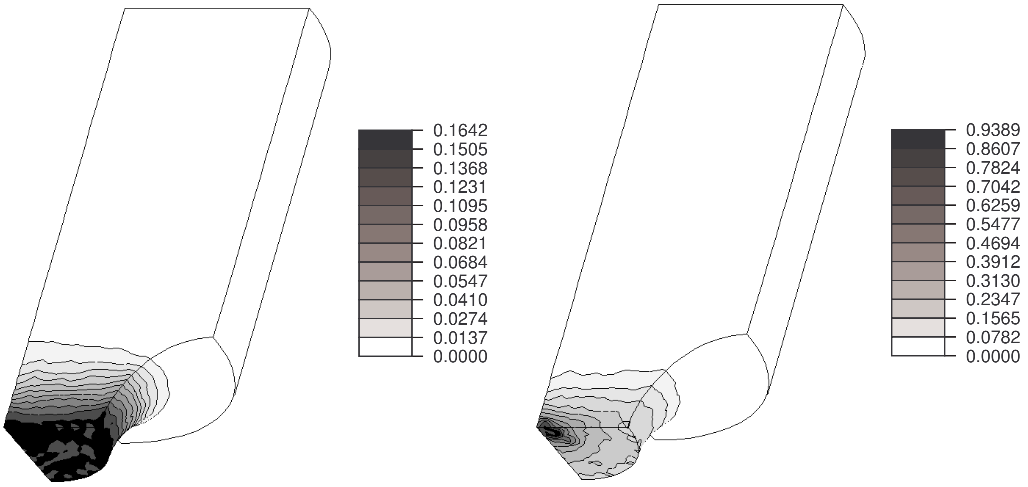

Figure 6.47: Three-dimensional notched bar. Damage contour plots.

It can be concluded that the evolution of the damage field observed in the three-dimensional simulation, conforms with the axisymmetric pattern described previously. The damage contour at the final stage of the loading [see Figure 6.47(d)] localises around the centre of the specimen, with a very sharp gradient. This result indicates that the 4-node tetrahedron proposed here, circumvents the volumetric locking that characterises conventional linear simplex elements. In addition, the new elements have shown no signs of spurious mechanisms. As mentioned before, this new method allows the use of an unstructured mesh generator, which is currently very robust and is able to handle complex geometry. In a similar situation, the average nodal pressure element (Bonet & Burton, 1998) produces considerable checkerboard-type hydrostatic pressure fluctuations. Such fluctuations, in conjunction with strongly pressure-dependent constitutive equations (such as the damage law adopted here) invalidate the finite element solution.

6.5 Concluding remarks

A thorough assessment of the volumetric nodal average concept (Bonet & Burton, 1998) has been presented. The assessment has been carried out based on an implict version of the formulation obtained within the framework of the *F-bar* methodology (de Souza Neto *et al.* , 1996). In this context, a linear triangle for implicit plane strain and axisymmetric analysis of nearly incompressible solids has been devised. A comprehensive set of numerical has been presented. The examples have shown that the nodal averaging technique substantially reduces the locking tendency of the linear triangle and produces quite reasonable predictions of deformed shapes as well as reaction forces. However, the examples have also shown that the element can produce considerable checkerboard – type hydrostatic pressure fluctuations. This fact, prevents the successful use of the average nodal volume technique in situations where an accurate prediction of hydrostatic pressure is required.

A new methodology which allows the use of two- and three-dimensional simplex finite elements in the large strain analysis of nearly incompressible solids has been proposed. The technique is an extension of the *F-bar* method of reference (de Souza Neto *et al.* , 1996). It relies essentially on the relaxation of the excessive volumetric constraint typical of low order elements through the enforcement of the incompressibility constraint over a *patch* of simplex elements. An important aspect of the present method is that (as the original *F-bar* procedure) it preserves the displacement-based format of the corresponding finite element equations as well as the strain-driven format of standard algorithms for integration of dissipative constitutive equations and can be used regardless of the material model adopted.

As far as the computational implementation of the new elements is concerned, the calculation of the corresponding element internal force vector is relatively straightforward and its incorporation into existing finite element codes requires only simple changes to the relevant routines of isoparametric simplex elements. However, the corresponding tangent stiffness – required in the implicit implementation of the technique – possesses a rather unconventional format. Its incorporation into an existing code requires more substantial changes, particularly in the global stiffness assembly operations. The unconventional stiffness format stems from the fact that the internal force vector of a particular element depends on the nodal displacements of all elements of its patch.

A comprehensive set of numerical examples, including some well known benchmark tests, have shown that the proposed technique has effectively overcome the volumetric locking that characterises conventional simplex elements. In addition, the new elements have shown no signs of spurious mechanisms. The examples involved hyperelastic as well as elasto-plastic problems, including strain localisation.

CHAPTER 7

ADAPTIVE REMESHING FOR HISTORY DEPENDENT PROBLEMS IN SOLID MECHANICS

THE numerical simulation of finite strain plasticity problems presents a higher degree of complexity compared to its elastic structural counterparts. Due to the nature of the strains that characterise a large number of industrially relevant solid mechanics problems, it is frequently the case that a mesh of high quality in the initial configuration of the workpiece, with optimal element aspect ratio throughout, degenerates to such an extent during the simulation that the numerical procedure may fail to produce any results of practical interest. In addition to acceptable element aspect ratio, mesh quality implies sufficient refinement in areas where the relevant fields present steeper gradients. These areas are the portions of the workpiece where most of the *action* localises, i.e., where the relevant dissipative mechanisms are most active. Such areas are not known in advance and, in addition, their location within the domain may vary as the simulation proceeds.

In this context, the introduction of an effective adaptive mesh refinement procedure, capable of ensuring that high quality meshes are used over the entire process simulation, is crucial. The ideal mesh should be fine enough to capture the solution accurately, but at the same time be as coarse as can be allowed, to limit computational effort and permit the practical use of a finite element framework within an industrial environment.

The present chapter focuses on some issues relevant for adaptive solutions of large deformations of elasto-(visco)plastic solids at finite strains, which ensure a successive improvement of the numerical solution. A detailed description of the basic ingredients of the adaptive remeshing strategy adopted in this thesis is also included. In particular Section 7.3 discusses some options for error indicators while Section 7.6 further discusses some aspects of transfer operators occurring in large deformation problems. The main objective is to develop an adaptive strategy, relevant for practical large-scale simulations, which reflects the dynamic nature of the physical phenomena. This strategy should be able to capture the progression of plastic deformation, damage and also to produce efficiently refined meshes in regions of possible material failure.

7.1 Introduction

Let $\boldsymbol{u}$ denote the exact solution and let $\boldsymbol{u}^h$ be the discrete finite element solution. It is possible to define the error in the displacement field by

$$\boldsymbol{e}_u = \boldsymbol{u} - \boldsymbol{u}^h. \tag{7.1}$$

In the same way, the error in the stress field can be defined as

$$\boldsymbol{e}_\sigma = \boldsymbol{\sigma} - \boldsymbol{\sigma}^h. \tag{7.2}$$

Over the last years, a considerable body of research has been focused on the development of adaptive strategies that provide a finite element discretization which is accurate and reliable. Adaptive techniques rely on *indicators* and/or *estimators* which are able to predict the error given by (7.1) or (7.2). These quantities reveal the error of the finite element solution (e.g. Johnson (1987) and references therein). Based on the error field distribution, a new refined mesh can be constructed which yields a better approximate solution.

Currently, the formal structure of adaptive finite element methods for linear elliptic problems is well understood and it is possible to provide a theoretical unifying framework, which encompasses most of the existing procedures. Such analysis has been presented by Verfürth (1996), for instance. The maturity reached in the theory of linear elliptic partial differential equations (Evans, 1999) and their finite element approximation has instigated the understanding of the mechanism of error propagation. This has lead to a solid foundation upon which effective and reliable techniques of error estimation and adaptive refinement may be established. Although certain issues still remain unresolved, it may be said that nowadays, adaptive strategies for linear problems can be routinely performed within finite element computations. Among numerous contributions, the work by Babuška & Rheinboldt (1978), Zienkiewicz & Zhu (1987), and surveys by Johnson & Hansbo (1992), Oden *et al.* (1989), and Zienkiewicz & Taylor (2000) illustrate the basic ideas and numerical strategies.

Even though some advances have been recorded for certain classes of nonlinear problems, the current position of adaptive approaches for history dependent nonlinear problems in solid mechanics is not so well established. In particular, the understanding of the mechanisms of error propagation, which also depend on *time*, and the correlated transfer operation can be considered to be on its early stages of development. This is reflected in the scarcity of studies dedicated to the matter and of originality of the approaches, which usually try to adapt ideas developed for linear problems. Relevant contributions are given by Ladèveze *et al.* (1986), Belytschko *et al.* (1989), Ortiz & Quigley IV (1991), Johnson & Hansbo (1992), Lee & Bathe (1994), Perić *et al.* (1994, 1996), Gallimard *et al.* (1996), Barthold *et al.* (1997) and Wriggers (2002) amongst others.

The key components, described consecutively in the following sections, required for the implementation and successes of an adaptive strategy are,

- Entity/Assignment based model definition;
- Indication of the error associated with a given finite element mesh;
- Prediction of the new mesh density;
- Mesh regeneration based upon the density of the new mesh;
- Accurate transfer of material and process data between the old and new finite element meshes.

7.2 Entity based model description

All the process data (e.g. loads and boundary conditions) of the problem, must be defined independently of the initially generated finite element mesh to enable the design of a flexible adaptive strategy. To support this requirement it is necessary to generate a so-called *System Hierarchy*.

The system hierarchy will typically consist of control points at the lowest level; these points are then joined using line entities. In turn, a set of lines will be joined together to form a surface and finally, for 3D geometries a set of volumes can be formed from the grouping of adjacent surfaces. These may be imported via CAD interfaces or defined parametrically within a graphical pre-processor.

This original model is then utilised throughout the simulation, in conjunction with the geometry defined by the current deformed state, to transfer the process data to newly generated meshes.

7.3 *A posteriori* error estimates

One of the main difficulties associated with the use of the finite element, and other approximate methods, is related to the accuracy, i.e., closeness of the approximation to the solution of the original problem. Since the closed form is not, in general, available the so-called error estimation techniques have been proposed. In this work, our attention will be focused in *a posteriori* error estimates, that is, estimates of a given measure of the error that are constructed after the finite element solution has been computed, and they utilize the finite element solution and the input data of the case under study.

A posteriori error estimates play an important role in two related aspects of finite element calculations. First, such estimates provide the user of a finite element code with valuable information about the overall accuracy and reliability of the calculation. Secondly, since most *a posteriori* error estimates are computed locally, they also contain significant information about the distribution of error among individual elements, referred to as error indicators, which can form the basis of adaptive procedures.

In the solution of history-dependent problems, error estimation is a crucially important component of any adaptive strategy. The effectiveness of the procedure is directly related to the ability of the adopted error estimation scheme to predict what parts of the discretised domain have to be refined/de-refined and what degree of mesh fineness is needed to maintain the solution error within the prescribed bounds. Therefore, in the next section a brief overview on some error estimators for non-linear problems is given. The objective is mainly to illustrate the motivating ideas behind each of the proposed techniques, rather than attempting to provide a (necessarily incomplete) list of error estimators.

7.3.1 Error estimation for non-linear problems. A brief overview

For history dependent nonlinear problems in solid mechanics, the theory of error estimation can be considered to be in its early stages of development. Although it is difficult to make a classification of the techniques of estimation in the presence of so many sources of nonlinearity, both in *time* and *space*, it may be useful to distinguish between several contributions as follows (Gallimard, 1994):

- Error estimators for problems where the time variable does not appear;
- Error estimators which attempt to estimate also the effects of the time discretization;
- Error in the constitutive equations;
- Methods based on heuristic considerations leading to the development of error indicators.

Nonlinear incremental problem These type of estimates, have been developed by looking at the error associated with the finite element approximation of the non-linear incremental boundary value problem obtained from a one-time step discretization of the initial problem.

One of the first approaches to a theoretically justified *a posteriori* error estimate for the finite element approximation of plasticity problems was given in Johnson & Hansbo (1992). These authors analysed the regularized version of the Hencky problem in small strain perfect plasticity with von Mises yield criterion. This problem has also been considered by Rannacher & Suttmeier (1998). As a special case, they obtain an *a posteriori* error estimate of the energy norm via a duality argument applied to a linearized dual problem. Duality has also been employed to derive *a posteriori* error estimates for nonlinear variational problems. The work of Repin & Xanthis (1996) represents an important contribution in this sense. Further developments were addressed by Han & Reddy (1999) and Alberty *et al.* (1999) amongst others.

Analysis of the time discretization error The error estimates presented above, though based on solid theoretical background, by definition do not account for the error deriving from the replacement of the rate quantities appearing in the initial boundary value problem. Furthermore, an inherent difficulty in obtaining a complete *a posteriori* error estimation is related to the different nature of discretization in *time* and *space*.

Rannacher & Suttmeier (1999) present a fairly complete analysis for the mixed-dual formulation of the quasi-static Prandtl-Reuss model. The same authors also set up a theoretical framework for *a posteriori* error analysis of the time discretization error based on duality. To this end, the solution of the problem is seen as arising from the use of a space-time approximation which uses discontinuous Galerkin method for the time discretization and standard finite elements for the discretization in space. A similar approach has also been adopted by Larsson *et al.* (2001) in the space-time discretization of viscoplasticity. Following an heuristic argument Barthold *et al.* (1997) proposed, in the context of small strain elasto-plasticity, a spatial error estimate based on comparative analysis of Prandtl-Reuss elasto-plasticity and Hencky plasticity. The error indicator was assumed to be dependent on the elastic (free energy function), plastic (dissipation) components and loading/unloading Kuhn-Tucker conditions. The time discretization error is also included through the L_2 norm of the numerical integration error in the flow rule calculations.

Error in the constitutive equations A family of error measures with clear physical meaning and capable of accounting for the effects of time and space discretization is given by the error in the constitutive equations. The application of this theory to assess the quality of a finite element solution consists in building a corresponding *admissible solution* that reflects the approximations associated with the finite element solution.

The definition of this error is due to Ladevèze (1985) in the context of the non-incremental LATIN method applied to the solution of the evolution of elasto-viscoplastic materials, which follow the conditions of Drucker's stability. This error measure was then further investigated in the work of Coffignal (1987) and applied by Ladèveze *et al.* (1986) to evaluate the incremental finite element solution of the same class of problems. The error measure has a global character in time and space. Furthermore, due to its definition, it is not possible to distinguish the contribution to the error arising from time and space discretization, thus it cannot be used to drive an adaptive process. To remedy this, Gallimard (1994) and Gallimard *et al.* (1996) have applied the concept of error in the constitutive equations by using only time and space discretization, respectively. In this way, the authors have obtained error indicators that separate the effects of time and space discretization, respectively, which can then be used to control the discretization process.

Heuristic error indicators The emergence of supercomputer architectures has allowed large-scale simulations of engineering problems and the incorporation of more detailed physics in the numerical model. This has led to a substantial increase in the complexity of the simulation and has inspired the development of different error measures. As a result, adaptive strategies of these problems are often based on heuristic error indicators or adaption indicators.

The use of this type of error indicators is motivated by the fact that, it is possible to distinguish the elements and time steps, which contribute mostly to the global accuracy of the approximation. As a result, they provide an effective tool for the adaptive strategy in the sense that they may be used as a guide for a sequence of discrete choices (e.g. to refine or coarsen a given element; to reduce or increase a given time step). The success of this heuristic strategy is highlighted by the amount of published works employing this approach when compared to the development of other error estimates. Therefore, the next section is exclusively dedicated to this type of error indicator where the main underlying idea is presented together with a brief overview of some error indicators, that have been successfully employed in practice.

7.3.2 Residual and recovery based error indicators

The work, originally introduced by (Babuška & Rheinboldt, 1978, 1979), to estimate errors, considers local residuals of the numerical solution. By investigating the residuals occurring in a patch of elements or even in a single element it becomes possible to estimate the errors which arise locally. The topic gained momentum when Zienkiewicz & Zhu (1987) introduced error estimates based on post-processing techniques of the finite element solutions. The advent of Zienkiewicz and Zhu's estimator has not only encouraged the application of adaptive refinement procedures [1] to practical engineering problems, but also instigated a healthy discussion on the best approach to *a posteriori* error indicator.

---

[1] Basically, there exist two adaptive procedures, namely p and h-adaptive techniques. The former is achieved by increasing the order of the interpolation polynomial whereas the latter by reducing the element size.

Since these early works many players entered the field and today the procedures available for error estimation are essentially reduced to two strategies: the so-called *residual estimators*, based on Babuška-type strategy, and *estimators based on recovery* that rely on super convergence properties, after Zienkiewicz and Zhu's technique.

- *Residual estimators:* These estimators are based on the local computation of a suitable norm of the solution over one element or a small patch of elements [e.g Babuška (1978); Babuška & Rheinboldt (1978); Babuška *et al.* (1994a); Padra & Venere (1995)]
- *Estimators based on recovery/projection:* These estimators are based on fact that many finite element meshes have superconvergence properties, which means that there are points where the stresses are approximated with higher accuracy [e.g. Zienkiewicz & Zhu (1987, 1992b); Perić *et al.* (1994); Labbe & Garon (1995); Ramsey & Sbresny (1995); Lee & Lo (1997); Yazdani *et al.* (1997)]

Although both the recovery and residual based procedures have proven their importance, it was relevant to establish which of the particular methods was most accurate. This assessment was possible with the introduction of a methodology based on the so-called *Babuška patch test.* According to this approach the merit of each error estimator is judged by a *robustness index.* After conducting many tests, it was concluded that the robustness index was optimal for the recovery methods, with the residual methodology giving poorer results. This work is reported in the book by Babuška & Strouboulis (2001) and references therein.

Recovery based error indicators

To illustrate the underlying idea of recovery based error indicators, let us start by writing the *energy norm of the error* as follows (Zienkiewicz & Taylor, 2000)

$$|\boldsymbol{e}| = \left(\int_\Omega (\boldsymbol{\sigma} - \boldsymbol{\sigma}^h) : \mathsf{D}^{-1} (\boldsymbol{\sigma} - \boldsymbol{\sigma}^h) \, \mathrm{d}\Omega \right)^{\frac{1}{2}} \tag{7.3}$$

where its relation to strain energy is evident. In the previous equation the value of the exact stress, $\boldsymbol{\sigma}$, is unknown. Therefore, the key idea of this approach consists in computing the error $|\boldsymbol{e}|$ by replacing, $\boldsymbol{\sigma}$, with $\boldsymbol{\sigma}^*$, recovered by a suitable post-processing of the finite element solution, that is

$$|\boldsymbol{e}| = \left(\int_\Omega (\boldsymbol{\sigma}^* - \boldsymbol{\sigma}^h) : \mathsf{D}^{-1} (\boldsymbol{\sigma}^* - \boldsymbol{\sigma}^h) \, \mathrm{d}\Omega \right)^{\frac{1}{2}} \tag{7.4}$$

The quality and reliability of this type of error indicator is however dependent on the accuracy of the recovered solution. The procedures to build $\boldsymbol{\sigma}^*$ are, generally, referred to as the *stress recovery* or *derivative recovery* techniques. These methods rely on the observation that, under some conditions on the domain, mesh and regularity of the solution, there exist certain points where the derivatives of the finite element solution, which are usually one order lower than that of the finite element solution itself $\boldsymbol{u}^h$, have superior accuracy. This phenomenon is known as *superconvergence* (Zienkiewicz & Zhu, 1992b,a). This so-called superconvergent patch recovery (SPR) method led to very accurate recovered values which generally converged at a higher rate than the original solution and which gave a solid basis for error estimation.

One of the first reported works on application of error indicators to metal forming applications has been presented by Zienkiewicz *et al.* (1988) for steady-state extrusion using flow formulation. Application of this error estimate was later extended to analyse shear localization (Zienkiewicz *et al.* , 1988) and expanded for porous material models (Zienkiewicz *et al.* , 1990). Several other applications to nonlinear problems followed a similar approach, such as the work by Fourment & Huang (1995) and Moal & Massoni (1995).

A posteriori error indicators based on the Zienkiewicz-Zhu adaptive strategy and the energy norm have been appropriately modified by Perić *et al.* (1994) to account for the elastoplastic deformation of the conventional and Cosserat continuum model. A comparative evaluation of various error indicators for isotropic, elasto-plastic and viscoplastic solids undergoing large deformations has been carried out by Tetambe *et al.* (1995). This study shows that the error computed using several error indicators increases from its initial value as the deformation continues in the plastic zone for finite strains.

The adaptive procedures for large-deformation finite element analysis of elastic and elasto-plastic problems implemented by Lee & Bathe (1994), are based on a pointwise indicator for the error, for both the stresses and the plastic strain increments. The error in the stress field is obtained by evaluating the difference between the unaveraged stress, $\boldsymbol{\sigma}^h$, and a smoothed stress, $\boldsymbol{\sigma}^*$. An estimate of the error on plastic strain increment is computed by considering the L_2-norm of the difference between the plastic strain increments obtained using the trapezoidal rule, which is second order accurate, and the Euler backward method.

An adaptive refinement strategy for strain localization problems was proposed by Ortiz & Quigley IV (1991) based on the assumption that the minimization of interpolation error, is attained when some suitable norm of the solution is equi-distributed over the elements in the mesh. Therefore, the finite elements are targeted for refinement when the variation of the solution over each element is above a prescribed tolerance throughout the mesh. The application of error indicators, based on minimization of interpolation error, has been undertaken by Demkowicz *et al.* (1985) and Radovitzky & Ortiz (1999), among others. The estimation of the local errors is based on interpolation error bounds and extraction formulas for highly accurate estimates of the derivatives of the exact solution which appear in the bound.

It is important to emphasize that many different norms or measures of error can be used and that for some problems the *energy norm* is not in fact 'natural'. A good example of this is given by problems of strain localization in plastic softening, where very steep gradients can develop. Therefore, for applications where the physical nature of the problem requires a sharp resolution of high gradients of the state variables over a small region of the mesh, an extension of conventional error measures or indicators have proved to be advantageous (Vaz Jr., 1998; Owen & Vaz Jr., 1999; Perić *et al.* , 1999). In the next section, recovery based error indicators are appropriately modified to account for failure analysis.

7.3.3 Error indicators for failure analysis

In order to effectively model material failure the essential idea is to correlate the adaptive procedure to the underlying failure mechanism. To achieve this goal, the error indicator is defined as the *rate* of fracture indicators based on the principle that the adaptive procedure should not only capture the progression of the plastic deformation but also provide refined meshes at regions of possible material failure (Perić *et al.* , 1999).

Here, several ductile fracture criteria available in the literature are briefly reviewed and the suitability of an *a posteriori* error estimate based on the rate of these criteria is also discussed.

Ductile fracture criteria Ductile fracture criteria are of an approximative character, in which microscopic phenomena are described macroscopically by either experimental analysis or mathematical/physical models. The former employs an empirical approximation of experimental data, from which a critical fracture parameter is defined (e.g. Brozzo *et al.* (1972); Norris *et al.* (1978); Atkins (1981)) whereas the latter is often based on restrictive assumptions of void geometry, such as spheres (Rice, 1969; Gosh, 1976) and cylinders (McClintock, 1968), or material description, such as rigid-plastic (Rice, 1969; Oyane *et al.* , 1978) and rigid-perfectly-plastic (Tai & Yang, 1987) materials. A detailed survey of the assumptions and relative merits of different ductile fracture criteria in metal forming operations (low strain-rate) is presented in Vaz Jr. (1998).

It has been widely accepted that ductile fracture criteria should reflect the state of increasing damage of the material, i.e., the process evolution causes the damage state to increase leading to material fracture. Many authors acknowledge (Cockcroft & Latham, 1968; Hancock & Mackenzie, 1976; Oyane *et al.* , 1978; Norris *et al.* , 1978; Atkins, 1981; Tai & Yang, 1987; Mudry, 1985; Lemaitre, 1985a) that a ductile fracture criterion must account for: *stress-strain history*, *hydrostatic stresses* and *a suitable stress ratio*. Therefore, history-dependent fracture indicators, I_Ξ, can be represented as

$$I_\Xi = \int \Xi : \mathrm{d}\,\zeta \tag{7.5}$$

in which ζ represents scalar, vectorial or tensorial quantities upon which the fracture path is dependent and Ξ expresses a generic experimental/analytical failure criterion.

Remark 7.1 *Numerical analysis of material failure in metal forming processes using fracture indicators has brought a new insight to the problem by instigating extensive comparisons between existing fracture criteria. Clift* et al. *(1990) pioneered the comparative analysis by comparing numerical and experimental results for simple upsetting, axisymmetric extrusion and strip compression and tension. A similar approach was employed by Gouveia* et al. *(1996), who, based on the upset test, assess some fracture indicators for billets of different geometries. This type of comparison has been continuously undertaken by several researchers for a variety of materials, geometries and processes.*

Error indicator In order to capture the phenomena associated with ductile fracture more efficiently, by heuristic considerations, an *a posteriori* error estimate employed in the adaptive procedure can now be derived using the rate of the fracture indicator I_Ξ as

$$\dot{I}_\Xi = \Xi : \dot{\zeta} \tag{7.6}$$

following the procedure originally proposed by Zienkiewicz & Zhu (1987) and extended by Perić *et al.* (1994) for small-strain elasto-plasticity.

It is important to remark that, the performance of the error estimate is directly affected by the criterion on which it is based and will inherit its characteristics (Vaz Jr., 1998). In other words, if the failure criterion is not able to predict the material degradation, its error indicator will not provide refined meshes at regions of possible material failure. For instance, the error estimate based on the *rate of plastic work* (Perić *et al.* , 1996) can be associated with the fracture criterion known as *total plastic work* (Freudenthal, 1950). Although it has been one of the first indicators to be used in ductile fracture analysis, severe criticism has been raised on its reliability to predict ductile fracture in bulk forming operations (Atkins & Mai, 1985; Gouveia *et al.* , 1996).

On the other hand, the prediction of ductile fracture onset within the context of *Continuum Damage Mechanics* (see Chapter 5), usually adopts the damage variable itself as indicator by assuming that failure takes place when the damage variable attains a critical value, $D = D_{cr}$. Recent comparative analysis suggest that damage-based measures are more reliable in predicting the correct site of fracture initiation (Vaz Jr. & Owen, 2001) and the use of fracture criteria based on *total damage work*, generally defined as:

$$I_{\omega_D} = \int_0^t (-Y)\dot{D}\,dt = \int (-Y)\,dD, \tag{7.7}$$

offers a promising alternative, due to the high gradient exhibited by the indicator near the critical failure zone. Therefore, Vaz Jr. (1998) has employed an error indicator based on the *rate of damage work* by recognizing the suitability of energy measures associated with the damage process to describe ductile failure.

7.3.4 Error indicator based on damage dissipation

Since our main concern in this thesis is the modelling of progressive damaging, a successful adaptive strategy should be able to produce meshes that are capable of predicting correctly the growth of internal damage as well as its possible localisation leading to fracture initiation. Such a scheme can only be devised if the underlying physical mechanisms of the problem, described by means of the elasto-(visco)plastic damage models discussed in Chapter 5 (see Sections 5.4 and 5.5), are accounted for in the definition of the error indicator.

In defining an error indicator suitable for the present context we shall follow the procedure originally proposed by Zienkiewicz & Zhu (1987) for linear elliptical problems and extended by Perić *et al.* (1994) for small-strain elasto-plasticity. The *projection* technique is adopted due to its simplicity and efficiency demonstrated in both linear elliptic (Babuška *et al.* , 1994a,b; Zhang & Zhu, 1995), and elasto-(visco)plastic non-linear problems (Fourment & Huang, 1995; Marusich & Ortiz, 1995; Lee & Lo, 1997; Perić *et al.* , 1999). Analogous to the approach of Perić *et al.* (1994, 1996), who proposed an indicator based on the plastic dissipation to capture plastic strain localisation, it makes sense here to adopt a procedure based on the *damage dissipation* or *rate of damage work*:

$$\omega_D = (-Y)\dot{D}\,, \tag{7.8}$$

where $-Y$ is the damage energy release rate defined in expression (5.60) and rewritten here,

$$\begin{aligned} Y \;=\; & \frac{-1}{2E(1-D)^2}\left[(1+\nu)\,\boldsymbol{\sigma}_+ : \boldsymbol{\sigma}_+ - \nu\,\langle \mathrm{tr}\,\boldsymbol{\sigma}\rangle^2\right] \\ & - \frac{h}{2E(1-hD)^2}\left[(1+\nu)\,\boldsymbol{\sigma}_- : \boldsymbol{\sigma}_- - \nu\,\langle -\mathrm{tr}\,\boldsymbol{\sigma}\rangle^2\right]. \end{aligned} \tag{7.9}$$

A similar definition, based on the original Lemaitre damage model described in Section 5.3 (page 70), without crack closure effects, has been successfully adopted by Vaz Jr. & Owen (2001) in the context of strain localisation with damage.

Let us now consider a generic mesh h and let $\dot{D}^h$ and $(-Y)^h$ denote, respectively, the rate of damage and the energy release rate fields predicted by the finite element solution obtained with the mesh h. A measure of the finite element solution approximation error within a generic element k, based on (7.8), can be defined as:

$$|e_{\omega_D}|_k^2 \equiv \int_{\Omega_k} \left[(-Y) - (-Y)^h\right] (\dot{D} - \dot{D}^h)\, d\Omega\,, \tag{7.10}$$

where the fields $\dot{D}$ and $-Y$ denote, respectively, the (usually unknown) exact solutions. Analogously, a *global* error, i.e., an error measure accounting for the solution over the entire finite element mesh, can be defined as:

$$|e_{\omega_D}|^2 = \sum_k |e_{\omega_D}|_k^2\,. \tag{7.11}$$

The error estimation technique consists of replacing the exact fields $-Y$ and D with some corresponding post-processed values of higher accuracy obtained from the available finite element solution. The work reported by Zienkiewicz & Zhu (1987), has shown that, for linear elliptic problems, the exact stress field, $\boldsymbol{\sigma}$, may be represented more accurately by the *smoothed* stresses, $\boldsymbol{\sigma}^*$, derived from a suitable *projection* of approximated stresses $\boldsymbol{\sigma}^h$ which satisfies

$$\int_\Omega \Pi\,(\boldsymbol{\sigma}^* - \boldsymbol{\sigma}^h)\, d\,\Omega = 0 \tag{7.12}$$

where Π is the projection matrix, which, in the present analysis, uses the interpolation functions[2].

Here, an extension of this concept is applied to the quantities associated with the elasto-plastic damaged problem. Accordingly, projected/smoothed fields Y^* and $\dot{D}^*$ are obtained by extrapolating their Gauss point values to nodes, finding the associated nodal average value and then interpolating the averages back to the Gauss points. The error indicator based on such projected/smoothed fields is then defined as:

$$\varepsilon^2_{\omega_D,k} := \int_k \left[(-Y)^* - (-Y)^h\right] (\dot{D}^* - \dot{D}^h)\, d\Omega \tag{7.13}$$

and

$$\varepsilon^2_{\omega_D} = \sum_k \varepsilon^2_{\omega_D,k}\,, \tag{7.14}$$

---

[2] The reader is referred to Zienkiewicz & Taylor (2000) for other projection techniques.

where $\varepsilon^2_{\omega_D,k}$ is the error estimated for a generic element k and $\varepsilon^2_{\omega_D}$ the corresponding global error.

After the evaluation of the error indicator, it is natural to seek methods by which the mesh can be improved. The simplest process consists in trying to achieve an equal error distribution between all elements (Li & Bettess, 1995; Díez & Huerta, 1999), i.e., the ideal mesh requires an equal distribution of element errors, $\eta_{\omega_D,k}$, which can be defined as (Zienkiewicz & Zhu, 1987):

$$\eta_{\omega_D,k} = \frac{|\boldsymbol{e}_{\omega_D}|_k}{\left(\dfrac{\omega_D + |\boldsymbol{e}_{\omega_D}|^2}{m}\right)^{1/2}} \approx \frac{\varepsilon_{\omega_D,k}}{\left(\dfrac{\omega^h_D + \varepsilon^2_{\omega_D}}{m}\right)^{1/2}}, \tag{7.15}$$

where m is the number of elements in the mesh and ω_D and ω^h_D are given respectively by:

$$\omega_D = \sum_k (-Y)\,\dot{D} \tag{7.16}$$

and

$$\omega^h_D = \sum_k (-Y)^h\,\dot{D}^h\,. \tag{7.17}$$

The above approximation is expected to hold asymptotically, i.e. for sufficiently small mesh size h.

Remark 7.2 *The decision to update the finite element mesh for many relevant practical problems, in which the geometric changes are usually large, is also supplemented by element distortion parameters of a similar form to that proposed by Dyduch* et al. *(1992) where corner angle and element slenderness may also trigger remeshing. The advantage of this approach is the fact that it is purely based on geometric considerations and it is totally independent of any constitutive material model employed.*

7.4 Prediction of the new mesh density

The mesh refinement procedure is constructed by simply looking at the elements with the largest error and dividing these to achieve some acceptable accuracy. The overall objective is to achieve a uniform distribution of local error (Zienkiewicz & Zhu, 1987). This procedure is subjected to additional optional constraints, on the minimum and maximum element sizes, to ensure that the overall cost of the solution remains acceptable.

For the estimator based on damage dissipation, the target error, that is, the prescribed maximum permissible error, η_k, and the current error, $\eta_{\omega_D,k}$, defines the *error index*, ξ_k, as

$$\xi^{\omega_D}_k = \frac{\eta_{\omega_D,k}}{\eta_k} = \frac{\varepsilon_{\omega_D,k}}{\eta_k\left(\dfrac{\omega^h_D + \varepsilon^2_{\omega_D}}{m}\right)^{1/2}}\,. \tag{7.18}$$

A new element characteristic size, $h_{\text{new},k}$, intended to bring the error within the prescribed target, is computed by assuming convergence rate of the error to be $O(h^p)$ according to the expression (Zienkiewicz & Zhu, 1987):

$$h_{\text{new},k} = \frac{h_{\text{old},k}}{(\xi_k^{\omega_D})^{1/p}}\,, \tag{7.19}$$

where $h_{\text{old},k}$ is the element size on the mesh h, with which the results have been obtained, p is the polynomial degree of the shape function (degree one for the simplex elements discussed in Chapter 6).

7.5 Mesh regeneration

An unstructured meshing approach is used for the mesh generation and subsequent mesh adaptation. The algorithm employed is based on the *Delaunay triangulation* technique, which is particularly suited to local mesh regeneration, or a Advancing Front procedure. An extension of both schemes to quadrilateral elements in 2-D is also available.

For three dimensional cases some serious implementation difficulties arise, particularly for problems whose geometry changes significantly during the loading process. Firstly, for arbitrary three dimensional geometries automatic methods for mesh generation and subsequent mesh adaptation can only be accomplished by an unstructured meshing approach. Consequently, tetrahedral elements must be employed, as procedures for the generation of good quality hexahedral meshes for arbitrary geometries in 3D still lack robustness. For metal forming operations it is particularly important to produce meshes which are free of sliver (near zero volume) elements, since when finite deformations are considered such elements can rapidly degenerate under further loading.

In this work, the three-dimensional mesh generation/adaptation employs an advancing front technique in view of its relatively simple way of controlling the mesh density and recovering geometric features of deformed surfaces. The basic steps used in mesh adaptation are outlined below

(1) Set up a background grid to define the mesh density for the new mesh;

(2) Generate a set of initial front facets of the boundary surfaces of the three-dimensional region to be meshed;

(3) Choose a front facet as a base to generate an element inside the three-dimensional region, according to mesh density information stored in the background grid;

(4) Update the front facet database by deleting and/or inserting appropriate facets;

(5) Repeat steps (3) and (4) until the set of front facets is empty.

Before each adaptive step, the background grid has to be formed, as outlined by step (1) above, to establish the new mesh density. In this work, the previously deformed mesh is employed as the background grid and the mesh densities, computed in the analysis phase, are assigned at each node.

The deformed boundary surfaces can only be represented by a set of discretely defined faces and points (triangulation). If appropriate care is not taken at the boundaries, performed by step (2) above, remeshing may result in unacceptable volume changes or even in geometric features such as corners being lost. To address the issue, a face-defined *surface remeshing technique* is adopted whereby a new (curved) surface mesh is generated by an advancing front method. Here, we adopt a similar approach as Escobar & Montenegro (1996) and Lohner (1996), to prepare the set of initial front facets.

To ensure that elements are well-shaped, the so-called *2.5 Dimension Delaunay simplexification* on curved surface meshes is performed, which implies that for each triangular element generated, no other mesh node in the resulting surface mesh lies inside its circumsphere. This may be obtained by locally swapping sides of neighbouring triangular elements. A surface mesh smoothing technique may also greatly improve the final mesh quality. The method consists of repeatedly averaging the position of all interior surface nodes by their surrounding surface nodes. In average, a total of four or five loops over the interior surface nodes is required to achieve a mesh of sufficient quality.

Once the three dimensional mesh is generated, according to mesh density information stored in the background grid, the same mesh smoothing technique allows the relaxation of interior points of the volume mesh, and results in a higher quality mesh.

The mesh regeneration scheme implemented is capable of performing the mesh adaption according to the mesh prediction data. These mesh prediction data, usually in the form of mesh density variation or mesh refinement indices, are interpreted from the error data created by some error indicator, as was discussed in Section 7.3.

7.6 Transfer operations for evolving meshes

Once a new mesh is generated with element sizes defined by (7.19), all variables of the problem at hand have to be transferred from the old mesh to the new one, so as to allow the solution scheme to proceed. In this class of problems, not only nodal displacements or nodal velocities have to be transferred, but also Gauss point variables, which creates a complex problem of compatibility and consistency. Therefore, the necessity for reliable and efficient *transfer operators* is of fundamental importance.

In general, the transfer procedures currently in use attempt to compute both the value of the nodal variables and Gauss point variables in the newly discretized domain, in terms of the values of the solution relative to the previous time interval $[t_{n-1}, t_n]$. Though it appears difficult to try to draw a classification, the fundamental approaches and ideas can be referred to the following procedures (Orlando, 2002; Orlando & Perić, 2004):

- Variationally consistent transfer;
- Weak enforcement continuity transfer;
- Smoothing transfer.

These transfer processes are briefly presented and particular reference is given to the specific problem at hand. It is also worth noting that all the following operations share the same underlying idea of firstly defining a field for the state variables, which depends on the old mesh. This field is then transformed, according to the specific procedure, into a new field on the new mesh which allows the sampling at the new Gauss points.

Variationally consistent transfer This class of transfers has been investigated by Ortiz and coworkers (Ortiz & Quigley IV, 1991; Camacho & Ortiz, 1997; Radovitzky & Ortiz, 1999). A variationally consistent transfer is a mapping procedure where the initial data is obtained from sampling at new Gauss points the solution of the variational formulation of the incremental boundary value problem for the time step $[t_{n-1}, t_n]$. For this to happen, the equations that define the secondary variables, and appearing as data of the problem, must be expressed in a variational form and consequently an interpolation for those variables must be prescribed. It is this variational formulation that provides the data for the fully discrete problem in the case of change of mesh. This observation, therefore, suggests enforcement of the constitutive incremental problem in a weak form and not in a pointwise manner, as implied by the standard displacement formulation.

Weak enforcement continuity transfer This transfer procedure is obtained from a Galerkin type approximation of the variational equation which imposes, in the weak form, the continuity across time t_n of the variables which appear as data of the incremental boundary value problem. For instance, Rashid (2002) enforces the continuity of a given field, in a Galerkin sense, by replacing the infinite dimensional space, with finite dimensional spaces. These are defined by piecewise constant functions, which represent the assumed distribution of the internal variables.

Smoothing transfer This procedure represents perhaps the most widely used remapping algorithm in solid mechanics applications due to its relatively simple implementation. The main steps can be summarized as:

- The values of the state variables at the old Gauss points, are first transferred to the nodes of the old mesh, possibly with some weighting;
- A weighted average is then carried out at each node, and a smooth field, is consequently constructed;
- Transfer of the nodal values from the old mesh to the new mesh is performed;
- The nodal quantities are projected to the new quadrature points.

Some of the above steps can be by-passed and each of them can be executed in different ways, delivering a fairly large spectrum of transfer procedures.

In this section general aspects of the smoothing transfer operation, adopted in this work, for evolving finite element meshes are provided for the case of a typical elasto-plastic material whose behaviour is described by a set of internal variables.

7.6.1 Smoothing transfer for implicit and explicit schemes

The efficiency and reliability of re-meshing techniques, for either implicit or explicit time integration schemes, are intimately related to some important aspects of the transfer operation. The following interdependent issues have to be addressed:

(i) consistency with the constitutive equations;
(ii) requirement of equilibrium;
(iii) compatibility of the history-dependent internal variable transfer with the displacement field on the new mesh;
(iv) compatibility with evolving boundary conditions;
(v) minimisation of the numerical diffusion of transferred state fields.

For implicit time integration schemes, item (ii) plays an important role in the definition of a transfer strategy. For instance, in Reference (Ortiz & Quigley IV, 1991) the general expression of the transfer operator is derived from the weak form of the equilibrium equations. Lee & Bathe (1994) observe that the transfer of all history-dependent variables causes solution inconsistency on the new mesh. Therefore, the authors proposed to transfer only the variables representing the plastic internal state and incorporating the computation of the remaining quantities in the solution procedure.

The consistency problem has also been addressed by Perić *et al.* (1996), in which the Newton-Raphson iterative procedure uses the displacements transferred from the old mesh for the time $n+1$ as trials for the first iteration. The above procedures can also guarantee both the compatibility of the history-dependent variables transfer with the displacement field on the new mesh and consistency with the constitutive equations. In fact, Lee & Bathe (1994) and

Perić *et al.* (1996) defined similar strategies to ensure compatibility with evolving boundary conditions. In both cases an interpolation procedure over the contactor nodes and segments in the old mesh is proposed.

Numerical diffusion is a well-known problem caused by discretization errors of the governing equations. This concept can be extended to transfer operations by observing the compatibility between the order of the elements and the interpolation functions. For example, if the element order is higher than the interpolation functions, or if continuity requirements are not observed, the quality of the transfer operations is certainly compromised.

Most issues raised above can be directly applied to explicit time integration schemes, except the requirements of equilibrium, since the algorithm does not incorporate self-equilibrium of the governing equations.

7.6.2 The transfer operation

In simulation of history dependent material processes between two finite element meshes, denoted by h and $h+1$, there exist two basic types of variables to be transferred, i.e., nodal values and quantities associated to the quadrature points. Displacement and velocity are typical examples of the first type, whereas as the equivalent plastic strain, stress tensor and damage amongst others, are characteristic of the second type. The basic principles described by Perić *et al.* (1996) for *implicit* schemes were applied to *explicit* schemes by Dutko *et al.* (1997) and constitute the backbone of the present work.

Figures 7.1 and 7.2 summarise, on a conceptual level, a typical transfer operation for an implicit and explicit time integration scheme, that includes both the mapping of the Gauss point variables and mapping of the nodal values.

$$\begin{tikzcd}
 & \boxed{h} & \boxed{h+1} \\
\boxed{t_n} & {}^{h}\boldsymbol{\Lambda}_n \arrow[r, "({}^{h+1}\boldsymbol{b}^{e}_{n},\, {}^{h+1}\boldsymbol{\alpha}_n) = \mathcal{T}_1[{}^{h}\boldsymbol{b}^{e}_{n},\, {}^{h}\boldsymbol{\alpha}_n]"] \arrow[d] & {}^{h+1}\tilde{\boldsymbol{\Lambda}}_n \arrow[d] \\
\boxed{t_{n+1}} & {}^{h}\boldsymbol{\Lambda}_{n+1} \arrow[r, "{}^{h+1}\boldsymbol{u}^{\mathrm{trial}}_{n+1} = \mathcal{T}_2[{}^{h}\boldsymbol{u}_{n+1}]"] & {}^{h+1}\boldsymbol{\Lambda}_{n+1}
\end{tikzcd}$$

Figure 7.1: Transfer operator diagram. *Implicit* scheme (Perić *et al.* , 1996).

The transfer operation is somewhat similar for both the implicit and explicit schemes in that the transfer operators are identical. However, the differing

$$\begin{tikzcd}
 & \boxed{h} & & \boxed{h+1} \\
\boxed{t_n} & {}^{h}\boldsymbol{\Lambda}_n \arrow[rr, "{({}^{h+1}\boldsymbol{\sigma}_n, {}^{h+1}\boldsymbol{\alpha}_n) = \mathcal{T}_1\,[{}^{h}\boldsymbol{\sigma}_n, {}^{h}\boldsymbol{\alpha}_n]}", "{{}^{h+1}\boldsymbol{v}_{n+1/2}, = \mathcal{T}_2\,[{}^{h}\boldsymbol{v}_{n+1/2}]}"'] & & {}^{h+1}\boldsymbol{\Lambda}_n
\end{tikzcd}$$

Figure 7.2: Transfer operator diagram. *Explicit* scheme Dutko *et al.* (1997).

stress update algorithms require different variables to be transfered to allow the progress of the solution on the new mesh:

- The implicit algorithm utilises a total Lagrangian formulation, so that the converged solution state of the current mesh, h, and current time t_n, can be described by a state array as
$$ {}^{h}\boldsymbol{\Lambda}_n \;:=\; ({}^{h}\boldsymbol{u}_n,\; {}^{h}\boldsymbol{F}_n,\; {}^{h}\boldsymbol{\tau}_n,\; {}^{h}\boldsymbol{b}^e_n,\; {}^{h}\boldsymbol{\alpha}_n) $$
where ${}^{h}\boldsymbol{u}_n, {}^{h}\boldsymbol{F}_n, {}^{h}\boldsymbol{\tau}_n, {}^{h}\boldsymbol{b}^e_n,\; {}^{h}\boldsymbol{\alpha}_n$ denote values of the displacement, deformation gradient, stress tensor, elastic Finger tensor and a vector of internal variables at time t_n for the mesh h;
- The explicit algorithm is incremental, such that the solution state on the current mesh, h, and current time t_n, can be described by a state array as
$$ {}^{h}\boldsymbol{\Lambda}_n \;:=\; ({}^{h}\boldsymbol{v}_{n+1/2},\; {}^{h}\boldsymbol{x}_n,\; {}^{h}\boldsymbol{\sigma}_n,\; {}^{h}\boldsymbol{\alpha}_n) $$
where ${}^{h}\boldsymbol{v}_{n+1/2},\; {}^{h}\boldsymbol{x}_n,\; {}^{h}\boldsymbol{\sigma}_n,\; {}^{h}\boldsymbol{\alpha}_n$ denote values of the velocity, updated coordinates, stress tensor and a vector of internal variables at time t_n or $t_{n+1/2}$ for the mesh h.

Assuming that the estimated error of the solution ${}^{h}\boldsymbol{\Lambda}_n$ respects the prescribed criteria, while these are violated by the solution ${}^{h}\boldsymbol{\Lambda}_{n+1}$, in this case a new mesh $h+1$ is generated and a new solution ${}^{h+1}\boldsymbol{\Lambda}_{n+1}$ needs to be computed.

Implicit time integration scheme: For implicit analysis, the internal variables ${}^{h+1}\boldsymbol{\alpha}_n$ completely define the history of the material on the new mesh $h+1$ at time t_n, noting that the constitutive update is performed with the backward Euler scheme. This new state

$$ {}^{h+1}\tilde{\boldsymbol{\Lambda}}_{n+1} \;:=\; (\bullet, \bullet, \bullet,\; {}^{h+1}\boldsymbol{b}^e_n,\; {}^{h+1}\boldsymbol{\alpha}_n) $$

where a symbol $\tilde{}$ denotes a reduced state array, is evaluated using a Gauss point transfer operation, $\mathcal{T}_1$ (see Figure 7.1):

$$ ({}^{h+1}\boldsymbol{b}^e_n,\; {}^{h+1}\boldsymbol{\alpha}_n) \;=\; \mathcal{T}_1\,[\,{}^{h}\boldsymbol{b}^e_n, {}^{h}\,\boldsymbol{\alpha}_n]. \tag{7.20} $$

At this stage, it is important to remark that various transfer procedures can be defined based on the choice of the operator, $\mathcal{T}_1$, and on the choice of the set, ${}^h\boldsymbol{\alpha}_n$, of state variables. Let us consider firstly the selection of variables for the set ${}^h\boldsymbol{\alpha}_n$, which consists of the minimum number of variables necessary to represent the material deformation history. Various numerical examples have revealed (Perić *et al.* , 1999) that a robust transfer operator should include the elastic finger tensor, ${}^h\boldsymbol{b}^e_n$. In Section 7.6.3, two different transfers operators are presented to map the set of variables ${}^h\boldsymbol{\alpha}_n$ from the Gauss points of the old mesh, h, to that of the new mesh, $h+1$.

The choice of the state variables that compose the set, ${}^h\boldsymbol{\alpha}_n$, together with the transfer operator, $\mathcal{T}_1$, have an effect on the accuracy and convergence of the problem and in preserving the incompressible nature of plastic flow, i.e. enforcing $\det\boldsymbol{F}^p = 1$. As remarked by Srikanth & Zabaras (2001) for transfer operators which compute intermediate values of the state variables at the nodal points of the two meshes as suggested by Lee & Bathe (1994) and Perić *et al.* (1999), special attention would have to be given to ensure $\det\boldsymbol{F}^p = 1$ (Camacho & Ortiz, 1997).

Additionally, the converged nodal displacements from time t_{n+1} are transfered using transfer operator, $\mathcal{T}_2$, from the trial displacements of the new mesh

$$ {}^{h+1}\boldsymbol{u}^{\mathrm{trial}}_{n+1} = \mathcal{T}_2[{}^h\boldsymbol{u}_{n+1}]. \tag{7.21}$$

Metal forming operations also require the transfer of the contact state between the current mesh, h and new mesh $h+1$. A penalty based algorithm is used to enforce the impenetrability constraint in both implicit and explicit formulations and the tangential behaviour is modelled via constitutive relationships formulated using the elasto-plastic theory of friction (Curnier, 1984; Laursen, 2002; Wriggers, 2002). The tangential contact stress state at time, t_n, on mesh, h, is defined by

$$ {}^h\Gamma_n = \left[{}^h\left(u_T\right)_n, {}^h\left(\boldsymbol{\sigma}_T\right)_n, {}^h\boldsymbol{\alpha}_n\right], \tag{7.22}$$

where u_T, $\boldsymbol{\sigma}_T$, $\boldsymbol{\alpha}$ are the tangential relative displacement, the tangential stress and internal variables. The tangential displacement is updated incrementally and the stress update is performed using the backward Euler scheme. Therefore the new reduced state, ${}^{h+1}\tilde{\Gamma}_n$ is evaluated using a boundary line transfer operator, $\mathcal{T}_3$, as

$$ \left({}^{h+1}(u_T)_n, {}^{h+1}\boldsymbol{\alpha}_n\right) = \mathcal{T}_3\left[{}^h\left(u_T\right)_n, {}^h\boldsymbol{\alpha}_n\right]. \tag{7.23}$$

Equilibrium is then sought on the $h+1$ mesh to provide the converged solution at time t_{n+1}.

Explicit time integration scheme: For the explicit dynamic case the discussion is restricted to the quasi-static class of problem. For this case the loading rate is slow giving rise to small changes in the material state between time steps. Consequently, in the explicit transfer strategy the solution is directly mapped from the state ${}^{h}\boldsymbol{\Lambda}_n$ to ${}^{h+1}\boldsymbol{\Lambda}_n$ in the deformed configuration. This updated state is evaluated using the Gauss point transfer operator, $\mathcal{T}_1$ (see Figure 7.2):

$$({}^{h+1}\boldsymbol{\sigma}_n,\, {}^{h+1}\boldsymbol{\alpha}_n) \;=\; \mathcal{T}_1\,[\,{}^{h}\boldsymbol{\sigma}_n,{}^{h}\,\boldsymbol{\alpha}_n] \tag{7.24}$$

and the nodal transfer operator, $\mathcal{T}_2$, to compute the velocity on the new mesh, $h+1$:

$${}^{h+1}\boldsymbol{v}_{n+1/2} \;=\; \mathcal{T}_2[{}^{h}\boldsymbol{v}_{n+1/2}]. \tag{7.25}$$

The contact is handled in a similar way with the state, ${}^{h}\Gamma_n$, being directly transferred to the state, ${}^{h+1}\Gamma_n$

For both the implicit and explicit schemes, some of the variables that take part in the state array, ${}^{h}\boldsymbol{\Lambda}_n$, are not included in the reduced state array, ${}^{h}\tilde{\boldsymbol{\Lambda}}_n$, but are transferred for post-processing purposes and do not directly determine the subsequent material response.

Remark 7.3 *Although the same operators $\mathcal{T}_1$, $\mathcal{T}_2$ and $\mathcal{T}_3$ have been used, there are fundamental differences between the transfer strategies proposed by Perić* et al. *(1996) for implicit and Dutko* et al. *(1997) for explicit time integration schemes. The former takes advantage of a total Lagrangian formulation to compute the new stresses for the new mesh $h+1$ at time $n+1$ thereby reducing the number of variables necessary to be transferred and ensuring consistency of the solution. The latter transfers both nodal and Gauss point information in the same time step due to the fact that explicit schemes do not require equilibrium at time step $n+1$ and time steps are markedly smaller than its implicit counterpart.*

For the case of evolving finite element meshes composed of simplex elements, the implementation of the general transfer operation is described in the following sections.

7.6.3 Mapping of internal variables - Transfer operator $\mathcal{T}_1$

The transfer operation, $\mathcal{T}_1$, performs the mapping of internal variables, between meshes h and $h+1$. The internal variables, which are defined at the quadrature points of the mesh h, are transferred by the operator $\mathcal{T}_1$ to the quadrature points of the new mesh $h+1$ of the body $\mathcal{B}$.

The construction of the transfer operator itself can be done in a variety of ways. Here, two different *local* transfer operators are described. The choice for transfer operators that has been made was guided by the future application of the methodology to classes of problems where large deformations of inelastic materials at finite strains and complex boundary conditions with possible frictional contact will be standard operating conditions. Therefore *simple*, but *generally applicable*, transfer operators are adopted.

Standard transfer operator

The algorithm comprises three distinct steps, i.e., projection of the Gauss point variables to nodes, transfer of the nodal values from the old to the new mesh and projection of the corresponding nodal quantities to the new quadrature points. Figure 7.3 illustrates the operation for constant strain triangles, where the subscripts N and G indicate nodal and Gauss point variables, respectively.

(a) ${}^{h}\tilde{\boldsymbol{\Lambda}}_{n,G} \rightarrow {}^{h}\tilde{\boldsymbol{\Lambda}}^{*}_{n,N}$ (b) ${}^{h}\tilde{\boldsymbol{\Lambda}}^{*}_{n,N} \rightarrow {}^{h+1}\tilde{\boldsymbol{\Lambda}}_{n,N}$

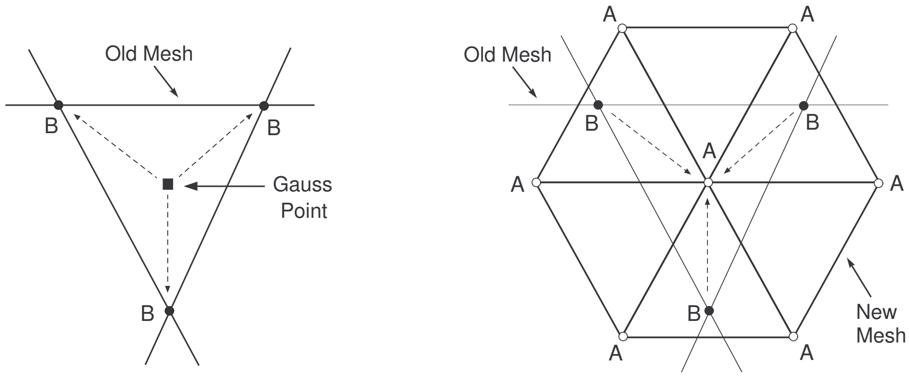
Old Mesh
B
B
Gauss
Point
B
A
A
Old Mesh
B
B
A
A
A
New
Mesh
B
A
A

(c) ${}^{h+1}\tilde{\boldsymbol{\Lambda}}_{n,N} \rightarrow {}^{h+1}\tilde{\boldsymbol{\Lambda}}_{n,G}$

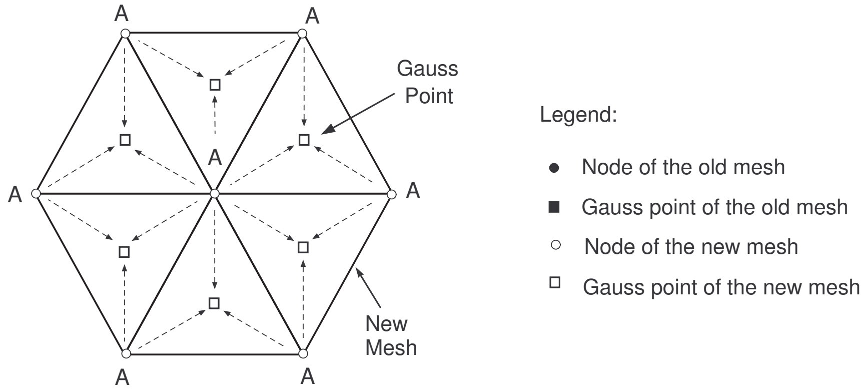
A
A
Gauss
Point
A
A
A
New
Mesh
A
A
Legend:
● Node of the old mesh
■ Gauss point of the old mesh
○ Node of the new mesh
□ Gauss point of the new mesh

Figure 7.3: Standard transfer operator, $\mathcal{T}_1$, of internal variables.

(1) The Gauss point components of the old mesh ${}^{h}\boldsymbol{\alpha}_{n,G}$ are projected to nodes ${}^{h}\boldsymbol{\alpha}_{n,N}$ using the finite element shape functions. The nodal point averages are then performed resulting in ${}^{h}\boldsymbol{\alpha}^{*}_{n,N}$ [see Figure 7.3 (a)]

(2) In the second step the nodal components of the state variables ${}^{h}\boldsymbol{\alpha}^{*}_{n,N}$ will be transferred from the old mesh h to a new mesh $h+1$ resulting

in ${}^{h+1}\boldsymbol{\alpha}^*_{n,N}$. This step of the transfer operation is the most complex one and can be subdivided as follows:

- *Construction of the background triangular mesh.* In the first stage, for every node A of the new mesh $h+1$ with known coordinates ${}^{h+1}\boldsymbol{x}_{n,A}$, the so-called background element, ${}^{h}\Omega^{(e)}$, is found in the old mesh h for which ${}^{h+1}\boldsymbol{x}_{n,A} \in {}^{h}\Omega^{(e)}$.
- *Evaluation of the local coordinates.* The second stage constitutes the evaluation of the local coordinates, $({}^{h}\xi_A, {}^{h}\eta_A)$, of the node A of the new mesh within the background element, ${}^{h}\Omega^{(e)}$, by solving

  $$ {}^{h+1}\boldsymbol{x}_{n,A} = \sum_{b=1}^{3} {}^{h}\boldsymbol{N}_b({}^{h}\xi_A, {}^{h}\eta_A)\, {}^{h}\boldsymbol{x}_{n,b} \tag{7.26} $$

  where ${}^{h}\boldsymbol{N}_b$ represent the interpolation functions of element ${}^{h}\Omega^{(e)}$. Since three-noded elements are used for the background mesh, local coordinates for each node of the new mesh can be obtained by resolving the linear system (7.26). However, for higher-order elements a Newton-Raphson iterative scheme can be used [3].
- *Mapping nodal values.* In the third stage, the state variables ${}^{h}\tilde{\boldsymbol{\Lambda}}_{n,B} = {}^{h}\boldsymbol{\alpha}^*_{n,B}$ are mapped from nodes B of the old mesh, h, to nodes A of the new mesh, $h+1$, by using the shape functions ${}^{h}\boldsymbol{N}_b({}^{h}\xi_A, {}^{h}\eta_A)$ as

  $$ {}^{h+1}\tilde{\boldsymbol{\Lambda}}_{n,A} = \sum_{b=1}^{3} {}^{h}\boldsymbol{N}_b({}^{h}\xi_A, {}^{h}\eta_A)\, {}^{h}\tilde{\boldsymbol{\Lambda}}_{n,b} \tag{7.27} $$

(3) In the final step, the state variables at the Gauss points of the new mesh ${}^{h+1}\tilde{\boldsymbol{\alpha}}_{n,G}$ can be easily obtained by employing the shape functions of the element ${}^{h+1}\Omega^{(e)}$, i.e.

$$ {}^{h+1}\tilde{\boldsymbol{\Lambda}}_{n,G} = \sum_{a=1}^{3} {}^{h+1}\boldsymbol{N}_a({}^{h+1}\xi_G, {}^{h+1}\eta_G)\, {}^{h+1}\tilde{\boldsymbol{\Lambda}}_{n,a} \tag{7.28} $$

in which $({}^{h+1}\xi_G, {}^{h+1}\eta_G)$ are the Gauss point coordinates.

Moving least square method

The standard transfer operator, described above, was for many years the most widely used method for smoothing stresses and other relevant variables in finite element programs. This approach, in many circumstances, introduces unacceptable levels of diffusion of the transferred variables. This is particularly true when the mesh contains fine elements neighbouring large elements. Subsequently, Zienkiewicz & Zhu (1992b) suggested a local projection technique in which stresses or strains can be accurately recovered by fitting polynomials over local patches at superconvergent points in the finite element solution. This method substantially outperforms the L_2 projection methods from the viewpoint of the accuracy of the projected stresses. However, these local superconvergent patch projections require the existence of superconvergent points and they do not perform as well when the gradients are very steep, as near crack tips or shear bands (Tabbara *et al.* , 1994).

---

[3] This procedure is also known as the *inverse isoparametric mapping technique* (Lee & Bathe, 1994).

In the present context, an excessive diffusion often results in a loss of ability to predict the (usually sharp) localisation of damage that precedes fracture initiation. A possible improvement upon the above procedure consists in adopting a variable transfer operation in which the Gauss point values of the old mesh, ${}^{h}\tilde{\boldsymbol{\Lambda}}_{n,G}$, are mapped directly to the Gauss points of the new one, ${}^{h+1}\tilde{\boldsymbol{\Lambda}}_{n,G}$, by means of a weighted least-squares method (Tabbara *et al.* , 1994; Morançay *et al.* , 1997).

To devise such a strategy, let us consider a particular domain discretized by two consecutive finite element meshes, which result from the adaptive procedure. In Figure 7.4, for the sake of clarity, we only depict the quadrature points of both overlapping finite element meshes.

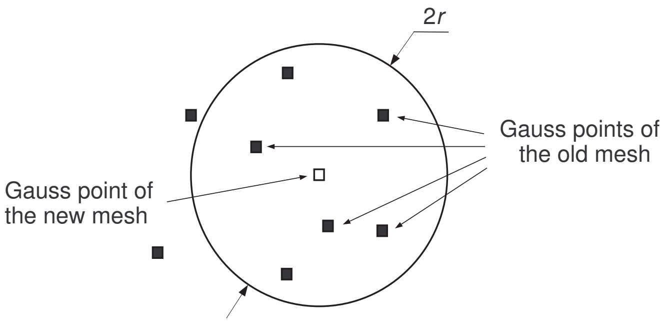

Figure 7.4: Transfer operator, $\mathcal{T}_1$, based on moving least square method.

The underlying idea of the method is to search for new state variables that are obtained from the expression

$$ {}^{h+1}\tilde{\boldsymbol{\alpha}}_{n,G} = \boldsymbol{p}\left({}^{h+1}\boldsymbol{x}_{n,G}\right)\boldsymbol{c}. \tag{7.29}$$

Where, ${}^{h+1}\boldsymbol{x}_{n,G}$, represents the coordinates of a Gauss point of the new mesh, ${}^{h+1}\tilde{\boldsymbol{\alpha}}_{n,G}$, the state variables to be estimated at, ${}^{h+1}\boldsymbol{x}_{n,G}$ and $\boldsymbol{p}\,(\bullet)$ is a polynomial basis. For example, a bilinear basis is given by

$$\boldsymbol{p} = [\,1 \;\; x \;\; y \;\; xy\,] \tag{7.30}$$

Finally, $\boldsymbol{c}$, is a vector of coefficients, c_i, to be determined, which depends on ${}^{h+1}\boldsymbol{x}_{n,G}$. To obtain these new state values it is necessary to minimise the function:

$$\sum_{i=1}^{n_{qp}} w\left({}^{h}\boldsymbol{x}_{n,G}^{i}\right)\left[\boldsymbol{p}\left({}^{h}\boldsymbol{x}_{n,G}^{i}\right)\boldsymbol{c} - {}^{h}\tilde{\boldsymbol{\alpha}}_{n,G}^{\,i}\right]^2 , \tag{7.31}$$

where ${}^{h}\boldsymbol{x}_{n,G}^{i}$ and ${}^{h}\tilde{\boldsymbol{\alpha}}_{n,G}^{\,i}$ represent the coordinates and the state variables at the integration points of the old mesh, and w is a weighting function defined by

$$w\left({}^{h}\boldsymbol{x}_{n,G}^{i}\right) = \cos^2\left(\frac{\pi\left\|{}^{h+1}\boldsymbol{x}_{n,G} - {}^{h}\boldsymbol{x}_{n,G}^{i}\right\|}{2\,r({}^{h+1}\boldsymbol{x}_{n,G})}\right) . \tag{7.32}$$

The number, n_{qp}, of old quadrature points is user defined and the more sampling points that are included the more accurate the mapping should be. Consequently, the distance between the Gauss point of the new mesh, ${}^{h+1}\boldsymbol{x}_{n,G}$, and the $\left({}^{h}\boldsymbol{x}_{n,G}\right)_{n_{qp}+1}$ closest neighbour of ${}^{h+1}\boldsymbol{x}_{n,G}$ in the old mesh automatically defines the radius, r, included in the definition of the weighting function.

It is clear that this mapping method does not require the extrapolation of state variables to and from the nodal positions prior to mapping between the old and new finite element meshes respectively. For each new Gauss point in the new finite element mesh, $h+1$, the algorithm comprises the following steps:

(1) Identify the coordinates of the quadrature point using the element shape functions

$$^{h+1}\boldsymbol{x}_{n,G} = \sum_{a=1}^{3} {}^{h+1}\boldsymbol{N}_a({}^{h+1}\xi_G, {}^{h+1}\eta_G)\, {}^{h+1}\boldsymbol{x}_{n,a} \tag{7.33}$$

where ${}^{h}\boldsymbol{N}_a$ represent the interpolation functions of element ${}^{h+1}\Omega^{(e)}$.

(2) Identify the closest number of neighbouring quadrature points from the old finite element mesh, ${}^{h}\boldsymbol{x}_{n,G}^{i}$. This operation uses an improved *KD-tree* based algorithm (de Berg *et al.* , 2000);

(3) Evaluate the weighting function w,

$$w\left({}^{h}\boldsymbol{x}_{n,G}^{i}\right) = \cos^2\left(\frac{\pi\left\|{}^{h+1}\boldsymbol{x}_{n,G} - {}^{h}\boldsymbol{x}_{n,G}^{i}\right\|}{2\,r({}^{h+1}\boldsymbol{x}_{n,G})}\right) ; \tag{7.34}$$

(4) Form a second order tensor, $\boldsymbol{A}$, from the weighting function and polynomial basis terms

$$\boldsymbol{A} = \sum_{i=1}^{n_{qp}} w\left({}^{h}\boldsymbol{x}_{n,G}^{i}\right)\left[\boldsymbol{p}\left({}^{h}\boldsymbol{x}_{n,G}^{i}\right)\right]\boldsymbol{p}\left({}^{h}\boldsymbol{x}_{n,G}^{i}\right) \tag{7.35}$$

(5) For each state variable to be mapped to the new mesh, $h+1$, from the old mesh, h, the following sequence of operations must be undertaken:

- Form the vector, $\boldsymbol{b}$, using the state variables, the weighting function and the polynomial basis terms

$$\boldsymbol{b} = \sum_{i=1}^{n_{qp}} {}^{h}\tilde{\boldsymbol{\alpha}}_{n,G}^{\,i} \;\; w\left({}^{h}\boldsymbol{x}_{n,G}^{i}\right)\left[\boldsymbol{p}\left({}^{h}\boldsymbol{x}_{n,G}^{i}\right)\right] \tag{7.36}$$

- Solve the following system of algebraic equations having the coefficient vector $\boldsymbol{c}$ as unknowns

$$\boldsymbol{c} = \boldsymbol{A}^{-1}\,\boldsymbol{b} \tag{7.37}$$

- Compute the new field value for the quadrature point, ${}^{h+1}\tilde{\boldsymbol{\alpha}}_{n,G}$, in analysis using the polynomial basis for the considered quadrature point and the coefficient vector obtained by expression (7.37),

$${}^{h+1}\tilde{\boldsymbol{\alpha}}_{n,G} = \boldsymbol{p}\left({}^{h+1}\boldsymbol{x}_{n,G}\right)\boldsymbol{c}. \tag{7.38}$$

Generally it is inferred that this method is more accurate than the previously described interpolation method. It has been suggested (Morançay *et al.* , 1997) that the use of a moving least square method ensures, in the case of some elastic-plastic constitutive laws, plastic admissibility of the computed internal field variables. It is also possible to enforce plastic admissibility by introducing an additional constraint in the minimization of Equation (7.31).

7.6.4 Mapping of the nodal variables - Transfer operator $\mathcal{T}_2$

The transfer operation between meshes h and $h+1$ for the nodal values has been formally defined for implicit schemes, in Equation (7.21) rewritten here,

$${}^{h+1}\boldsymbol{u}_{n+1}^{\text{trial}} = \mathcal{T}_2[{}^{h}\boldsymbol{u}_{n+1}], \tag{7.39}$$

and for explicit schemes by Equation (7.25):

$${}^{h+1}\boldsymbol{v}_{n+1/2} = \mathcal{T}_2[{}^{h}\boldsymbol{v}_{n+1/2}]. \tag{7.40}$$

Since the displacement field and velocity field, are fully prescribed by the nodal values and the element shape functions of the new mesh $h+1$, the task of transferring nodal values is performed by repeating the step of *mapping of the nodal values* as

$${}^{h+1}\tilde{\boldsymbol{\Lambda}}_{n,A} = \sum_{b=1}^{3} {}^{h}\boldsymbol{N}_b({}^{h}\xi_A, {}^{h}\eta_A)\,{}^{h}\tilde{\boldsymbol{\Lambda}}_{n,b} \tag{7.41}$$

where ${}^{h}\boldsymbol{N}_b({}^{h}\xi_A, {}^{h}\eta_A)$ are the shape functions of the element, and $({}^{h}\xi_A, {}^{h}\eta_A)$ are the local coordinates of the node A of the new mesh within the background element, which have been previously determined at the second step of the transfer operator - $\mathcal{T}_1$.

7.6.5 Mapping of the contact variables - Transfer operator $\mathcal{T}_3$

The mapping of the contact variables - transfer operator $\mathcal{T}_3$, is analogous to the mapping of the nodal values - transfer operator $\mathcal{T}_2$. The reason for this is that, in this work, all the relevant contact information is stored in the nodes.

The only difference stems from the fact that this transfer operator - $\mathcal{T}_3$, is performed over the contact boundary, Γ, which is a one-dimensional region for a 2D problem and a bi-dimensional domain for a 3D problem.

Remark 7.4 *Details of implementation of the transfer operation given in Section 7.6.2 are described for the case of evolving finite element meshes composed of simplex elements. With minor modifications this procedure is applicable to other types of finite elements. For the standard transfer operator, in the case of a mesh composed of quadrilateral or higher order elements we proceed by simply subdividing these elements into a local mesh of simplex elements. This extension for the diffuse approximation method is straightforward and does not require any additional operation.*

7.7 Numerical examples

The applicability of the overall adaptive strategy is illustrated in this section by means of finite element simulations. In the first set of examples, the performance of the *F-bar-Patch* element (proposed in Chapter 6), for adaptive analysis is assessed. The second set of examples is concerned with the ability of the error measure based on *damage dissipation* (Section 7.3.4) to provide refined meshes at regions of possible material failure in small and large scale computations. It is important to remark that the examples discussed are characterised by the presence of extremely high strains. These are typical applications where remeshing becomes an essential component of the finite element analysis and are ideal to test the performance of the proposed adaptive strategy.

7.7.1 Suitability for adaptive analysis

Whenever a new mesh is chosen, all relevant variables that define the problem at hand must be appropriately transferred from the old mesh to the new one so that the solution procedure can continue. Formulations such as enhanced assumed strain methods (Simo & Armero, 1992; Simo *et al.* , 1993; Korelc & Wriggers, 1996; Glaser & Armero, 1997) and incompatible modes elements (Crisfield *et al.* , 1995) are based on the enrichment of the element strain field with the internal deformation modes defined by a set of local internal element parameters. For such methodologies, the appropriate transfer of internal parameters between meshes not trivial and seems not to be clear at present. In contrast, such an issue does not arise in methodologies such as the *F-bar* procedure described in Chapter 6 and geometrically non-linear extensions of the classical *B-bar* method (Moran *et al.* , 1990). The absence of element internal parameters makes the incorporation of such methods into adaptive remeshing environments rather straightforward.

Plane strain spike forming

The suitability of the 3-noded *F-bar-Patch* triangle for adaptive analysis is illustrated here in the simulation of *plane strain spike forming.* In this test, a rectangular specimen is forged between two rolls and a flat die. The initial tool/workpiece geometry of the problem is schematically illustrated in Figure 7.5(a) together with the initial mesh discretization, Figure 7.5(b), where only half of the problem is represented due to symmetry conditions. The initial workpiece geometry is represented using 92 triangular *F-bar-Patch* elements.

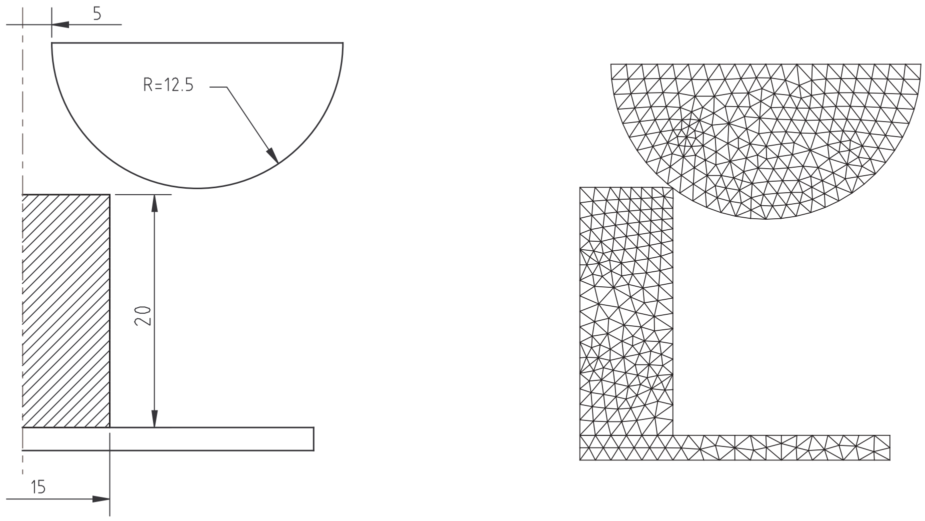

(a) (b)

Figure 7.5: Adaptive analysis of plane spike forming (dimensions in [mm]). (a) Geometry, and; (b) Initial finite element mesh.

The deformation pattern of the process is such that the material near the outside lateral surfaces flows radially, while the portion near the centre of the top surface is extruded forming a spike. It is possible to distinguish three different deformation modes during the operation:

(a) the height of the spike is reduced with increasing deformation;
(b) the spike height remains approximately constant;
(c) the spike height increases rapidly with increasing deformation.

Experimental evidence (Rodič *et al.* , 1992) reveals that during the first stage described above, the effect of friction on the material flow is almost negligible while in the third stage it is of prime importance.

The workpiece material is modelled by an isotropically hardening von Mises elasto-plastic constitutive model and the rolls are treated as rigid bodies. The frictional contact condition on the rolls/workpiece interface is modelled by the standard Coulomb friction law in conjunction with a penalty method to impose contact impenetrability. The total movement of the rolls is $15[mm]$, which is sufficiently large to prevent solution without remeshing. In this industrial forming process, the workpiece is subjected to extremely high strains. This is a typical application where remeshing becomes an essential component of the finite element analysis. If remeshing is not included, many elements will be severely distorted producing unacceptably inaccurate solutions. The material properties for 99.7% Aluminium alloy and other simulation parameters are listed in Table 7.1.

Table 7.1: Material data and simulation parameters.

Description	**Symbol**	**Value**
Elastic Modulus	E	125 $[GPa]$
Poisson's ratio	ν	0.3
Initial yield stress	σ_{y0}	40 $[MPa]$
Yield stress	$\sigma_y(\bar{\varepsilon}^{\mathrm{p}})$	$90 \cdot (\bar{\varepsilon}^{\mathrm{p}})^{0.52}$
Friction	m	0.2
Target error	η_{wp}	2.2 %
Maximum element size	h_{max}	1.2 $[mm]$
Minimum element size	h_{min}	0.8 $[mm]$

Throughout the simulation of the process 35 mesh adaptions were performed, each of which involved a complete new mesh definition. Deformed meshes obtained after adaptive remeshing are shown in Figure 7.6. Convergence of the finite element solution is established on the basis of the standard Euclidean norm of the out-of-balance forces with a tolerance of 10^{-3}. The criterion for mesh refinement is based on the *total plastic work* (Perić *et al.* , 1994). The internal history dependent variables, are mapped directly between gauss points of an old and new mesh by the weighted least-squares method, described in Section 7.6.3, using 8 sampling points. The nodal and contact variables are transfered from the old mesh to the new one using the standard transfer operator and an unstructured meshing approach based on the *Delaunay triangulation* is adopted for both initial and subsequent mesh adaptations.

The solution compares well with the experimental predictions (Rodič *et al.* , 1992) in terms of the flow pattern and the location of the neutral point i.e. location where no relative movement occurs on the rolls/workpiece interface, without the occurrence of spurious locking or hourglassing modes despite the very large compressive deformations attained.

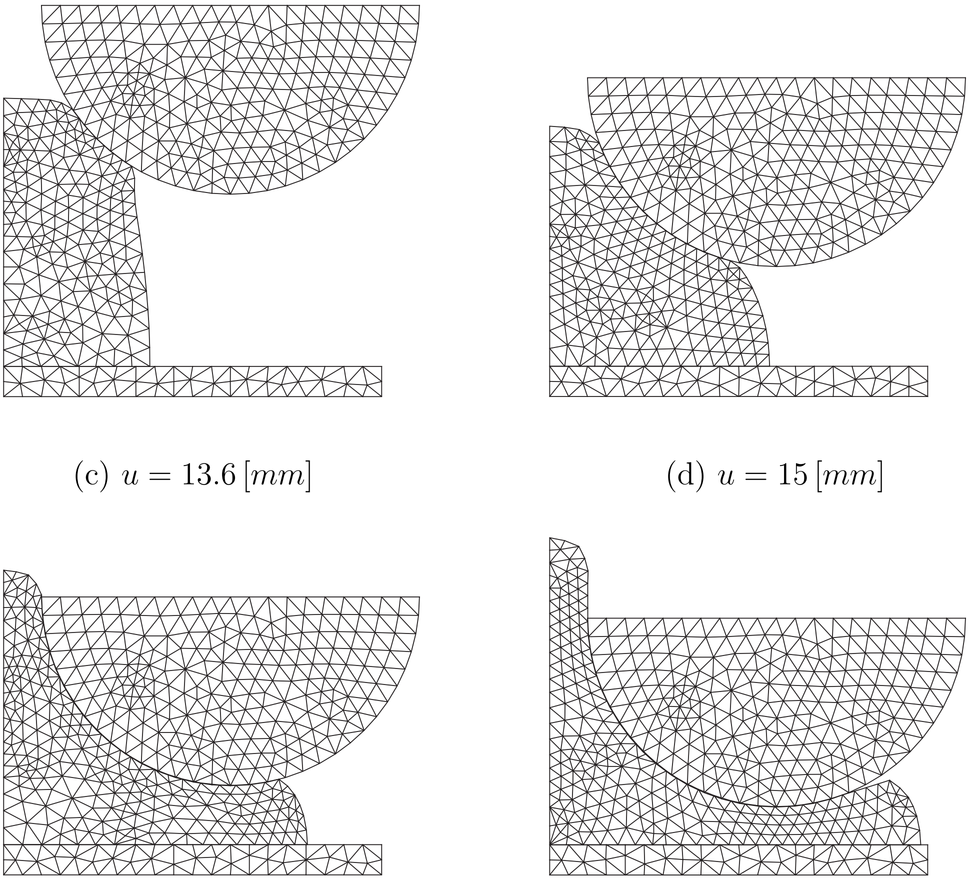

(a) $u = 6.1\,[mm]$

(b) $u = 10.9\,[mm]$

(c) $u = 13.6\,[mm]$

(d) $u = 15\,[mm]$

Figure 7.6: Plane strain spike forming. Evolution of the deformed mesh.

Axisymmetric piercing

The simulation of the *axisymmetric piercing* of a cylindrical workpiece is presented to illustrate the suitability of the 3-noded *F-bar-Patch* triangle combined with appropriate transfer operator for adaptive analysis. The geometry of the problem is schematically illustrated in Figure 7.7(a). Due to symmetry, only half of the problem is analysed. The workpiece is initially discretized with 168 triangular *F-bar-Patch* elements [see Figure 7.7(b)].

The workpiece is assumed to be made of an elasto-plastic material with linear hardening, while the punch is assumed to be rigid. Frictional contact between workpiece and tool is defined by a coulomb law in conjunction with a penalty method to impose contact impenetrability. The movement of the punch promotes highly localized compressive forces, which deform the workpiece to such an extent that the use of adaptive remeshing becomes crucial. The material properties adopted and other simulation parameters are summarized in Table 7.2. In the analysis an error indicator based on the rate of

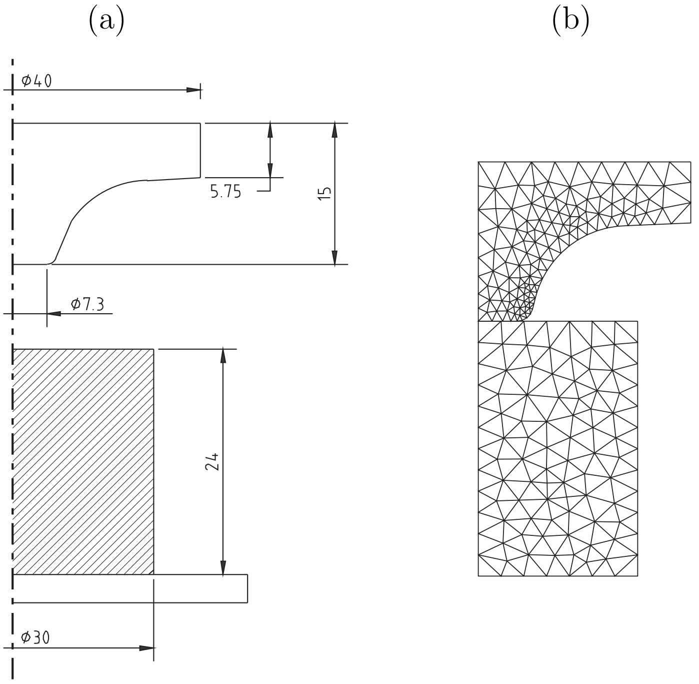

Figure 7.7: Adaptive analysis of axisymmetric piercing (dimensions in $[mm]$). (a) Geometry, and; (b) Initial finite element mesh.

plastic work is used (Perić *et al.* , 1994). Convergence of the finite element solution is established on the basis of the standard Euclidean norm of the out-of-balance forces with a tolerance of 10^{-3}. The internal history dependent variables are mapped directly between gauss points of an old and new mesh by the weighted least-squares method, using 8 sampling points, and the nodal and contact variables are transfered using the standard transfer operator. An unstructured meshing approach based on the *Delaunay triangulation* is adopted for both initial and subsequent mesh adaptations. Figure 7.8 presents the distribution of the effective plastic strain for three different compression stages.

Table 7.2: Material data and simulation parameters.

Description	**Symbol**	**Value**
Elastic Modulus	E	210 $[GPa]$
Poisson's ratio	ν	0.3
Initial yield stress	σ_{y_0}	100 $[MPa]$
Hardening modulus	H	900$[MPa]$
Friction	m	0.1
Target error	η_{wp}	2.0 %
Maximum element size	h_{max}	1.6 $[mm]$
Minimum element size	h_{min}	0.2 $[mm]$

(a)$_1$ $u = 4\,[mm]$ (b)$_1$ $u = 4\,[mm]$

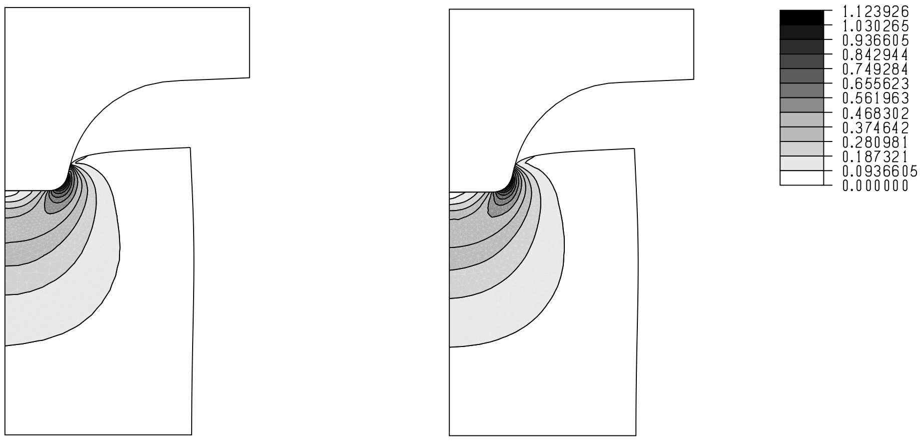

(a)$_2$ $u = 8\,[mm]$ (b)$_2$ $u = 8\,[mm]$

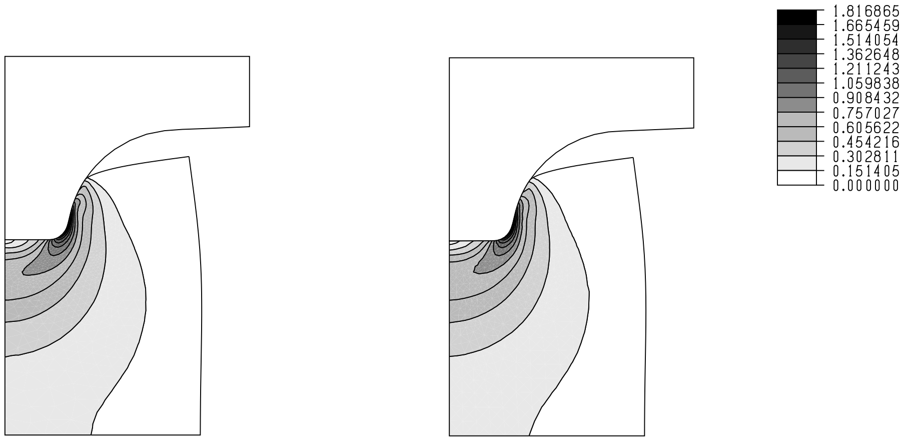

(a)$_3$ $u = 12\,[mm]$ (b)$_3$ $u = 12\,[mm]$

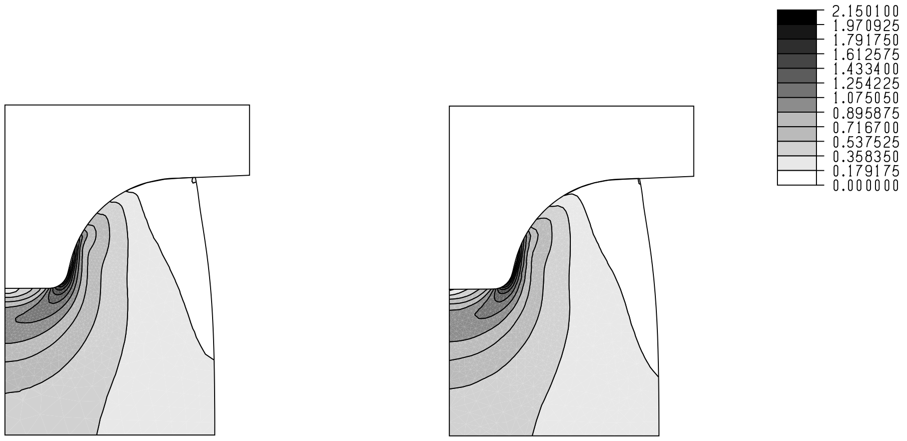

Figure 7.8: Axisymmetric piercing. Evolution of effective plastic strain for:(a) *F-bar-Patch*; (b) *F-bar* quadrilateral .

In this example, due to the geometry of the punch the process is characterized by large plastic deformation near the centre of the workpiece and contact interface. As the punch advances, the excess material flows around the punch which causes a greater increase of plastic deformation. Despite frequent remeshings convergence was attained without problems. For comparison, the distribution of the effective plastic strain obtained with the *F-bar* quadrilateral, exactly in the same circumstances, is also shown [see Figure 7.8(b)]. The plots show a very good agreement and no hourglassing patterns were observed.

7.7.2 Mesh prediction based on damage dissipation

The examples presented in this section are used to assess the performance of the numerical algorithms proposed in Chapter 5 (Section 5.4, page 82) and correlate the adaptive procedure to the underlying failure mechanism. Therefore, the error measure based on *damage dissipation* (Section 7.3.4) should provide refined meshes at regions of possible material failure.

Upsetting of a tapered specimen

The upsetting test of axisymmetric specimens is one of the most commonly used tests to study bulk metal forming processes because it is able to reproduce similar stress/strain states to the ones observed in these processes. This problem was analysed by Gouveia *et al.* (1996) where the experimental procedure is described: upsetting of a tapered specimen for a UNS L52905 (Unified Numbering System ASTM-SAE) lead alloy. The geometry of the problem, boundary conditions and the finite element mesh adopted are given in the Figure 7.9. The mesh discretises one symmetric quarter of the problem with

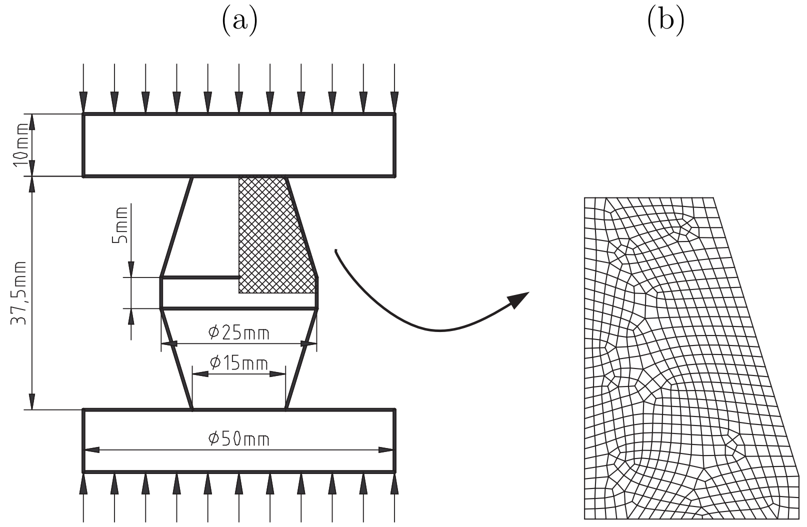

Figure 7.9: Tapered specimen: (a) problem geometry and (b) initial mesh.

the appropriate symmetric boundary conditions imposed to the relevant edges. This test presents interesting results regarding the fracture initiation site. In general, fracture initiation occurs either at the specimen centre or external surface near the equator. The simulation was executed until a 65% reduction was achieved on the total height. The frictional contact condition on the tool/workpiece interface is modelled by the standard Coulomb friction law in conjunction with a penalty method to impose contact impenetrability. The normal and tangential penalty values employed in this simulation are, respectively, $P_n = 1.2\times10^7\ [N/mm]$ and $P_t = 1\times10^5\ [N/mm]$. The incipient fracture at the external surface of the specimen near the equator was detected by Gouveia *et al.* (1996) through an optical microscope inspection. The material properties adopted are listed in Table 7.3.

Table 7.3: Material data for lead alloy and other simulation parameters.

Description	**Symbol**	**Value**
Specific mass	ρ	11340 $[kg/m^3]$
Elastic Modulus	E	18000 $[MN/m^2]$
Poisson's ratio	ν	0.4
Initial yield stress	σ_{y_0}	43 $[MPa]$
Yield stress	$\sigma_y(\bar{\varepsilon}^{\mathrm{p}})$	$66.656 \cdot (\bar{\varepsilon}^{\mathrm{p}})^{0.10158}$
Friction	m	0.35
Damage data (exponent)	s	1.0
Damage data (denominator)	r	1.5 $[MPa]$
Crack closure parameter	h	0.05
Plastic threshold	$\bar{\varepsilon}^p_{th}$	0
Error checking		100 time steps
Target error	η_{wd}	2 %
Target error	η_{wp}	0.5 %
Maximum element size	h_{max}	1.0 $[mm]$
Minimum element size	h_{min}	0.2 $[mm]$

The target errors, η_K, for each case have been chosen to provide meshes able to combine small numbers of elements and the damage parameters r and s provide low damage at the final stage. This is important to minimize the effect of the damage variable in the overall material behaviour in order to compare the error estimates. During the compression of the specimen several mesh refinements were undertaken and the robustness and reliability of the adaptive procedure is strongly affected by the choice of error estimator.

Estimate based on the damage dissipation: The evolution of the deformed mesh, here controlled by the damage dissipation-based error estimator, as well as the damage rate obtained in the finite element analysis are illustrated in Figure 7.10. The damage evolution (not shown here), conforms to the following pattern: in the early stages of the loading process the maximum value of damage is detected at the external surface near the contact regions because of the displacement restriction of the contact surfaces. This promotes a high gradient for the damage rate, $\dot{D}$, observed in Figure 7.10(a) and consequently a refined mesh is obtained. When a compression of 40% is reached, the damage is growing simultaneously in the specimen centre and in the exterior surface near the equator. The reason for the damage growth at the specimen centre relies on the highly compressive state achieved in the specimen centre. This damage growth is drastically reduced by the introduction of the crack closure parameter. Otherwise, the damage would grow at a very fast rate and localise in the centre of the specimen. The tensile stresses obtained in the exterior surface near the equator also promote damage evolution. The damage rate contour depicted in Figure 7.10(b) illustrates this behaviour and the mesh refinement in this region. Throughout the upsetting process, the value of damage increases faster at the exterior surface of the tapered specimen because the material flow in the radial direction promotes states with purely tensile principal stresses. This can be observed in Figure 7.11(a) by the damage rate combined

(a) reduction of 1%. (b) reduction of 26%.

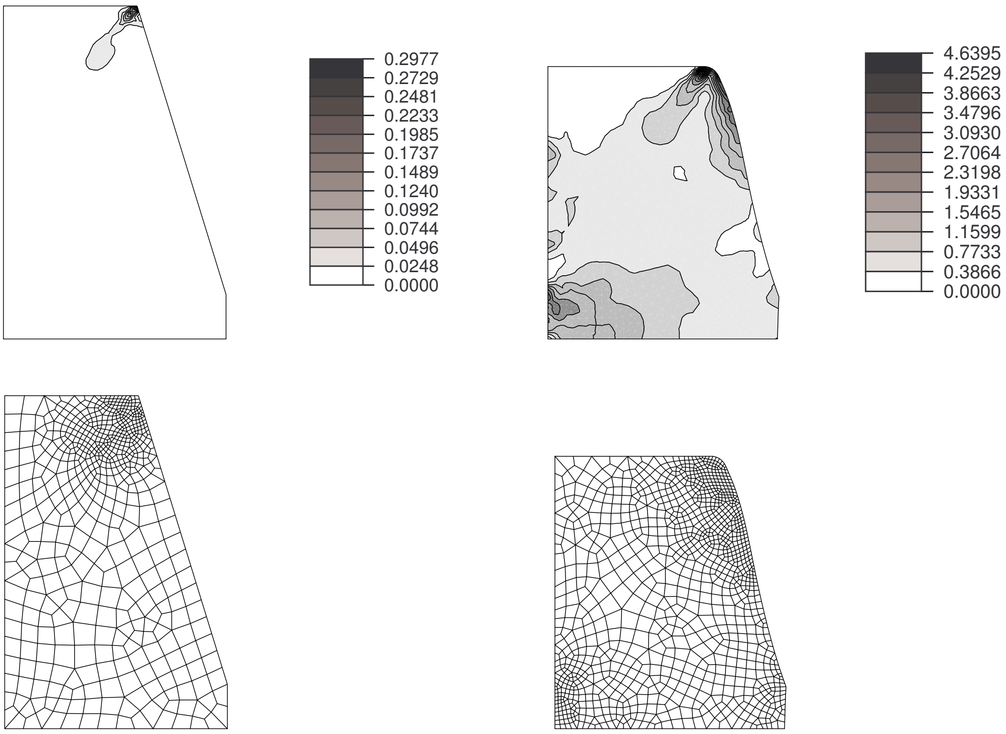

Figure 7.10: Tapered specimen: initial evolution of damage rate and deformed mesh.

with the contour of energy release rate (not shown here), Y, which is extremely localised over all the exterior surface of the specimen. The mesh refinement is then obtained at the exterior surface of the specimen. At the final stage, the damage is localised over the region close to the external surface near the equator. Although, there is a small gradient of the damage rate in this zone a fine mesh is predicted in that region [see Figure 7.11(b)]. This result, shows that the error estimator was able to capture the damage evolution and produce refined meshes at regions of material failure. The damage contour and total damage work at the last stage of the compression can be seen in Figure 7.12.

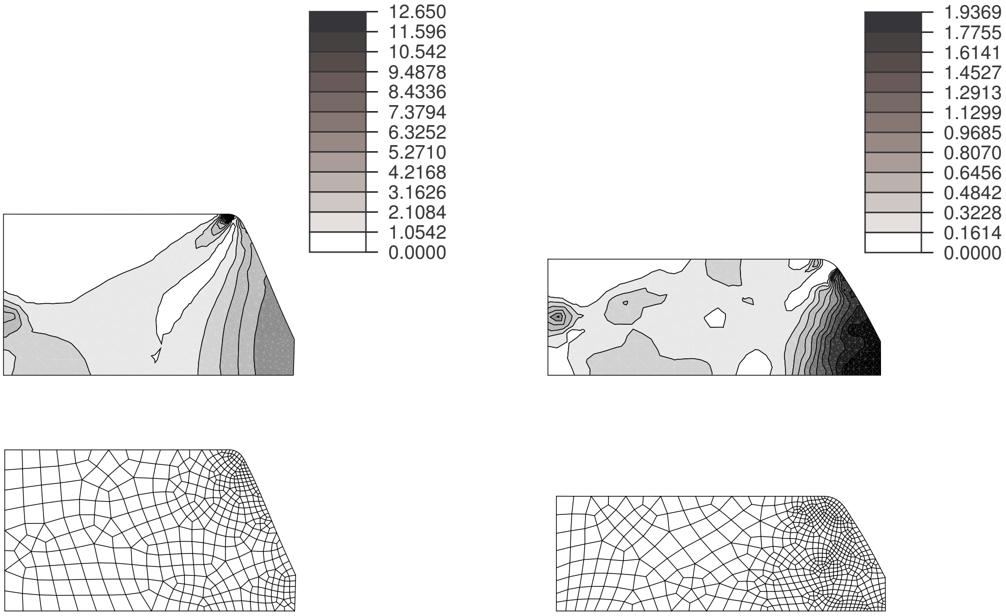
(a) reduction of 46%.

(b) reduction of 65%.

Figure 7.11: Tapered specimen: final evolution of damage rate and deformed mesh.

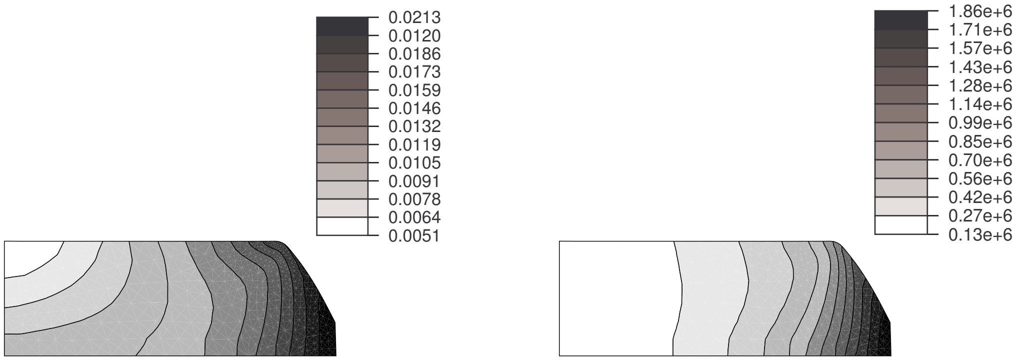
(a) reduction of 65%.

(b) reduction of 65%.

Figure 7.12: Tapered specimen: (a) damage variable; (b) Total damage work.

Again, the criterion based on *total damage work*, correctly predicts the location of fracture onset and also exhibits a high gradient near the critical failure zone. Therefore, the use of the *damage work release parameter* (-Y) by the error indicator ensured a proper description of damage progression. It is important to remark that the robustness and reliability of total damage work is affected by the choice of damage model upon which it is based. As strain paths become more complex, particularly when both tensile and compressive states are present, an erroneous estimate of damage based on the standard Lemaitre model (Lemaitre, 1983, 1985a), will inhibit the ability of the total damage work indicator to predict fracture onset.

Estimate based rate of plastic work: The same problem was simulated using the error estimator based on the rate of plastic work to predict mesh density during the adaptive procedure. The only difference relies on the numerical value for the target error, $\eta_{wp} = 0.5\%$. The strain rate and deformed mesh obtained in the finite element analysis are at two different stages of the analysis is illustrated in Figure 7.13. Clearly, the higher density regions do not correspond to the areas of greater damage evolution, making this estimator inappropriate for the type of problems addressed in this thesis.

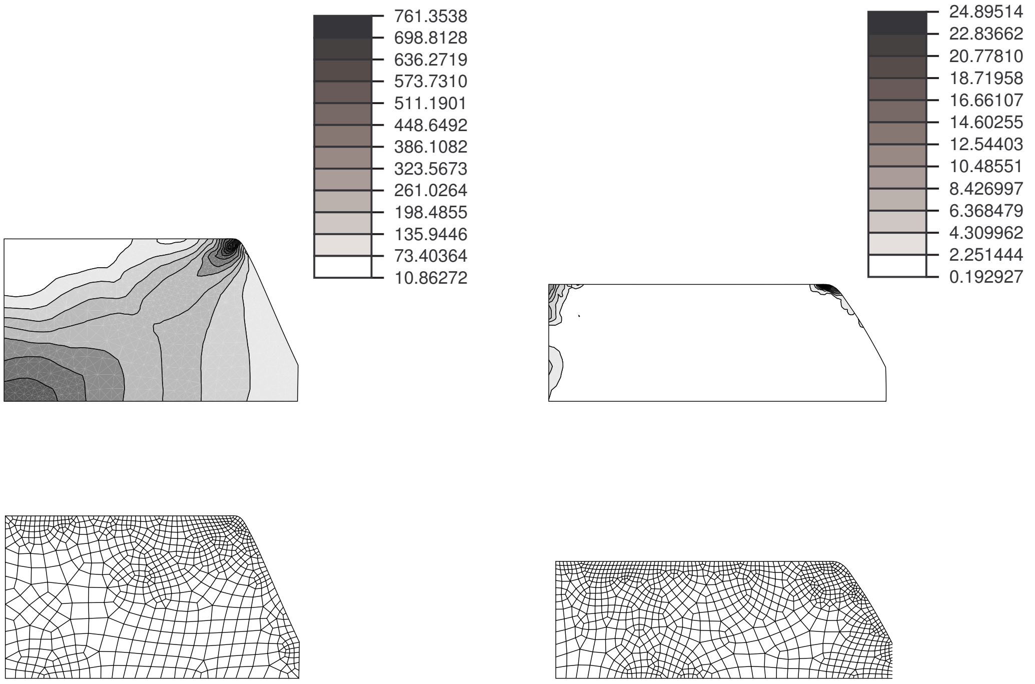
(a) reduction of 46%.

(b) reduction of 65%.
761.3538
698.8128
636.2719
573.7310
511.1901
448.6492
386.1082
323.5673
261.0264
198.4855
135.9446
73.40364
10.86272
24.89514
22.83662
20.77810
18.71958
16.66107
14.60255
12.54403
10.48551
8.426997
6.368479
4.309962
2.251444
0.192927

Figure 7.13: Tapered specimen: strain rate and deformed mesh using plastic dissipation-based error estimator.

Remark 7.5 *In this example the damage parameters* r *and* s *employed promoted a low damage at the final stage. If higher values of the damage variable are attained, the (usually sharp) localisation of damage that precedes fracture initiation, would improve further the performance of the damage dissipation-based error estimator*

Three-dimensional backward extrusion

A general feature encountered in the finite element simulation of forming operations, such as forging, extrusion or deep drawing, is that the evolving geometry is complex and often characterised by intricate contact conditions. The fully three-dimensional analysis of such problems is by no means trivial and some serious implementation difficulties arise. Particularly important is the generation of good quality meshes for arbitrary geometries which are free of *sliver* (near zero volume) elements. When finite deformations are considered such elements can rapidly degenerate under further loading. This together with the enforcement of the contact constraints, increases the complexity of finite element simulation to an extent that, sometimes, the solution obtained fails to provide an accurate description of the material response.

In this example, the computational framework developed in this thesis is applied to the three-dimensional analysis of a backward extrusion problem. It incorporates the damage constitutive model developed in Chapter 5, the *F-bar-Patch* tetrahedral element proposed in Chapter 6 and the estimator based on damage dissipation presented in this Chapter. The complete initial geometry of the problem is shown in Figure 7.14. It is possible to observe that the cross-section of the tool at section A-A contains very small radii, which constrain the material flow between the punch and die. The two-dimensional simulation

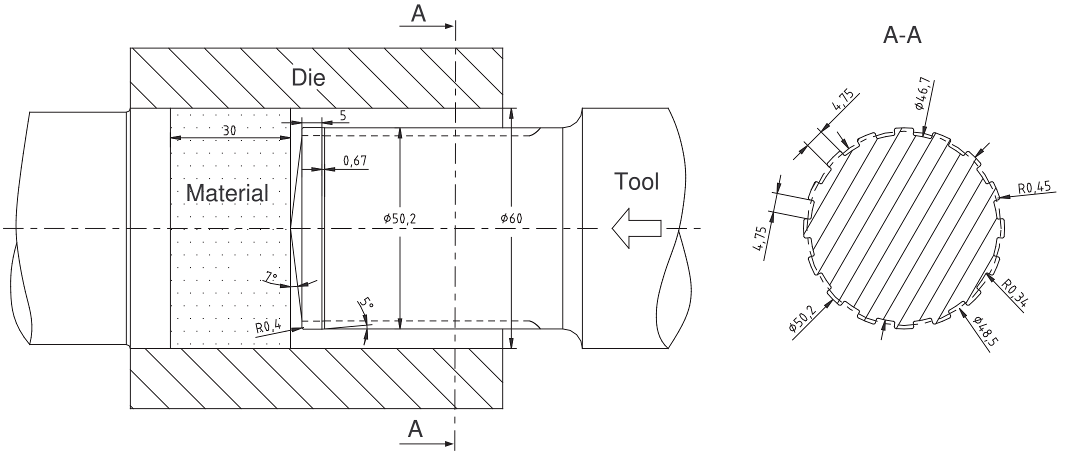

Figure 7.14: Backward extrusion: Problem geometry (dimensions in [mm]).

of the problem was undertaken in Chapter 5. We remark that in the two-dimensional analysis the primary objective was simply to outline the specific behaviour of the damage variable that increases in different ways under tensile and compressive regimes. Therefore, the geometry of the tool was simplified and considered axisymmetric to allow a faster two-dimensional estimate.

The frictional contact condition at the tool/workpiece interface is modelled, as in the two-dimensional case, by the standard Coulomb friction law in conjunction with the classical penalty method. The normal and tangential penalty values employed in the analysis are, respectively, $P_n = 4.5 \times 10^5\,[N/mm]$ and $P_t = 2 \times 10^5\,[N/mm]$. All components of the adaptive procedure employed, in this example, are the same as in the two-dimensional simulation, except for the number of sampling points used by the transfer operator which is here increased to 12. A prescribed total displacement of $u = 24.8\,[mm]$ is applied to the tool. Due to symmetry, only a 1/32 symmetric slice of the geometry is simulated, with appropriate boundary conditions imposed on the symmetry planes. The deformed geometry obtained at an intermediate stage of the simulation is plotted in Figure 7.15 side by side with the real workpiece.

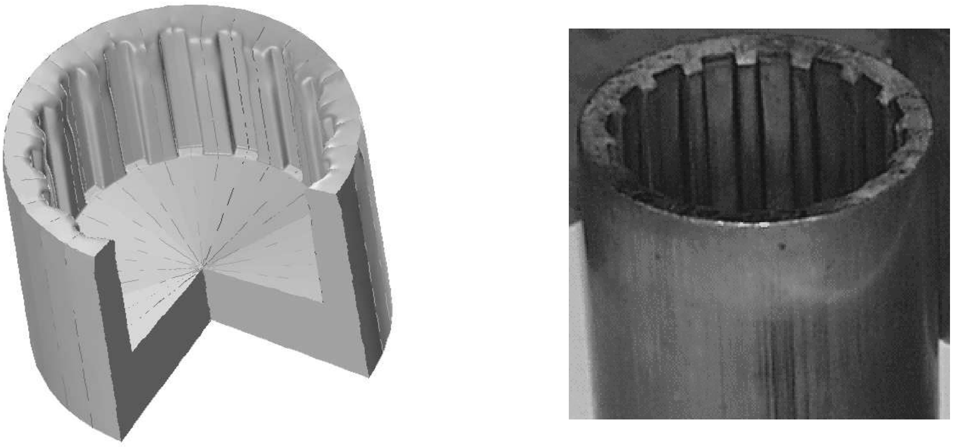

(a) Simulated geometry (b) Real workpiece

Figure 7.15: Three dimensional backward extrusion.

In order to maintain the numerical error within prescribed bounds [see Table 4.3, page 103], it was necessary to perform more than a thousand adaptive remeshings. The solid was discretised, during the analysis, with a total number of elements that ranged from 4,000 (initial mesh) to 500,000 finite elements (intermediate mesh). The criterion employed to predict the mesh density, based on the *damage dissipation*, ensured that the finite element mesh maintained a good aspect ratio and the adaptive scheme was able to produce sufficiently fine meshes in regions where the gradient of damage rate is high and coarsened elsewhere. Figure 7.16 illustrates the evolving finite element mesh for a prescribed displacement of $u = 12.4\,[mm]$. Some details of the geometry are enlarged for ease of visualisation.

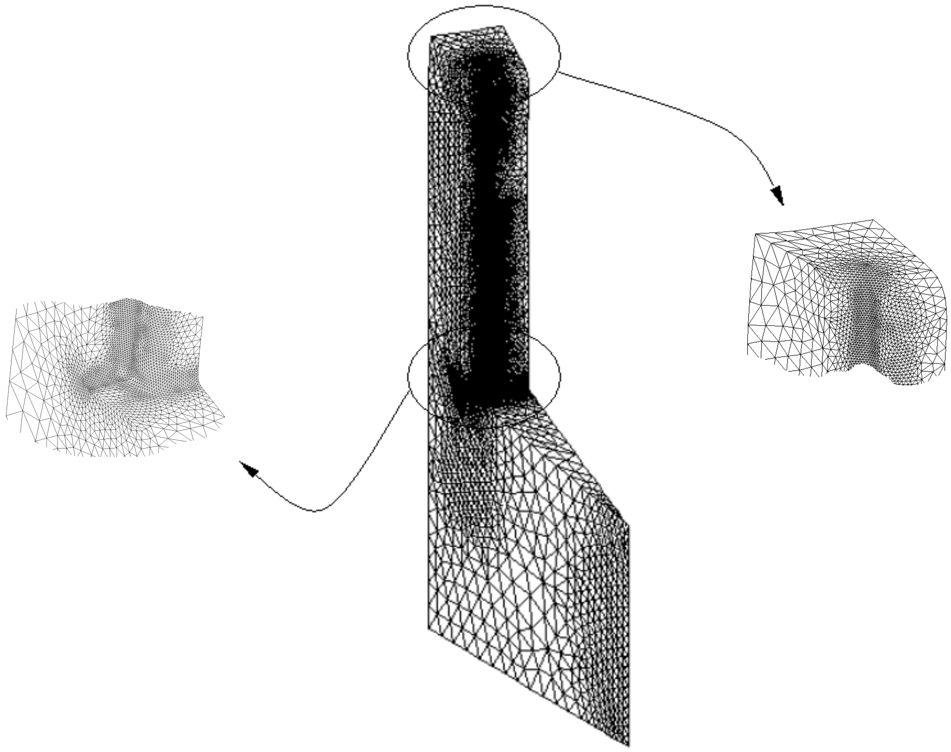

Figure 7.16: Finite element mesh for a prescribed displacement of $u = 12.4\,[mm]$.

The ideal adaptive scheme should be able to attain a numerical solution with a high level of accuracy allied to an economical computational cost. The correlation between the adaptive procedure and the underlying failure mechanism enforced by the error estimator, has proved successful. Nevertheless, whenever a new finite element mesh is generated, it is important to ensure that the discretised domain boundary preserves important aspects of the original geometry. If appropriate care is not taken, some geometric features such as corners, edges, etc, may be lost. To avoid this, some regions of the evolving mesh were specified to maintain a small element size, even if the prediction based on damage dissipation allows a larger size.

The evolution of the damage variable field obtained in the finite element analysis is illustrated in the contour plots shown in Figure 7.17. It can be seen that damage starts developing at the interior surface of the workpiece and the critical area is located at the outside corner of the punch teeth. This result agrees with experimental observations which show that defects are often present at the surface. The material that is in contact with the die does not suffer any damage and only within a critical radius near the internal surface does the damage field starts to develop.

(a) $u = 6.2\,[mm]$ (b) $u = 12.4\,[mm]$

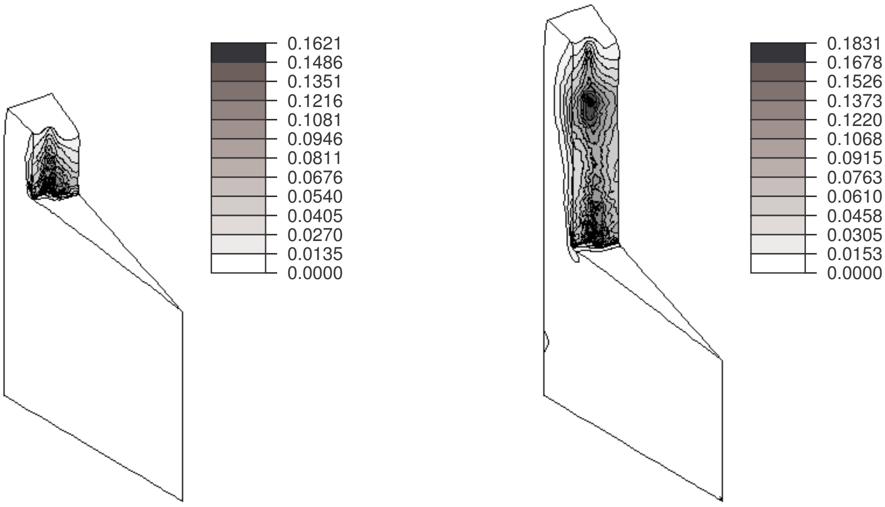

(c) $u = 18.6\,[mm]$ (d) $u = 24.8\,[mm]$

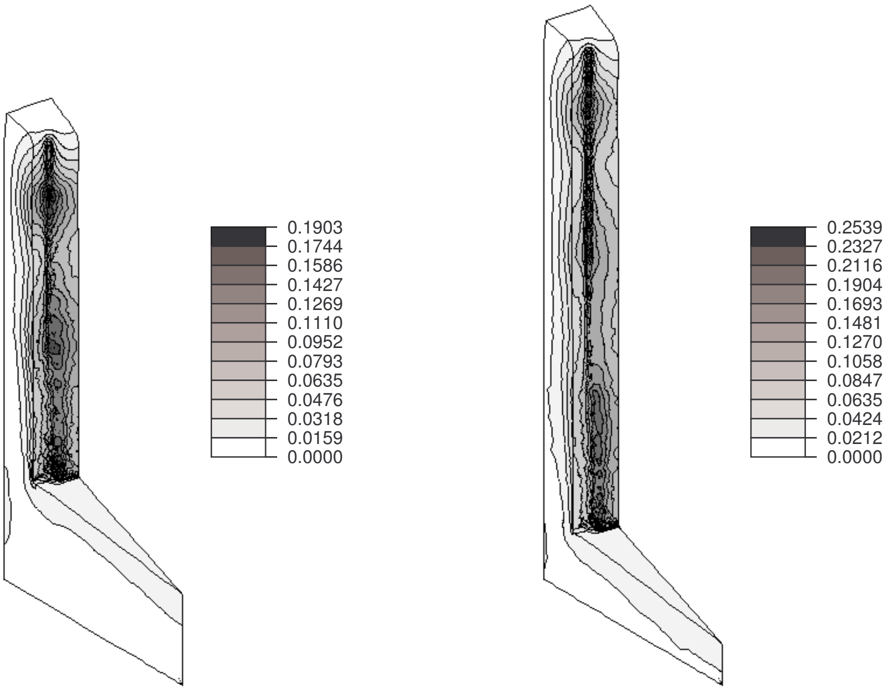

Figure 7.17: Three dimensional backward extrusion: damage contour plots.

We remark that the damage prediction estimated by the improved damage model combined with *F-bar-Patch* tetrahedra is nearly identical to that predicted in the simulation with the axisymmetric four-noded quadrilateral element (Belytschko & Bindeman, 1991) [see Section 5.4.4, page 102]. This example outlines the assembly of different numerical techniques, to model the gradual deterioration of ductile metals and predict material failure, demonstrating the robustness and reliability of the overall framework in relevant practical problems.

7.8 Concluding remarks

The introduction of an adaptive mesh refinement procedure, capable of ensuring that high quality meshes are used over the entire simulation, has become an essential tool in the analysis of realistic metal forming problems due to the large inelastic strains involved. An additional degree of complexity is introduced by the presence of internal deterioration which introduces local stress concentrations and drives plastic deformation. In particular, close to material failure, the energy dissipation associated with such mechanisms has a dominant effect. Therefore, two important aspects have been addressed in this chapter, i.e. *error estimates* and *transfer operators*.

Over recent years, several *error estimates* have been proposed for inelastic problems based not only on mathematical aspects, but also on physical considerations. The present work focuses on the development of *a posteriori* error estimates, based on the Zienkiewicz & Zhu (1987) recovery/projection technique, for elasto-plastic solids undergoing internal deterioration. The error estimate is proposed based on the principle that mesh refinement should be able to capture the portions of the workpiece where most of the *action* localises, i.e., where the relevant dissipative mechanisms are most active. Accordingly, an error estimator based on *damage dissipation* is suggested for ductile metals. In the examples presented, the estimator was able to capture the dynamic nature of the physical phenomena efficiently.

The *transfer operators* introduced by Perić *et al.* (1996) for *implicit* and by Dutko *et al.* (1997) for *explicit* time integration schemes were extended to account for the variables associated with damage. The transfer operation between meshes for the nodal and contact variables is performed directly using the standard transfer operator. For the internal variables a transfer operation in which the Gauss point values of the old mesh are mapped directly to the Gauss points of the new one, by means of a weighted least-squares method, is employed. This mapping prevents excessive diffusion of the transferred variables and ensures more efficiently the incompressible nature of plastic flow. To illustrate the ease with which *F-bar-Patch* elements can be employed within the adaptive procedure several numerical simulations were presented.

Chapter 8

Conclusion and Final Remarks

TOPICS related to constitutive modelling and numerical simulation of failure in finitely straining ductile materials have been discussed in this thesis. Attention is focused on the construction of a framework for prediction of failure. In particular, a model for finite strain elasto-(visco)plastic damage, a low order finite element for the numerical treatment of incompressibility and an adaptive mesh refinement strategy for this class of problems, constitute the building blocks of the overall approach. The theory and computational implementation of the corresponding models has been described in detail. Emphasis is given to the efficient numerical implementation of the proposed theories for large scale problems.

The strategy used for the numerical simulation of the proposed models is based in both explicit and implicit displacement based finite element procedures. In the implicit integration, particular attention has been given to the exact linearisation of the models presented which provide the basis for the full Newton-Raphson procedure for the iterative solution of the associated non-linear finite element equations. Although the use of explicit transient dynamic solutions for predominantly quasi-static simulations may be arguable, the reduced computational effort involved in large scale industrial problems and a simpler treatment of frictional contact (eliminating convergence problems associated with implicit analysis) justify its use. Furthermore, explicit integration is particularly advantageous in problems involving fragmentation (not addressed in this work) where crack initiation and propagation are present together with complicated contact conditions.

The following sections provide a short summary and the main conclusions regarding the topics of research considered in this thesis.

8.1 Summary and conclusions

The aim of this thesis, which is stated in Section 1.1, has been achieved. Namely, the construction of an efficient framework, to model the gradual internal deterioration of ductile metals and predict material failure in relevant practical problems. Several computational aspects have been addressed, leading to the enhancement of existing algorithms and development of new techniques, amongst which are *constitutive modelling*, *element technology* and *adaptive remeshing*. In the following, a more detailed list of the achievements and conclusions of this work is provided.

8.1.1 Damage constitutive modelling

The prediction of damage growth and fracture initiation in finitely deforming ductile solids is an important factor and a major component in metal forming processes. Constitutive models based on damage mechanics have not only provided more consistent formulations to address the problem, but have also proved to give more reliable prediction of the fracture initiation site due to the coupled effects of plastic deformation and material degradation.

In Chapter 5, a model for elasto-plastic and elasto-viscoplastic damage were presented. The models, which in addition to isotropic hardening include the important effect of crack closure in the damage evolution, have been obtained by suitably modifying Lemaitre's fully coupled damage equations (Lemaitre, 1996). Introduction of the coupled constitutive equations did not affect appreciably the performance of the models, enabling efficient simulation of the effects of material deterioration in large scale computations. This was due to the fact that the return mapping integration algorithm was reduced to a non-linear *single equation*. The accuracy and stability of the material related stress integration procedure has been carried out relying on the analysis of iso-error maps. The consistent linearization of the associated incremental boundary value problem has been carefully considered and a closed formula for the tangent operator consistent with the integration algorithm has also been presented.

Numerical simulations have shown the performance of the algorithms in the presence of combined tensile/compressive stress states, which may have important consequences in failure analysis of metal forming processes. Finally, it is remarked that the extension to the finite strain range, for both implicit and explicit time integration schemes, can be promptly obtained by means of the framework described in Chapter 4.

8.1.2 Element technology for near incompressibility

Due to their inherent simplicity, standard isoparametric simplex elements (linear triangles in 2-D and linear tetrahedra in 3-D) are known to provide an excellent framework in which complex geometry and contact conditions coupled with remeshing procedures can be dealt with in an effective and efficient manner. Therefore, in Chapter 6, the numerical treatment of incompressibility for simplex elements, has been addressed. In Section 6.3, a thorough assessment of the volumetric nodal average concept (Bonet & Burton, 1998) has been presented. The assessment has been carried out based on an implict version of the formulation obtained within the framework of the *F-bar* methodology (de Souza Neto *et al.* , 1996). In this context, a linear triangle for implicit plane strain and axisymmetric analysis of nearly incompressible solids has been devised. A comprehensive set of numerical simulations has been presented. The examples have shown that the nodal averaging technique substantially reduces the locking tendency of the linear triangle and produces quite reasonable predictions of deformed shapes as well as reaction forces. However, the examples have also shown that the element can produce considerable checkerboard – type hydrostatic pressure fluctuations. This fact prevents the successful use of the average nodal volume technique in situations where an accurate prediction of hydrostatic pressure is required.

In Section 6.4, a new methodology which allows the use of two- and three-dimensional simplex finite elements in the large strain analysis of nearly incompressible solids has been proposed. The technique is an extension of the *F-bar* method (de Souza Neto *et al.* , 1996). It relies essentially on the relaxation of the excessive volumetric constraint through the enforcement of the incompressibility constraint over a *patch* of simplex elements. An important aspect of the present method is that it preserves the displacement-based format of the corresponding finite element equations as well as the strain-driven format of standard algorithms for integration of dissipative constitutive equations and can be used regardless of the material model adopted. The computational implementation of the new elements is described in detail for both implicit and explicit time integration schemes. A comprehensive set of numerical examples, including some well known benchmark tests, have shown that the proposed technique has effectively overcome the volumetric locking that characterises conventional simplex elements. In addition, the new elements have shown no signs of spurious mechanisms.

8.1.3 Adaptive remeshing for history dependent problems

The introduction of an adaptive mesh refinement procedure, capable of ensuring that high quality meshes are used over the entire simulation, has become an essential tool in the analysis of realistic metal forming problems due to the large inelastic strains involved. An additional degree of complexity is introduced by the presence of internal deterioration which introduces local stress concentrations and drives plastic deformation. Therefore, two important aspects have been addressed in Chapter 7, i.e. *error estimates* and *transfer* *operators.*

In the present work, the development of *a posteriori* error estimates was based on Zienkiewicz & Zhu (1987) recovery/projection technique, for elasto-plastic solids undergoing internal deterioration. The error estimate is proposed based on the principle that mesh refinement should be able to capture the regions of the workpiece where most of the *action* localises, i.e., where the relevant dissipative mechanisms are most active. In the examples presented, the estimator was able to capture the dynamic nature of the physical phenomena efficiently.

The *transfer operators* introduced by Perić *et al.* (1996) for *implicit* and by Dutko *et al.* (1997) for *explicit* time integration schemes were extended to account for the variables associated with damage. For the internal variables a transfer operation in which the Gauss point values of the old mesh are mapped directly to the Gauss points of the new one, by means of a weighted least-squares method, is employed. This mapping prevents excessive diffusion of the transferred variables and ensures more efficiently the incompressible nature of plastic flow. To illustrate the ease with which *F-bar-Patch* elements can be employed within the adaptive procedure several numerical simulations were presented.

8.2 Suggestions for future research

In the context of nonlinear solid mechanics problems considered in this work, there has been considerable advancement in several topics of finite element research. In many areas, such techniques have reached a high degree of predictive capability and are essential instruments to address realistic engineering problems. Some aspects concerning the continuity of the present study and general issues regarding future research are briefly discussed below:

- An experimental program should be carried out to validate the damage constitutive models. The experimental identification of material parameters is relatively simple due to the phenomenological nature of such theories;
- A complete analysis of forming operations requires a fully coupled thermo-mechanical model to account for the heat conduction within the work-piece and tool. Furthermore, cyclical conditions are often present in the process. As a result, an extension of the constitutive models is recommended in order to capture the damage evolution and predict ductile fracture under such conditions;
- Most numerical simulations, as in the present case, adopt Coulomb's friction law. Thus, the development and application of more realistic models is recommended;

- Metal cutting operations represent some of the most challenging computational problems. In this type of processes failure in the form of fracturing is the major phenomenon controlling the process. Therefore, it is suggested to extend the range of applicability of the proposed framework to operations such as metal cutting.

Bibliography

Alberty, J., Carstensen, C., & Zarrabi, D. 1999. Adaptive numerical analysis in primal elastoplasticity with hardening. *Comp. Meth. Appl. Mech. Engng.*, **171**, 175–204.

Andrade Pires, F.M., de Souza Neto, E.A., & de la Cuesta Padilla, J.L. 2003a. An Average Nodal Volume Linear Triangle For Implicit Finite Element Analysis of Nearly Incompressible Solids. *In:* Oñate, E., & Owen, D.R.J. (eds), *Computational Plasticity: Fundamentals and Applications – Proceedings of the Seventh International Conference held in Barcelona,* 7 − 10th *April.* Barcelona, Spain: CIMNE.

Andrade Pires, F.M., de Souza Neto, E.A., & Owen, D.R.J. 2003b. Computatinal Modelling Of Fracturing Solids. *Pages 177–182 of:* Benallal, A., & S.P.B., Proena (eds), *Recent Developments In The Modelling Of Rupture In Solids - Proceedings of the International Symposium held at Foz do Iguau,* 4th − 7th *August.*

Andrade Pires, F.M., de Souza Neto, E.A., & de la Cuesta Padilla, J.L. 2004a. An assessment of the average nodal volume formulation for the analysis of nearly incompressible solids under finite strains. *Comm. Num. Meth. Eng.*, **20**, 569–583.

Andrade Pires, F.M., de Souza Neto, E.A., & Owen, D.R.J. 2004b. Finite Element Modelling of Ductile Fracture Prediction in Inelastic Solids. *In:* Neittaanmaäki, P., Rossi, T., Majava, K., & Pironneau, O. (eds), *ECCOMAS 2004 - European Congress on Computational Methods in Applied Sciences and Engineering, ,* 24 − 28th *July.*

Andrade Pires, F.M., de Souza Neto, E.A., & Owen, D.R.J. 2004c. On the Finite Element Prediction of Damage Growth and Fracture Initiation in Finitely Deforming Ductile Materials. *Comp. Meth. Appl. Mech.*, **193**, 5223–5256.

Argyris, J.H., & Kleiber, M. 1977. Incremental Formulation in Nonlinear Mechanics and Large Strain Elasto-plasticity – Natural Approach. Part I. *Comp. Meth. Appl. Mech. Engng.*, **11**, 215–247.

Argyris, J.H., Doltsinis, J.St., & Kleiber, M. 1978. Incremental Formulation in Nonlinear Mechanics and Large Strain Elasto-plasticity – Natural Approach.Part II. *Comp. Meth. Appl. Mech. Engng.*, **14**, 259–294.

Arnold, G., Hubert, O., Dutko, M., & Billardon, R. 2002. Identification of a Continuum Damage Model from Micro-Hardness Measurements. *Int. J. Forming Processes*, **5**, 163–173.

Atkins, A.G. 1981. Possible explanation for unexpected departures in hydrostatic tension-fracture strain relations. *Metal Sci.*, **15**, 81–83.

Atkins, A.G., & Mai, Y.W. 1985. *Elastic and Plastic Fracture.* Chichester: Ellis Horwood Ltd.

Atluri, S.N. 1984. On Constitutive Relations at Finite Strains: Hypo-Elasticity and Elasto-Plasticity with Isotropic or Kinematic Hardening. *Comp. Meth. Appl. Mech. Engng.*, **43**, 137–171.

Babuška, I. 1978. Error Estimates For Adaptive Finite Element Computations. *SIAM J. Numer. Anal.*, **15**, 736–754.

Babuška, I., & Rheinboldt, W.C. 1978. A Posteriori Error Estimates For The Finite Element Method. *Int. J. Num. Meth. Engng.*, **12**, 1597–1615.

Babuška, I., & Rheinboldt, W.C. 1979. Adaptive approaches and reliability estimates in finite element analysis. *Comp. Meth. Appl. Mech. Engng.*, **17**, 519–540.

Babuška, I., & Strouboulis, T. 2001. *The Finite Element Method and Its Reliability.* Oxford: Clarendon Press.

Babuška, I., Strouboulis, T., Updhyay, C.S., Gangaraj, S.K., & Copps, K. 1994a. An objective criterion for assessing the reliability of "a posteriori" error estimators in finite element computations. *IACM Bulletin of the Int. Assoc. Comp. Mech.*, **9**, 27–37.

Babuška, I., Strouboulis, T., Updhyay, C.S., Gangaraj, S.K., & Copps, K. 1994b. Validation of a posteriori error estimates by numerical approach. *Int. J. Num. Meth. Eng.*, **37**, 1073–1123.

Barthold, F.-J., Schmidt, M., & Stein, E. 1997. Bulk Forming Simulation by Adaptive Explicit FEM. *Pages 597–602 of:* Oñate, E., Owen, D.R.J., & Hinton, E. (eds), *Computational Plasticity: Fundamentals and Applications.* Barcelona: CIMNE.

BASISTA, M., KRAJČINOVIĆ, D., & ŠUMARAC, D. 1992. Micromechanics, Phenomenology and Statistics of Brittle Deformation. *Pages 1479–1490 of:* OWEN, D.R.J., OÑATE, E., & HINTON, E. (eds), *Computational Plasticity: Fundamentals and Applications – Proceedings of the Third International Conference held in Barcelona, 6th–10 th April 1992.* Swansea: Pineridge Press.

BATHE, K.-J. 1996. *Finite Element Procedures.* Englewood Cliffs, New Jersey: Prentice-Hall.

BELYTSCHKO, T. 1983. An overview of semidiscretization and time integration procedures. *Pages 1–65 of: Computational Methods for Transient Analysis.* North-Holland: Amesterdam.

BELYTSCHKO, T., & BINDEMAN, L.P. 1991. Assumed strain stabilization of the 4-node quadrilateral with 1-point quadrature for nonlinear problems. *Comp. Meth. App. Mech. Engng.*, **88**, 311–340.

BELYTSCHKO, T., ONG, J.S.J., LIU, W.K., & KENNEDY, J.M. 1984. Hourglass Control in Linear and Non Linear Problems. *Comp. Meth. App. Mech. Engng.*, **43**, 251–276.

BELYTSCHKO, T., WONG, B.L., & PLAKACZ, E.J. 1989. Fission-Fusion Adaptivity in Finite Elements for Nonlinear Dynamics of Shells. *Comp. Struct.*, **33**, 1307–1323.

BELYTSCHKO, T., LIU, W.K., & MORAN, B. 2000. *Nonlinear Finite Elements for Continua and Structures.* New York: Wiley.

BENALLAL, A., BILLARDON, R., & DOGHRI, I. 1988. An Integration Algorithm and the Corresponding Consistent Tangent Operator for Fully Coupled Elastoplastic and Damage Equations. *Comm. Appl. Num. Meth.*, **4**, 731–740.

BENALLAL, A., BILLARDON, R., & LEMAITRE, J. 1991. Continuum Damage Mechanics and Local Approach to Fracture: Numerical Procedures. *Comp. Meth. Appl. Mech. Engng.*, **92**, 141–155.

BONET, J., & BURTON, A.J. 1998. A Simple Average Nodal Pressure Tetrahedral Element for Incompressible and Nearly Incompressible Dynamic Explicit Applications. *Comm. Num. Meth. Engng.*, **14**, 437–449.

BONET, J., MARRIOT, H., & HASSAN, H. 2001. An Average Nodal Deformation Gradient Linear Tetrahedral Element For Large Strain Explicit Dynamic Applications. *Comm. Num. Meth. Engng.*, **17**, 551–561.

Brozzo, P., Deluca, B., & Rendina, R.A. 1972. A new method for the prediction of the formability limits of metal sheets. *In: Proc. 7th Biennial Conf. Int. Deep Drawing Research Group.*

Brunig, M. 2003. An anisotropic ductile damage model based on irreversible thermodynamics. *Int. J. of Plasticity*, **19**, 1679–1713.

Camacho, G.T., & Ortiz, M. 1997. Adaptive Lagrangian modelling of ballistic penetration of metallic targets. *Comp. Meth. Appl. Mech. Engng.*, **142**, 269–301.

Carlson, D.E., & Hoger, A. 1986. The Derivative of a Tensor-Valued Function of a Tensor. *Quart. Appl. Math.*, **44**(3), 409–423.

Cescotto, S., & Zhu, Y.Y. 1995. Modelling of Ductile Fracture Initiation During Bulk Forming. *Pages 987–998 of:* Owen, D.R.J., Oñate, E., & Hinton, E. (eds), *Computational Plasticity: Fundamentals and Applications – Proceedings of the Fourth International Conference held in Barcelona, 3rd–6 th April 1995.* Swansea: Pineridge Press.

Chaboche, J.L. 1978. *Description Thermodynamique et Phénoménologique de la Viscoplasticité Cyclique avec Endommagement.* Tech. rept. 1978–3. Office National d'Etudes et de Recherches Aérospatiales.

Chaboche, J.L. 1981. Continuous Damage Mechanics – A Tool to Describe Phenomena Before Crack Initiation. *Nuclear Engng. Design*, **64**, 233–247.

Chaboche, J.L. 1984. Anisotropic Creep Damage in the Framework of Continuum Damage Mechanics. *Nuclear Engng. Design*, **79**, 309–319.

Chaboche, J.L. 1988. Continuum Damage Mechanics: Part I – General Concepts and Part II – Damage Growth, Crack Initiation and Crack Growth. *J. Appl. Mech.*, **55**, 59–72.

Chadwick, P., & Ogden, R.W. 1971. A Theorem in Tensor Calculus and its Application to Isotropic Elasticity. *Arch. Rat. Mech. Anal.*, **44**, 54–68.

Chandrakanth, S., & Pandey, P.C. 1993. A new ductile damage evolution model. *Int. J. of Fracture*, **60**, 73–76.

Clift, S.E., Hartley, P., Sturgess, C.E.N., & Rowe, G.W. 1990. Fracture prediction in plastic deformation process. *Int. J. Mech. Sci.*, **32**, 1–17.

Cockcroft, M.G., & Latham, D.J. 1968. Ductility and workability of metals. *J. Inst. Metals*, **96**, 33–39.

COFFIGNAL, G. 1987. *Optimisation et Fiabilité des Calculs Eléments Finis en Elastoplasticité.* Ph.D. thesis, Université Pierre et Marie Curie - Paris 6, France.

COLEMAN, B.D., & GURTIN, M.E. 1967. Thermodynamics with Internal State Variables. *J. Chemical Physics*, **47**(2), 597–613.

CRISFIELD, M.A. 1991. *Non-linear Finite Element Analysis of Solids and Structures. VOLUME 1: Essentials.* Chichester: John Wiley & Sons.

CRISFIELD, M.A. 1997. *Non-linear Finite Element Analysis of Solids and Structures. VOLUME 2: Advanced Topics.* Chichester: John Wiley & Sons.

CRISFIELD, M.A., & MOITA, G.F. 1996. A Co-rotational Formulation for 2-D Continua Including Incompatible Modes. *Int. J. Num. Meth. Engng.*, **39**, 2619–2633.

CRISFIELD, M.A., MOITA, G.F., JELENIĆ, G., & LYONS, L.P.R. 1995. Enhanced Lower-Order Element Formulations for Large Strains. *Pages 293–320 of:* OWEN, D.R.J., OÑATE, E., & HINTON, E. (eds), *Computational Plasticity: Fundamentals and Applications – Proceedings of the Fourth International Conference held in Barcelona, 3rd–6th April 1995.* Swansea: Pineridge Press.

CUITIÑO, A., & ORTIZ, M. 1992. A Material-Independent Method for Extending Stress Update Algorithms from Small-Strain Plasticity to Finite Plasticity with Multiplicative Kinematics. *Engng. Comp.*, **9**, 437–451.

CURNIER, A. 1984. A Theory of Friction. *Int. J. Solids Struct.*, **20**(7), 637–647.

DE BERG, M., VAN KREVELD, M., OVERMARS, M., & SCHWARZKOPF, O. 2000. *Computational Geometry - Algorithms and Applications.* New York: Springer Verlag.

DE BORST, R. 2001. Some recent issues in computational failure mechanics. *Int. J. Num. Meth. Engng.*, **52**, 63–95.

DE BORST, R., & PAMIN, J. 1996. Some novel developments in finite element procedures for gradient dependent plasticity. *Int. J. Num. Meth. Engng.*, **39**, 2477–2505.

DE SOUZA NETO, E.A. 2002. A Fast One-Equation Integration Algorithm for the Lemaitre Ductile Damage Model. *Comm. Num. Meth. Engng.*, **18**, 541554.

de Souza Neto, E.A. 2004. On General Isotropic Tensor Functions of One Tensor. *Int. J. Num. Meth. Eng.*, **61**, 880–895.

de Souza Neto, E.A., Perić, D., & Owen, D.R.J. 1994. A Model for Elasto-Plastic Damage at Finite Strains: Computational Issues and Applications. *Engng. Comp.*, **11**(3), 257–281.

de Souza Neto, E.A., Perić, D., & Owen, D.R.J. 1995. Finite Elasticity in Spatial Description: Linearization Aspects with 3-D Membrane Applications. *Int. J. Num. Meth. Engng.*, **38**, 3365–3381.

de Souza Neto, E.A., Perić, D., Dutko, M., & Owen, D.R.J. 1996. Design of Simple Low Order Finite Elements for Large Strain Analysis of Nearly Incompressible Solids. *Int. J. Solids Struct.*, **33**, 3277–3296.

de Souza Neto, E.A., Andrade Pires, F.M., & Owen, D.R.J. 2003. A New F-bar-Based Method for Linear Triangles and Tetrahedra in the Finite Strain Analysis of Nearly Incompressible Solids. *In:* Oñate, E., & Owen, D.R.J. (eds), *Computational Plasticity: Fundamentals and Applications – Proceedings of the Seventh International Conference held in Barcelona,* 7 – 10th *April.* Barcelona, Spain: CIMNE.

de Souza Neto, E.A., Perić, D., & Owen, D.R.J. 2005a. *Computational methods for plasticity: theory and application.* (in press).

de Souza Neto, E.A., Andrade Pires, F.M., & Owen, D.R.J. 2005b. F-bar-Based Linear Triangles and Tetahedra for Finite Strain Analysis of Nearly Incompressible Solids. Part I: Formulation and Benchmarking. *Int. J. Num. Meth. Eng.*, **62**, 353–383.

Demkowicz, L., Devloo, Ph., & Oden, J.T. 1985. On h-type mesh-refinement strategy based on minimization of interpolation errors. *Comp. Meth. Appl. Mech. Engng.*, **53**, 67–89.

Dieter, G. 1986. *Mechanical Metallurgy.* McGraw-Hill.

Díez, P., & Huerta, A. 1999. A unified approach to remeshing strategies for finite element h-adaptivity. *Comp. Meth. Appl. Mech. Engng.*, **176**, 215–229.

Doghri, I. 1995. Numerical Implementation and Analysis of a Class of Metal Plasticity Models Coupled with Ductile Damage. *Int. J. Num. Meth. Engng.*, **38**, 3403–3431.

Doll, S., Hauptmann, R., Schweizerhof, K., & Freischlager, C. 2000. On Volumetric Locking of Low-Order Solid and Solid-Shell Elements for Finite Elastoviscoplastic Deformations and Selective Reduced Integration. *Engng. Comp.* (in press).

DUTKO, M., PERIĆ, D., OWEN, D.R.J., WEI, Z., & YU, J. 1997. Bulk forming simulation by adaptive explicit FEM. *Pages 1305–1312 of:* OWEN, D.R.J., OÑATE, E., & HINTON, E. (eds), *Computational Plasticity: Fundamentals and Applications.* Barcelona, Spain: CIMNE.

DYDUCH, M., HABRAKEN, A.M., & CESCOTTO, S. 1992. Automatic adaptive remeshing for numerical simulations of metal forming. *Comp. Meth. Appl. Mech. Engng.*, **101**, 238–298.

ENGEL, L., & KLINGELE, H. 1981. *An Atlas of Metal Damage.* Wolfe Science BOOKs.

ESCOBAR, J.M., & MONTENEGRO, R. 1996. Several aspects of three-dimensional Delauny triangulation. *Advances Engng Software*, **27**, 27–39.

ETEROVIC, A.L., & BATHE, K.-J. 1990. A Hyperelastic Based Large Strain Elasto-Plastic Constitutive Formulation with Combined Isotropic-Kinematic Hardening Using the Logarithmic Stress and Strain Measures. *Int. J. Num. Meth. Engng.*, **30**, 1099–1114.

EVANS, L.C. 1999. *Partial Differential Equations.* American Mathematical Society.

FLANAGAN, D.P., & TAYLOR, L.M. 1987. An Accurate Numerical Algorithm for Stress Integration with Finite Rotations. *Comp. Meth. Appl. Mech. Engng.*, **62**, 305–320.

FONSEKA, G.U., & KRAJČINOVIĆ, D. 1981. The Continuous Damage Theory of Brittle Materials – Part 2:Uniaxial and Plane Response Modes. *J. Appl. Mech.*, **48**, 816–824.

FOURMENT, O.C., & HUANG, G.C. 1995. Error Estimators for Viscoplastic Materials: Application to Forming Processes. *Engng. Comp.*, **12**, 469–490.

FREUDENTHAL, A.M. 1950. *The Inelastic Behaviour of Engineering Materials and Structures.* John Wiley & Sons, New York.

GALLIMARD, L. 1994. *Contrôle adaptatif des calculs en élastoplasticité et en viscoplasticité.* Ph.D. thesis, LMT - E.N.S. de Cachan, France.

GALLIMARD, L., LADEVÈZE, P., & PELLE, J.P. 1996. Error Estimation and Adaptivity in Elastoplasticity. *Int. J. Num. Meth. Engng.*, **39**, 189–217.

GEERS, M.G.D., ENGELEN, R.A.B., & UBACHS, J.M.R. 2001. On the numerical modelling of ductile damage with an implicit gradient-enhanced formulation. *Revue Europeene des Elements Finis*, **10**, 173–191.

GLASER, S., & ARMERO, F. 1997. On the Formulation of Enhanced Strain Finite Element Methods in Finite Deformations. *Engng. Comp.*, **14**(7), 759–791.

GOSH, A.K. 1976. A criterion for ductile fracture in sheets under biaxial loading. *Metall. Trans. A*, **7**, 523–533.

GOUVEIA, B.P.P.A., RODRIGUES, J.M.C., & MARTINS, P.A.F. 1996. Fracture predicting in bulk metal forming. *Int. J. Mech. Sci.*, **38**, 361–372.

GUO, Y., ORTIZ, M., BELYTSCHKO, T., & REPETTO, E.A. 2000. Triangular composite finite elements. *Int. J. Num. Meth. Engng.*, **47**, 287–316.

GURSON, A.L. 1977. Continuum Theory of Ductile Rupture by Void Nucleation and Growth – Part I: Yield Criteria and Flow Rule for Porous Media. *J. Engng. Mat. Techn.*, **99**, 2–15.

GURTIN, M.E. 1981. *An Introduction to Continuum Mechanics.* Academic Press.

HAN, W., & REDDY, B.D. 1999. *Plasticity: Mathematical Theory and Numerical Analysis.* 2nd edn. Springer Verlag.

HANCOCK, J.W., & MACKENZIE, A.C. 1976. On the Mechanism of Ductile Fracture in High-Strength Steels Subjected to Multi-Axial Stress-States. *J. Mech. Phys. Solids*, **24**, 147–169.

HIBBITT, H.D., MARCAL, P.V., & RICE, J.R. 1970. A Finite Element Formulation for Problems of Large Strain and Large Displacement. *Int. J. Solids Struct.*, **6**, 1069–1086.

HILBER, H.M., & HUGHES, T.J.R. 1978. Collocation, Dissipation and Overshoot for Time Integration Schemes in Structural Dynamics. *Earthquake Engng. Struct. Dyn.*, **6**, 99–118.

HILL, R. 1950. *The Mathematical Theory of Plasticity.* London: Oxford Univ. Press.

HOFF, C., & TAYLOR, R.L. 1990. Higher Derivative Explicit One Step Algorithm for Non-Linear Dynamic Problems: Part 1: Design and Theory. *Int. J. Num. Meth. Engng.*, **29**, 275–290.

HOLZAPFEL, G.A. 2000. *Nonlinear Solid Mechanics. A Continuum Approach for Engineering.* London: John Wiley & Sons.

HUGHES, T.J., TAYLOR, R.L., & SACKMAN, J.L. 1975 (July). *Finite Element Formulation and Solution of Contact-Impact Problems in Continuum Mechanics – III.* Tech. rept. UC SESM 75-7. Dept. of Civil Eng., University of California, Berkeley.

HUGHES, T.J.R. 1980. Generalization of Selective Integration Procedures to Anisotropic and Nonlinear Media. *Int. J. Num. Meth. Engng.*, **15**, 1413–1418.

HUGHES, T.J.R. 1984. Numerical Implementation of Constiitutive Models: Rate-Independent Deviatoric Plasticity. *Pages 29–63 of:* ET AL., NEMAT-NASSER (ed), *Theoretical Foundations for Large-Scale Computations for Nonlinear Material Behavior.* Dordrecht, The Netherlands: Martinus Nijhoff.

HUGHES, T.J.R. 1987. *The Finite Element Method. Linear Static and Dynamic Finite Element Analysis.* Englewood Cliffs, New Jersey: Prentice-Hall.

HUGHES, T.J.R., & PISTER, K. 1978. Consistent Linearization in Mechanics of Solids and Structures. *Comp. Struct.*, **8**, 391–397.

HUGHES, T.J.R., & WINGET, J. 1980. Finite Rotation Effects in Numerical Integration of Rate Constitutive Equations Arising in Large-Deformation Analysis. *Int. J. Num. Meth. Engng.*, **15**, 1862–1867.

JANSON, J. 1978. A Continuous Damage Approach to the Fatigue Process. *Engng. Fract. Mech.*, **10**, 651–657.

JIRASEK, M. 1998. Nonlocal models for damage and fracture: comparison of approaches. *Int. J. Solids Structures*, **35**, 4133–4145.

JOHANSSON, M., MAHNKEN, R., & RUNESSON, K. 1999. Efficient integration technique for generalized viscoplasticity coupled with damage. *Int. J. Num. Meth. Engng.*, **44**, 1727–1747.

JOHNSON, C. 1987. *Numerical solution of Partial Differential Equations by the Finite Element Method.* Cambridge Univ. Press.

JOHNSON, C., & HANSBO, P. 1992. Adaptive Finite Element Methods in Computational Mechanics. *Comp. Meth. Appl. Mech. Engng.*, **101**, 143–181.

KACHANOV, L.M. 1958. Time of the Rupture Process under Creep Condition. *Izv. Akad. Nauk. SSSR, Otd. Tekhn. Nauk.*, **8**, 26–31.

KESTIN, J., & BATAILLE, J. 1977. Irreversible Thermodynamics of Continua and Internal Variables. *Pages 39–67 of: Proceedings of the Int. Symp. on Continuum Models of Discrete Systems.* Univ. of Waterloo Press.

KOJIĆ, M., & BATHE, K.-J. 1987. Studies of Finite Element Procedures – Stress Solution of a Closed Elastic Strain Path with Stretching and Shearing Using the Updated Lagrangian Jaumann Formulation. *Comp. Struct.*, **26**, 175–179.

KORELC, J., & WRIGGERS, P. 1996. Consistent Gradient Formulation for a Stable Enhanced Strain Method for Large Deformations. *Engng. Comp.*, **13**(1), 103–123.

KRAJČINOVIĆ, D. 1983. Constitutive Equations for Damaging Materials. *J. Appl. Mech.*, **50**, 355–360.

KRAJČINOVIĆ, D. 1985. Continuous Damage Mechanics Revisited: Basic Concepts and Definitions. *J. Appl. Mech.*, **52**, 829–834.

KRAJČINOVIĆ, D., & FONSEKA, G.U. 1981. The Continuous Damage Theory of Brittle Materials – Part 1: General Theory. *J. Appl. Mech.*, **48**, 809–815.

KRAJČINOVIĆ, D., & SELVARAJ, S. 1984. Creep Rupture of Metals - An Analytical Model. *J. Engng. Mat. Tech., Trans. ASME*, **106**, 809–815.

KRIEG, R.D., & KRIEG, .D.B. 1977. Accuracies of Numerical Solution Methods for the Elastic-Perfectly Plastic Model. *J. Pressure Vessel Tech., ASME*, **99**, 510–515.

KUHL, E., & RAMM, E. 1999. Simulation of strain localization with gradient enhanced damage models. *Comput. Materials Science*, **16**, 176–185.

LABBE, P., & GARON, A. 1995. A robust implementation of Zienkiewicz and Zhu's local patch recovery method. *Comm. Num. Meth. Eng.*, **11**, 427–434.

LADÈVEZE, P. 1983. On an Anisotropic Damage Theory. *Pages 355–363 of:* BOEHLER, J.P. (ed), *Proc. CNRS Int. Coll. 351 – Failure Criteria of Structured Media.* Villars-de-Lans.

LADEVÈZE, P. 1985. Sur une famille d'algorithmes en mécanique des structures. *Pages 41–44 of: Comptes Rendus Académie des Sciences, II.*

LADEVÈZE, P., & LEMAITRE, J. 1984. Damage Effective Stress in Quasi Unilateral Conditions. *In: 16th Int. Congress Theor. Appl. Mech.*

LADÈVEZE, P., COFIGNAL, G., & PELLE, J.P. 1986. Accuracy of elastoplastic and dynamic analysis. *Pages 181–203 of:* BABUŠKA, I., ZIENKIEWICZ, O.C., GAGO, J., & DE OLIVEIRA, E.R. (eds), *In Accuracy Estimates and Adaptive Refinements in Finite Element Computations.* John Wiley: New York.

LARSSON, F., RUNESSON, K., & HANSBO, P. 2001. Computation of goal-oriented a posteriori error measures in space-time finite elements for viscoplasticity. *Pages 499–510 of:* WALL, W.A., BLETZINGER, K.U., & SCHWEIZERHOF, K. (eds), *Trends in Computational Structural Mechanics.* CIMNE.

LAURSEN, T.A. 2002. *Computational Contact and Impact Mechanics.* Berlin: Springer-Verlag.

LE ROY, G., EMBURY, J.D., & ASHBY, M.F. 1981. A model of ductile fracture based on the nucleation and growth of voids. *Acta Metallica*, **29**, 1509–1522.

LECKIE, F.A., & HAYHURST, D.R. 1974. Creep Rupture of Structures. *Proc. Roy. Soc. Lond. A*, **340**, 323–347.

LECKIE, F.A., & ONAT, E.T. 1981. Tensorial Nature of Damage Measuring Internal Variables. *Pages 140–155 of: Proceedings of the IUTAM Symposium on Physical Nonlinearities in Structures.* Springer.

LEE, C.K., & LO, S.H. 1997. Automatic adaptive 3-D finite element refinement using different-order tetrahedral elements. *Int. J. Num. Meth. Engng.*, **40**, 2195–2226.

LEE, E.H. 1969. Elastic-Plastic Deformation at Finite Strains. *J. Appl. Mech.*, **36**, 1–6.

LEE, E.H., & LIU, D.T. 1967. Finite Strain Elastic-Plastic Theory with Application to Plane-Wave Analysis. *J. Appl. Phys.*, **38**, 19–27.

LEE, J., & FENVES, G.L. 2001. A return-mapping algorithm for plastic-damage models: 3d and plane stress formulation. *Int. J. Num. Meth. Engng.*, **50**, 487–506.

LEE, N.S., & BATHE, K.J. 1994. Error Indicators and Adaptive Remeshing in Large Deformation Finite Element Analysis. *Finite Elem. Anal. Des.*, **16**, 99–139.

LEMAITRE, J. 1983. A Three-Dimensional Ductile Damage Model Applied to Deep-Drawing Forming Limits. *Pages 1047–1053 of: ICM 4 Stockholm*, vol. 2.

LEMAITRE, J. 1984. How to Use Damage Mechanics. *Nuclear Engng. Design*, **80**, 233–245.

LEMAITRE, J. 1985a. A Continuous Damage Mechanics Model for Ductile Fracture. *J. Engng. Mat. Tech.*, **107**, 83–89.

LEMAITRE, J. 1985b. Coupled Elasto-Plasticity and Damage Constitutive Equations. *Comp. Meth. Appl. Mech. Engng.*, **51**, 31–49.

LEMAITRE, J. 1987. Formulation and Identification of Damage Kinetic Constitutive Equations. *Pages 37–89 of:* KRAJČINOVIĆ, D., & LEMAITRE, J. (eds), *Continuum Damage Mechanics: Theory and Applications.* Springer-Verlag.

LEMAITRE, J. 1990. Micro-Mechanics of Crack Initiation. *Int. J. Fracture*, **42**, 87–99.

LEMAITRE, J. 1996. *A Course on Damage Mechanics.* 2nd edn. Springer.

LEMAITRE, J., & CHABOCHE, J.L. 1990. *Mechanics of Solid Materials.* Cambridge Univ. Press.

LEMAITRE, J., & DUFAILLY, J. 1987. Damage Measurements. *Engng. Fract. Mech.*, **28**(8), 643–661.

LEMAITRE, J., DESMORAT, R., & M., SAUZAY. 2000. Anisotropic Damage Law of Evolution. *Eur. J. Mech. A/Solids*, **19**, 187–208.

LI, L.Y., & BETTESS, P. 1995. Notes on mesh optimal criteria in adaptive finite element computations. *Comm. Num. Meth. Engng.*, **11**, 911–915.

LOHNER, R. 1996. Regridding surface triangulations. *J. Computational Physics*, **126**, 1–10.

MARQUIS, D., & LEMAITRE, J. 1988. Constitutive Equations for the Coupling Between Elasto-Plasticity Damage and Aging. *Revue Phys. Appl.*, **23**, 615–624.

MARSDEN, J.E., & HUGHES, T.J.R. 1983. *Mathematical Foundations of Elasticity.* Englewood Cliffs, New Jersey: Prentice-Hall.

MARUSICH, T.D., & ORTIZ, M. 1995. Modelling and Simulation of High Speed Machining. *Int. J. Num. Meth. Engng.*, **38**, 3675–3694.

MCCLINTOCK, F. A. 1968. A Criterion for Ductile Fracture by the Growth of Holes. *J. Appl. Mech.*, **35**, 363–371.

McMeeking, R.M., & Rice, J.R. 1975. Finite-Element Formulations for Problems of Large Elastic-Plastic Deformation. *Int. J. Solids Struct.*, **11**, 601–616.

Miehe, C. 1993. Computation of Isotropic Tensor Functions. *Comm. Num. Meth. Engng.*, **9**, 889–896.

Miehe, C., & Lambrecht, M. 2001. Algorithms for computation of stresses and elasticity moduli in terms of Seth-Hill's family of generalized strain tensors. *Comm. Num. Meth. Engng.*, **17**(5), 337–353.

Miehe, C., Schröder, J., & Schotte, J. 1999. Computational Homogenization Analysis in Finite Plasticity - Simulation of Texture Development in Polycrystalline Materials. *Computer Methods in Applied Mechanics and Engineering*, **171**(3–4), 387–418.

Moal, A., & Massoni, E. 1995. Finite Element Simulation of the Inertia Welding of two Similar Parts. *Engng. Comp.*, **12**, 497–512.

Moran, B., Ortiz, M., & Shih, F. 1990. Formulation of Implicit Finite Element Methods for Multiplicative Finite Deformation Plasticity. *Int. J. Num. Meth. Engng.*, **29**, 483–514.

Morançay, L., Homsi, H., & Roelandt, J.M. 1997. Application of Remeshing Techniques to the Simulation of Metal Cutting by Punching. *Pages 611–618 of:* Owen, D.R.J., Oñate, E., & Hinton, E. (eds), *Computational Plasticity: Fundamentals and Applications – Proceedings of the Fifth International Conference*. Barcelona, Spain: International Center for Numerical Methods in Engineering (CIMNE).

Mudry, F. 1985. *Methodology and application of local criteria for prediction of ductile tearing*. D.Reidel Publishing Co.

Murakami, S.and Kamiya, K. 1997. Constitutive and Damage Evolution Equations of Elastic-Brittle Materials on Irreversible Thermodynamics. *Int. J. Mech. Sci.*, **39**, 473–486.

Murakami, S. 1987. Anisotropic Aspects of Material Damage and Application of Continuum Damage Mechanics. *Pages 91–133 of:* Krajčinović, D., & Lemaitre, J. (eds), *Continuum Damage Mechanics: Theory and Applications*. Springer-Verlag.

Murakami, S. 1988. Mechanical Modeling of Material Damage. *J. Appl. Mech.*, **55**, 280–286.

MURAKAMI, S. 1990. Role of Continuum Damage Mechanics in Fracture Analysis. *In:* KLEIBER, M., & KÖNIG, J.A. (eds), *Inelastic Solids and Structures.* Pineridge Press, Swansea.

MURAKAMI, S., & OHNO, N. 1981. A Continuum Theory of Creep and Creep Damage. *Pages 422–443 of:* PONTER, A.R.S. (ed), *Proceedings of the IUTAM Symposium on Creep in Structures, Leicester, 1980.* Berlin: Springer.

NAGTEGAAL, J.C. 1982. On the Implementation of Inelastic Constitutive Equations with Special Reference to Large Deformation Problems. *Comp. Meth. Appl. Mech. Engng.*, **33**, 469–484.

NAGTEGAAL, J.C., & DE JONG, J.E. 1981. Some Computational Aspects of Elastic-Plastic Large Strain Analysis. *Int. J. Num. Meth. Engng.*, **17**, 15–41.

NAGTEGAAL, J.C., & DE JONG, J.E. 1982. Some Aspects of Non-Isotropic Work-Hardening in Finite Strain Plasticity. *Pages 65–102 of:* LEE, E.H., & MALLET, R.L. (eds), *Plasticity of Metals at Finite Strain: Theory, Experiment and Computation.* Troy: Div. Appl. Mech. Stanford Univ. and Dept. Mech. Engng.

NAGTEGAAL, J.C., PARKS, D.M., & RICE, J.M. 1974. On Numerically accurate Finite Element Solutions in the Fully Plastic Range. *Comp. Meth. Appl. Mech. Engng.*, **4**, 153–177.

NEDJAR, B. 2001. Elastoplastic-damage modelling including the gradient of damage: formulation and computational aspects. *Int. J. Solids Struct.*, **38**, 5421–5451.

NEEDLEMAN, A., & TVERGAARD, V. 1984. An analysis of ductile rupture in notched bars. *J. of Mech. Physics of Solids*, **32**, 461.

NEMAT-NASSER, S. 1982. On Finite Deformation Elasto-Plasticity. *Int. J. Solids Structures*, **18**(10), 857–872.

NORRIS, D.M., REAUGH, J.E., MORAN, B., & QUIÑONES, D.F. 1978. A plastic-strain, mean-stress criterion for ductile fracture. *J. Engng. Mat. Tech., Trans. ASME*, **100**, 279–286.

ODEN, J.T. 1972. *Finite Elements of Nolinear Continua.* London: McGraw-Hill.

ODEN, J.T., DEMKOWICZ, L., RACHOWICZ, W., & WESTERMANN, T.A. 1989. Toward a universal h-p adaptive finite element strategy. Part 2: A posteriori error estimation. *Comp. Meth. Appl. Mech. Engng.*, **77**, 113–180.

Ogden, R.W. 1984. *Non-Linear Elastic Deformations.* Chichester: Ellis Horwood.

Onat, E.T., & Leckie, F.A. 1988. Representation of Mechanical Behavior in the Presence of Changing Internal Structure. *J. Appl. Mech.*, **55**, 1–10.

Orlando, A. 2002. *Analysis of adaptive finite element solutions in elastoplasticity with reference to transfer operation techniques.* Ph.D. thesis, Univ. of Wales Swansea, UK.

Orlando, A., & Perić, D. 2004. Analysis of transfer procedures in elastoplasticity based on the error in the constitutive equations: Theory and numerical illustration. *Int. J. Num. Meth. Engng.*, **60**, 1595–1631.

Ortiz, M. 1996. Computational micromechanics. *Comp. Mech.*, **18**(5), 321–338.

Ortiz, M., & Popov, E.P. 1985. Accuracy and Stability of Integration Algorithms for Elastoplastic Constitutive Relations. *Int. J. Num. Meth. Engng.*, **21**, 1561–1576.

Ortiz, M., & Quigley IV, J.J. 1991. Adaptive Mesh Refinement in Strain Localization Problems. *Comp. Meth. Appl. Mech. Engng.*, **90**, 781–804.

Ortiz, M., & Simo, J.C. 1986. An Analysis of a New Class of Integration Algorithms for Elastoplastic Constitutive Relations. *Int. J. Num. Meth. Engng.*, **23**, 353–366.

Owen, D.R.J., & Hinton, E. 1980. *Finite Elements in Plasticity: Theory and Practice.* Swansea: Pineridge Press.

Owen, D.R.J., & Vaz Jr., M. 1999. Computational Techniques Applied to High-Speed Machining Under Adiabatic Strain Localization Conditions. *Comp. Meth. Appl. Mech. Engng.*, **171**, 445–461.

Owen, D.R.J., Feng, Y.T., de Souza Neto, E.A., Cottrell, M.G., Wang, F., & Andrade Pires, F.M. 2002. The Modelling of Multi-Fracturing Solids and Particulate Media. *In:* Mang, H.A., Rammerstorfer, F.G, & Eberhardsteiner, J. (eds), *Proceedings of the Fifth World Congress on Computational Mechanics (WCCM V).* Vienna University of Technology, Austria.

Owen, D.R.J., de Souza Neto, E.A., Andrade Pires, F.M., & Feng, Y.T. 2003. Continuum/Discrete Representations of Fracturing Solids. *In: 7th U.S National Congress on Computational Mechanics - CD-ROM Conference Proceedings Albuquerque, New Mexico, 27th -31st July.* ISBN: 0-9743254-0-6, http://www.esc.sandia.gov/usnccm.html.

Owen, D.R.J., Andrade Pires, F.M., Feng, Y.T., de Souza Neto, E.A., & Cottrell, M.G. 2004a. Continuous/Discrete Representation of Fracturing Solids. *J. Appl. Mech. ASME.* (submitted for publication).

Owen, D.R.J., Andrade Pires, F.M., de Souza Neto, E.A., & Feng, Y.T. 2004b. Continuum/discrete strategies for the modelling of fracturing solids. *In: Multi-physics and Multi-scale Computer Models in Non-linear Analysis and Optimal Design of Engineering Structures Under Extreme Conditions, 13th - 17th June.* http://arw-bled2004.scix.net.

Owen, D.R.J., Feng, Y.T., de Souza Neto, E.A., Cottrell, M.G., Wang, F., Andrade Pires, F.M., & Yu, J. 2004c. The Modelling of Multi-Fracturing Solids and Particulate Media. *Int. J. Num. Meth. Eng.*, **60**(1), 317–339.

Oyane, M., Shima, S., & Tabata, T. 1978. Considerations of basic equations, and their application in the forming of metal powders and porous metals. *J. Mech. Work. Tech.*, **1**, 325–341.

Padra, C., & Venere, M.J. 1995. On adaptivity for diffusion problems using triangular elements. *Engng. Comp.*, **12**, 75–84.

Peerlings, R.H.J., de Borst, R., Brekelmans, W.A.M., & de Vree, J.H.P. 1996. Gradient enhanced damage for quasi-brittle materials. *Int. J. Num. Meth. Eng.*, **39**, 3391–3403.

Perić, D. 1992. On Consistent Stress Rates in Solid Mechanics: Computational Implications. *Int. J. Num. Meth. Engng.*, **33**, 799–817.

Perić, D. 1993. On a Class of Constitutive Equations in Viscoplasticity: Formulation and Computational Issues. *Int. J. Num. Meth. Engng.*, **36**, 1365–1393.

Perić, D., & Owen, D.R.J. 1991. A Model for Large Deformation of Elasto-Viscoplastic Solids at Finite Strains: Computational Issues. *Pages 299–312 of:* Besdo, D., & Stein, E. (eds), *Proceedings of the IUTAM Symposium on Finite Inelastic Deformations – Theory and Applications.* Berlin: Springer.

Perić, D., & Owen, D.R.J. 1992. Computational Model for 3-D Contact Problems with Friction Based on the Penalty Method. *Int. J. Num. Meth. Engng.*, **35**, 1289–1309.

Perić, D., & Owen, D.R.J. 2004. *Encyclopedia of Computational Mechanics: Computational modelling of forming processes.* Vol. 2. USA, Australia, Germany, Canada: John Wiley & Sons, Ltd.

Perić, D., Owen, D.R.J., & Honnor, M.E. 1992. A Model for Finite Strain Elasto-Plasticity Based on Logarithmic Strains: Computational Issues. *Comp. Meth. Appl. Mech Engng.*, **94**, 35–61.

Perić, D., Owen, D.R.J., Schönauer, M., & Souza Neto, E.A. de. 1993 (July). Computational Strategies for Finite Strain Plasticity Problems Including Adaptivity Concepts. *In: Proceedings of the 12th Int. Symp. on Finite Element Methods in South Africa.*

Perić, D., Yu, J., & Owen, D.R.J. 1994. On Error Estimates and Adaptivity in Elastoplastic Solids: Application to the Numerical Simulation of Strain Localization in Classical and Cosserat Continua. *Int. J. Num. Meth. Engng.*, **37**, 1351–1379.

Perić, D., Hochard, Ch., Dutko, M., & Owen, D.R.J. 1996. Transfer Operators for Evolving Meshes in Small Strain Elasto-Plasticity. *Comp. Meth. Appl. Mech. Engng.*, **137**, 331–344.

Perić, D., Vaz Jr, M., & D.R.J., Owen. 1999. On adaptive strategies for large deformations of elasto-plastic solids at finite strains: Computational issues and industrial applications. *Comp. Meth. Appl. Mech. Engng.*, **176**, 279–312.

Pinsky, P.M., Ortiz, M., & Pister, K.S. 1983. Numerical Integration of Rate Constitutive Equations in Finite Deformation Analysis. *Comp. Meth. Appl. Mech. Engng.*, **40**, 137–158.

Rabotnov, Y.N. 1963. On the Equations of State for Creep. *Page 307 of: Progress in Applied Mechanics, Prager Anniversary VOLUME.* New York: MacMillan.

Radovitzky, R., & Ortiz, M. 1999. Error estimation and adaptive meshing in strongly nonlinear dynamic problems. *Comp. Meth. Appl. Mech. Engng.*, **172**, 203–240.

Ramsey, A.C.A., & Sbresny, H. 1995. Evaluation of some error estimators for the four-noded lagrangian quadrilateral. *Comm. Num. Meth. Eng.*, **11**, 497–506.

Rannacher, R., & Suttmeier, F.T. 1998. A posteriori error control in finite element methods via duality techniques: Application to perfect plasticity. *Comp. Mech.*, **21**, 123–133.

Rannacher, R., & Suttmeier, F.T. 1999. A posteriori error estimation and mesh adaptation for finite element models in elasto-plasticity. *Comp. Meth. Appl. Mech. Engng.*, **176**, 333–361.

RASHID, M.M. 2002. Material state remapping in computational solid mechanics. *Int. J. Num. Meth. Engng.*, **55**, 431–450.

REPIN, S.I., & XANTHIS, L. 1996. A posteriori error estimation for elastoplastic problems based on duality theory. *Comp. Meth. Appl. Mech. Engng.*, **138**, 317–339.

RICE, J.R. 1968. A Path Independent Integral and the Approximate Analysis of Strain Concentration by Notches and Cracks. *J. Appl. Mech.*, **35**, 379–386.

RICE, J.R. 1969. On the Ductile Enlargement of Voids in Triaxial Stress Fields. *J. Mech. Phys. Solids*, **17**, 201–217.

RODIČ, T., OWEN, D.R.J., SCHÖNAUER, TERČELJ, & GUMMERT, H. 1992. Inverse identification and reconstruction approaches for the investigation of friction and wear in plane strain spike forming tests. *Pages 361–374 of:* OWEN, D.R.J., OÑATE, E., & HINTON, E. (eds), *Computational Plasticity: Fundamentals and Applications – Proceedings of the third International Conference held in Barcelona,* $6-10^{\text{th}}$ *April.* Swansea, UK: Pineridge Press.

RUBINSTEIN, R., & ATLURI, S.N. 1983. Objectivity of Incremental Constitutive Relations Over Finite Time Steps in Computational Finite Deformation Analysis. *Comp. Meth. Appl. Mech. Engng.*, **36**, 277–290.

SAANOUNI, K., CHABOCHE, J.L., & LESNE, P.M. 1989. Creep Crack-Growth Prediction by a Non-Local Damage Formulation. *Pages 404–414 of:* MAZARS, J., & BAZANT, Z.P. (eds), *Cracking and Damage, Strain Localization and Size Effect.* Amsterdam: Elsevier.

SCHACHT, T., UNTERMANN, N., & STECK, E. 2003. The influence of crystallographic orientation on the deformation behavior of single crystals containing microvoids. *Int. J. of Plasticity*, **19**, 1605–1626.

SIMO, J.C. 1985. On the Computational Significance of the Intermediate Configuration and Hyperelastic Stress Relations in Finite Deformation Elastoplasticity. *Mech. of Materials*, **4**, 439–451.

SIMO, J.C. 1992. Algorithms for Static and Dynamic Multiplicative Plasticity that Preserve the Classical Return Mapping Schemes of the Infinitesimal Theory. *Comp. Meth. Appl. Mech. Engng.*, **99**, 61–112.

SIMO, J.C., & ARMERO, F. 1992. Geometrically Non-Linear Enhanced Strain Mixed Methods and the Method of Incompatible Modes. *Int. J. Num. Meth. Engng.*, **33**, 1413–1449.

SIMO, J.C., & GOVINDJEE, S. 1991. Non-Linear B-Stability and Symmetry Preserving Return Mapping Algorithms for Plasticity and Viscoplasticity. *Int. J. Num. Meth. Engng.*, **31**, 151–176.

SIMO, J.C., & HUGHES, T.J.R. 1998. *Computational Inelasticity.* New York: Springer-Verlag.

SIMO, J.C., & HUGHES, T.R.J. 1987. General Return Mapping Algorithms for Rate-Independent Plasticity. *Pages 221–231 of:* C.S. DESAI ET AL. (ed), *Constitutive Laws for Engineering Materials: Theory and Applications.* Elsevier.

SIMO, J.C., & JU, J.W. 1987. Strain- and Stress-Based Continuum Damage Models – I. Formulation and II. Computational Aspects. *Int. J. Solids Struct.*, **23**, 821–869.

SIMO, J.C., & MIEHE, C. 1992. Associative coupled thermoplasticity at finite strains: Formulation, numerical analysis and implementation. *Comp. Meth. Appl. Mech. Engng.*, **98**, 41–104.

SIMO, J.C., & ORTIZ, M. 1985. A Unified Approach to Finite Deformation Plasticity Based on the Use of Hyperelastic Constitutive Equations. *Comp. Meth. Appl. Mech. Engng.*, **49**, 221–245.

SIMO, J.C., & PISTER, K.S. 1984. Remarks on the Rate Constitutive Equations for Finite Deformation Problems: Computational Implications. *Comp. Meth. Appl. Mech. Engng.*, **46**, 201–215.

SIMO, J.C., & RIFAI, S. 1990. A Class of Mixed Assumed Strain Methods and the Method of Incompatible Modes. *Int. J. Num. Meth. Engng.*, **29**, 1595–1638.

SIMO, J.C., & TAYLOR, R.L. 1985. Consistent Tangent Operators for Rate-Independent Elastoplasticity. *Comp. Meth. Appl. Mech. Engng.*, **48**, 101–118.

SIMO, J.C., & TAYLOR, R.L. 1991. Quasi-Incompressible Finite Elasticity in Principal Stretches. Continuum Basis and Numerical Algorithms. *Comp. Meth. Appl. Mech. Engng.*, **85**, 273–310.

SIMO, J.C., TAYLOR, R.L., & PISTER, K.S. 1985. Variational and Projection Methods for the VOLUME Constraint in Finite Deformation Elasto-Plasticity. *Comp. Meth. Appl. Mech. Engng.*, **51**, 177–208.

SIMO, J.C., ARMERO, F., & TAYLOR, R.L. 1993. Improved Versions of Assumed Enhanced Strain Tri-Linear Elements for 3D Finite Deformation Problems. *Comp. Meth. Appl. Mech. Engng.*, **110**, 359–386.

SPENCER, A.J.M. 1980. *Continuum Mechanics.* London: Longman.

SRIKANTH, A., & ZABARAS, N. 2001. An Updated Lagrangian Finite Element Sensitivity Analysis of Large Deformations Using Quadrilateral Elements. *Int. J. Num. Meth. Engng.*, **52**(10), 1131–1163.

STEIN, E., STEINMANN, P., & MIEHE, C. 1995. Instability phenomena in plasticity: Modelling and computation. *Computational Mechanics*, **17**, 74–87.

STEINMANN, P., MIEHE, C., & STEIN, E. 1994. Comparison of Different Finite Deformation Inelastic Damage Models within Multiplicative Elastoplasticity for Ductile Metals. *Computational Mechanics*, **13**, 458–474.

SUSSMAN, T., & BATHE, K.-J. 1987. A Finite Element Formulation for Nonlinear Incompressible Elastic and Inelastic Analysis. *Comp. Struct.*, **26**, 357–409.

TABBARA, M., BLACKER, T., & BELYTSCHKO, T. 1994. Finite element derivative recovery by moving least interpolants. *Comp. Meth. Appl. Mech. Engng.*, **117**, 211–223.

TAI, W.H. 1990. Plastic Damage and Ductile Fracture in Mild Metals. *Engng. Fract. Mech.*, **37**(4), 853–880.

TAI, W.H., & YANG, B.X. 1986. A new microvoid-damage model for ductile fracture. *Engng. Fract. Mech.*, **25**(3), 377–384.

TAI, W.H., & YANG, B.X. 1987. A new damage mechanics criterion for ductile fracture. *Engng. Fract. Mech.*, **27**, 371–378.

TAYLOR, R.L. 2000. A mixed-enhanced formulation for tetrahedral finite elements. *Int. J. Num. Meth. Engng.*, **47**, 205–227.

TAYLOR, R.L., BERESFORD, P.J., & WILSON, E.L. 1976. A Non-Conforming Element for Stress Analysis. *Int. J. Num. Meth. Engng.*, **10**, 1211–1219.

TETAMBE, R.P., YUNUS, S.M., RAJAKUMAR, C., & SAIGAL, S. 1995. Examination of flux projection-type error estimators in nonlinear finite element analysis. *Comp. & Strut.*, **54**, 641–653.

THOMAS, R.M., & GLADWELL, I. 1988. Variable-Order Variable-Step Algorithms for Second Order Systems, Part 1: The Methods. *Int. J. Num. Meth. Engng.*, **62**, 55–80.

THOMASON, P.F. 1990. *Ductile fracture of metals.* Oxford: Pergamon Press.

THOUTIREDDY, P., MOLINARI, J.F., REPETTO, E.A., & ORTIZ, M. 2002. Tetrahedral composite finite elements. *Int. J. Num. Meth. Engng.*, **53**, 1337–1351.

TRUESDELL, C. 1969. *Rational Thermodynamics.* New York: McGraw-Hill.

TRUESDELL, C., & NOLL, W. 1965. The Non-Linear Field Theories of Mechanics. *In:* FLÜGGE, S. (ed), *Handbuch der Physik*, vol. III/3. Springer-Verlag.

TVERGAARD, V. 1981. Influence of Voids on Shear Band Instabilities under Plane Strain Conditions. *Int. J. Fracture*, **17**, 389–407.

TVERGAARD, V. 1982. Material Failure by Void Coalescence in Localized Shear Bands. *Int. J. Solids Struct.*, **18**, 659–672.

TVERGAARD, V., & NEEDLEMAN, A. 1984. Analysis of the Cup-Cone Fracture in a Round Tensile Bar. *Acta Metall.*, **32**, 157–169.

TVERGAARD, V., & NIORDOSON, C. 2004. Non local plasticity effects on interaction of different size voids. *Int. J. of Plasticity*, **20**, 107–120.

TVERGAARD, V., NEEDLEMAN, A., & LO, K.K. 1981. Flow Localization in the Plane Strain Tensile Test. *J. Mech. Phys. Solids*, **29**, 115–142.

VAZ JR., M. 1998. *Computational Approaches to Simulation of Metal Cutting Processes.* Ph.D. thesis, Dept. of Civil Engineering, Univ. of Wales Swansea.

VAZ JR., M., & OWEN, D.R.J. 2001. Aspects of Ductile Fracture and Adaptive mesh Refinement in Damaged Elasto-plastic Materials. *Int. J. Num. Meth. Engng.*, **50**, 29–54.

VERFÜRTH, R. 1996. *A Review of A Posteriori Error Estimator and Adaptive Mesh-Refinement Techniques.* Teubner, Chichester, New York, Stuttgart, Leipzig: Wiley.

WEBER, G., & ANAND, L. 1990. Finite Deformation Constitutive Equations and a Time Integration Procedure for Isotropic, Hyperelastic-Viscoplastic Solids. *Comp. Meth. Appl. Mech. Engng.*, **79**, 173–202.

WRIGGERS, P. 2002. *Computational Contact Mechanics.* J. Wiley and Sons: New York.

WRIGGERS, P., & REESE, S. 1996. A Note on Enhanced Strain Methods for Large Deformations. *Comp. Meth. Appl. Mech. Engng.*, **135**, 201–209.

YAZDANI, A.A., GAKWAYA, A., & DHATT, G. 1997. *A posteriori* error estimator based on the second derivative of the displacement field for two-dimensional elastic problems. *Comp. & Struc.*, **62**, 317–338.

ZHANG, Z., & ZHU, J. 1995. Analysis of the superconvergent patch recovery technique and a posteriori error estimator in the finite element method (I). *Comp. Meth. Appl. Mech. Eng.*, **123**, 173–187.

ZHU, Y.Y., & CESCOTTO, S. 1995. Unified and mixed formulation of the 4-node quadrilateral elements by assumed strain method: application to thermomechanical problems. *Int. J. Num. Meth. Engng.*, **38**, 685–716.

ZIENKIEWICZ, O.C., & TAYLOR, R.L. 2000. *The Finite Element Method – Vol.1: The Basis, and Vol.2: Solid Mechanics.* 5th edn. Butterworth-Heinemann.

ZIENKIEWICZ, O.C., & ZHU, J.Z. 1987. A Simple Error Estimator and Adaptive Procedure For Practical Engineering Analysis. *Int. J. Num. Meth. Engng.*, **24**, 337–357.

ZIENKIEWICZ, O.C., & ZHU, J.Z. 1992a. The superconvergent patch recovery (SPR) and a posteriori error estimates. – Part 1: The recovery technique and Part 2: Error estimates and adaptivity. *Int. J. Num. Meth. Engng.*, **33**, 1331–1382.

ZIENKIEWICZ, O.C., & ZHU, J.Z. 1992b. The superconvergent patch recovery (SPR) and adaptive finite element refinement. *Comp. Meth. Appl. Mech. Eng.*, **101**, 207–224.

ZIENKIEWICZ, O.C., WOOD, W.L., HINE, N.W., & TAYLOR, R.L. 1984. A Unified Set of Single Step Algorithms, Part 1: General Formulation and Applications. *Int. J. Num. Meth. Engng.*, **20**, 1529–1552.

ZIENKIEWICZ, O.C., LIU, Y.C., & HUANG, G.C. 1988. Error Estimation and Adaptivity in Flow Simulations for Forming Problems. *Int. J. Num. Meth. Engng.*, **25**, 23–42.

ZIENKIEWICZ, O.C., HUANG, G.C., & LIU, Y.C. 1990. Adaptive FEM Computation of Forming Process - Application to Porous and Non-Porous Materials. *Int. J. Num. Meth. Engng.*, **30**, 1527–1553.

ZIENKIEWICZ, O.C., ROJEK, J., TAYLOR, R.L., & PASTOR, M. 1998. Triangles and tetrahedra in explicit dynamic codes for solids. *Int. J. Num. Meth. Engng.*, **43**, 565–583.

Appendix A

Isotropic functions of a symmetric tensor

This appendix presents, for the sake of completeness, some important definitions, properties and expressions involving a class of isotropic real tensor functions of one symmetric tensor. Isotropic tensor-valued functions of one tensor play an important role in continuum mechanics. Well known examples are the square root, $\sqrt{\boldsymbol{X}}$, and the logarithm, $\ln[\boldsymbol{X}]$, of a real symmetric second order tensor, $\boldsymbol{X}$. Such functions and their properties are exploited in various parts of this thesis in connection with the definition of elasto-plastic damage and elasto-viscoplastic damage constitutive models as well as with their computer implementation.

In the context of computational continuum mechanics, one is frequently faced with the need for evaluation of functions of this type. Also, in the non-linear context, function derivatives are frequently required in connection with the linearisation of the underlying problem.

The methodology presented here has been proposed by de Souza Neto *et al.* (2004). By exploiting the eigenprojection-based spectral representation of such functions, eigenprojection-based closed formulae for the function derivatives are obtained. Closed form expressions for the derivative of functions of this class, employing the eigenprojection-based representation, have been derived by Carlson & Hoger (1986). Complete algorithms using compact expressions for computation of functions of the above class (and their derivatives) – valid at *invertible* arguments only – have been proposed by Miehe (1993).

A.1 Isotropic tensor-valued functions

A symmetric tensor-valued function of a symmetric tensor

$$\boldsymbol{Y}(\boldsymbol{X}) : \mathscr{L} \subset \mathscr{I} \rightarrow \mathscr{I} \tag{A.1}$$

is said to be isotropic if

$$\boldsymbol{Q}\boldsymbol{Y}(\boldsymbol{X})\boldsymbol{Q}^T = \boldsymbol{Y}(\boldsymbol{Q}\boldsymbol{X}\boldsymbol{Q}^T) \tag{A.2}$$

for all rotations $\boldsymbol{Q}$.

The following important property holds for any isotropic function defined as above. If $\boldsymbol{Y}$ is isotropic, then $\boldsymbol{Y}(\boldsymbol{X})$ and $\boldsymbol{X}$ are coaxial and $\boldsymbol{Y}(\boldsymbol{X})$ and $\boldsymbol{X}$ commute

$$\boldsymbol{Y}(\boldsymbol{X})\boldsymbol{X} = \boldsymbol{X}\boldsymbol{Y}(\boldsymbol{X}) \tag{A.3}$$

The remainder of this appendix focuses exclusively on the *principal values* representation of isotropic tensor functions and many of the formulae presented are used in the computation of function values as well as function derivatives. The principal values representation is established in the following section.

A.2 Spectral decomposition

Given a tensor $\boldsymbol{T}$, a non-zero vector $\boldsymbol{u}$ is said to be an *eigenvector* of $\boldsymbol{T}$ associated with the *eigenvalue* (or *principal value*) w if

$$\boldsymbol{T}\boldsymbol{u} = w\,\boldsymbol{u}. \tag{A.4}$$

The space of all vectors $\boldsymbol{u}$ satisfying the above equation is called the *characteristic space* of $\boldsymbol{T}$ corresponding to w. The following properties hold:

(i) The eigenvalues of a positive definite tensor are strictly positive.
(ii) The characteristic spaces of a symmetric tensor are mutually orthogonal.

A.2.1 Spectral theorem

Let $\boldsymbol{X}$ be a symmetric tensor. Then $\boldsymbol{X}$ admits the representation

$$\boldsymbol{X} = \sum_{i=1}^{n} x_i\, \boldsymbol{e}_i \otimes \boldsymbol{e}_i \tag{A.5}$$

where $\{x_i\}$ are the *eigenvalues* of $\boldsymbol{X}$ and $\{\boldsymbol{e}_i\}$ is an orthonormal basis of the corresponding unit *eigenvectors*. Relative to the basis $\{\boldsymbol{e}_i\}$, $\boldsymbol{X}$ has the following *diagonal* matrix representation

$$[\boldsymbol{X}] = \begin{bmatrix} x_1 & 0 & \cdots & 0 \\ 0 & x_2 & \cdots & 0 \\ \vdots & \vdots & \ddots & \vdots \\ 0 & 0 & \cdots & x_n \end{bmatrix}. \tag{A.6}$$

The direction of an eigenvector $\boldsymbol{e}_i$ is called a *principal axis* or *principal direction* of $\boldsymbol{X}$.

A.2.2 Eigenprojections

Alternatively, with $p \leq n$ defined as the number of *distinct* eigenvalues of $\boldsymbol{X}$, one may write:

$$\boldsymbol{X} = \sum_{i=1}^{p} x_i \, \boldsymbol{E}_i \, . \tag{A.7}$$

where the symmetric tensors $\boldsymbol{E}_i$ are called the *eigenprojections* of $\boldsymbol{X}$. Each eigenprojection $\boldsymbol{E}_i$ is the orthogonal projection operator on the characteristic space of $\boldsymbol{X}$ associated with x_i. The eigenprojections have the property

$$\boldsymbol{I} = \sum_{i=1}^{p} \boldsymbol{E}_i \, , \tag{A.8}$$

and, if $p = n$ (no repeated eigenvalues), then

$$\boldsymbol{E}_i = \boldsymbol{e}_i \otimes \boldsymbol{e}_i \tag{A.9}$$

for $i = 1, ..., n$, with no summation implied on i. Also, the eigenprojections satisfy:

$$\boldsymbol{E}_i : \boldsymbol{E}_j = \delta_{ij} \qquad i, j = 1, ..., p \, , \tag{A.10}$$

where ':' denotes the double contraction (internal product) between two tensors and δ_{ij} is the Krönecker delta. In closed form, $\boldsymbol{E}_i$ are given by the expression:

$$\boldsymbol{E}_i = \begin{cases} \displaystyle\prod_{\substack{j=1 \\ j \neq i}}^{p} \frac{1}{x_i - x_j} (\boldsymbol{X} - x_j \, \boldsymbol{I}) & \text{if } p > 1 \\ \\ \boldsymbol{I} & \text{if } p = 1 \end{cases} \tag{A.11}$$

A.2.3 Characteristic equation. Principal invariants

Every eigenvalue x_i of a symmetric tensor, $\boldsymbol{X}$, satisfies the *characteristic equation*:

$$\det(\boldsymbol{X} - x_i \, \boldsymbol{I}) \; = \; 0 \, . \tag{A.12}$$

Two-dimensional space

In two-dimensional space, expression (A.12) reduces to the quadratic equations:

$$x_i^2 - I_1 \, x_i + I_2 = 0 \qquad i = 1, 2 \, , \tag{A.13}$$

where I_1 and I_2 are the principal invariants of $\boldsymbol{X}$:

$$\begin{aligned} I_1 &= \mathrm{tr}[\boldsymbol{X}] = x_1 + x_2 \\ I_2 &= \det[\boldsymbol{X}] = x_1\, x_2 \ , \end{aligned} \tag{A.14}$$

Solution of the quadratic equation (A.13) provides the exact formula for the eigenvalues x_i of $\boldsymbol{X}$:

$$x_1 = \frac{I_1 + \sqrt{I_1^2 - 4\, I_2}}{2} \qquad \text{and} \qquad x_2 = \frac{I_1 - \sqrt{I_1^2 - 4\, I_2}}{2} \tag{A.15}$$

If $x_1 \neq x_2$, (A.11)$_1$ results in the following closed formula for computation of the eigenprojections of $\boldsymbol{X}$ in 2-D:

$$\boldsymbol{E}_\alpha \ = \ \frac{1}{2\, x_\alpha - I_1}\, [\boldsymbol{X} + (x_\alpha - I_1)\boldsymbol{I}\,] \,. \tag{A.16}$$

On the other hand, if $x_1 = x_2$, then (A.11)$_2$ applies.

Three-dimensional space

In three-dimensional space, the *characteristic equation* of a symmetric second order tensor reads:

$$x_i^3 - I_1\, x_i^2 + I_2\, x_i - I_3 = 0\,, \tag{A.17}$$

where the principal invariants are now I_1, I_2 and I_3, defined as:

$$\begin{aligned} I_1 &= \mathrm{tr}[\boldsymbol{X}] = x_1 + x_2 + x_3 \\ I_2 &= \tfrac{1}{2}\{(\mathrm{tr}\boldsymbol{X})^2 - \mathrm{tr}[\boldsymbol{X}^2]\} = x_1\, x_2 + x_2\, x_3 + x_1\, x_3 \\ I_3 &= \det[\boldsymbol{X}] = x_1\, x_2\, x_3\,. \end{aligned} \tag{A.18}$$

The eigenvalues x_i correspond to the solution of the characteristic equation which, in three dimensions, is the cubic equation (A.17). Since $\boldsymbol{X}$ is real by assumption, its eigenvalues x_i are real and the solution of (A.17) is given exactly by the following expressions:

$$\begin{aligned} x_1 &= -2\,\sqrt{Q}\ \cos\left[\tfrac{\theta}{3}\right] + \frac{I_1}{3} \\ x_2 &= -2\,\sqrt{Q}\ \cos\left[\tfrac{\theta+2\pi}{3}\right] + \frac{I_1}{3} \\ x_3 &= -2\,\sqrt{Q}\ \cos\left[\tfrac{\theta-2\pi}{3}\right] + \frac{I_1}{3}\,, \end{aligned} \tag{A.19}$$

where Q and θ are defined as:

$$Q = \frac{I_1^2 - 3\, I_2}{9} \tag{A.20}$$

and

$$\theta = \cos^{-1}\left[\frac{R}{\sqrt{Q^3}}\right], \tag{A.21}$$

with

$$R = \frac{-2\,I_1^3 + 9\,I_1\,I_2 - 27\,I_3}{54}\,. \tag{A.22}$$

If x_i is not repeated, the following closed formula for the eigenprojection $\boldsymbol{E}_i$ in 3-D is obtained from (A.11):

$$\boldsymbol{E}_i = \frac{x_i}{2\,x_i^3 - I_1\,x_i^2 + I_3}\left[\boldsymbol{X}^2 - (I_1 - x_i)\,\boldsymbol{X} + \frac{I_3}{x_i}\,\boldsymbol{I}\right]. \tag{A.23}$$

If x_j is repeated (with multiplicity 2) and $x_i \neq x_j$, then $\boldsymbol{E}_i$ is given by the above expression and $\boldsymbol{E}_j$ is given simply by:

$$\boldsymbol{E}_j = \boldsymbol{I} - \boldsymbol{E}_i\,. \tag{A.24}$$

If $x_1 = x_2 = x_3$, then $(A.11)_2$ applies.

A.3 A class of isotropic tensor functions

Let us consider now that y is a function of a *single* argument [1]. Given $y : \mathbb{R} \rightarrow \mathbb{R}$, a class of isotropic tensor functions of a symmetric tensor can be constructed as:

$$\boldsymbol{Y}(\boldsymbol{X}) \equiv \sum_{i=1}^{p} y(x_i)\,\boldsymbol{E}_i\,, \tag{A.25}$$

Functions expressed as such define an important class of isotropic tensor-valued functions of one tensor. The families of strain measures defined by (3.33) [page 26] and (3.36), for instance, are members of this class. The *tensor logarithmic*:

$$\boldsymbol{Y}(\boldsymbol{X}) = \ln[\boldsymbol{X}]\,,$$

is a particularly important member of this class of functions. Is this case, the function y, in 3-D, reads:

$$y(x_i) \equiv \ln\, x_i\,.$$

Functions such as, for instance, the tensor square root and the tensor exponential can also be expressed in the format (A.25) by setting $y(x_i) \equiv \sqrt{x_i}$ and $y(x_i) \equiv \exp(x_i)$, respectively.

---

[1] For further discussions on *general* tensor-valued functions of one real symmetric tensor, the reader is referred to (Chadwick & Ogden, 1971; Miehe & Lambrecht, 2001; de Souza Neto, 2004)

A.3.1 Two dimensions

After closed form evaluation of x_i and $\boldsymbol{E}_i$ of Section A.2.3, for the two-dimensional space, the following expression is used to compute $\boldsymbol{Y}(\boldsymbol{X})$:

$$\boldsymbol{Y}(\boldsymbol{X}) = \begin{cases} \displaystyle\sum_{i=1}^{2} y(x_i)\, \boldsymbol{E}_i & \text{if } x_1 \neq x_2 \\ y(x_1)\, \boldsymbol{I} & \text{if } x_1 = x_2 \end{cases} \tag{A.26}$$

The derivative of $\boldsymbol{Y}(\boldsymbol{X})$ in two dimensions is found to be given by:

$$\mathsf{D}(\boldsymbol{X}) = \begin{cases} \frac{y(x_1)-y(x_2)}{x_1-x_2}\, [\mathsf{I} - \boldsymbol{E}_1 \otimes \boldsymbol{E}_1 - \boldsymbol{E}_2 \otimes \boldsymbol{E}_2] + \displaystyle\sum_{\alpha=1}^{2} y'(x_\alpha)\, \boldsymbol{E}_\alpha \otimes \boldsymbol{E}_\alpha & \\ & \text{if } x_1 \neq x_2 \\ y'(x_1)\, \mathsf{I} & \text{if } x_1 = x_2 \end{cases} \tag{A.27}$$

where I is the fourth order tensor defined by the cartesian components:

$$\mathsf{I}_{ijkl} = \tfrac{1}{2}(\delta_{ik}\delta_{jl} + \delta_{il}\delta_{jk}) \,, \tag{A.28}$$

i.e., it is an identity operator in the space of symmetric second order tensors:

$$\mathsf{I} : \boldsymbol{S} = \boldsymbol{S} \qquad \forall\, \boldsymbol{S} \in \mathrm{Sym}\,. \tag{A.29}$$

A.3.2 Three dimensions

The eigenvalues and eigenprojection tensors of $\boldsymbol{X}$ are firstly evaluated following the equations of Section A.2.3, for the three-dimensional case. With those at hand, the function $\boldsymbol{Y}(\boldsymbol{X})$ is computed as

$$\boldsymbol{Y}(\boldsymbol{X}) = \begin{cases} \displaystyle\sum_{i=1}^{3} y(x_i)\, \boldsymbol{E}_i & \text{if } x_1 \neq x_2 \neq x_3 \\ y(x_a)\, \boldsymbol{E}_a + y(x_b)\, (\boldsymbol{I} - \boldsymbol{E}_a) & \text{if } x_a \neq x_b = x_c \\ y(x_1)\, \boldsymbol{I} & \text{if } x_1 = x_2 = x_3 \end{cases} \tag{A.30}$$

where the subscripts (a, b, c) are cyclic permutations of $(1, 2, 3)$.

The computation of the derivative, $\mathsf{D}(\boldsymbol{X})$, follows the expressions

$$\mathsf{D}(\boldsymbol{X}) = \begin{cases} \displaystyle\sum_{a=1}^{3} \Big\{ \tfrac{y(x_a)}{(x_a-x_b)(x_a-x_c)} \Big[\frac{\mathrm{d}\boldsymbol{X}^2}{\mathrm{d}\boldsymbol{X}} - (x_b+x_c)\,\mathsf{I} \\ \qquad\qquad - \left[(x_a - x_b) + (x_a - x_c)\right] \boldsymbol{E}_a \otimes \boldsymbol{E}_a \\ \qquad\qquad\quad - \ (x_b - x_c)\,(\boldsymbol{E}_b \otimes \boldsymbol{E}_b - \boldsymbol{E}_c \otimes \boldsymbol{E}_c) \Big] + \ y'(x_a)\ \boldsymbol{E}_a \otimes \boldsymbol{E}_a \Big\} & \text{if } x_1 \neq x_2 \neq x_3 \\ s_1 \dfrac{\mathrm{d}\boldsymbol{X}^2}{\mathrm{d}\boldsymbol{X}} - s_2\,\mathsf{I} - s_3\, \boldsymbol{X} \otimes \boldsymbol{X} + s_4\, \boldsymbol{X} \otimes \boldsymbol{I} + s_5\, \boldsymbol{I} \otimes \boldsymbol{X} - s_6\, \boldsymbol{I} \otimes \boldsymbol{I} & \text{if } x_a \neq x_b = x_c \\ y'(x_1)\,\mathsf{I} & \text{if } x_1 = x_2 = x_3 \end{cases} \tag{A.31}$$

where $\mathrm{d}\boldsymbol{X}^2/\mathrm{d}\boldsymbol{X}$ denotes the derivative of the square of a tensor. Its cartesian components are given by:

$$\left[\frac{\mathrm{d}\boldsymbol{X}^2}{\mathrm{d}\boldsymbol{X}}\right]_{ijkl} = \frac{1}{2}\left(\delta_{ik} X_{lj} + \delta_{il} X_{kj} + \delta_{jl} X_{ik} + \delta_{kj} X_{il}\right). \tag{A.32}$$

The scalars s_1, s_2,..., s_6 have been defined as:

$$\begin{aligned} s_1 &= \tfrac{y(x_a)-y(x_c)}{(x_a-x_c)^2} - \tfrac{y'(x_c)}{x_a-x_c} \\ s_2 &= 2x_c\, \tfrac{y(x_a)-y(x_c)}{(x_a-x_c)^2} - \tfrac{x_a+x_c}{x_a-x_c}\, y'(x_c) \\ s_3 &= 2\, \tfrac{y(x_a)-y(x_c)}{(x_a-x_c)^3} - \tfrac{y'(x_a)+y'(x_c)}{(x_a-x_c)^2} \\ s_4 &= s_5 = x_c\, s_3 \\ s_6 &= x_c^2\, s_3 \end{aligned} \tag{A.33}$$

As remarked by De Souza Neto *et al.* (2004), the closed expressions (A.27) and (A.31) for the function derivative are equivalent to those derived by Carlson & Hoger (1986). Their equivalence can be established by considering the standard identity for the directional derivative of the square of a tensor in a generic direction $\boldsymbol{T}$:

$$\frac{\mathrm{d}\boldsymbol{X}^2}{\mathrm{d}\boldsymbol{X}}[\boldsymbol{T}] = \boldsymbol{X}\boldsymbol{T} + \boldsymbol{T}\boldsymbol{X}\,,$$

together with the identity:

$$(\boldsymbol{E}_i \otimes \boldsymbol{E}_i)\,\boldsymbol{T} = \boldsymbol{E}_i\, \boldsymbol{T} \boldsymbol{E}_i\,,$$

demonstrated in Carlson & Hoger (1986), and the closed formulae (A.11) for $\boldsymbol{E}_i$.

Appendix B

Linearisation of the internal virtual work

In this appendix we present the derivation of the linearised version of the virtual work equations. Linearisation of the virtual work gives rise to the tangent moduli which take part in the assemblage of the tangent stiffness matrix - a crucial component of the implicit finite element solution procedure described in Chapter 4. In particular, we show the basic steps in the linearisation of the virtual work equation leading to the element tangent stiffness expressions (6.42) and (6.43).

B.1 The virtual work equation

Let $\mathcal{B}$ be a body which occupies an open region of $\mathbb{R}^3$ with a regular boundary $\partial\mathcal{B}$ in its initial configuration. The deformation $\boldsymbol{\varphi} : \mathcal{B} \to \mathbb{R}^3$ maps the initial configuration of $\mathcal{B}$ onto its current configuration $\boldsymbol{\varphi}(\mathcal{B})$. We consider $\mathcal{B}$ subjected to body forces in its interior and surface tractions prescribed on the portion $\Gamma_{\boldsymbol{\sigma}}$ of the boundary $\partial\mathcal{B}$. On the remaining part Γ_u of the boundary, the deformation is prescribed by the function $\bar{\boldsymbol{u}}$, i.e., the set of kinematically admissible displacements of $\mathcal{B}$ is defined by:

$$\mathcal{C} = \left\{\boldsymbol{u} : \mathcal{B} \to \mathbb{R}^3, \text{sufficiently smooth} \,|\boldsymbol{u} = \bar{\boldsymbol{u}} \text{ on } \Gamma_u\right\}$$

Limited to the quasi-static case, the *principle of virtual work* (here stated in its spatial version) establishes that $\mathcal{B}$ is in equilibrium if and only if its Cauchy stress field satisfies:

$$G(\boldsymbol{u}, \boldsymbol{\eta}) := G^{\text{int}}(\boldsymbol{u}, \boldsymbol{\eta}) - \int_{\varphi(\mathcal{B})} \boldsymbol{b} \cdot \boldsymbol{\eta} \, \mathrm{d}v - \int_{\varphi(\Gamma_{\boldsymbol{\sigma}})} \boldsymbol{t} \cdot \boldsymbol{\eta} \, \mathrm{d}a = 0 \quad \forall \boldsymbol{\eta} \in \mathcal{V} \quad \text{(B.1)}$$

where $\boldsymbol{b}$ and $\boldsymbol{t}$ are respectively the body force and surface traction fields referred to the current configuration and the internal virtual work is defined as:

$$G^{\mathrm{int}}\,(\boldsymbol{u},\,\boldsymbol{\eta}) = \int_{\varphi(\mathcal{B})} \boldsymbol{\sigma} : \nabla_x\,\boldsymbol{\eta} - \boldsymbol{b}\cdot\boldsymbol{\eta}\,\mathrm{d}v \tag{B.2}$$

where $\nabla_x(\cdot)$ denotes the gradient of $(\cdot)$ with respect to the current configuration $\boldsymbol{\varphi}(\mathcal{B})$. The space of virtual displacements, $\mathcal{V}$, is defined as:

$$\mathcal{V} = \left\{\boldsymbol{\eta} : \boldsymbol{\varphi}(\mathcal{B}) \to \mathbb{R}^3, \text{sufficiently smooth}\,|\boldsymbol{\eta} = 0 \text{ on } \boldsymbol{\varphi}(\Gamma_u)\right\}.$$

In the present context, the dependence of the functional G on $\boldsymbol{u}$ stems only from the internal virtual work through the constitutive dependence of $\boldsymbol{\sigma}$ on $\boldsymbol{F}$ $[\boldsymbol{\sigma} = \boldsymbol{\sigma}(\boldsymbol{F})]$ and the functional dependence of $\boldsymbol{F}$ on the field $\boldsymbol{u}$. The fundamental quasi-static boundary problem is stated as: 'Find a kinematically admissible displacement field, $\boldsymbol{u} \in \mathcal{C}$, such that $\mathcal{B}$ is in equilibrium'.

B.2 Virtual work linearisation

The linearisation of the above *boundary value problem* with respect to the unknown $\boldsymbol{u}$ about an arbitrary argument $\boldsymbol{u}^*$ consists in finding the field $\boldsymbol{d}$ such that:

$$L(\boldsymbol{d},\,\boldsymbol{\eta}) \equiv G^{\mathrm{int}}(\boldsymbol{u}^*,\,\boldsymbol{\eta}) + \mathrm{D}\,G^{\mathrm{int}}(\boldsymbol{u}^*,\,\boldsymbol{\eta})[\boldsymbol{d}] = 0$$

where L is the linearised virtual work functional and

$$D\,G^{\mathrm{int}}(\boldsymbol{u}^*,\,\boldsymbol{\eta})[\boldsymbol{d}] = \left.\frac{\mathrm{d}}{\mathrm{d}\,\varepsilon}\right|_{\varepsilon\,=\,0} G^{\mathrm{int}}(\boldsymbol{u}^* + \epsilon\,\boldsymbol{d},\,\boldsymbol{\eta}) \tag{B.3}$$

is the directional derivative of the internal virtual work functional at $\boldsymbol{u}^*$ in the direction of $\boldsymbol{d}$.

In order to derive a spatial formula for the linearised virtual work functional, from which the spatial tangent stiffness can be obtained, we proceed as follows. Firstly we map (B.2) to the material configuration. Then, we linearise the material form and map the linearised expression back to the spatial configuration.

B.2.1 Map internal virtual work to the material configuration

Let us start by observing the following relation for the first Piola-Kirchoff stress:

$$\boldsymbol{P} \equiv \left(\det\boldsymbol{F}\right)\,\boldsymbol{\sigma}\,\boldsymbol{F}^{-\mathrm{T}} = \left(\det\boldsymbol{F}\right)\hat{\boldsymbol{\sigma}}(\bar{\boldsymbol{F}})\,\boldsymbol{F}^{-\mathrm{T}} = \left(\frac{\sum_{i\in\mathcal{P}} v_i}{\sum_{j\in\mathcal{P}} V_j\,\det\boldsymbol{F}}\right)^{-\frac{2}{3}} \hat{\boldsymbol{P}}(\bar{\boldsymbol{F}}) \tag{B.4}$$

where we have defined

$$\hat{\boldsymbol{P}}(\bar{\boldsymbol{F}}) \equiv (\det\bar{\boldsymbol{F}})\,\hat{\boldsymbol{\sigma}}(\bar{\boldsymbol{F}})\ \boldsymbol{F}^{-\mathrm{T}} \tag{B.5}$$

and the fact that the modified deformation gradient $\bar{\boldsymbol{F}}$ is used in the computation of the stress has been taken into account. With the above definition, we write the following *material version* of the F-bar-Patch internal virtual work functional:

$$G^{\mathrm{int}}_{(e)}\,(\boldsymbol{u},\boldsymbol{\eta}) = \int_{\Omega^{(e)}} \left(\frac{\sum_{i\in\mathcal{P}} v_i}{\sum_{j\in\mathcal{P}} V_j\ \det\boldsymbol{F}}\right)^{-\frac{2}{3}} \hat{\boldsymbol{P}}(\bar{\boldsymbol{F}}) : \nabla_p\,\boldsymbol{\eta}\,\mathrm{d}v \tag{B.6}$$

where the dependence of G^{int} on $\boldsymbol{u}$ comes from the dependence of $\bar{\boldsymbol{F}}$ on $\boldsymbol{u}$.

B.2.2 Linearisation in the material configuration

The directional derivative of G^{int} in a direction $\boldsymbol{d}$ is given by:

$$\mathrm{D}G^{\mathrm{int}}_{(e)}(\boldsymbol{u},\,\boldsymbol{\eta})[\boldsymbol{d}] = \left.\frac{\mathrm{d}}{\mathrm{d}\,\varepsilon}\right|_{\varepsilon=0} \int_{\Omega^{(e)}} \left[\frac{\left(\sum_{i\in\mathcal{P}} V_i \det\boldsymbol{F}_i\right)_\epsilon}{\sum_{j\in\mathcal{P}} V_j \det\boldsymbol{F}_\epsilon}\right]^{-\frac{2}{3}} \hat{\boldsymbol{P}}(\bar{\boldsymbol{F}}_\epsilon) : \nabla_p\,\boldsymbol{\eta}\,\mathrm{d}v \tag{B.7}$$

Applying the chain rule to the previous expression,

$$\begin{aligned}\mathrm{D}G^{\mathrm{int}}_{(e)}(\boldsymbol{u},\,\boldsymbol{\eta})[\boldsymbol{d}] = &\int_{\Omega^{(e)}} \left.\frac{\mathrm{d}}{\mathrm{d}\,\varepsilon}\right|_{\varepsilon=0} \left\{\left[\frac{\left(\sum_{i\in\mathcal{P}} V_i \det\boldsymbol{F}_i\right)_\epsilon}{\sum_{j\in\mathcal{P}} V_j \det\boldsymbol{F}_\epsilon}\right]^{-\frac{2}{3}}\right\} \hat{\boldsymbol{P}}(\bar{\boldsymbol{F}}) : \nabla_p\,\boldsymbol{\eta}\,\mathrm{d}v \\ &+ \int_{\Omega^{(e)}} \left(\frac{\sum_{i\in\mathcal{P}} V_i \det\boldsymbol{F}_i}{\sum_{j\in\mathcal{P}} V_j \det\boldsymbol{F}}\right)^{-\frac{2}{3}} \left.\frac{\mathrm{d}}{\mathrm{d}\,\varepsilon}\right|_{\varepsilon=0} \left[\hat{\boldsymbol{P}}(\bar{\boldsymbol{F}}_\epsilon)\right] : \nabla_p\,\boldsymbol{\eta}\,\mathrm{d}v\end{aligned} \tag{B.8}$$

Let us consider the derivation needed for the first term of (B.8):

$$\begin{aligned}\left.\frac{\mathrm{d}}{\mathrm{d}\,\varepsilon}\right|_{\varepsilon=0} \left[\frac{\left(\sum_{i\in\mathcal{P}} V_i \det\boldsymbol{F}_i\right)_\epsilon}{\sum_{j\in\mathcal{P}} V_j \det\boldsymbol{F}_\epsilon}\right]^{-\frac{2}{3}} = -\frac{2}{3}\left(\frac{\bar{J}}{J}\right)^{-\frac{5}{3}} \\ \left[\frac{\sum_{i\in\mathcal{P}} v_i(\boldsymbol{F}_i^{-\mathrm{T}} : \nabla_p\,\boldsymbol{d}_i - \boldsymbol{F}^{-\mathrm{T}} : \nabla_p\,\boldsymbol{d})}{J\,V_{\mathrm{patch}}}\right]\end{aligned} \tag{B.9}$$

where J, $\bar{J}$, v_i and V_{patch} stand for $\det\boldsymbol{F}$, $\det\bar{\boldsymbol{F}}$, $V_i \det\boldsymbol{F}_i$ and $\sum_{j\in\mathcal{P}} V_j$, respectively. It is also necessary to linearise $\hat{\boldsymbol{P}}(\bar{\boldsymbol{F}})$,

$$\left.\frac{\mathrm{d}}{\mathrm{d}\,\varepsilon}\right|_{\varepsilon=0} \left[\hat{\boldsymbol{P}}(\bar{\boldsymbol{F}}_\epsilon)\right] = \frac{\mathrm{d}\hat{\boldsymbol{P}}(\bar{\boldsymbol{F}}_\epsilon)}{\mathrm{d}\bar{\boldsymbol{F}}_\epsilon} : \left.\frac{\mathrm{d}\bar{\boldsymbol{F}}_\epsilon}{\mathrm{d}\epsilon}\right|_{\epsilon=0} \tag{B.10}$$

From the definition of the first elasticity tensor,

$$\frac{\mathrm{d}\hat{\boldsymbol{P}}(\bar{\boldsymbol{F}}_\epsilon)}{\mathrm{d}\bar{\boldsymbol{F}}_\epsilon} = \mathsf{A}(\bar{\boldsymbol{F}}) \tag{B.11}$$

only the linearisation of $\bar{\boldsymbol{F}}_\epsilon$ needs to be carried out. From the definition of $\bar{\boldsymbol{F}}$,

$$\left.\frac{\mathrm{d}\bar{\boldsymbol{F}}_\epsilon}{\mathrm{d}\epsilon}\right|_{\epsilon=0} = \left.\frac{\mathrm{d}}{\mathrm{d}\,\varepsilon}\right|_{\varepsilon=0} \left\{ \left[\frac{\left(\sum_{i\in\mathcal{P}} V_i \det\boldsymbol{F}_i\right)_\epsilon}{\sum_{j\in\mathcal{P}} V_j \det\boldsymbol{F}_\epsilon} \right]^{\frac{1}{3}} \right\} \boldsymbol{F} + \left(\frac{\sum_{i\in\mathcal{P}} V_i \det\boldsymbol{F}_i}{\sum_{j\in\mathcal{P}} V_j \det\boldsymbol{F}} \right)^{\frac{1}{3}} \frac{\mathrm{d}\boldsymbol{F}_\epsilon}{\mathrm{d}\epsilon} \tag{B.12}$$

Rearranging the terms after substitution in (B.12) of the previous result (B.9) leads to:

$$\begin{aligned} \left.\frac{\mathrm{d}}{\mathrm{d}\,\varepsilon}\right|_{\varepsilon=0} \left[\hat{\boldsymbol{P}}(\bar{\boldsymbol{F}}_\epsilon)\right] &= \mathsf{A}(\bar{\boldsymbol{F}}) : \left(\frac{\bar{J}}{J}\right)^{\frac{1}{3}} \nabla_p\,\boldsymbol{d} \\ &+ \mathsf{A}(\bar{\boldsymbol{F}}) : \left\{ \frac{1}{3}\left(\frac{\bar{J}}{J}\right)^{-\frac{2}{3}} \left[\frac{\sum_{i\in\mathcal{P}} v_i(\,\boldsymbol{F}_i^{-\mathrm{T}} : \nabla_p\,\boldsymbol{d}_i - \boldsymbol{F}^{-\mathrm{T}} : \nabla_p\,\boldsymbol{d})}{J\,V_{\text{patch}}} \right] \boldsymbol{F} \right\} \end{aligned} \tag{B.13}$$

Then, we obtain the final expression for the directional derivative of G^{int} in the *material configuration*:

$$\begin{aligned} \mathrm{D}G^{\text{int}}_{(e)}\,(\boldsymbol{u},\,\boldsymbol{\eta})\,[\boldsymbol{d}] &= \left(\frac{\bar{J}}{J}\right)^{-\frac{1}{3}} \int_{\Omega^{(e)}} \nabla_p\,\boldsymbol{\eta} : \mathsf{A}(\bar{\boldsymbol{F}}) : \nabla_p\,\boldsymbol{d}\,\mathrm{d}v \\ -\frac{2}{3}\left(\frac{\bar{J}}{J}\right)^{-\frac{5}{3}} &\int_{\Omega^{(e)}} \nabla_p\,\boldsymbol{\eta} : \left[\frac{\sum_{i\in\mathcal{P}} v_i(\boldsymbol{F}_i^{-\mathrm{T}} : \nabla_p\,\boldsymbol{d}_i - \boldsymbol{F}^{-\mathrm{T}} : \nabla_p\,\boldsymbol{d})}{J\,V_{\text{patch}}} \right] \hat{\boldsymbol{P}}(\bar{\boldsymbol{F}})\,\mathrm{d}v \\ +\frac{1}{3}\left(\frac{\bar{J}}{J}\right)^{-\frac{4}{3}} &\int_{\Omega^{(e)}} \nabla_p\,\boldsymbol{\eta} : \mathsf{A}(\bar{\boldsymbol{F}}) : \left[\frac{\sum_{i\in\mathcal{P}} v_i(\,\boldsymbol{F}_i^{-\mathrm{T}} : \nabla_p\,\boldsymbol{d}_i - \boldsymbol{F}^{-\mathrm{T}} : \nabla_p\,\boldsymbol{d})}{J\,V_{\text{patch}}} \right] \boldsymbol{F}\,\mathrm{d}v \end{aligned} \tag{B.14}$$

B.2.3 Map the linearised expression to the spatial configuration

The next step now is to obtain the *spatial version* of the expression for the directional derivative of G^{int}. By noting that, for an arbitrary second order tensor $\boldsymbol{M}$, we have

$$(\boldsymbol{M} \otimes \boldsymbol{F}^{-\mathrm{T}}) : \nabla_p\,\boldsymbol{d} = (\boldsymbol{F}^{-\mathrm{T}} : \nabla_p\,\boldsymbol{d})\,\boldsymbol{M} = (\boldsymbol{I} : \nabla_p\,\boldsymbol{d}\boldsymbol{F}^{-1})\,\boldsymbol{M} = (\boldsymbol{M} \otimes \boldsymbol{I}) : \nabla_x\,\boldsymbol{d}$$

the directional derivative of G^{int} can be rewritten as

$$
\begin{aligned}
\mathrm{D}G^{\text{int}}_{(e)}\,(\boldsymbol{u},\,\boldsymbol{\eta})\,[\boldsymbol{d}] = {} & \left(\frac{\bar{J}}{J}\right)^{-\frac{1}{3}} \int_{\Omega^{(e)}} \nabla_p\,\boldsymbol{\eta} : \mathsf{A}(\bar{\boldsymbol{F}}\,) : \nabla_p\,\boldsymbol{d}\,\mathrm{d}v \\
& - \frac{2}{3}\left(\frac{\bar{J}}{J}\right)^{-\frac{5}{3}} \int_{\Omega^{(e)}} \nabla_p\,\boldsymbol{\eta} : [\hat{\boldsymbol{P}}(\bar{\boldsymbol{F}}\,) \otimes \boldsymbol{I}\,] : \left[\frac{\sum_{i\in\mathcal{P}} v_i(\nabla_x\,\boldsymbol{d}_i - \nabla_x\,\boldsymbol{d})}{J\,V_{\text{patch}}}\right] \mathrm{d}v \\
& + \frac{1}{3}\left(\frac{\bar{J}}{J}\right)^{-\frac{4}{3}} \int_{\Omega^{(e)}} \nabla_p\,\boldsymbol{\eta} : \mathsf{A}(\bar{\boldsymbol{F}}\,) : \left[\frac{\sum_{i\in\mathcal{P}} v_i(\boldsymbol{F} \otimes \boldsymbol{I}) : (\nabla_x\,\boldsymbol{d}_i - \nabla_x\,\boldsymbol{d})}{J\,V_{\text{patch}}}\right] \mathrm{d}v
\end{aligned}
\tag{B.15}
$$

The first integral in the sum above (B.15) can be written as:

$$
\begin{aligned}
& \left(\frac{\bar{J}}{J}\right)^{-\frac{1}{3}} \int_{\Omega^{(e)}} \nabla_p\,\boldsymbol{\eta} : \mathsf{A}(\bar{\boldsymbol{F}}\,) : \nabla_p\,\boldsymbol{d}\,\mathrm{d}v = \\
& \quad = \left(\frac{\bar{J}}{J}\right)^{-\frac{1}{3}} \int_{\Omega^{(e)}} (\nabla_p\,\boldsymbol{\eta})_{ij}\,[\,\mathsf{A}(\bar{\boldsymbol{F}}\,)]_{ijkl}\,(\nabla_p\,\boldsymbol{d})_{kl}\,\mathrm{d}v \\
& \quad = \left(\frac{\bar{J}}{J}\right)^{-\frac{1}{3}} \int_{\varphi\left(\Omega^{(e)}\right)} (\nabla_x\,\boldsymbol{\eta})_{ij}\,\boldsymbol{F}_{jk}\,[\,\mathsf{A}(\bar{\boldsymbol{F}}\,)]_{iklm}\,(\nabla_x\,\boldsymbol{d})_{ln}\,\boldsymbol{F}_{nm}\,\frac{1}{J}\,\mathrm{d}v \\
& \quad = \int_{\varphi\left(\Omega^{(e)}\right)} (\nabla_x\,\boldsymbol{\eta})_{ij}\,\frac{1}{\bar{J}}\,\bar{\boldsymbol{F}}_{jk}\,\bar{\boldsymbol{F}}_{nm}\,[\,\mathsf{A}(\bar{\boldsymbol{F}}\,)]_{iklm}\,(\nabla_x\,\boldsymbol{d})_{ln}\,\mathrm{d}v \\
& \quad = \int_{\varphi\left(\Omega^{(e)}\right)} (\nabla_x\,\boldsymbol{\eta})_{ij}\,[\,\mathsf{a}(\bar{\boldsymbol{F}}\,)]_{ijln}\,(\nabla_x\,\boldsymbol{d})_{ln}\,\mathrm{d}v \\
& \quad = \int_{\varphi\left(\Omega^{(e)}\right)} \nabla_x\,\boldsymbol{\eta} :\ \mathsf{a}(\bar{\boldsymbol{F}}\,) :\ \nabla_x\,\boldsymbol{d}\,\mathrm{d}v
\end{aligned}
\tag{B.16}
$$

The *spatial version* of the second term in the sum (B.15) is to be evaluated now:

$$
\begin{aligned}
& -\frac{2}{3}\left(\frac{\bar{J}}{J}\right)^{-\frac{5}{3}} \int_{\Omega^{(e)}} \nabla_p\,\boldsymbol{\eta} : [\hat{\boldsymbol{P}}(\bar{\boldsymbol{F}}\,) \otimes \boldsymbol{I}\,] : \left[\frac{\sum_{i\in\mathcal{P}} v_i(\nabla_x\,\boldsymbol{d}_i - \nabla_x\,\boldsymbol{d})}{J\,V_{\text{patch}}}\right] \mathrm{d}v = \\
& \quad = -\tfrac{2}{3\,J\,V_{\text{patch}}} \left(\tfrac{\bar{J}}{J}\right)^{-\frac{5}{3}} \sum_{i\in\mathcal{P}} \int_{\Omega^{(e)}} (\nabla_p\,\boldsymbol{\eta})_{kj}\,[\hat{\boldsymbol{P}}(\bar{\boldsymbol{F}}\,)]_{kj}\,\delta_{lm}\,v_i(\nabla_x\,\boldsymbol{d}_i - \nabla_x\,\boldsymbol{d})_{lm}\,\mathrm{d}v
\end{aligned}
$$

$$
\begin{aligned}
&= -\tfrac{2}{3J\,V_{\text{patch}}} \left(\tfrac{J}{\bar{J}}\right)^{\frac{5}{3}} \sum_{i\in\mathcal{P}} \int_{\varphi\left(\Omega^{(e)}\right)} (\nabla_x \boldsymbol{\eta})_{kj} \boldsymbol{F}_{jl}\, [\hat{\boldsymbol{P}}(\bar{\boldsymbol{F}})]_{kl}\, \delta_{mn} v_i\, (\nabla_x \boldsymbol{d}_i - \nabla_x \boldsymbol{d})_{mn} \frac{\mathrm{d}v}{J} \\
&= -\tfrac{2}{3J\,V_{\text{patch}}} \left(\tfrac{J}{\bar{J}}\right) \sum_{i\in\mathcal{P}} \int_{\varphi\left(\Omega^{(e)}\right)} (\nabla_x \boldsymbol{\eta})_{kj} \bar{\boldsymbol{F}}_{jl}\, [\hat{\boldsymbol{P}}(\bar{\boldsymbol{F}})]_{kl}\, \delta_{mn} v_i\, (\nabla_x \boldsymbol{d}_i - \nabla_x \boldsymbol{d})_{mn} \frac{\mathrm{d}v}{\bar{J}} \\
&= -\tfrac{2}{3\,v_{\text{patch}}} \sum_{i\in\mathcal{P}} \int_{\varphi\left(\Omega^{(e)}\right)} v_i (\nabla_x \boldsymbol{\eta})_{kj} \frac{1}{\bar{J}}\, \bar{\boldsymbol{F}}_{jl}\, [\hat{\boldsymbol{P}}(\bar{\boldsymbol{F}})]_{kl}\, \delta_{mn}\, (\nabla_x \boldsymbol{d}_i - \nabla_x \boldsymbol{d})_{mn}\, \mathrm{d}v \\
&= -\tfrac{2}{3\,v_{\text{patch}}} \sum_{i\in\mathcal{P}} \int_{\varphi\left(\Omega^{(e)}\right)} v_i (\nabla_x \boldsymbol{\eta})_{kj} [\,\hat{\boldsymbol{\sigma}}(\bar{\boldsymbol{F}})]_{kj}\, \delta_{lm}\, (\nabla_x \boldsymbol{d}_i - \nabla_x \boldsymbol{d})_{lm}\, \mathrm{d}v \\
&= -\tfrac{2}{3\,v_{\text{patch}}} \sum_{i\in\mathcal{P}} \int_{\varphi\left(\Omega^{(e)}\right)} v_i (\nabla_x \boldsymbol{\eta}) : [\,\hat{\boldsymbol{\sigma}}(\bar{\boldsymbol{F}}) \otimes \boldsymbol{I}] : (\nabla_x \boldsymbol{d}_i - \nabla_x \boldsymbol{d})\, \mathrm{d}v
\end{aligned}
\tag{B.17}
$$

For the *spatial version* of the third term in the sum (B.15), we have:

$$
\begin{aligned}
&\frac{1}{3}\left(\frac{J}{\bar{J}}\right)^{\frac{4}{3}} \int_{\Omega^{(e)}} \nabla_p \boldsymbol{\eta} : \mathsf{A}(\bar{\boldsymbol{F}}) : \left[\frac{\sum_{i\in\mathcal{P}} v_i (\boldsymbol{F} \otimes \boldsymbol{I}) : (\nabla_x \boldsymbol{d}_i - \nabla_x \boldsymbol{d})}{J\,V_{\text{patch}}}\right] \mathrm{d}v = \\
&= \tfrac{1}{3\,J\,V_{\text{patch}}} \left(\tfrac{J}{\bar{J}}\right)^{\frac{4}{3}} \sum_{i\in\mathcal{P}} \int_{\Omega^{(e)}} (\nabla_p \boldsymbol{\eta})_{kj} [\mathsf{A}(\bar{\boldsymbol{F}})]_{kjlm}\, v_i\, \boldsymbol{F}_{lm} \delta_{op} (\nabla_x \boldsymbol{d}_i - \nabla_x \boldsymbol{d})_{op}\, \mathrm{d}v \\
&= \tfrac{1}{3\,J\,V_{\text{patch}}} \left(\tfrac{J}{\bar{J}}\right)^{\frac{4}{3}} \sum_{i\in\mathcal{P}} \int_{\varphi\left(\Omega^{(e)}\right)} (\nabla_x \boldsymbol{\eta})_{kj} \boldsymbol{F}_{jl} [\mathsf{A}(\bar{\boldsymbol{F}})]_{klmo}\, v_i\, \boldsymbol{F}_{mo} \delta_{pq} (\nabla_x \boldsymbol{d}_i - \nabla_x \boldsymbol{d})_{pq} \frac{\mathrm{d}v}{\bar{J}} \\
&= \tfrac{1}{3\,J\,V_{\text{patch}}} \left(\tfrac{J}{\bar{J}}\right) \sum_{i\in\mathcal{P}} \int_{\varphi\left(\Omega^{(e)}\right)} (\nabla_x \boldsymbol{\eta})_{kj} \bar{\boldsymbol{F}}_{jl} [\mathsf{A}(\bar{\boldsymbol{F}})]_{klmo}\, v_i\, \bar{\boldsymbol{F}}_{mo} \delta_{pq} (\nabla_x \boldsymbol{d}_i - \nabla_x \boldsymbol{d})_{pq} \frac{\mathrm{d}v}{\bar{J}} \\
&= \tfrac{1}{3\,v_{\text{patch}}} \sum_{i\in\mathcal{P}} \int_{\varphi\left(\Omega^{(e)}\right)} v_i\, (\nabla_x \boldsymbol{\eta})_{kj}\, [\mathsf{a}(\bar{\boldsymbol{F}})]_{kjmr}\, \bar{\boldsymbol{F}}^{-1}_{ro}\, \bar{\boldsymbol{F}}_{mo}\, \delta_{pq} (\nabla_x \boldsymbol{d}_i - \nabla_x \boldsymbol{d})_{pq}\, \mathrm{d}v \\
&= \tfrac{1}{3\,v_{\text{patch}}} \sum_{i\in\mathcal{P}} \int_{\varphi\left(\Omega^{(e)}\right)} v_i\, (\nabla_x \boldsymbol{\eta})_{kj}\, [\mathsf{a}(\bar{\boldsymbol{F}})]_{kjmr}\, \delta_{mr}\, \delta_{pq} (\nabla_x \boldsymbol{d}_i - \nabla_x \boldsymbol{d})_{pq}\, \mathrm{d}v \\
&= \tfrac{1}{3\,v_{\text{patch}}} \sum_{i\in\mathcal{P}} \int_{\varphi\left(\Omega^{(e)}\right)} v_i\, (\nabla_x \boldsymbol{\eta}) : \mathsf{a}(\bar{\boldsymbol{F}}) : (\boldsymbol{I} \otimes \boldsymbol{I}) : (\nabla_x \boldsymbol{d}_i - \nabla_x \boldsymbol{d})\, \mathrm{d}v
\end{aligned}
\tag{B.18}
$$

By using the previous results, it is possible to write the *spatial version* of the directional derivative of $G^{\text{int}}_{(e)}$:

$$
\mathrm{D}G^{\text{int}}_{(e)}\,(\boldsymbol{u},\, \boldsymbol{\eta})\,[\boldsymbol{d}] = \int_{\varphi\left(\Omega^{(e)}\right)} \nabla_x \boldsymbol{\eta} :\, \mathsf{a}(\bar{\boldsymbol{F}}) :\, \nabla_x \boldsymbol{d}\, \mathrm{d}v
$$

$$\begin{aligned}
&-\frac{2}{3\,v_{\text{patch}}}\sum_{i\in\mathcal{P}}\int_{\varphi\left(\Omega^{(e)}\right)} v_i(\nabla_x\,\boldsymbol{\eta}) : [\,\hat{\boldsymbol{\sigma}}(\bar{\boldsymbol{F}}\,)\otimes\boldsymbol{I}\,] : (\nabla_x\,\boldsymbol{d}_i - \nabla_x\,\boldsymbol{d})\,\mathrm{d}v \\
&+\frac{1}{3\,v_{\text{patch}}}\sum_{i\in\mathcal{P}}\int_{\varphi\left(\Omega^{(e)}\right)} v_i\,(\nabla_x\,\boldsymbol{\eta}) : \mathsf{a}(\bar{\boldsymbol{F}}\,) : (\boldsymbol{I}\otimes\boldsymbol{I}) : (\nabla_x\,\boldsymbol{d}_i - \nabla_x\,\boldsymbol{d})\,\mathrm{d}v
\end{aligned} \tag{B.19}$$

The final expression for the *spatial version* of the directional derivative of $G^{\text{int}}_{(e)}$ can be rewritten as

$$\begin{aligned}
&\mathrm{D}G^{\text{int}}_{(e)}\,(\boldsymbol{u},\,\boldsymbol{\eta})\,[\boldsymbol{d}] = \int_{\varphi\left(\Omega^{(e)}\right)} \nabla_x\,\boldsymbol{\eta} :\, \mathsf{a}(\bar{\boldsymbol{F}}\,) :\, \nabla_x\,\boldsymbol{d}\,\mathrm{d}v \\
&+\int_{\varphi\left(\Omega^{(e)}\right)} \nabla_x\,\boldsymbol{\eta} : \left\{\frac{1}{3}\,\mathsf{a}(\bar{\boldsymbol{F}}\,) : (\boldsymbol{I}\otimes\boldsymbol{I}) - \frac{2}{3}\,[\,\hat{\boldsymbol{\sigma}}(\bar{\boldsymbol{F}}\,)\otimes\boldsymbol{I}\,]\right\} : \left(\frac{v_e}{v_{\text{patch}}} - 1\right)\nabla_x\,\boldsymbol{d}\,\mathrm{d}v \\
&+\int_{\varphi\left(\Omega^{(e)}\right)} \nabla_x\,\boldsymbol{\eta} : \left\{\frac{1}{3}\,\mathsf{a}(\bar{\boldsymbol{F}}\,) : (\boldsymbol{I}\otimes\boldsymbol{I}) - \frac{2}{3}\,[\,\hat{\boldsymbol{\sigma}}(\bar{\boldsymbol{F}}\,)\otimes\boldsymbol{I}\,]\right\} : \sum_{s\in\mathcal{P},s\neq e}\frac{v_s}{v_{\text{patch}}}\nabla_x\,\boldsymbol{d}_s\,\mathrm{d}v
\end{aligned} \tag{B.20}$$

Finally, the replacement of the gradient operators, tangent modulus and other relevant tensors with the corresponding finite element matrices in the previous expression leads to the tangent stiffness formulae:

$$\mathbf{K}_e = \mathbf{K}_{ee} + \mathbf{K}_{es} \tag{B.21}$$

where the the first term, $\mathbf{K}_{ee}$ is given by

$$\mathbf{K}_{ee} \;=\; \int_{\varphi(\Omega_e)} \mathbf{G}_e^T\;\mathbf{a}\;\mathbf{G}_e\,\mathrm{d}v \;+\; \left(\frac{v_e}{v_{\text{patch}}} - 1\right)\int_{\varphi(\Omega_e)} \mathbf{G}_e^T\;\mathbf{q}\;\mathbf{G}_e\;\mathrm{d}v \tag{B.22}$$

and the second term in (B.21) is given by

$$\mathbf{K}_{es} = \frac{v_e}{v_{\text{patch}}}\int_{\varphi(\Omega_e)} \mathbf{G}_e^T\,\mathbf{q}\;\mathbf{G}_s\,\mathrm{d}v\,, \qquad s\in\mathcal{P}\,;\; s\neq e\,, \tag{B.23}$$

where $\mathbf{a}$ is the matrix form of the fourth order spatial elasticity tensor now evaluated at $\boldsymbol{F} = \bar{\boldsymbol{F}}$, $\mathbf{G}_i$ denotes the conventional discrete (full) gradient operator of a generic element i and $\mathbf{q}$ is the matrix form of the fourth order tensor defined by:

$$\mathsf{q} = \tfrac{1}{3}\,\mathsf{a} : (\boldsymbol{I}\otimes\boldsymbol{I}) - \tfrac{2}{3}\,(\boldsymbol{\sigma}\otimes\boldsymbol{I})\;, \tag{B.24}$$

also computed at $\boldsymbol{F} = \bar{\boldsymbol{F}}$.